



**HAL**  
open science

## Optics and spectroscopy of gold nanowires

Priya Vasanthakumar

► **To cite this version:**

Priya Vasanthakumar. Optics and spectroscopy of gold nanowires. Other [cond-mat.other]. Université Paris Sud - Paris XI; Università degli studi (Pise, Italie), 2012. English. NNT : 2012PA112080 . tel-00922344

**HAL Id: tel-00922344**

**<https://theses.hal.science/tel-00922344>**

Submitted on 18 Apr 2014

**HAL** is a multi-disciplinary open access archive for the deposit and dissemination of scientific research documents, whether they are published or not. The documents may come from teaching and research institutions in France or abroad, or from public or private research centers.

L'archive ouverte pluridisciplinaire **HAL**, est destinée au dépôt et à la diffusion de documents scientifiques de niveau recherche, publiés ou non, émanant des établissements d'enseignement et de recherche français ou étrangers, des laboratoires publics ou privés.



UNIVERSITE PARIS-SUD

ÉCOLE DOCTORALE:  
ONDES ET MATIÈRE

Laboratoire AIMÉ COTTON

THÈSE DE DOCTORAT  
DISCIPLINE Physique

UNIVERSITÀ DI PISA

SCUOLA DI DOTTORATO  
IN SCIENZE DI BASE  
“GALILEO GALILEI”

NANO-LAB

DOTTORATO DI RICERCA  
in FISICA

Defended on 05/14/2012

by

PRIYA VASANTHAKUMAR

# OPTICS AND SPECTROSCOPY OF GOLD NANOWIRES

Co-supervisor: Anne DÉBARRE Directrice de recherche, CNRS, Laboratoire Aimé Cotton

Co-supervisor: Maria ALLEGRINI Professor, Università di Pisa

## Composition du jury

President of jury: Kenichi KONISHI, Professor, University of Pisa

Referees: Francesco BUATIER de MONGEOT, Professor, University of Genova  
Pierre-Michel ADAM, Professor, University of Technology of Troyes

Members: Odile STEPHAN, Professor, University Paris Sud  
Maria ALLEGRINI, co-Supervisor, Nano-Lab , University of Pisa  
Anne DÉBARRE, co-Supervisor, lab. Aimé Cotton, Univ. Paris Sud

Invited member: Mauro TONELLI, Professor, University of Pisa  
Francesco FUSO, Professor, University of Pisa



---

# Contents

<b>Summary</b>	<b>7</b>
<b>Resume</b>	<b>15</b>
<b>Introduction</b>	<b>23</b>
0.1 Nanoscience . . . . .	24
0.2 The Optical properties of metal nanostructures . . . . .	24
0.3 The interest in gold . . . . .	25
0.4 Plasmonics . . . . .	26
<b>1 Samples</b>	<b>31</b>
1.1 Gold nanowires arrays . . . . .	31
1.2 Gold nanobeads . . . . .	34
1.3 Gold nanowires . . . . .	34
<b>2 Plasmons</b>	<b>35</b>
2.1 Introduction . . . . .	35
2.2 Surface plasmon polariton excitation . . . . .	36
2.3 Surface plasmon propagation length . . . . .	38
2.4 Mie theory . . . . .	39
2.5 Gans theory . . . . .	42
2.6 Surface plasmon dependence on size . . . . .	42
2.7 Surface plasmon dependence on shape . . . . .	43
2.8 Surface plasmon dependence on refractive index . . . . .	44
<b>3 SERS</b>	<b>45</b>
3.1 Introduction . . . . .	45
3.1.1 Evolution of SERS . . . . .	46
3.2 Raman Spectroscopy . . . . .	46
3.3 SERS Enhancement Mechanisms . . . . .	48
3.3.1 Electromagnetic enhancement . . . . .	48
3.3.2 Chemical enhancement . . . . .	49

3.4	Enhancement Factor . . . . .	51
3.4.1	Single molecule enhancement factor . . . . .	51
3.4.2	Average enhancement factor . . . . .	51
3.5	Important parameters that dominates the SERS . . . . .	52
3.6	Surface enhanced resonance Raman scattering . . . . .	52
3.7	Experimental set up . . . . .	53
3.7.1	Dark field . . . . .	54
3.7.2	Probe molecules . . . . .	54
3.7.3	Sample preparation . . . . .	56
<b>4</b>	<b>SERS measurements - Isolated nanowires</b>	<b>59</b>
4.1	Introduction . . . . .	59
4.2	CTAB coated nanowires . . . . .	60
4.3	Dark field spectroscopy . . . . .	63
4.4	Propagation measurements . . . . .	67
4.5	Plasmon propagation dependence on Wavelength . . . . .	70
4.5.1	702 nm . . . . .	71
4.5.2	728 nm . . . . .	71
4.5.3	750 nm . . . . .	74
4.5.4	770 nm . . . . .	75
4.5.5	Summary of the different mechanisms . . . . .	76
4.5.6	Comparison . . . . .	76
4.6	Propagation Lengths . . . . .	81
4.7	SERS . . . . .	82
4.8	Dependence of SERS on wavelength . . . . .	83
4.9	Blinking . . . . .	88
4.10	Silane coated nanowires . . . . .	90
4.11	Background . . . . .	92
4.12	Single molecule regime evidenced by a two analyte analysis of propagation . . . . .	92
4.13	Single molecule regime . . . . .	95
4.14	Synopsis . . . . .	98
<b>5</b>	<b>SERS - Nanowire arrays</b>	<b>101</b>
5.1	Introduction . . . . .	101
5.2	Dipolar coupling model . . . . .	102
5.3	Electrostatic approximation . . . . .	102
5.4	Discrete dipole approximation . . . . .	103
5.5	Comparison between electrostatic approximation and DDSCAT . . . . .	105
5.6	Dependence on Inter particle distance . . . . .	106
5.7	Simulation of an ideal sample sample . . . . .	107

---

5.8	ATTO 740 . . . . .	108
5.9	Rhodamine 6G . . . . .	116
5.10	Effect of two reporters . . . . .	120
5.11	Polarization dependence of SERS . . . . .	123
5.11.1	Polarized hot-spot along the nanowires . . . . .	123
5.11.2	Charge transfer effect . . . . .	126
5.11.3	Polarized hot-spot across the nanowires . . . . .	127
5.12	Wavelength dependence of SERS . . . . .	131
5.13	Synopsis . . . . .	136
<b>6</b>	<b>SNOM</b>	<b>137</b>
6.1	Introduction . . . . .	137
6.2	Rayleigh criterion and diffraction limit . . . . .	137
6.3	Breaking the diffraction barrier . . . . .	140
6.4	Why SNOM? . . . . .	140
6.5	A brief history and evolution of SNOM . . . . .	141
6.6	Basic working principles of SNOM . . . . .	142
6.7	Shear force . . . . .	143
6.8	Experimental Set up . . . . .	143
<b>7</b>	<b>SNOM measurements - Nanowire arrays</b>	<b>147</b>
7.1	Introduction . . . . .	147
7.2	Constant excitation mode . . . . .	149
7.2.1	Produced maps . . . . .	152
7.3	Sample 1 . . . . .	154
7.3.1	Local field enhancement . . . . .	159
7.4	Sample 2 . . . . .	163
7.5	Reference samples . . . . .	167
7.6	Fixed excitation mode . . . . .	168
7.7	Sample 5 . . . . .	170
7.8	Synopsis . . . . .	177
	<b>Conclusions</b>	<b>183</b>
	<b>Appendix</b>	<b>187</b>
.1	DDSCAT . . . . .	187
.1.1	Input . . . . .	187
.1.2	Non-standard Shapes or Structures . . . . .	188
.1.3	Program Execution . . . . .	189
.1.4	Output . . . . .	190

References

191

---

# SUMMARY

The research addressed in this dissertation deals with the optical properties of metal nanostructures and in particular it is focused on plasmonic features of gold nanowires, which are investigated and assessed through different optical techniques like scanning near field optical microscopy (SNOM) and surface enhanced Raman spectroscopy (SERS).

To understand and control the interaction between light and matter is fundamental to science and to technology. As the field of photonics constantly strives to do so to make ever smaller devices, the diffraction limit of light emerges as a fundamental limitation. A number of new and novel applications like lab on a chip have inspired new ways to circumvent this issue. One solution to the problem, that is widely acknowledged and is fast growing is the research on plasmonics. Plasmonics is a blooming field in optoelectronics/nanophotonics that uses the peculiar optical properties of metal nanostructures to manipulate light at nanometer scales towards combined optical and electronic functions. There is a constant effort to have a better understanding of the plasmons and in this work, we present our contribution to such the ever growing research with the use of novel experiments.

The thesis is in cotutelle between the University of Pisa and University of Paris Sud and research has been done to Nanolab Department of Physics, University of Pisa and at Laboratoire Aimé Cotton CNRS and Université Paris-Sud. In this thesis work, the investigation of the optical properties pertaining to the gold nanowires is carried on by near-field techniques in Pisa and by SERS in Orsay.

The identification and characterization of local field enhancement effects on gold nanostructures and their relation to the morphology have been obtained with a custom made SNOM setup. With the aid of spatial resolution offered by non-propagating fields, SNOM owns the unique ability of mapping the space distribution of e.m. fields at the surface of a nanostructured sample without the constraints imposed by optical diffraction in conventional and confocal microscopy. As a consequence, optical properties can be retrieved on a lateral size scale comparable, or even better than the physical size of the nanostructures.

SERS on these samples addresses the effects of field enhancement associated with plasmon excitation. A sensitive probe of the enhancement is the detection of Raman signatures of suitable dye molecules adsorbed at the surface. With the use

of different dyes and different experimental parameters (wavelength, polarization), an effort has been made to disentangle the various contributions to SERS arising from such samples.

The deployment of these highly specialized techniques aims at improving the understanding of the plasmon excitation mechanisms in real systems, (different from the model systems often reported in the literature), while allowing for a detailed evaluation of their applicative potential in rapidly growing areas such as nanophotonics and high-sensitivity optical detection.

An outline of the thesis structure is given below.

In the introduction, we talk of the importance of studying the optical properties of metal nanoparticles and reasons for our choice of gold nanoparticles. Gold systems are scarcely investigated when compared to silver because of the limited losses of silver compared to gold in the visible range of wavelengths. However, in the near infra red region, the losses of gold and silver become comparable and gold is very useful in the case of biological systems since it is biocompatible in nature.

The chapter 2 describes the samples that we have used for our measurements. The SERS and SNOM measurements were done on gold nanowire arrays. These arrays have been custom made by the group of Prof. Buatier De Mongeot using an unconventional technique which is cost effective and straight forward compared to the other fabrication methods. The macroscopic transmission properties of these samples are discussed. We have also used the isolated gold nanowires in the SERS experiments. They are chemically grown commercial nanowires purchased from Nanopartz. There are two different nanowires used. One coated with cetyl trimethylammonium bromide (CTAB) and another with silane. They are 6  $\mu\text{m}$  in length and 30 nm in diameter (nominal). We have also used 50 nm nanobeads from BB international, for the SERS measurements along with the nanowires.

The chapter 3 gives an introduction to the concept of surface plasmons, both localized and propagating in nature. The often used theories to describe the plasmon in nanoparticles like the Mie theory are presented shortly. Various techniques used for exciting the surface plasmons are discussed. The dependence of the plasmon on various factors like size, shape and the refractive index of the surrounding medium are reviewed. Such a discussion is important to understand the results of our measurements which are presented in the later chapters.

The chapter 4 elaborates on the fundamentals of the SERS in a simple manner. The chapter has been written in such a way to give a basic idea of the important processes in the SERS. The experimental set up used along with the sample preparation are described in detail. The set up includes dark field microscopy for imaging the samples at the diffraction limit and uses a continuous wave tunable Ti:Sa laser with an output from 700 nm to 900 nm and a maximum power of 3 W. The intensity and the polarization of the incident beam can be varied by a

broadband half wave plate and a polarizer, respectively, which are controlled with a home written software. The properties of the dyes that have been used as probe for the SERS has been discussed.

The chapter 5 discusses the results of the SERS measurements on the isolated gold nanowires. The initial idea was to combine enhancement and propagation measurements on these nanowires. However, it was seen that it was difficult to see any propagation with just the nanowires. So nanobeads were added to these nanowires, which act as a mediator to couple the excitation to the nanowire. Such a technique to use nanobeads has been reported in literature. In the results, firstly, examples of dark field images and the plasmon spectra obtained at various locations are presented. It is seen clearly that the plasmon spectrum depends strongly on the position of measurement. Both the shape of the spectrum and the position of the resonance peak varies according to various factors like the presence of beads or the asymmetry at the end of the nanowire etc.. Next we have reported the plasmon propagation of the nanowires at different wavelengths. Four different wavelengths have been chosen : 702 nm, 728 nm, 750 nm and 770 nm. The choice was made to investigate the effect of wavelength on propagation while at the same time to correlate the plasmon spectrum to the propagation to understand the dependence of propagation to the plasmon shape. The propagation is visualized directly as the SERS or enhanced fluorescence signal that is the outcome of the interaction between the nanowire and the dye molecule used. The results put into evidence the conditions needed to observe plasmon propagation : the propagation is higher when the excitation wavelength is closer to the maximum of the plasmon resonance. The best is attained when the plasmon matches the molecular resonance. We have reported here a propagation distance of about 3.8  $\mu\text{m}$ . The maximum propagation length previously reported for gold nanowires in literature is 2.5  $\mu\text{m}$  by Krenn et al. Next the results on the SERS measurements are presented. The wavelength dependence of SERS was investigated. Such studies with the wavelength are hardly reported since very few Raman setups use tunable excitation source. We have seen that the evolution with the wavelength follows the same trend as that of plasmon propagation. The distance dependence of the SERS is presented and it is seen that with the increasing distance from the excitation point, the signal intensity falls gradually as expected. It is an additional evidence of the plasmon propagation witnessed. We have explained the various SERS mechanisms witnessed in our system with examples like blinking and the single molecule regime. The single molecule regime was attained in a number of hot-spots easily and was proved by using a two analyte technique. Two dyes, Rh6G and ATTO 740 were used together on the substrate and the results gave an irrefutable evidence for the single molecule SERS. The spectra recorded with both the dyes showed only the typical signature of one molecule at a time and never both. It is clear that only one kind of molecule

occupies the hot-spot at a time and it is replaced by the other kind when it moves away due to various factors like thermal effects. The novelty of our experiment is that we are able to correlate several optical properties of a system. At any given location on the nanowire, we have the dark field image, the plasmon spectrum at the location, the propagation and the SERS signal. Such a comprehensive study of the gold nanowire has not been reported in literature so far to the best of our knowledge. It gives a better understanding of the SERS and propagation properties of the gold nanowires.

The chapter 6 reviews the results obtained with SERS measurements on gold nanowire arrays (chapter 2). In the beginning of the chapter, I present the results of the simulations made in order to understand the behaviour of such systems. The motivation behind the simulations was also to explain some of our results. We have used the software DDSCAT based on discrete dipole approximation (DDA) for our calculations. We have made a comparison between the DDA and electrostatic approximation considering a simple situation. The nanowires were represented by slender ellipsoids. However their length was limited by the conditions for validity of the approximations. We have simulated the behaviour of the plasmon resonance with change in excitation polarization, size and the refractive index of the surrounding medium. The field around two or three closeby ellipsoids at two different excitation polarizations has been studied. It confirms the theory already reported that the field is maximum at the gap between two ellipsoids when the polarization is along the line joining the centers and much weaker in the other direction.

The underlying idea behind these measurements was to discriminate between the SERS enhancement factor corresponding to the nanowire plasmons on one hand from that related to molecular resonance excitation on the other hand. In fact the heterogeneity of the sample allowed us to disentangle different effects that contribute to SERS in such systems. The prerequisite was a large difference in SERS enhancement factors for polarization horizontal and vertical to the nanowire direction. In principle, a higher enhancement is expected if the polarization of the excitation (V configuration) is across the nanowires than when it is along (H configuration) it. However, the experimental results did not show a clear polarization dependence of the SERS signal with just ATTO 740 molecule and the signal was unstable. Then, a second molecule rhodamine 6G was co-deposited which is not in resonance with the plasmon of the sample. The SERS with Rh6G on the sample was made to ensure that it did not give any signal on its own, except on a very limited number of locations. There were two different effects observed on addition of rhodamine, a global effect and a local one. The global effect is the plasmon red shift of the sample which is confirmed by the appearance of strong low to medium frequency lines (which occurs only when the sample is deeply in resonance with the

molecule). This is in accordance with our simulations, which shows the plasmon is red shifted with an increasing refractive index of the surrounding molecule. The next important effect is on a local scale; the stability of the ATTO 740 increases and the enhancement is considerably increased. The reason behind such an effect is not exactly known, since it requires lot more studies of photochemical nature. However, we have given the possible processes that can occur with the help of literature, especially the effect of ions on SERS substrates or the process of competitive binding with metal in the presence of another ion. The polarization studies on the sample are reported and it is seen clearly that the signal falls rapidly by changing the polarization even by  $20^\circ$ . However, in this case the signal along H is higher than that along V direction. This situation occurs when the molecule sits between two particles along a nanowire rather than between two nanowires as is seen from our simulations. This can also be an evidence of the charge transfer effect between ATTO 740 and the metal and is explained in detail. Wavelength dependence of the signals has been investigated ranging from 700 nm to 780 nm keeping in mind to investigate the range both below and above the molecular resonance at 740 nm. An example is reported. The results show that the highest enhancement is reached when the wavelength is at around 745 nm, which is between the plasmon resonance of the sample, measured at the location, and the molecular resonance. The trend remains the same for both the polarization directions but the signal in V direction is quite high compared to the other one. The non zero signal in the H direction is explained with the electric field simulations around the ellipsoids.

The novel idea of these experiments is the use of two molecules to explore the contributions to SERS effects. Though an experiment was reported with two molecules by Ru et al, it was to serve as an evidence to single molecule regime. In our case the use of combined molecules represents thus a powerful, and partially unexplored, tool to understand the coupling between plasmon excitations occurring in closely packed gold nanostructures.

The chapter 7 gives an introduction to the basic concepts in the SNOM. The short history of the near field microscopy is presented with an effort to give a gist of the important ideas that help to understand the near field microscopy. The experimental set up used is explained in detail. Thanks to its sensitivity to near fields and to the associated sub-wavelength spatial resolution, SNOM has been frequently used in the past to analyze the occurrence and features of plasmons in nanostructured metal samples. A major step forward has been made in the realization of the collection mode apparatus with the implementation of a spatially controlled, quasi-diffraction limited illumination spot. Moreover, control of the polarization direction and the possibility to use different wavelengths are implemented in the setup. The unique capabilities of the apparatus for plasmon investigation involves the use of two different operating modes. A *constant* illumination mode, where

the illumination spot is kept fixed with respect to the near-field probe, can be used to build the map of the near field intensity at the sample surface and to correlate it with the morphology at the local scale, simultaneously recorded. The other operating mode, denoted as fixed illumination, allows for coupling radiation at a predefined position of the sample and observing the near-field intensity upon such localized excitation.

The chapter 8 examines the results of the near field experiments on the nanowire arrays. The motivation for the use of the collection mode SNOM and the novelty of the used illumination conditions (oblique, from top and in the far field) are explained along with the limitations of the measurements, related essentially to the impossibility for the SNOM to collect the near field at a very short distance from the surface, hence to mimic the conditions felt by the adsorbed molecules in SERS experiments. The main core of the chapter is devoted to the scans made in the constant illumination mode, aimed at identifying sites of field enhancement and at correlating them with the sample structure and morphology. The use of two wavelengths, the control of the polarization direction and the analysis of distinct samples, including blank ones (reference samples), enable unraveling the genuine role played by the plasmon excitation. Different tools are deployed to analyze the results, including both statistical methods (Probability Distribution Function - PDF, and Auto-Correlation Function - ACF) inspired by the literature dealing with random metal nanoparticle systems, and data manipulation strategies tuned to identify hot spots. In particular, it is found that field enhancement takes place only in the conditions leading to excite the plasmon resonance of the sample (V configuration and laser wavelength well within the resonance curve), whereas other illumination conditions (H configuration or wavelength far from the resonance peak) lead to maps dominated by simple scattering in the near field from individual nanoparticles or topography modulations. Careful correlation of the optical and topographical maps indicate that hot spots tend to sit mostly in the depressed regions of the sample, roughly corresponding to the inter-wire gap, and their occurrence is more likely in the vicinity of defects such as, bends, bifurcations, entanglement etc.. Measurements are also reported where the fixed illumination mode is used. Motivation for this approach is found in the search for propagation phenomena due to the co-operative excitation of plasmon oscillations in adjacent nanowires. Those measurements, which are still awaiting for further confirmation on other samples and for a larger statistics, demonstrate the role of plasmon resonance in ruling the scattering process in the near field and suggest the occurrence of unexpected phenomena when the polarization of the excitation radiation is at 45 degrees with respect to the nanowire axis.

While being partially unexplained, the results of the near field investigation point at a complicated interplay between the disorder at the local scale, due to the

nanoparticle-like morphology of the sample, and the global anisotropic ordering imposed by the nanowire structure, that both make our investigated samples markedly different with respect to samples considered in the literature, either model systems, typically produced according to a predefined regularity or random nanostructured samples following a fractal spatial distribution.

The final chapter, conclusion, summarizes the results obtained with our work and opens up new questions that deserve further efforts to be investigated.



---

# RESUME

Mon travail de doctorat s'intéresse aux propriétés optiques de nanostructures métalliques. Il est plus particulièrement centré sur l'étude des propriétés des plasmons de nanofils en or. Pour les analyser, j'ai mis en œuvre différentes méthodes, comme la microscopie de champ proche optique à balayage (SNOM) et la spectroscopie Raman par exaltation de surface (SERS).

La compréhension et le contrôle des interactions entre la lumière et la matière sont essentiels en recherche fondamentale comme pour les applications. Dans la course à la miniaturisation en photonique, la limite de diffraction est un obstacle fondamental. Plusieurs développements récents et des applications innovantes, comme les laboratoires sur puce (Lab on chip) ont inspiré des voies nouvelles pour dépasser la barrière de diffraction. La plasmonique est une des voies possibles qui a retenu l'attention ces dernières années. Ce domaine se développe très rapidement et correspond à un champ de recherche très actif en optoélectronique et en nanophotonique. Il exploite les propriétés optiques particulières des structures métalliques pour manipuler la lumière à l'échelle nanométrique dans le but de combiner fonctions optiques et électroniques. Un effort important est consenti pour obtenir une meilleure compréhension des plasmons. Je présente, dans ce manuscrit, ma contribution à cette recherche en pleine expansion, obtenue grâce à différentes expériences.

Ce doctorat a été réalisé en cotutelle entre l'Université de Pise et l'Université Paris-Sud et les recherches ont été effectuées au Nano-lab du département de Physique de l'Université de Pise et au laboratoire Aimé Cotton du CNRS et de l'Université Paris-Sud. Ce travail de thèse a été consacré à l'étude des propriétés optiques des nanofils en or par des méthodes de champ proche optique à Pise et par SERS à Orsay.

La mise en évidence et la caractérisation des effets locaux d'exaltation de champ sur des nanostructures en or et leur relation avec la morphologie ont été obtenues grâce à un microscope de champ proche optique construit au Nanolab. En exploitant la résolution spatiale liée à la détection de champs évanescents, la microscopie en champ proche offre la possibilité unique de cartographier les champs électromagnétiques à la surface d'un échantillon nanostructuré en s'affranchissant de la limite de diffraction, contrairement au cas des microscopies conventionnelles.

ou confocale. Cela permet d'étudier les propriétés optiques des nanostructures avec une résolution spatiale du même ordre ou même meilleure que la dimension des nanostructures sub-longueurs d'onde.

La spectroscopie SERS des échantillons est utilisée pour étudier les effets d'exaltation des champs créés par excitation des plasmons. Le signal Raman de molécules de colorants adsorbées sur la surface métallique est une sonde sensible de ces effets d'exaltation. Un effort particulier a été fait pour identifier les différentes contributions à l'exaltation Raman dans les échantillons étudiés en combinant la réponse de plusieurs molécules et en étudiant l'évolution du signal en fonction de paramètres comme la longueur d'onde ou la polarisation.

La mise en œuvre de ces techniques très spécialisées a eu pour objectif d'améliorer la compréhension des mécanismes d'excitation des plasmons dans des échantillons réels (différents des systèmes modèles souvent décrits dans la littérature), tout en permettant d'évaluer leur potentiel applicatif dans les domaines en pleine expansion de la nanophotonique et de la détection optique de très haute sensibilité.

Le résumé ci-dessous donne un aperçu du contenu de la thèse.

L'introduction permet d'exposer l'intérêt d'étudier les propriétés optiques des nanoparticules métalliques et d'expliquer les raisons du choix de l'étude de particules en or. Les systèmes en or sont moins étudiés que leurs équivalents en argent parce que les pertes intrinsèques des plasmons sont plus faibles pour l'argent que pour l'or dans le domaine des longueurs d'onde visibles. Dans le domaine du proche infrarouge cependant, ces pertes deviennent comparables mais l'or conserve un atout supplémentaire très utile, sa biocompatibilité. Dans cette introduction, le travail de la thèse est replacé dans ce contexte.

Dans le chapitre 2, je décris les échantillons qui sont utilisés dans les études. Les mesures SERS et en champ proche ont été réalisées sur des réseaux de nanofils d'or. Ces réseaux ont été produits par le groupe du professeur Buatier de Mongeot en utilisant un procédé en deux étapes, original, simple et peu onéreux comparé à d'autres méthodes. Les propriétés macroscopiques des échantillons, comme le dichroïsme en transmission sont présentées. J'ai également étudié par SERS les propriétés de nanofils en or isolés. Ceux-ci sont synthétisés par des méthodes de chimie humide et ils ont été achetés chez Nanopartz. Deux types différents de nanofils ont été utilisés : les premiers enrobés par du cetyltriméthylammonium bromide (CTAB), les seconds par des silanes. Ils ont une longueur nominale de 6  $\mu\text{m}$  et un diamètre de 30 nm. J'ai également utilisé des billes d'or de 50 nm de diamètre dans les études SERS des nanofils.

Le chapitre 3 introduit le concept des plasmons de surface, et plus précisément les concepts de plasmons localisés ou propagatifs. Les principes de base des théories les plus couramment utilisées pour décrire les plasmons de surface des nanoparticules, comme la théorie de Mie sont brièvement rappelés. On décrit plusieurs

méthodes utilisées pour exciter les plasmons de surface. Les effets de différents paramètres comme la taille, la forme et l'indice de réfraction du milieu environnant sur les résonances plasmons sont examinés. Cette discussion est importante pour comprendre les résultats des mesures décrites dans les chapitres suivants.

Le chapitre 4 aborde les fondements de l'effet SERS de façon simple. Le chapitre a été rédigé pour donner un aperçu des principaux mécanismes du SERS, accessible à un non spécialiste. Le dispositif expérimental et la préparation des échantillons sont décrits en détail. L'expérience combine un microscope de champ noir qui permet de réaliser des images des échantillons avec une résolution donnée par la limite de diffraction et un microscope Raman confocal, construit au laboratoire, utilisant un laser Ti-Sa continu accordable de 700nm à 900nm, avec une puissance nominale maximum de 3W. L'intensité et la polarisation du faisceau incident sont contrôlées à l'aide d'un polariseur et d'une lame demi-onde larges bandes dont les orientations sont pilotées par un logiciel développé au laboratoire. Les propriétés des molécules de colorants utilisées comme sondes de l'effet SERS sont décrites.

Le chapitre 5 expose les résultats des mesures SERS réalisées sur les nanofils isolés. L'idée initiale des expériences était de combiner des mesures d'exaltation de champ et de propagation dans ces systèmes. Il s'est avéré très difficile d'observer de la propagation dans les nanofils en or. J'ai alors mélangé aux nanofils des nanobilles en or. Elles servent de coupleurs entre l'excitation et les nanofils. Cette méthode a été décrite dans la littérature. Je décris d'abord un ensemble de résultats qui combine les images en champ noir des nanofils isolés et les spectres des plasmons obtenus en différents points des nanofils. Cette étude met clairement en évidence la dispersion des profils spectraux de la résonance plasmon en fonction de la position le long du nanofil. Aussi bien la forme que la position du maximum du profil varient en fonction de paramètres tels que la présence d'une bille sur le nanofil ou la forme de l'extrémité du nanofil, etc. Je montre ensuite les propriétés de propagation des plasmons en fonction de la longueur d'onde. Quatre longueurs d'onde différentes ont été choisies : 702 nm, 728 nm, 750 nm and 770 nm. L'enjeu de l'expérience a été de corrélérer l'effet de propagation à la résonance plasmon et d'analyser leur relation. La propagation est observée par le biais du signal SERS ou de la fluorescence exaltée qui résulte de l'interaction entre le champ proche du nanofil et la molécule de colorant sonde. J'ai mis en évidence les conditions nécessaires à l'observation de la propagation des plasmons : la longueur d'onde d'excitation doit être proche du maximum de la résonance plasmon au point d'injection du plasmon propagatif et proche de la résonance moléculaire. La distance de propagation la plus grande que j'ai observée est  $3,8 \mu\text{m}$ . La plus grande distance de propagation observée jusque-là dans les nanofils d'or a été obtenue par Krenn et al et vaut  $2,5 \mu\text{m}$ . La suite du chapitre décrit l'analyse de l'effet SERS et en particulier l'évolution du profil Raman avec la longueur d'onde d'excitation. De telles mesures sont

rarement effectuées car les dispositifs Raman ne sont en général pas accordables en longueur d'onde. L'évolution du signal Raman avec la longueur d'onde montre la même tendance que celle de la propagation plasmon. La dépendance de l'intensité du signal avec la distance de la molécule au point d'excitation du plasmon propagatif a été étudiée et l'intensité décroît progressivement comme prévu. C'est une preuve directe que le signal Raman sert de sonde de la propagation des polaritons de plasmons de surface. Nous avons expliqué les différents effets obtenus dans la résonance Raman, comme le clignotement. J'ai démontré, de façon claire, en utilisant simultanément sur le même échantillon deux molécules différentes, la Rh6G et l'ATTO 740, que le régime de la molécule unique était atteint dans un grand nombre de sites actifs. Le signal détecté en ces points correspond seulement à la signature d'une des espèces, jamais aux deux. Cela démontre sans ambiguïté que le point chaud est très localisé, qu'une seule molécule y réside à la fois et qu'elle est remplacée par une autre molécule quand elle s'éloigne du point chaud par différents effets dont la diffusion spatiale d'origine thermique. L'originalité de mon travail est d'avoir réussi à corréler plusieurs propriétés optiques sur un même nanofil isolé. En tous points du nanofil, on enregistre l'ensemble des données suivantes : l'image en champ noir, le spectre de la résonance plasmon au point choisi, l'image de la propagation et le signal SERS. C'est la première étude aussi complète réalisée sur des nanofils en or isolés à notre connaissance. Elle permet de progresser à la fois dans la compréhension de l'effet SERS sur de tels substrats et sur les propriétés de propagation.

Le chapitre 6 fait la synthèse des résultats obtenus par SERS sur les réseaux de nanofils décrits au chapitre 2. Le chapitre s'ouvre sur les résultats de simulations réalisées pour guider l'interprétation des observations. J'ai utilisé le logiciel DDSCAT construit sur l'approximation de la discrétisation par des dipôles (DDA). J'ai comparé dans des situations simples les résultats du modèle DDA à celui de l'approximation dipolaire. Les nanofils sont représentés par des ellipsoïdes allongés. Cependant leur longueur est limitée par les conditions de validité des modèles. J'ai effectué des simulations pour suivre l'évolution de la résonance plasmon en fonction de la polarisation du champ exciteur, de la taille de l'ellipsoïde et de l'indice de réfraction du milieu environnant. Le champ autour de deux ou trois ellipsoïdes proches a également été calculé pour deux polarisations orthogonales du champ. Le calcul confirme que le champ dans l'intervalle entre les particules est maximum quand la polarisation du champ exciteur est alignée selon la droite qui joint leur centre et très faible dans la direction perpendiculaire.

L'idée qui sous-tendait ces mesures était de pouvoir séparer les facteurs d'exaltation liés aux plasmons de surface des nanofils d'une part de ceux liés à une excitation de la molécule à résonance. De fait, c'est l'hétérogénéité des échantillons qui a permis de distinguer différentes contributions à l'effet SERS. Le présupposé était qu'il

existait une différence importante des facteurs d'exaltation pour les polarisations de l'excitation parallèle et perpendiculaire à la direction moyenne des nanofils. En principe, on attend une exaltation plus importante quand la polarisation est perpendiculaire aux nanofils (polarisation V) par rapport au cas où la polarisation est parallèle aux nanofils (polarisation H). Cependant les résultats expérimentaux n'ont pas montré de dépendance claire de l'intensité du signal Raman avec la polarisation avec la seule molécule d'ATTO 740 comme sonde et le signal est très instable. Ensuite, une autre molécule qui n'est pas en résonance avec le plasmon de l'échantillon, celle de Rh6G, a été codéposée. J'ai vérifié que le signal SERS de la rhodamine n'était pas détectable, hormis en un nombre très limité de sites. Deux effets différents ont alors été obtenus, un effet global et un effet local. L'effet global est un décalage vers le rouge de la longueur d'onde de la résonance plasmon qui se traduit par l'apparition de raies plus fortes dans le domaine basses et moyennes fréquences du spectre Raman (Un tel résultat peut s'interpréter comme un effet de résonance entre la molécule et le plasmon). Ce résultat est en accord avec les simulations qui montrent que la longueur d'onde du plasmon est décalée vers le rouge lorsque l'indice de réfraction du milieu environnant augmente. Le deuxième effet important apparaît localement. La stabilité des molécules d'ATTO 740 est accrue et l'exaltation augmente de façon importante. Je n'ai pas d'explication simple pour ce phénomène dont la compréhension nécessiterait des études de physico-chimie approfondies. J'ai suggéré quelques pistes à partir des données de la littérature, en particulier sur le rôle des ions sur l'efficacité SERS, et sur le phénomène compétitif de liaison des molécules avec la surface en présence d'un deuxième ion. Les études en polarisation sont décrites et je montre une première situation dans laquelle l'intensité du signal chute très rapidement lorsque la polarisation tourne de seulement  $20^\circ$ . Dans l'exemple qui est décrit le signal est maximum lorsque la polarisation est alignée selon le nanofil. Cette situation se produit quand la molécule est située dans l'intervalle entre deux particules situées sur le nanofil plutôt que dans l'intervalle entre deux nanofils successifs, comme le montre les simulations. Cet effet pourrait aussi être une manifestation d'un effet de transfert de charge entre la molécule d'ATTO 740 et la surface, comme je l'explique. La dépendance en longueur d'onde de signaux SERS a également été étudiée dans la gamme 700-780 nm qui englobe la résonance de la molécule à 740 nm. Un exemple est discuté. Les résultats indiquent que l'exaltation maximale en configuration V est atteinte à 745 nm, longueur d'onde située entre la résonance plasmon du site étudié et la résonance moléculaire. Cette tendance se confirme également dans la configuration H pour laquelle le signal est beaucoup plus faible. Le rapport des intensités des signaux Raman dans les deux situations est corroboré par les simulations du champ électrique autour des ellipsoïdes.

L'idée originale de ces études est l'utilisation de deux molécules pour explorer les

effets SERS. Une expérience de ce type a déjà été réalisée par Ru et al, mais avec pour objectif de démontrer sans ambiguïté l'existence d'un régime de molécule unique. Dans ma thèse, l'utilisation simultanée de deux molécules s'est avérée une méthode puissante et partiellement inexplorée pour comprendre les effets de couplage entre les plasmons dans des échantillons de nanostructures en or denses.

Dans le chapitre 7, j'introduis les concepts de base de la microscopie de champ proche optique à balayage (SNOM). Un court rappel historique permet de donner les principes essentiels qui sous-tendent la microscopie de champ proche. Le dispositif expérimental est expliqué en détail. Une avancée importante du dispositif fonctionnant en mode collection a été obtenue par l'adjonction d'un mode d'éclairage de l'échantillon qui combine un spot dont la taille est quasi-limitée par la diffraction et dont on peut contrôler la position et d'un dispositif d'excitation à deux couleurs dont la polarisation peut être contrôlée. Les deux images aux deux longueurs différentes (rouge et verte) sont obtenues simultanément dans un balayage unique, en exploitant la possibilité de commuter les lasers de façon synchrone à la fin de chaque ligne, le laser vert étant allumé pendant le balayage aller et le laser rouge pendant le balayage retour. Le dispositif permet également de réaliser des analyses en polarisation. J'introduis dans ce chapitre la méthode originale qui a été utilisée dans mon travail. Les possibilités uniques offertes par ce microscope pour l'étude des plasmons impliquent l'utilisation de deux différents modes de fonctionnement. Le premier est une configuration d'illumination constante dans laquelle la position de la tâche d'éclairage est fixe par rapport à la sonde de champ proche. Les mesures obtenues dans ce cas, reflètent la distribution de l'intensité du champ proche excité à la surface de la nanostructure (à résonance et hors résonance dans notre étude). Cela permet d'observer les points chauds créés par les plasmons très localisés et corrélés au désordre morphologique des échantillons. L'autre mode de fonctionnement, dit à illumination fixe, permet d'exciter l'échantillon à une position prédéfinie et de cartographier l'intensité du champ proche créé par cette excitation locale.

Le chapitre 8 décrit les résultats des expériences de champ proche optique réalisées sur des réseaux de nanofils. La motivation pour utiliser le mode collection et le choix des autres paramètres sont expliqués ainsi que les limites de cette méthode. Je commence par montrer les images obtenues avec le mode d'illumination constante. La reproductibilité des mesures entre images successives est illustrée sur un exemple typique. Il y a un léger décalage spatial entre les images qui est pris en compte dans le traitement ultérieur. Je discute les résultats obtenus sur deux échantillons déposés sur des substrats de verre ondulés. Les images optiques et topographiques sont montrées avec un post-traitement minimal. J'ai tracé la fonction de densité de probabilité (PDF : probability density function) des images optiques. La distribution des cartes enregistrées avec l'excitation verte et

avec l'excitation rouge obtenues avec une polarisation parallèle (configuration H) est de type gaussien comme prévu. Ce résultat est en accord avec la littérature qui prévoit que les événements de diffusion isolés sans contribution des plasmons conduit à une distribution gaussienne. Les cartes d'auto-corrélation sont dressées. Elles sont corrélées avec les cartes topographiques. L'exaltation de champ local est analysée en détail à partir des résultats obtenus en comparant les effets de la polarisation et de la longueur d'onde d'excitation. Ils mettent en évidence que l'exaltation des points chauds dans les images optiques est très importante pour l'excitation rouge et la polarisation perpendiculaire (configuration V) ce qui est attendu puisque l'excitation est en résonance avec le plasmon de l'échantillon à cette longueur d'onde. Les tracés des contours des cartes optiques sont reportés sur les cartes topographiques et il ressort clairement que les points chauds sont plutôt situés dans les creux et qu'ils apparaissent préférentiellement au voisinage des défauts des nanofils, comme les courbures ou les bifurcations etc. Les mesures sur des échantillons de référence sont également décrites. Aucun point chaud ou autre phénomène relié aux propriétés de résonance plasmonique ne sont observés. La conclusion résume les résultats obtenus dans mon travail de doctorat et ouvre des perspectives sur des études qu'il serait intéressant de réaliser.



---

# Introduction

*"There is plenty of room at the bottom."*

This famous lecture given by Richard Feynman in 1959 gave the first hint of the possibility of manipulating things at the atomic level. This is generally considered to be the foreseeing of the nanotechnology.

The nano world is not exactly new to the human race. Right from the fascinating Roman Lycurgus cup (fig.1) to the beautifully stained glasses, nanoscience has been used throughout history, albeit unintentionally. The bronze cup lined with colored glass dates back to the 4th century AD, scatters dull green light and transmits red light. Studies have shown that they contain nanoparticles (70 nm) of an alloy of silver and gold.



Figure 1: The Roman cup of 4th century AD representing the myth of King Lycurgus. It reflects a pale green light (left) and transmits a red light (right). Studies at the British museum show that they contain metal nanoparticles which are responsible for the phenomenon (from the british museum website).

The first recognized scientific study of nanoparticles started with the work of Michael Faraday [1], in 1857, on the gold colloidal solution. In his seminal article on finely particulated gold, he described many unusual and wonderful properties

of these solutions, but the most important revelation lies in his supposition that, rather than a solution of dissolved gold atoms or inorganic compounds, the gold was present in the form of "pure gold in a divided state". This is the fundamental root of all nanoscience [2].

## 0.1 Nanoscience

In very simple terms, nanoscience refers to the science of individual atoms and molecules. It deals with structures from one nanometer to a few hundreds of nanometers. The properties of the materials at the nanometer dimensions are significantly different from their bulk counterparts. The manipulation and engineering of individual atoms to develop new functionality is known as nanotechnology. Nanoscience has gained enormous importance in the last few decades because it paves way to create new nanostructures, understand their novel properties and ultimately to make devices which could revolutionize many sides of human life. Another major contribution to the rapid growth of this field is the availability of instruments to *see* and *handle* the nanoparticles. The first breakthrough came when scanning tunneling microscope (STM) was invented by IBM Zurich in 1980. Few years down the lane, atomic force microscopy (AFM) followed and today there are a number of high precision instruments to compliment the work on nanoscale. The highly promising aspect of the nanoparticles as mentioned earlier, is their unique physical and chemical properties. In particular, the most fascinating and useful is the optical property, especially that of metal nanoparticles. Nanophotonics is a sub sect of nanoscience, dedicated to understand the peculiar properties of light and light-matter interaction in various nanostructures.

## 0.2 The Optical properties of metal nanostructures

The Optical properties are one of the most useful and one of the widely studied property of nanostructures using a variety of spectroscopic tools. The optical properties are related to other properties including the electronic properties and hence is useful in a number of disciplines like physics, chemistry, biology, electrical engineering etc. The other interest is that its probably the only property which changes from bulk to the nanoscale system that can be seen visually. For example, the colour of gold nanoparticles can range from violet to red depending on the size of the nanoparticle (figure 2). Also, they play an important role in many technological applications like optoelectronics and biomedicine.



Figure 2: Solution of different sized gold nanoparticles. The colour changes according to the size of the nanoparticle. From[3].

The term optical properties encompass a lot of phenomena in itself like absorption, scattering, reflectance, transmittance, second harmonic generation and others. The nanoparticles have peculiar optical properties compared to their bulk counterparts. For example, the resonant absorption of nanometer sized particles gives rise to surface plasmon polaritons which will be discussed in detail in the later chapters. In particular, the metal nanoparticles interact with light stronger than any other chromophore. Hence they can be used for a wide variety of applications.

Another interesting fact is that the optical properties of nanomaterials depend on a number of factors like the shape, size and various other factors including the surrounding environment. Thus, it readily offers a wide range of tunability for the devices based on the optical properties. The thesis deals with the study of optical properties of the metal nanostructures and that of gold nanowires in particular.

### 0.3 The interest in gold

In the ancient times the colloidal gold was regarded as the 'elixir of life'. Not without a reason. The colloidal gold or the nanogold is unique in terms of its optical and electronic properties. In addition, gold nanoparticles offer a variety of applications. Multifunctionality is the keyword to denote gold nanoparticles. They are used in various fields like electronics, medicine and material sciences. The various properties and uses of gold nanoparticles are shown in figure 3.

In the field of electronics, what is done with the gold nanoparticles is nothing short of revolution. The concept of printed electronics has been achieved with the nanoparticle inks made of gold. Number of works are carried out in this line since it cuts down the cost as well as the complexity of the fabrication processes. They

show huge potential for use in advanced data storage technologies.

In the recent years, gold nanoparticles are also extensively researched for their applications in biology. In addition to the high electron density, which offers good contrast, facile synthesis, they also have good biocompatibility, thanks to the inertness of gold[4]. Their use as contrast agents in cellular and biological imaging is tremendous since they are found to be easily conjugated to the commonly used biomolecules. They are non-cytotoxic and non susceptible to chemical or thermal degradation. Hence they play a major role in the cancer diagnosis and also in the drug delivery [5].

In the field of materials science, research has been carried along various routes. It has been reported that the use of gold nanoparticles in the polymer solar cells increases the power conversion efficiency up to 20% [6]. Gold at the nanoscale is also catalytically active and efficient. Work is being carried out to tap this new functionality [7].

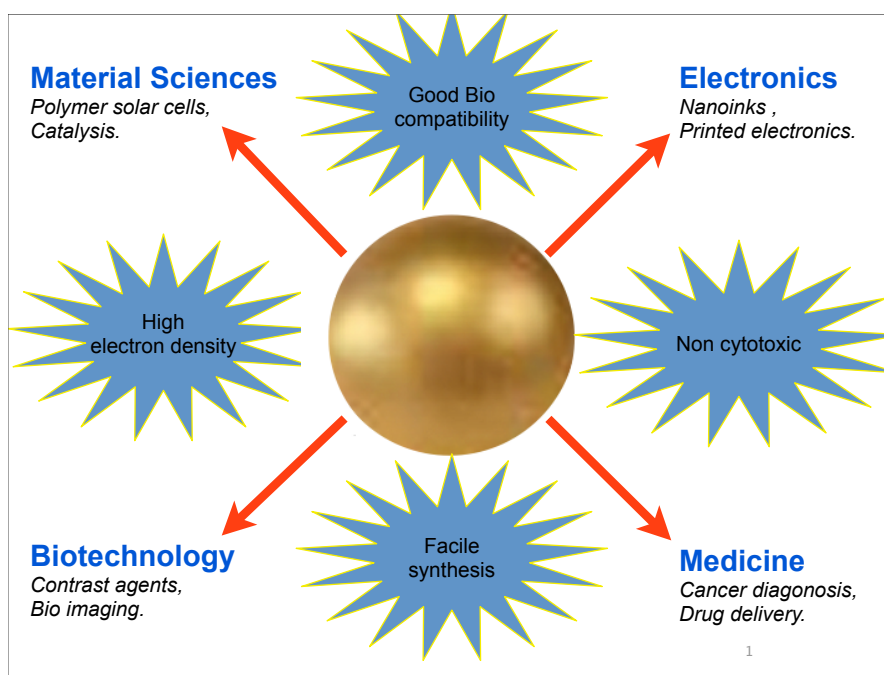


Figure 3: Figure representing the various properties and uses of gold nanoparticles in different fields. Easily explains our preference for gold nanoparticles.

## 0.4 Plasmonics

Moore's law which predicts the ever shrinking size of the transistors cannot be sustained indefinitely. Even if there is a strong will and competition to make

smaller and smaller devices, there are also a few limitations. In order to have faster and better device performances, the electronics were thought to be replaced with photonics. Photonic devices, while having better capabilities, are also larger in size. For example, optical interconnects such as fiber optic cables can carry digital data with a capacity 1000 times that of their electronic counterparts but they are also 1000 times larger than that of the electronic components. The ideal solution to overcome this limitation would have to be a circuit with nanoscale features that could carry at the same time optical signals and electric current.

The integration of optical and electronic circuits is limited by their largely varying sizes. The electronic circuits can be made in few tens of nanometres while the dimensions of the optical components are limited by the diffraction of light. The surface plasmon based photonics or PLASMONICS offers a solution to this problem as it has the capacity of the photonics and also the smaller dimensions provided by the electronics. It exploits the unique optical properties of the metallic nanoparticles to route and manipulate light at nanometer length scales [8].

Surface plasmons are the quanta of surface-charge-density oscillations of a metal. The increased interest in the surface plasmons in the recent times can be attributed to the fact that the advances in nanotechnology allows us to synthesize, design and characterize the metals on the nanometre scale. The direct consequence of this ability is that the properties of the surface plasmons can be controlled and can be tailored to meet specific applications. They propagate along the surface of a conductor. The surface plasmons are a result of the interaction of the light waves with the free electrons of a conductor. The interaction results in the collective oscillations of the electron density at the surface of the metal which are intimately coupled to electromagnetic fields. In the past, surface plasmons have attracted considerable attention due to their unique properties and their applications in optical sensor devices. They will be discussed in detail in the following chapters.

Surface plasmons allow to concentrate and to channel the light in sub wavelength structures [9].

The concentration of the light in sub wavelength structures is advantageous, since the excitation of surface plasmons in metal nanostructures can generate sizable electromagnetic field enhancements due to the large transient surface dipoles induced by the plasmons. Such field enhancements are the physical basis for Surface Enhanced Raman Scattering (SERS), an analytical sensing technique growing in importance since it was reported three decades ago. Due to its low invasiveness and extremely high sensitivity and as a consequence of the huge increase in the Raman cross sections provided by the surface plasmons, SERS has become a valuable tool in the investigation of living specimens. It is one of the two techniques that has been used in this thesis to study the optical properties of the gold nanostructures. Sub wavelength optical imaging is realized using the Scanning Near field Opti-

cal Microscopy (SNOM). The working principle of this device is the use of sub wavelength apertures in metal coated optical probes. In these systems the spatial resolution is ultimately determined by the aperture size rather than the wavelength of light. This offers the unique capability to investigate the behavior and the mechanisms involved in the plasmon resonance with a spatial resolution beyond the diffraction limit, comparable, or even better than the nanostructure size.

For these reasons, the two parallel techniques have been used in my study to understand more precisely the plasmon response of the gold nanowires.

In my work, SNOM is used to map the near-field distribution over the surface of nanostructured gold samples, aimed at pointing out the occurrence of plasmon localization as a function of the illumination parameters (wavelength, polarization). SERS on the same samples as well as on different nanostructures, addresses the effects of field enhancement associated with plasmon excitation. A sensitive probe of the enhancement is the detection of Raman signatures of suitable dye molecules adsorbed at the surface. The full range of measurements, complemented by the use of commercial gold nanostructures, is primarily intended to understand the mechanisms involved in the enhancement process and to assess their potential for highly-sensitive detection and analysis.

The following is the brief outline of the structure of the thesis.

Chapter 2 describes about the various samples that have been used in our studies and their properties.

Chapter 3 begins by explaining in layman terms what is a surface plasmon followed by the description of the dependence of the plasmon wavelength with various parameters like the environment, size and shape of the nanoparticles. As an example, the plasmon calculation for a simple shape such as sphere has been illustrated. The concepts explained in this chapter form the background for the thesis as they are inevitable to explain the results of the measurements.

Chapter 4 starts with the evolution of SERS and goes on to explain the main features of the SERS like the various enhancement factors. It gives an insight to the various dyes that have been used for the experiment. It also gives the sketch of the experimental set up used for the measurements in this thesis along with the sample preparation.

Chapter 5 discusses the results of the SERS measurements on the isolated nanowires. Chapter 6 elaborates on the various results obtained with the SERS measurements on the nanowire arrays. This along with the chapter 5 discusses the various phenomena contributing to SERS in our case.

Chapter 7 outlines the theory necessary to understand the SNOM along with some history of the technique. This chapter also gives the experimental details of the near field set up used in our studies along with the synthetic details.

Chapter 8 reviews the results of our SNOM measurements. The SNOM images

show interesting features which are discussed in detail. The optical and topographical maps are compared and overlapped to relate the plasmon effects to that of the topography.

The final chapter, conclusion, is a culmination of all the work that precedes this chapter and explores the possibilities and future directions to the work. The results of the thesis and its impact in the field are also presented in this chapter.



---

*Experimental confirmation of a prediction is merely a measurement. An experiment disproving a prediction is a discovery.*

Enrico Fermi

# 1

## Samples

### 1.1 Gold nanowires arrays

The first sample of interest is gold nanowire arrays fabricated by the group of Francesco Buatier de Mongeot from University of Genova. Thanks to their unconventional and original method of synthesis, self organized arrays of gold nanowires with tunable optical properties could be obtained. This method combines the self organized formation of a ripple pattern on the dielectric substrate by defocused ion beam sputtering and the deposition of gold at grazing angle to form the gold nanowires [10]. The samples are made with a two step process:

- The glass substrates were patterned by exploiting the self- organization mechanism induced by surface erosion through ion bombardment at off normal incidence [11]. The amorphous glass substrates were irradiated with a defocused  $\text{Ar}^+$  ion beam in a custom designed UHV chamber. The ripple pattern was a result of sputtering at an angle  $\theta = 35^\circ$  (with respect to the surface normal), an ion energy of  $E=800$  eV and an ion flux of  $5 \times 10^{15}$  ions/cm<sup>2</sup>s. This leads to well modulated ripples defined by a periodicity in the typical range 100-200 nm (depending on the process parameters) [12].
- After the formation of ripples on the glass substrate, the gold was deposited *in situ* by thermal evaporation at a rate of 2 nm/min at a grazing angle of incidence ( $\phi = 80^\circ$ ) from the substrate normal. Under these conditions, the substrate, due to shadowing effects, modulates the spatial distribution of the

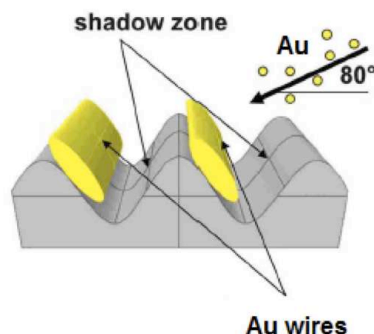


Figure 1.1: Experimental geometry adopted for the shadow deposition of Au NWs: the nucleation takes place preferentially near the top of the illuminated regions. (From Ref. [10] )

Au flux inducing the nucleation of metal clusters preferentially near the top of illuminated ridges where the flux is higher [10]. During the deposition, the substrate is maintained at a temperature of 240 K, essentially to reduce thermally activated diffusion of the metal. Continuous deposition results in the formation of polycrystalline nanowires on the top of the illuminated ridges (fig. 1.1).

The morphological and optical characteristics of the sample are determined by the deposition parameters. The aspect ratio  $w/h$  of the nanowire (fig. 1.2) establishes the degree of interconnection between the nanowires that, along with the ripple periodicity, determines the frequency of the localized surface plasmon resonance (LSPR). The width  $w$  is fixed since it is imposed by the ripples on the glass substrate and so the  $w/h$  ratio can be manipulated using the thickness of the deposition layer. A typical thickness value is 20 nm. The figure 1.3 shows the AFM morphology of one of the samples studied with SERS along with the corresponding optical transmission spectra taken in Genova. The AFM images show a

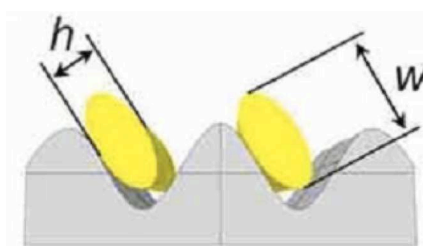


Figure 1.2: Illustration of the width and height of the NW whose ratio determines the LSPR of the sample (From Ref. [10]).

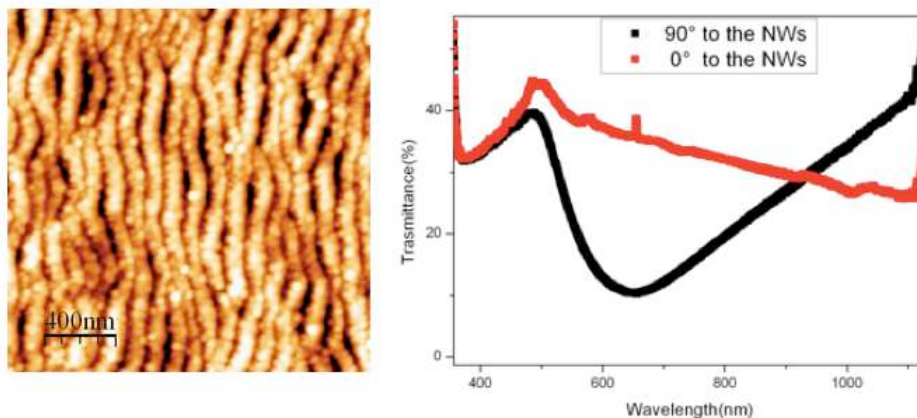


Figure 1.3: AFM image and transmission spectra of sample taken in Genova. This is one of the samples analyzed with Raman spectroscopy.

rather irregular nanowire structure. The average distance between two nanowires is around 110 nm. The optical transmittance spectra are obtained by means of conventional (macroscopic) measurements. The sample is illuminated by means of a compensated deuterium-halogen lamp (DH-2000-BAL, Mikropak) coupled through an optical fiber system (core 600  $\mu\text{m}$ ) to a stage for the transmission measurements. Incidence polarization was varied from TE (electric field parallel to NWs) to TM (perpendicular) by means of a Glan-taylor polarizer cube. Collection of the light is performed by optical fiber and processed by a PC controlled high resolution solid state spectrometer (HR4000, Ocean Optics). The figure displays the sample transmittance of two mutually orthogonal polarizations as a function of the wavelength of the incident radiation. The samples show a broad absorption feature in case of polarization vertical to the nanowire axis, peaking around 640 nm. Such a feature can be ascribed to the occurrence of LSPR, corresponding to excitation of the surface electron density in the transverse direction of the nanowires. Transmission of light horizontal to the sample does not exhibit any pronounced feature. Due to the different fabrication parameters used for different samples, the interwire spacing and the aspect ratio are specific for each sample. This leads to remarkable differences in the optical transmission spectra, where the absorption feature pertaining to the LSPR is always present upon orthogonal polarization, but the width and peak position achieve specific values for each distinct sample. This confirms the ability of the technique in tailoring the optical properties. The overall homogeneity and regularity of the morphology turn out to be affected by the fabrication parameters: in particular, in samples produced with thinner gold deposition (e.g., shorter deposition time) a granular structure is observed, probably as a consequence of a non complete coalescence during the growth of the gold layer.

## 1.2 Gold nanobeads

Spherical gold nanoparticles were used in the SERS experiments on isolated nanowires. Gold nanobeads of different sizes ( 50 and 80 nm) were purchased from BB international (Cardiff, United Kingdom) and used without any further processing. These beads are dispersed in deionized (DI) water and are capped with citrate to avoid the agglomeration.

## 1.3 Gold nanowires

These are commercial nanowires purchased from Nanopartz. These nanowires are 30 nm in axial diameter and 6  $\mu\text{m}$  in length. In the bare form, these nanowires are immersed in DI water with excess CTAB capping agent to minimize aggregation. The concentration according to the producer data is  $6 \times 10^8$  nanoparticles/ml. Nanowires with silane coating have also been used. These are brought from Nanopartz and have the same dimensions of the previous ones ( 30 nm in axial diameter and 6  $\mu\text{m}$  in length). The figure 1.4 shows the transmission electron microscope image of a nanowire (taken from the Nanopartz website).

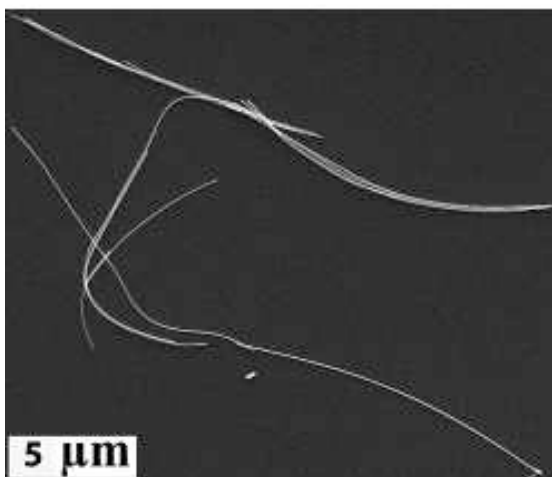


Figure 1.4: Transmission electron microscope image of a gold nanowire (From Nanopartz).

---

*If we knew what it was we were doing, it would not be called research, would it?*

Albert Einstein

# 2

## Plasmons

### 2.1 Introduction

The interaction of metals with electromagnetic waves is largely characterized by its free electrons. Plasmons are generally described as a collective oscillation of the free electrons. It can also be called as the quanta of surface charge density oscillations. In classical physics, it can be visualized as the oscillations of the electron gas of a metal with respect to the fixed ionic cores.

#### Surface plasmons

When the surface of a metal is excited by the electromagnetic radiation, the light can be coupled to standing or propagating plasmon modes [13]. In the recent years, the advancement in the technology has brought great interest in the surface plasmons for the possibilities that it offers in the photonics field. In particular, the nanofabrication techniques developed in the recent times makes it possible to structure metal surfaces which can be used to control the surface plasmons and their propagation.

#### Localized surface plasmons

When a surface plasmon is confined to a nanoparticle, there is a contribution to the collective oscillation from the free electrons of the particle. These are known as localized surface plasmons (LSP). The LSPs are of great interest because the

electric field around the particle is greatly enhanced which paves way for a number of applications. The localized surface plasmon resonances (LSPR) of the noble metals like silver or gold falls in the visible spectrum, thus making it very affordable to work with for use in various applications. Additionally, as we will see in the following sections, the LSPR depends on the size of the particle. So it can be in the near infra red region for gold particles depending on their shape. This possibility gives us an additional advantage to be able to tune the LSPR according to our experimental requirements. A number of reviews are available on surface plasmons [14, 15, 16] and since it is a huge field in itself, we will discuss only a few topics.

## 2.2 Surface plasmon polariton excitation

In this section we see some aspects of the surface plasmon polaritons that are related to our studies. The dispersion relation of the surface plasmons is given by the equation [17]

$$k_{SP} = \frac{\omega}{c} \sqrt{\frac{\epsilon_1 \epsilon_m}{\epsilon_1 + \epsilon_m}} \quad (2.1)$$

where,  $k_{SP}$  is the SP wavevector and  $\epsilon_1$  and  $\epsilon_m$  are the real part of dielectric function of the metal and dielectric function of the medium respectively.

The relation between the wave vector along the propagation direction and the frequency is given by the dispersion relation and the propagating SPs are  $p$ -polarised (TM) electromagnetic waves. These two facts set the conditions for excitation of SP.

In order to excite the SP on a planar metal surface, the excitation should have a wavevector equal to that of the SP and it should also be  $p$ -polarised. That is, both the energy and momentum conservation conditions need to be fulfilled. Various experimental techniques have been used to match the wavevector of the excitation radiation and to fulfill the necessary wavevector conservation. From the dispersion relation, it can be seen that for a given energy  $\hbar\omega$ , the SP wavevector is always larger than the magnitude of the wavevector of the light in air. Thus the SPs cannot be excited by illuminating light of any frequency that propagates in free space. Excitation of the plasmon is possible only when the phase matching conditions are achieved. In order to excite the plasmon, the frequency of excitation induces that of the plasmon, the conditions being that the wavevector components parallel to the surface is unchanged on each side of the surface.

### Total internal reflection

This is one of the very first techniques used in this field. Two different configurations are mostly used in this method; Kretschmann and Otto.

In the Kretschmann configuration [18, 19], the substrate is illuminated through a prism at an angle of incidence greater than the critical angle for total internal reflection. This condition increases the wavevector of the light in the optically dense medium. The incident light is coupled to the SPs at the angle of incidence at which the photon wavevector in prism coincides with the SP wavevector at the air-metal interface [20]. With this configuration it is not possible to excite the SPs on the interface between the prism and the metal.

The figure 2.1 shows the various prism configurations used to excite the surface plasmons.

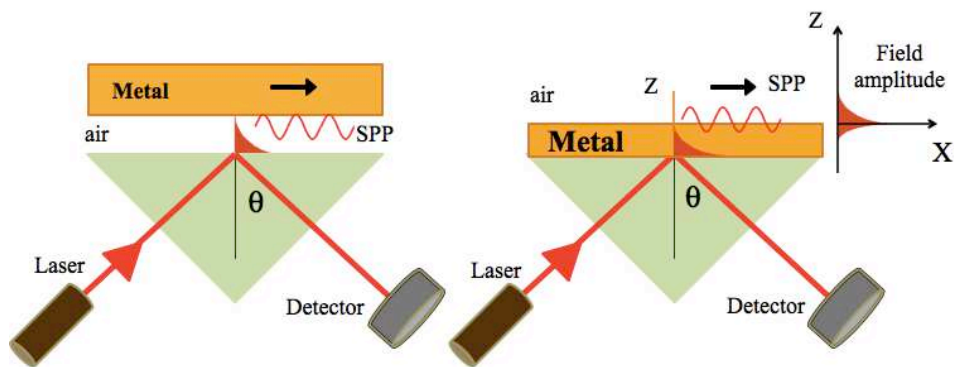


Figure 2.1: Experimental arrangements to realize the excitation of surface plasmons. Left: Otto configuration. Right: Kretschmann configuration.

In the Otto configuration, the prism is used on top of the metal surface with a small air gap. This was proposed by Otto in 1968 [21]. This configuration is used in case of thick metal films or surfaces of bulk metals. Photon tunneling occurs through the air gap between the prism and surface and the resonance conditions are similar to that of the previous configuration.

### Diffraction grating

The wavevector conservation for SP excitation can also be achieved using grating. By engraving a surface grating structure whose depth remains small compared to its spatial period, diffraction of the incident radiation is facilitated. The components of this diffracted light whose wavevectors match with that of the SP wavevector will couple efficiently. Since diffraction is the guiding principle behind

this technique, the coupling is possible only at certain specific frequencies and angles and therefore the coupling conditions are very sharp [17].

### Random surface roughness

A randomly rough surface behaves as a combination of gratings. The diffracted components of light in the near field region will have all the wavevectors. Thus the SPs can be excited as the photons will always couple to the SP modes. This technique is easy to use without any special modifications like addition of defects or beads. However, since coupling is also random, the efficiency is very low. It is a non resonant excitation and there will be a lot of stray reflected light that is not coupled to the SP.

### Point defects

Point defects act as localized sources for the excitation of SPs. They couple efficiently to the surface and the SPs propagate away from that point.

Another technique introduced recently is to use beads as they act as secondary sources by scattering light. The scattered light will have all the components of wavevector and hence they can couple to the SP efficiently in a rough surface [22]. Other techniques are also used to efficiently couple the incident light to the SP like increasing the refractive index of the incident medium.

## 2.3 Surface plasmon propagation length

The SP propagation length is one of the important factors considered to define the efficiency of a system. As described earlier, the excitation of the SP modes is not straightforward. However, once it has been achieved and the excitation light is converted into SP mode, it will propagate along the metal surface. As the SP propagates, there will be attenuation due to the losses primarily from absorption in the metal. The SP intensity decays with the square of the electric field. The intensity decreases by a factor of  $\exp(-2k_{sp}'' x)$  at a distance  $x$ . The  $k_{sp}''$  is the imaginary part of the complex surface plasmon wavevector,  $k_{sp} = k_{sp}' + ik_{sp}''$ . The SP propagation length  $L_{SP}$ , is defined as the distance after which the intensity of the SP falls by a factor of  $1/e$  [23]. It is given by

$$L_{SP} = \frac{1}{2k_{sp}''} = \frac{c}{\omega} \left( \frac{\epsilon_1 + \epsilon_m}{\epsilon_1 \epsilon_d} \right)^{\frac{3}{2}} \frac{(\epsilon_1)^2}{\epsilon_2} \quad (2.2)$$

where,  $\epsilon_1$  and  $\epsilon_2$  are the real and imaginary parts of the dielectric function of the metal, that is  $\epsilon = \epsilon_1 + i\epsilon_2$ .  $c$  is the speed of light and  $\omega$  is the optical excitation

frequency.

The equation (2.2) predicts that with the decrease in frequency, the propagation length increases. Higher propagation lengths can be achieved with silver than gold since silver has lowest losses in the visible spectrum ( $\epsilon_2$  is small for silver in the visible spectrum compared to other metals). However, beyond the visible spectrum, in the near infrared region the SP propagation lengths of both silver and gold are comparable [24]. This is because beyond the absorption losses come from intraband transitions which is vanishingly small in the near infra red region. The electron-electron collisions induce the intra and interband transitions, which are internal 'propagation' losses. The figure 2.2 gives a schematic of such losses.

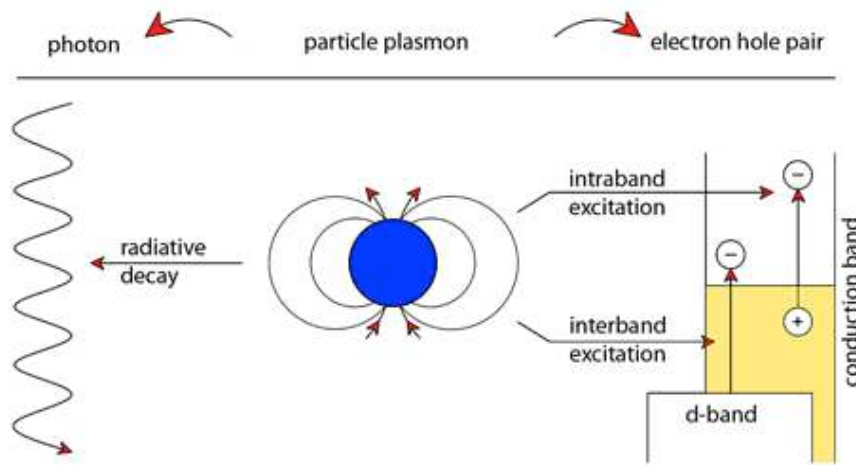


Figure 2.2: Schematic showing the interband and intraband transitions that causes internal losses in a metal during propagation.

The unwanted coupling of the radiation at the interface (leakage) also contributes to the radiative losses and hence to the damping of the SPP modes. In order to achieve higher propagation lengths and to implement the SPP based circuits, these losses have to be taken care of in such a way that one is able to re-route the SPs to lose its energy to freely propagating light without scattering the SPP mode [9].

## 2.4 Mie theory

After this, we discuss about the localized surface plasmons (LSP).

In the introduction chapter, we had seen how the size of the nanoparticles change their physical aspects. Gustav Mie was the first person to explain the red colour of the gold nanoparticle solutions in the early 20th century. He developed an

analytical solution for an electromagnetic wave interaction with small spheres, known popularly as the Mie theory [25]. It describes the scattering and absorption of light by spherical particles and their behaviour with wavelength. In the range of very small particles ( $d \ll \lambda$ , quasi-static approximation), the Mie scattering agrees with the Rayleigh scattering. The following is essentially a concise version of the highlights of the Mie theory. The scattered fields due to a plane wave incident on a homogenous conducting sphere is calculated with the appropriate boundary conditions. The solution of these calculations leads us to the total scattering, extinction and absorption cross sections given by,

$$\sigma_{sca} = \frac{2\pi}{|k|^2} \sum_{L=1}^{\infty} (2L+1)(|a_L|^2 + |b_L|^2) \quad (2.3)$$

$$\sigma_{ext} = \frac{2\pi}{|k|^2} \sum_{L=1}^{\infty} (2L+1)[\text{Re}(a_L + b_L)] \quad (2.4)$$

$$\sigma_{abs} = \sigma_{ext} - \sigma_{sca} \quad (2.5)$$

where,  $k$  is the incoming wavevector and  $L$  is the summation of the partial waves.  $L=1$  corresponds to the dipole oscillation and  $L=2$  to the quadrupole and so on.  $a_L$  and  $b_L$  are parameters composed of the Riccati- Bessel functions  $\psi_L$  and  $\chi_L$ .

$$a_L = \frac{m\psi_L(mx)\psi_L'(x) - \psi_L'(mx)\psi_L(x)}{m\psi_L(mx)\chi_L'(x) - \psi_L'(mx)\chi_L(x)} \quad (2.6)$$

$$b_L = \frac{\psi_L(mx)\psi_L'(x) - m\psi_L'(mx)\psi_L(x)}{\psi_L(mx)\chi_L'(x) - m\psi_L'(mx)\chi_L(x)} \quad (2.7)$$

Here,  $m = n/n_m$ , where  $n = n_R + in_I$  is the complex refractive index of the metal and  $n_m$  is the real refractive index of the surrounding medium. Also  $x = kr$ , where  $r$  is the radius of the nanoparticle. For the nanoparticles whose dimensions are much smaller than the wavelength of light,  $x \ll 1$ . Also, only the dipole oscillations can contribute significantly to the extinction cross section.

Ricatti- Bessel functions can be approximated using power series expansions. Bohren and Huffmann retained certain number of expressions ensuring the scattering coefficients are accurate to terms of the order of  $x^6$ . The other assumptions of Bohren and Huffmann are  $|m|x \ll 1$  and  $|b_1| \ll |a_1|$  [26]. This will be used later in the thesis when discussing the SERS results. Here we keep the terms to the order of  $x^3$ . The equations 2.6 and 2.7 are simplified as

$$a_1 \approx -\frac{i2x^3 m^2 - 1}{3 m^2 + 2} \quad (2.8)$$

$$b_1 \approx 0 \quad (2.9)$$

and the higher orders of  $a_L$  and  $b_L$  are zero. Let us substitute

$$m = \frac{(n_R + in_I)}{n_m} \quad (2.10)$$

in the equation to find the real part of  $a_1$  as required by the equation 2.6. This leads us to

$$a_1 = -i \frac{2x^3}{3} \frac{n_R^2 - n_I^2 + i2n_R n_I - n_m^2}{n_R^2 - n_I^2 + i2n_R n_I + 2n_m^2} \quad (2.11)$$

The complex dielectric function of a metal is given by

$$\epsilon = \epsilon_1 + i\epsilon_2 \quad (2.12)$$

and the relation with the refractive index of the metal is given by

$$\epsilon_1 = n_R^2 - n_I^2 \quad (2.13)$$

$$\epsilon_2 = 2n_R n_I \quad (2.14)$$

The dielectric function of the surrounding medium is given by

$$\epsilon_m = n_m^2 \quad (2.15)$$

Substituting these relations, we get

$$a_1 = \frac{2x^3}{3} \frac{-i\epsilon_1^2 - i\epsilon_1\epsilon_m + 3\epsilon_2\epsilon_m - i\epsilon_2^2 + i2\epsilon_m^2}{(\epsilon_1 + 2\epsilon_m)^2 + (\epsilon_2)^2} \quad (2.16)$$

Substituting  $a_1$  in the equation 2.3 and considering only the dipole (case of very small particles), we get,

$$\sigma_{ext} = \frac{18\pi\epsilon_m^{3/2}V}{\lambda} \frac{\epsilon_2(\lambda)}{[\epsilon_1(\lambda) + 2\epsilon_m]^2 + \epsilon_2(\lambda)^2} \quad (2.17)$$

and,

$$\sigma_{sca} = \frac{32\pi^4\epsilon_m^2V}{\lambda^4} \frac{(\epsilon_1 - \epsilon_m)^2 + (\epsilon_2)^2}{(\epsilon_1 + 2\epsilon_m)^2 + (\epsilon_2)^2} \quad (2.18)$$

where,  $V$  is the particle volume. These are the widely used expressions for nanoparticle plasmon resonances [13].

Mie calculated the scattering and extinction for only spherical particles and the theory is strictly valid for very small nanoparticles (5 - 100 nm). Bohren and Huffman further developed the theory to accommodate a number of structures apart from spheres like ellipsoids, cylinders and even irregular shapes [26].

## 2.5 Gans theory

Gans theory was formulated essentially to calculate the scattering and extinction of irregular shaped particles. It helped to overcome the problem to solve the scattering problem of a particle with an irregular geometric shape. The conditions for validity of the Rayleigh - Gans approximation are  $|m - 1| \ll 1$  and  $kd|m - 1| \ll 1$ , where  $d$  is the characteristic linear dimension of the particle and  $m$  is its complex refractive index relative to that of the surrounding medium [26]. The case usually discussed in literature is that of ellipsoids. So I present here one such example.

The following is a gist of the Gans approximation. Here, we consider a collection of randomly oriented nanorods with an aspect ratio  $R$ . Their scattering and extinction cross sections can be calculated using the Gans theory [13].

The extinction cross section  $\sigma_{ext}$  for elongated ellipsoids is given by

$$\sigma_{ext} = \frac{\omega}{3c} \epsilon_m^{3/2} V \sum_{L=j} \frac{(1/P_j^2) \epsilon_2}{\epsilon_1 + [(1 - P_j)/P_j] \epsilon_m^2 + \epsilon_2^2} \quad (2.19)$$

where,  $P_j$  are the depolarization factors along the three axes of the nanorod A, B and C with  $A > B = C$ , defined as

$$P_A = \frac{1 - e^2}{e^2} \left[ \frac{1}{2e} \ln \left( \frac{1 + e}{1 - e} \right) - 1 \right] \quad (2.20)$$

$$P_B = P_C = \frac{1 - P_A}{2} \quad (2.21)$$

and the aspect ratio  $R$  is included in  $e$  as follows

$$e = \left[ 1 - \left( \frac{B}{A} \right)^2 \right]^{1/2} = \left( 1 - \frac{1}{R^2} \right)^{1/2} \quad (2.22)$$

## 2.6 Surface plasmon dependence on size

In our work, we have studied different samples with different environments. To have an idea of such systems, I briefly discuss the effect of some important parameters like size, shape and refractive index of the medium on the plasmon resonance. The surface plasmon resonance (SPR) of a nanoparticle depends strongly on its size. For the smallest particles, the SPR is dominated by absorption. When the size increases, the scattering takes over. The size dependence of SPR is one of the factors that can be visualized easily. A common example is the different colour of the nanoparticles with different diameters.

The Mie theory gives the dependence of SPR on size strictly for small spherical particles compared to the wavelength. The condition for small but finite particles is approximated by using the equation (2.6). Plasmon resonance frequency is defined as the frequency at which the cross section of a particle reaches a maximum. The condition for the denominator  $a_1$  to vanish is

$$m\psi_1(mx)\chi_1'(x) - \psi_1'(mx)\chi_1(x) = 0 \quad (2.23)$$

By expanding  $\psi_1$  to terms of order  $x^4$  and  $\chi_1$  to terms of order  $x$ , we get,

$$\epsilon = -(2 + \frac{12}{5}x^2)\epsilon_m \quad (2.24)$$

This equation gives us an idea of what happens as the size of the sphere increases. An increase in the particle size shifts the frequency to lower values, i.e to longer wavelengths [26]. We will use the term red-shift to denote it in the later part of the thesis.

Thus speaking qualitatively, as the size increases, the SPR resonances shift to the red. When the size increases, higher order resonance modes come to play. The dipolar resonance approximation is no longer valid and multipolar resonances are active.

Another major influence of the size is the line shape of the plasmon resonance. This is due to the combination of interband transitions and higher order plasmon modes. The interband transitions cause increased line width for smaller particles whereas the higher modes play the same role in larger nanoparticles.

## 2.7 Surface plasmon dependence on shape

The surface plasmon resonance (SPR) dependence of shape is evident already from the necessity of Gans theory, which describes the SPR for non-spheroidal particles. Another important factor associated with shape factor and plays a major role is the aspect ratio especially in the elongated nanoparticles like the nanorods or ellipsoids. By changing the aspect ratio of the system the SPR can be tuned according to the needs. In fact, the same principle applies to the sample of nanowire arrays that we have used. The change in the aspect ratio of the nanowire allows to tailor the SPR to suit our requirements [5].

As with the varying size, the change in shape leads to the increase in the number of SPR modes associated with the nanoparticle. For example, in the case of nanorods, there are two plasmon resonances associated with each axis. One is the longitudinal SPR related to the major axis and the other one is the transverse SPR related to the minor axis. Each of the SPR can occur at different frequencies with a large separation. More spectral peaks are observed in case of multipolar excitation.

The effect of the particle shape on the SPR has been demonstrated using various shaped nanostructures like spheres, triangles and cubes by Mock et al [27].

## 2.8 Surface plasmon dependence on refractive index

From the Drude model of the electronic structure of metals, we get

$$\epsilon_1 = 1 - \frac{\omega_p^2}{\omega^2 + \gamma^2} \quad (2.25)$$

where  $\omega_p$  is the plasma frequency and  $\gamma$  is the damping factor of bulk material. For visible and near infrared frequencies,  $\gamma \ll \omega_p$ . Hence

$$\epsilon_1 = 1 - \frac{\omega_p^2}{\omega^2} \quad (2.26)$$

The extinction cross section will be maximum when  $\epsilon_1 = -2\epsilon_m$  (resonance condition).

$$\omega_{max} = \frac{\omega_p}{\sqrt{2\epsilon_m + 1}} \quad (2.27)$$

where  $\omega_{max}$  is the SPR peak frequency. Converting the frequency to wavelength and using the relation between refractive index and dielectric constant, we get

$$\lambda_{max} = \lambda_p \sqrt{2n_m^2 + 1} \quad (2.28)$$

where  $\lambda_{max}$  is the SPR peak frequency and  $\lambda_p$  is the bulk plasma frequency. This equation gives the effect of the refractive index of the surrounding medium on the surface plasmons.

Mock et al have studied the local refractive index dependence of plasmon resonance spectra of individual silver nanoparticles by using medium of different indices [28]. They show that the plasmon resonance is highly sensitive to small changes in local refractive index and the shape and resonance mode also affects the sensitivity of these changes.

Apart from these, the plasmon resonance also depend on a number of other parameters like the material, substrate etc. All the factors that influence the plasmon peak like shape, size and refractive index are inter-related.

---

*All truths are easy to understand once they are discovered; the point is to discover them.*

Galileo Galilei

# 3

## SERS

### 3.1 Introduction

Spectroscopic techniques play a vital role in basic as well as applied research, specially because techniques such as Raman spectroscopy give a lot of information on a wide variety of materials. Surface enhanced Raman spectroscopy (SERS) is one of the widely researched fields in the recent years.

The discovery of SERS in the early 1970s came as a boon to bridge the gap between the Raman and Fluorescence spectroscopic techniques. The Raman cross section for a molecule is typically of the order of  $10^{-30}$  cm<sup>2</sup> which is extremely small resulting in weak signal. On the other end of the scale, the fluorescence spectroscopy gives a signal of relatively higher intensity owing to a large cross section, typically of the order of  $10^{-16}$  cm<sup>2</sup>. The problem here is posed by the fluorescence of the surrounding molecules which demand the use of highly sophisticated experimental setup for detection of analyte at trace levels. Fleischmann and coworkers found unexpectedly high Raman signals from Pyridine adsorbed on a rough silver electrode [29]. Various experiments were carried out at different laboratories and it was ensured that the strong Raman signal is truly the result of enhancement of Raman scattering itself and not due to increased molecules [30, 31]. This effect was named Surface Enhance Raman Spectroscopy (SERS) and it helped to overcome the inherent problem of low sensitivity in Raman spectroscopy. In addition the fluorescence background is quenched making it a truly effective technique [32].

In the initial days of discovery of SERS, the enhancement factor of the Raman

scattering reported was of the order of  $10^3$  to  $10^5$ . In the recent years, there are many reports that claim an enhancement factor of the order of  $10^{10}$  to  $10^{12}$ .

### 3.1.1 Evolution of SERS

In these 35 years since the discovery of SERS, much work has been carried out to achieve an understanding of the nature and origin of the effect and also to push the limits of enhancement even higher with different materials and structures. In fact the interest in SERS has been renewed with the development of efficient synthesis methods of nanometric metallic structures. This is an attempt to summarize the work carried out in this field since its discovery.

It has been shown that the SERS phenomenon is a result of two major contributions, an electromagnetic enhancement and chemical enhancement, the former being the most important [32]. Studies have shown that large enhancements occur at the junctions between the nanoparticles, which act as hot-spots [33, 34]. The hot-spots can be defined as the regions where the enhancement is increased manifold due to a number of factors. Electromagnetic enhancement factors up to  $10^{12}$  have been reported, which allows for single molecule detection [33, 34, 35, 36]. More recently, it has been demonstrated that much lower enhancement factor, of the order of  $10^7$ , is sufficient to observe single molecule SERS signal. SERS has been widely explored as a tool for chemical and biological sensing [35, 37]. Investigations have been carried out by different groups in various nanostructures like single nanowires, coupled nanowires, nanowire arrays and nanoparticle aggregates [38, 39]. Polarization dependence of SERS hotspots as well as plasmon propagation along nanowires using SERS has been analyzed [40]. Most of these work has been done on the silver nanosystems since the enhancement is very good and the effect is easier to observe. However, the silver nanoparticles are not as biocompatible or stable as compared to gold and this severely affects their use in biological sensing [41].

## 3.2 Raman Spectroscopy

Raman spectroscopy is a spectroscopic technique based on inelastic scattering of monochromatic light, usually from a laser source. Raman scattering, discovered by the Indian physicist C.V. Raman in 1928 [42]. It occurs when a photon incident on a molecule interacts with the electron cloud of that molecule. In classical terms, the interaction can be viewed as a perturbation of the molecule's electric field. In quantum mechanics, the Raman effect describes a scattering interaction between light and matter. In Raman spectroscopy, the wavelength and intensity of light inelastically scattered from a sample is measured. Inelastic scattering means that

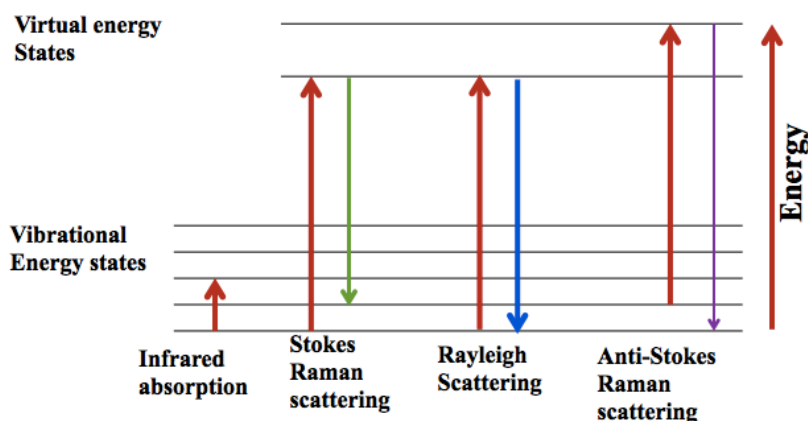


Figure 3.1: Energy level diagram showing the states and scattering in the Raman signal.

the frequency of photons in monochromatic light changes upon interaction with a sample.

In Raman spectroscopy an incident photon, with energy  $h\nu_L$  where  $h$  is Planck's constant and  $\nu_L$  is the frequency of the excitation laser, excites a molecule into a virtual state that is lower in energy than an electronic transition, a new photon is created and scattered from this virtual level. The scattering event occurs almost instantaneously, typically in  $10^{-14}$  s or less. If a molecule begins in the vibrational ground state, then the final state can be either the vibrational ground state (elastic scattering), called Rayleigh scattering, or an excited vibrational state, called Stokes-Raman scattering. In Stokes-Raman scattering photons lose energy by exciting a vibration within the sample molecule and thus the scattered light appears at a lower frequency than the incident photon. In this case, the Raman scattered light will have an energy of  $h(\nu_L - \nu_R)$ , where  $\nu_R$  is the frequency of the Raman scattered light. The molecule can also begin in an excited vibrational state and proceed, via the virtual state, the vibrational ground state. This process is called anti-Stokes-Raman scattering and in this case photons gain energy from the molecular vibrations and the scattered signal appears at a higher frequency. In anti-Stokes-Raman scattering the Raman scattered light will have an energy of  $h(\nu_L + \nu_R)$ .

The individual bands in the Raman spectrum are characteristic of specific molecular motions. By measuring the energy of the emitted photon after the scattering event, and knowing the energy of the incident photon, the structure of the molecule being probed can be assessed.

The processes of Rayleigh, Stokes-Raman, and anti-Stokes Raman scattering are depicted schematically in figure 3.1. The lower energy levels in the figure represent the ground electronic state while the upper levels represent the first excited

electronic state. Within the ground and excited electronic states are vibrational and rotational energy levels.

### 3.3 SERS Enhancement Mechanisms

The SERS, in short, is about amplifying the Raman signals of the molecules that are attached to the metal surfaces. As mentioned earlier, years of work has shown that more than one effect contributes to this observed total amplification or enhancement of many orders of magnitude. Traditionally they are attributed to the electromagnetic and chemical effects.

#### 3.3.1 Electromagnetic enhancement

The electromagnetic enhancement factor is considered to contribute to the major part of the enhancement in SERS. The phenomenon is a result of the coupling between the incident electromagnetic field and the SERS substrate. The electromagnetic contribution to the SERS is one of the widely studied subject and several theories have been put forward to calculate the electromagnetic enhancement factor. The most popular and widely used is the  $|E|^4$  approximation, which we will describe shortly. The analyte molecules are adsorbed on the surface of the substrate either by physisorption or chemisorption. These molecules are very close to the surface and hence benefit from the localized field enhancements that occur when the local surface plasmons are excited. The electromagnetic contribution does not require a physical contact of the molecule with the metal. However, it decreases with the increasing separation distance.

#### The $|E|^4$ approximation

In the Stokes scattering, the power of the scattered beam is expressed as

$$P_S(\omega_S) = N\sigma_{RS}I_{\omega_L} \quad (3.1)$$

where  $N$  is the number of Stokes-active scatterers within the excitation spot,  $\sigma_{RS}$  is the scattering cross section, and  $I_{\omega_L}$  the intensity of the excitation beam.

A important factor in the total enhancement of  $P_S$  is the increased electromagnetic field due to excitations of localized surface plasmons and a crowding of the electric field lines (lightning rod effect) at the metal interface. If the near field at the location of the molecule is enhanced by a factor  $L(\omega)$

$$L(\omega) = \frac{|E_{Loc}(\omega)|}{|E_0|} \quad (3.2)$$

where is the local field amplitude  $|E_{Loc}|$  and the amplitude of Raman scattered light is proportional to  $\alpha L(\omega')E_0$  where  $\alpha$  is the right combination of the components of the Raman tensor. This field in turn will be enhanced by a factor  $L(\omega')$ ,  $\omega'$  being the frequency of the Raman scattered light. The scattered field is written as  $\alpha L(\omega)L(\omega')E_0$  and the intensity is  $|K|^2|L(\omega)L(\omega')|^2I_0$ . The SERS enhancement factor is therefore given by

$$F = \left| \frac{\alpha}{\alpha_0} \right|^2 |L(\omega)L(\omega')|^2 \quad (3.3)$$

Since the difference in frequency between the incoming and scattered photons is in general much smaller than the line width, of a localized surface plasmon mode,  $|L(\omega)| \approx L(\omega')$ , which brings us to the important result that the electromagnetic contribution to the total SERS enhancement is proportional to the fourth power of the field enhancement factor.

This is known as the  $|E|^4$  approximation [43].

$$F \simeq |L(\omega_L)|^4 \frac{|E_{Loc}(\omega_L)|^4}{|E_0|^4} \quad (3.4)$$

This is known as the zero-Stokes shift enhancement factor in the  $|E|^4$  approximation. This approximation does not take into account the adsorption geometry of the probe, Raman tensor of the mode or scattering geometry of the set up. Hence even if it can give a good idea about the SERS enhancement factor, it is not accurate. Another drawback with this approximation is that it neglects the polarization factor. Nevertheless, it gives a typical figure to compare the theory and the experiments [44]. The enhancement due to the LSP of a single particle depends on the size and is not often very high. The electromagnetic enhancement is high

- at the junction between two particles if the gap is less than 10 nm (which we will see in the coming chapters with the help of simulations).
- at the "tip" of a sharp edged nanowire (lightning rod effect).
- fractals.

### 3.3.2 Chemical enhancement

Chemical effect contribution to the total enhancement in SERS is not well studied or completely understood as the electromagnetic factor. The first indication of chemical contribution being operative, traces to the initial experiments on SERS by Vanduyne and others [30]. The dependence of enhancement factor on the electrode potential was the key. The best electromagnetic factors observed fell

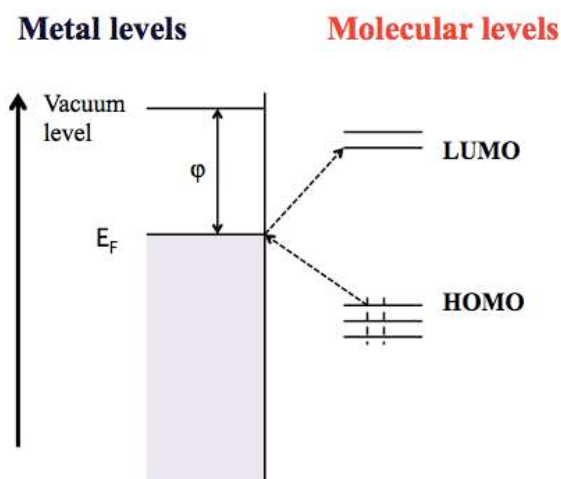


Figure 3.2: Energy level diagram for a 'molecule-metal' system showing possible resonant raman processes.

short of at least two orders of magnitude of the total observed enhancement and the SERS effect was also observed from molecules on metal surfaces which are flat on nanometer scale. Various experiments also showed that the SERS effect is molecule specific. That is, the enhancement was not observed for every molecule near the metal nanostructure. Instead it was dependent on the chemical nature of the molecule. These observations gave a clear indication of the 'chemical' or 'electronic' SERS effect.

Chemical enhancement involves change in the electronic structure of the metal on adsorption of the molecule (figure 3.2). A number of different mechanisms have been proposed as the origin of this effect. The first one involves different types of interaction between the plasmons (substrate) and the molecules. The interaction between the metal and the molecule causes a broadened electronic level in the molecule and thus the resonance Raman effect becomes active. Dynamical charge transfer is yet another mechanism discussed as the origin of chemical enhancement, where the photon annihilation causes the excitation of the electron into a hot electron state. This excited electron is transferred to the lowest unoccupied molecular orbital (LUMO) of the adsorbed molecule. The next step is the transfer of the hot electron from the LUMO back to the metal and finally the return of the electron to its initial state and the Stokes photon creation [45]. This effect will be further discussed in detail when we present the results.

## 3.4 Enhancement Factor

The enhancement factor is important because this is what defines SERS and differentiates it from the Raman. However the absolute definition of the SERS enhancement factor is not possible to be given and hence it is hard to find to compare all the SERS experiments on the same scale. The reasons for this disparity will be explained in the coming arguments. However in general terms, the enhancement factor can be described as *the ratio of the enhancement obtained to what would be obtained for the same molecule in non SERS conditions*[24].

This definition is very broad. It is seen that not every molecule that is adsorbed on the SERS substrate gives a good enhancement. It strongly depends on the position at which the analyte molecule is adsorbed. The local field enhancements or the *hot spots* are distributed unevenly on the surface. Hence the enhancement factor can be classified as the single molecule and average enhancement factor.

### 3.4.1 Single molecule enhancement factor

As the name suggests this gives the enhancement of the molecule at a specific position of the substrate. It depends on a number of factors such as the field at the spot where the molecule is, hot-spot, orientation of the molecule on the substrate and the polarization of the excitation. Unfortunately, even if it is possible to determine exactly the polarization of the excitation with respect to the substrate by knowing the exact geometry of the substrate, the other two are impossible to determine. There is generally no control, as of now, over the number of hot-spots present in a substrate, their location or the orientation of the analyte molecule. A huge effort is made by the research groups to create well defined substrates so as to have a control over the enhancement sites. Therefore, even if we have two substrates that are identical in preparation, the enhancement factor cannot be compared in the true sense as we have no control over the molecule. The maximum single molecule enhancement factor can be very huge depending on the substrate and the molecule. Up to an enhancement of  $10^6$  have been reported for the single molecule.

### 3.4.2 Average enhancement factor

This gives the spatially averaged enhancement factor and in principle represents the property of the substrate in total. Typically the average enhancement factor is several orders of magnitude lower than that of single molecule enhancement factor and are reported up to  $10^3$  in the literature.

### 3.5 Important parameters that dominates the SERS

The enhancement in SERS depends on a number of parameters which are explained in short below.

The substrates play a major role in determining the enhancement. The characteristics of the substrate like the material from which it is made and the technique used to prepare play a major role. Silver is preferred over gold in a number of experiments because of its ability to give huge enhancements in the visible range where lasers are readily available. If the metal is deposited on another material such as glass, then the refractive index of the material can play a role too.

Another important factor is the analyte itself. The characteristics of the analyte molecule used like the adsorption properties of the molecules and their interaction with the substrate in question are important. Some analytes are even known to cause a shift in the plasmon resonance of the substrate.

The excitation parameters like the wavelength, polarization, intensity and time of the spectra are crucial. Too high an intensity of the excitation light for a long period can cause photo bleaching of the molecules in certain substrates.

Last but not least, the sensitivity of the detection set up is decisive since a detection system with higher sensitivity can give a good resolution to obtain the single molecule enhancement at the hot-spots.

### 3.6 Surface enhanced resonance Raman scattering

The surface enhanced resonance Raman scattering (SERRS) technique is derived from SERS. It occurs when the excitation wavelength is chosen to overlap the absorption band of the analyte molecule. There is a huge enhancement due to the additional contribution of the resonance Raman scattering. The SERRS technique was originally reported by Stacy and Van Duyne [46]. This is because the scattering intensity is increased by a factor of  $10^2$  to  $10^6$ . The enhancement obtained is very much greater than either resonance Raman or SERS, enabling very sensitive analysis and low detection limits to be achieved. The SERRS technique is sensitive, selective and produces structural information and characteristic fingerprint spectra. The characteristic spectra routinely observed with SERRS permits identification of mixtures without the need of special preparations.

## 3.7 Experimental set up

The set up (fig 3.3) gives us the opportunity to record the SERS spectra and includes dark field microscopy for imaging the samples. The sample is illuminated

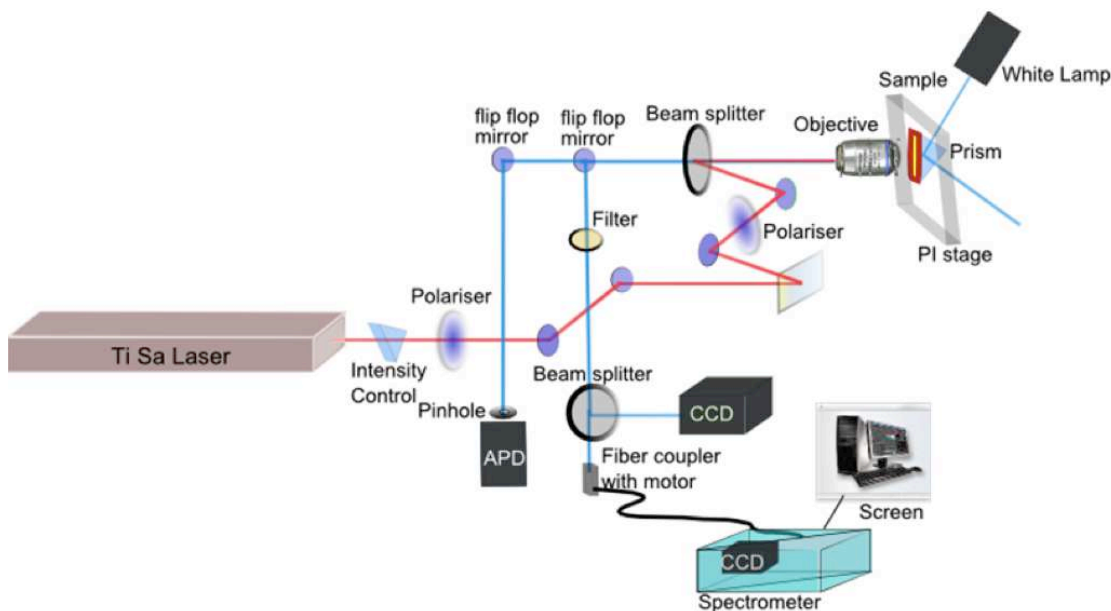


Figure 3.3: Illustration of the Raman setup. The red line shows the excitation path and the blue line, the detection path.

using a continuous tunable Ti:Sa laser with an output from 700 nm to 1100 nm and a maximum power of 3 W. The pump laser is a 532 nm Nd-Yag diode pumped laser. The intensity and the polarization of the incident beam are adjusted using a half wave plate and a polarizer respectively, which are controlled using a home written software. The sample is mounted on a Piezo stage which allows for a translation of 200  $\mu\text{m}$  in the three directions and is illuminated through a high numerical aperture objective (60X, NA= 0.95). The beam size on the sample is around 800 nm. The signal from the sample is collected with the same objective in the back scattering geometry. The laser line is cut off using the appropriate filters (two filters of OD  $\approx$  4) depending on the wavelength. The signal passes through a beam splitter which allows for the signal to be sent to two detection paths simultaneously. A part of the signal is sent to the CCD for imaging (dark field) and another part to spectrometer (HR640, Jobin-Yvon) with a grating of 100 lines/mm. The interest of such a low spectral resolution system is to enable for the recording of the spectrum on a wide range of interest in a single acquisition. It is important when the enhancement is very important allowing for the detection of the signal of a few molecules, which can rapidly blink. Other gratings are available.

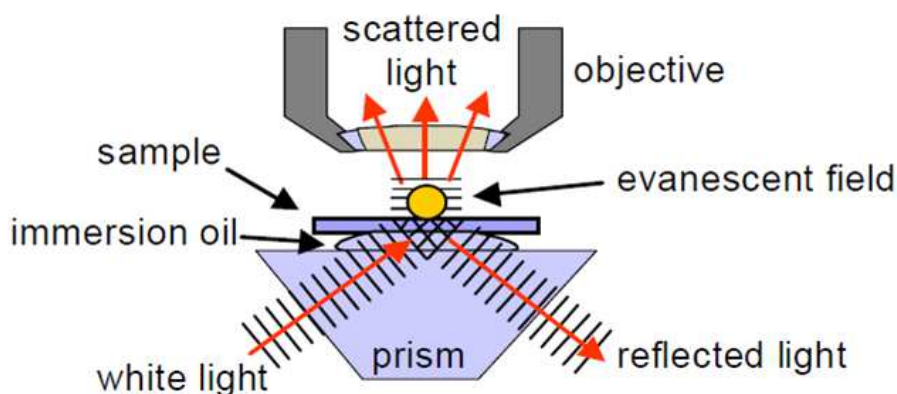


Figure 3.4: Total internal reflection setup (from Ref. [41]).

They can be used to record a reference spectrum on the molecules of interest. The spectra are recorded by a nitrogen cooled CCD.

The filtered signal back scattered through the objective could also be redirected to an avalanche photodiode by means of a flip-flop mirror. This allows for confocal/photonic imaging of the Raman signal. This kind of imaging provides a map of place where the signal is strong. It can give a better understanding of the occurrence and density of hot-spots on the sample.

### 3.7.1 Dark field

The nanowires are imaged using dark field microscopy. With this set up, we ensure the position of excitation and that of collection on the sample. The dark field is achieved by using the properties of evanescent waves. Their first characteristic is the intensity profile, which exponentially decays away from the source that created them. This means that evanescent waves are highly localized to a surface or edge. They are most often created by means of a total internal reflection prism illuminated above its critical angle (figure 3.4). In our set-up the prism is illuminated with a tungsten halogen light source. The evanescent waves are created at the surface of the sample, which has been attached to the prism with an index matching liquid. A benefit of evanescent illumination of the sample is that it is a dark field method in which the background illumination does not reach the collection optics, resulting in a large signal contrast for light scattered by the deposited particles.

### 3.7.2 Probe molecules

The dyes Rhodamine 6G, ATTO 740 and Atto 680 have been used in these measurements depending on the sample.

Rhodamine 6G (Rh6G) is one of the most commonly used dye for the SERS study. It has been widely analysed as a probe molecule and so its structure, properties and SERS spectra are well known. The basic building blocks common to all rhodamines are the dibenzopyrene chromophore (xanthene) and a derivative of a benzoic acid molecule (carboxyphenyl group) which is linked in ortho-position to the centre ring of the xanthene. The rhodamines are singly charged, positive ions; there is no static electric dipole moment along the long axis of the molecule in either the ground nor the excited state.

The single unit of Rhodamine consists of two linked chromophores which are sensitive to different spectral regions of electromagnetic radiation (figure 3.5). One chromophore is positively charged xanthene ion which is strongly attracted to the metal surface by Coulomb interactions and has a strong absorption in the visible and the other chromophore is the carboxyphenyl or benzoic acid group absorbing in the near-UV region. Therefore they are suited to investigate the role of resonance enhancement in SERS [47].

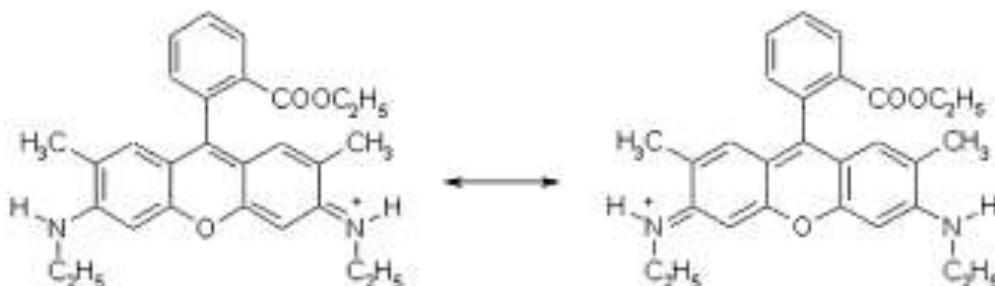


Figure 3.5: Two possible mesomeric forms of rhodamine 6G which have the same weight (from Ref. [47]).

The electromagnetic and the chemical interaction of the Rh6G with the Ag nanoparticles have been studied [48]. It is hydrophobic in nature with its absorption peak at 532 nm and emission at 552 nm.

The figure 3.6 gives the absorption and emission spectra of rhodamine 6G.

ATTO 740 is a new dye, which is cationic in nature and has absorption peak at 740 nm and emission at 760 nm. The Raman lines of ATTO 740 have not been reported yet. ATTO 740 has been chosen to give the ability to resonantly excite the molecule and to explore the role of this additional source of enhancement of the Raman signal. Few dyes can be efficiently excited in the NIR range of the excitation source and ATTO 740 present an absorption efficiency quite large.

Atto 680 is a neutral dye with its absorption peaking around 676 nm and emission at 720 nm. This dye has recently been used in a Raman study and the wavenumbers of different lines has been reported [49].

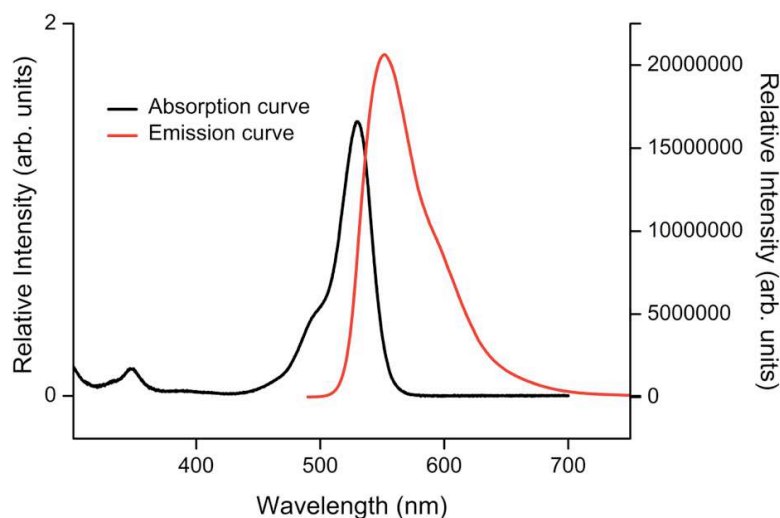


Figure 3.6: Absorption and emission spectra of rhodamine 6G (data from photochem cad).

The figure 3.7 gives the absorption and emission spectra of ATTO 740. The dye has an absorption peak at 740 nm and the emission peak at 760 nm.

The dyes have been used at low concentration, generally around  $10^{-5}$  or  $10^{-6}$  M, in order to avoid the blinding of Raman signals by fluorescence. When the isolated nanowires were incubated with the dyes the number of molecules adsorbed on them were not huge. The dyes were dissolved in ethanol and then diluted with deionised water.

### 3.7.3 Sample preparation

Around  $2 \mu\text{l}$  of the dye was deposited on the nanowire arrays by drop casting and allowed to dry. We did not try to spin cast the dye solution, nor to dip the sample into the dye solution because of the small size of the samples (to be able to use the sample multiple times and for near field measurements). Nanowire arrays are deposited on  $12 \text{ mm} \times 12 \text{ mm}$  coverslips. A complete study needs to deposit on the same sample several dye solutions in order to have reference spectra. The only way to do is to deposit small drops of the given solution, to let it incubate for few minutes then to carefully withdraw the excess without damaging the sample. As far as possible, a whole set of measurements is performed on the same sample, since the plasmon properties varies from a sample to the other.

For the single nanowires around  $100 \mu\text{l}$  of the CTAB nanowires were mixed with  $100 \mu\text{l}$  of 50 nm beads and  $70 \mu\text{l}$  of dye and vortexed gently for 30 seconds. The beads serve either as antenna, allowing for coupling of the excitation light into nanowire

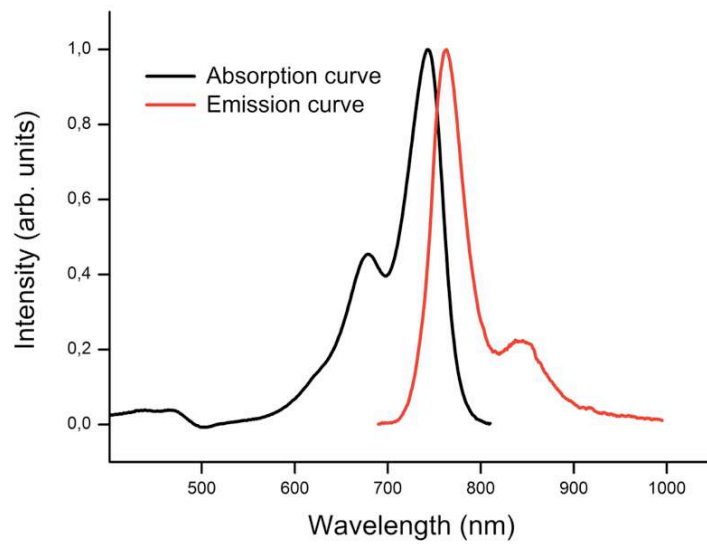


Figure 3.7: Absorption and emission spectra of ATTO 740 (data from ATTOTECH).

plasmons [22] or as artificial hot-spots for Raman spectroscopy [50]. About 80  $\mu\text{l}$  of this solution was drop casted on clean glass cover slips. With the dark field image, it is seen that the nanowires are well dispersed.



# 4

## SERS measurements - Isolated nanowires

### 4.1 Introduction

Plasmonic properties of isolated finite nanowires have been studied widely on a large scale in the recent period due to the availability of a number of fabrication methods. Recently, chemically grown commercial nanowires are also available making it all the more easier. A substantial part of the work has been done on semiconductor nanowires. They have been introduced in the early 90s and since then extensive studies have been carried out on such nanowires and much insight has been gained on tuning their optical properties by controlling their size. The semiconductor nanowires have been grown using different techniques like epitaxy, vapour-liquid-solid (VLS) growth or lithographic techniques [51].

The other class of nanowires that are routinely used are the metal nanowires. Silver nanowires have been largely studied as mentioned in the previous chapter. Most of them are prepared by lithography since it is easier to study the various contributing factors to the SERS in such a case. Recently, new nanowires have been studied that are made of partly silver and partly gold or that of nanowires of metals coupled to inorganic dielectrics [51].

Here I present the results of our SERS measurements on the commercial nanowires. As said earlier they are of two kinds, one coated with cetyl trimethylammonium bromide (CTAB) and another with silane. The CTAB layer made it difficult to deposit the nanowires on glass substrates and also prevented the dye molecules we have used for SERS to come in contact with the nanowires which will be explained

in detail in the coming paragraphs. So the silane coated nanowires were used which were supposed to have better adherence to glass and thus making it easier to deposit and thickness of silane layer is 2 nm.

We have studied the LSPR of the nanowire and correlated it to the structure, imaged using the dark field microscopy. In addition, SERS of these samples have been studied. Here we have used the SERS as a probe of the plasmonic properties of the isolated nanowires, to map the field around the nanowire and to access the propagation effects. The study of these properties will be a guide to disentangle and understand the different processes that can take place in more complicated systems like the nanowire arrays which will be explained in the next chapter. The relation between the local morphology and the LSPR, and their combined effect on the SERS have been also been investigated. Propagation properties of isolated finite nanowires and wavelength dependence of propagation has been analyzed. These kinds of studies allow us to put into evidence the key parameters of the SERS enhancement such as the role of plasmons, the dependence on the excitation wavelength. The influence of the wavelength is rarely studied since only few Raman set ups use tunable excitation.

## 4.2 CTAB coated nanowires

The studies were made on the isolated nanowires deposited on a glass substrate. Initially we tried to make the deposition by spin coating. However, this technique proved to be inefficient in spite of making a number of systematic trials as the density of the nanowires in the solution is less and the CTAB coating did not prove to be very compatible with the glass surface for deposition. Later, drop casting method was adopted wherein about 50  $\mu\text{l}$  of the nanowire solution was dropped on the glass substrate and allowed to dry in ambient conditions. The dye used for the study (either ATTO 740 or Rhodamine 6G) is deposited over this. CTAB is a surfactant and the CTAB coating prevents the nanowires from forming clusters. For this purpose, it has been used in excess in the solution. The thickness of the CTAB on the nanowire is about 6 nm. The combined effect of these two results in a thick layer of CTAB over the nanowires (seen as white deposition) making it difficult to detect the nanowires in the dark field imaging. The SERS measurements on this system only resulted in a huge fluorescence background and effectively no Raman. We assumed that the absence of Raman was due to the CTAB layer because it acts as a barrier between the nanowire and the molecule. As a result, the molecule is too far from the nanowire to give an efficient SERS effect. Many attempts were made to remove the excess CTAB in the solution and at least partially on the nanowires being careful not to break or damage the nanowires in anyway.

After many systematic trials, this drawback was overcome by keeping the solution at 25°C for 3-4 hours. The CTAB apparently melts which is evident as the solution turns clear pink and the white deposits are not visible anymore. The solution is left undisturbed allowing the nanowires to settle down owing to gravity. The samples prepared by carefully depositing only the solution from the bottom of the eppendorf which suits very well for our purpose of study as there are a good number of isolated nanowires that can be analyzed. The figure. 4.1 gives an idea of the density of nanowires present in the substrate.

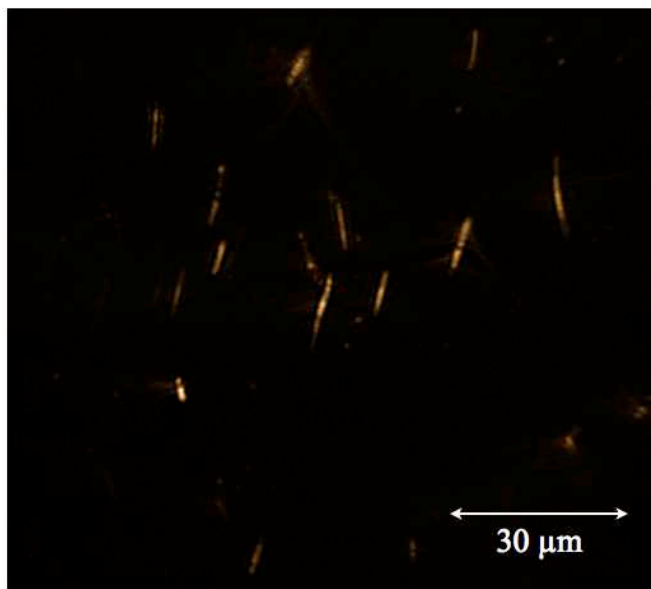


Figure 4.1: Dark field image of the nanowires present on the substrate after drop casting.

The bare nanowires did not yield any appreciable SERS signal or show any plasmon propagation at the excitation power we have used (5 kW/cm<sup>2</sup> unless specified otherwise). Sometimes a weak fluorescence is noticed at some points on the nanowire. Although these results are negative, they are expected. It was important to check if SERS was observed on nanowires deposited as such, since CTAB itself could be the SERS probe needed to map the field around the NW. Some experiments that have been reported indeed use the coating itself as the probe. One such is that of the experiment by El sayed et al where he uses CTAB - capped nanorods as SERS markers for cancer cells [52]. This work demonstrates that CTAB SERS spectrum displays 4 main lines in agreement with CTAB SERS spectrum on copper. These lines at 1000 cm<sup>-1</sup>, 1076 cm<sup>-1</sup>, 1140 cm<sup>-1</sup> and 1265 cm<sup>-1</sup> have been assigned to C-N stretch of the head group, to  $\gamma_{asymm}$  (C-C) and  $\gamma_{sym}$ (C-C) vibrations and to the  $\delta$ (C-H) vibrations of the -CH<sub>2</sub>-N<sup>+</sup>(CH<sub>3</sub>)<sub>3</sub> group [53, 54, 55]. The SERS signature of CTAB capping the nanorods is claimed to be much stronger when the

nanorods are conjugated in cancer cells compared to healthy cells. The interpretation relies on the aggregated configuration of the assembled rods on the cancer cell surface. As a result, the difference with our system is two fold : first in the nanorod study, the collected signal probably comes from the junctions or the gaps between the aggregated nanorods and second, the intensity of the excitation of the order of  $5 \times 10^6 \text{ W/cm}^2$ , which is hundred times larger than the ones we use in our study. The absence of SERS signature on the nanowires deposited alone is thus not surprising. Nevertheless, the absence of SERS from CTAB is not a definitive proof that plasmon surface is not launched in some pristine nanowires. It rather suggests that as such isolated nanowires are not good platforms for CTAB-SERS. The absence of SERS signature of CTAB on the isolated nanowire yields important information. It gives a reference for the analysis of further results.

It is known that the use of highly focused beams is an alternative to prism total reflection configuration for plasmon launching. Here, we use a dry objective with a high numerical aperture of 0.95. It ensures a large spread in excitation wavevectors directions since the maximum available angle is  $70^\circ$ . As a consequence, wave vector mismatch can be overcome. The drawback of the configuration is a high loss in energy since only a few rays satisfy the requirements for plasmon launching. Even if the plasmon could be launched, the small energy of the propagation mode will be readily dissipated and the propagation length will be very less. The near field energy will be vanishingly weak and no SERS signal is likely to be observed. The absence of SERS signal also gives important information regarding the sample itself.

It has been demonstrated that kinks or defects at the surface of nanowires can act as launching sites as well as photon emissive sites for a plasmon propagating along the nanowire [56]. At these given locations, the symmetry rules are partly released and a plasmon can be easily launched with a highly focused beam. We have explored the effect of excitation not only at the ends of different nanowires but also at different points along the same nanowire and we did not see SERS either, even when the excitation intensity was increased up to  $5 \times 10^5 \text{ W/cm}^2$ . It is a good indication that these chemically grown nanowires are of good quality.

In order to efficiently launch propagating plasmons into the nanowire, we have added to the solution of nanowires, gold nanobeads that act as mediators to launch the plasmons and to couple light out of the nanowire to the far field. Such nano antennas have already been demonstrated to be very efficient in silver nanowire systems [57]. We have mixed equal quantities of 50 nm gold nanobeads and nanowires and deposited on glass substrates. The beads serve dual purpose. They act both as antennas for plasmon launching and also for photon radiation [22]. Also, the linking of the beads to the nanowires creates artificial hotspots where the enhancement is expected to be large [58]. To ensure that the beads do not give additional

signal independently by themselves, studies have been made by depositing only the beads on the glass substrate. The dark field images of these samples show a number of bright spots confirming the presence of the beads. No SERS signal is observed under low power ( $130 \mu\text{W}$ ) or high power conditions ( $1.2 \text{ mW}$ ). This is expected since the gold substrates including the nano-patterned ones are known to be less efficient as SERS substrates than their silver counterparts. It explains the very low number of SERS studies on gold.

Our study aims to determine if such a nanowire - nanobead system can serve as an efficient SERS substrate in a confined environment, for example in microfluidic environment or lab on chip etc. We also get additional information on the plasmon propagation in gold nanowires on which very few reports have been made. All the measurements that are to be reported in this chapter are made on such a system along with the appropriate dye unless stated otherwise. The dye molecule or the analyte functions as a probe. Since no detectable SERS signal or propagation has been observed in case of the nanowires or nanobeads alone, we can rule out any possible artifacts or spurious signals as a result of the background scattering.

Here we report our studies on the plasmon spectra of the system and its dependence on the position on the nanowire, SERS dependence on the wavelength and on the plasmon spectra. We present the correlated structural - optical and spectroscopic studies performed at various points on the nanowire-nanobead system.

### 4.3 Dark field spectroscopy

In the chapter on plasmons, we have already seen that the LSPR depends on various factors like the shape, size and refractive index. Thus the plasmon spectra of the nanowire is a representative of the external environment where it is measured and can differ from one place to another even on the same nanowire owing to a number of factors. We have tried to correlate the morphology of the nanowire - nanobead system to the LSPR spectrum. The correlation of the structure to the spectra is very important and explains various results that we have obtained. The pioneer of such experiments was reported by Mock et al [27] who reported the correlation of structure to the LSPR spectrum of single nanoparticles. They performed the dark field spectroscopy and transmission electron microscopy (TEM) on silver nanoparticles with various shapes. Many experiments of the same kind have been done after this but they are usually made on single nanoparticles or aggregates. As said earlier the experiments of such kind reporting on nanowires are very few. The surface plasmon resonance is not generally displayed.

In our experiment the structure has been obtained using the optical dark field spectroscopy. The signal recorded in dark field imaging is that of extinction. It results from the balance between absorption and scattering. In our case the particle

is thin but long and hence the scattering dominates the absorption even if we work in the red part of the visible spectrum, where the imaginary part of the refractive index of gold is non negligible (Fig 4.2). As a result, the signal mainly reports on the local scattering properties of the nanowire. The image in dark field is given by the convolution of the scattering signal at a given excitation location by the point spread function (PSF) of the microscope. In our set-up, neglecting aberrations because of the thickness of the sample, the impulse response is a spot of about  $0.9 \mu\text{m}$  in the object plane which corresponds to a spot of about  $60 \mu\text{m}$  in the image plane owing to the magnification of  $\times 60$  of the microscope. The nanowire is very thin ( $30 \text{ nm}$ ) and the width of the nanowire seen on the image is given by the image PSF.

Even if the dark field imaging is not useful to directly discriminate small kinks or defects by a change in the shape of the image, their presence is nevertheless reported as a variation in the intensity of the scattering. As will be explained below, the additional spectral analysis of the signal gives the opportunity of detecting the presence of small objects on the nanowire. In short, the dark field imaging is a very fruitful method to precisely locate the nanowire and the position of excitation on the nanowire. Further it gives access to the orientation of the nanowires, which can prove to be very useful for polarization measurements.

The figure. 4.2 gives the dark field image of a nanowire and the corresponding bright field image. The bright field image is obtained by removing the total reflection prism and by directly illuminating the sample from the opposite side of the objective. The image of the nanowire is obtained owing to the long shape of the particle but the contrast remains quite low, sometimes making it difficult to interpret the image because of the possible diffraction patterns due to the residue of immersion oil. Nevertheless, it allows us to be sure that we are studying a nanowire and not another system, like a chain of beads. When imaging a sample with a high bead density it is easy to observe a nearly linear chain of beads which can be mistaken for nanowires. However, with bright field, they can be easily identified since their images differ from that of a nanowire because of diffraction effects.

The interesting point on the bright field image given below is the apparent gap between the two aligned linear structures on the upper half of the figure. It suggests that two nanowires are present, which is confirmed by the change of intensity in the corresponding dark-field image at the same position. Moreover the length of the lowest nanowire is very close to  $6 \mu\text{m}$  in line with the expected value. The circular structures seen on the figure are most probably the image of small index of refraction oil bubbles left on the cover slip after removing of the prism.

Here I present some of the plasmon spectra at different points on the same nanowire. The examples presented here are of a system consisting of nanowires, nanobeads

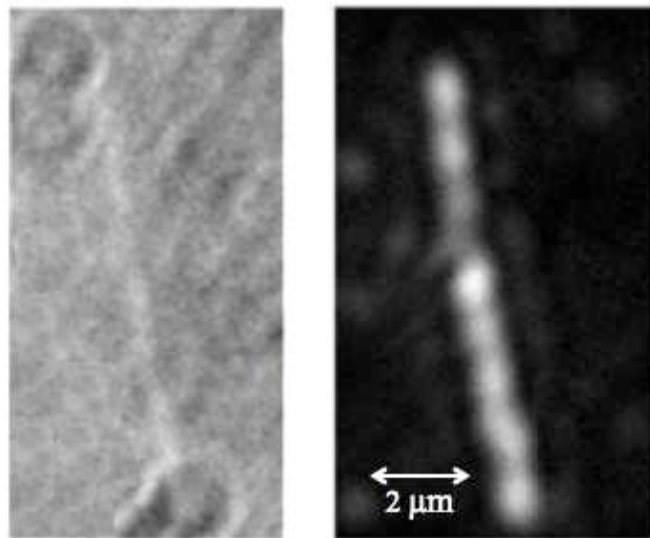


Figure 4.2: Dark field image of the nanowire (right) corresponding bright field image (left).

with ATTO 740 molecules. The figure. 4.3 shows the plasmon spectrum at the middle of the nanowire with the corresponding dark field image. The cross shows the detection spot on the nanowires.

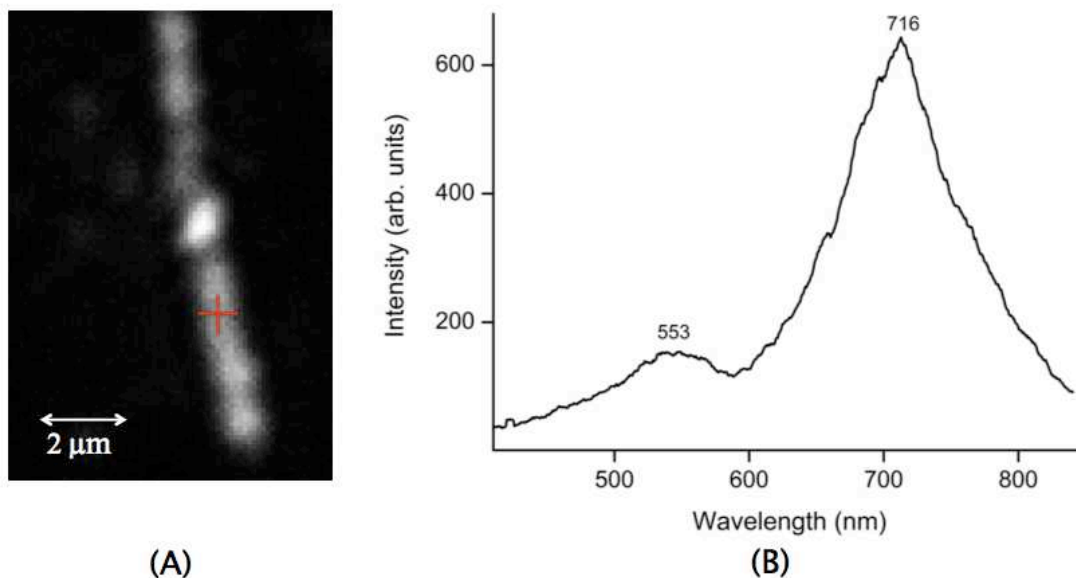


Figure 4.3: Dark field image of the nanowire (A) with the plasmon spectra (B) corresponding to the position given by the red cross.

The plasmon spectrum shows two peaks or rather two bumps. The presence of a bump at 553 nm suggests the presence of a bead on top of the nanowire, whereas the plasmon of the nanowire itself corresponds to the bump at 716 nm. Studies have already shown that the nanobead placed on the nanowire exhibits near field coupling which influences to a large extent the plasmon resonances [59]. The bright spots observed on the nanowires could be either the beads present on the nanowires or the kinks (extremely sharp bends or defects on the nanowires [56]). The only way to differentiate the presence of the beads is by the plasmon spectrum recorded at that point.

The figure. 4.4 shows the plasmon spectrum at the end of the nanowire with the corresponding dark field image.

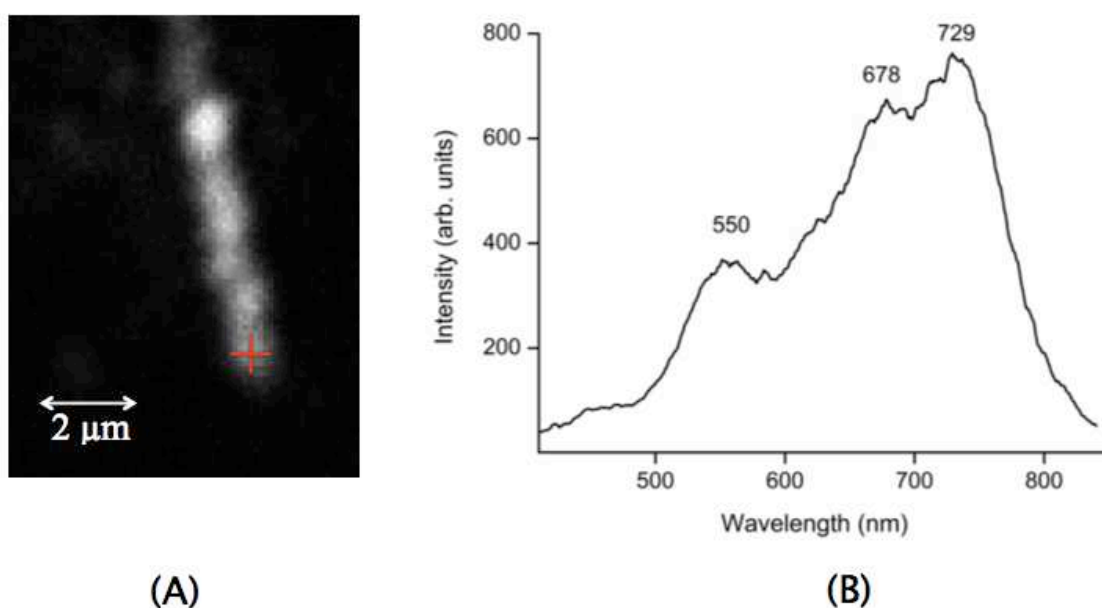


Figure 4.4: Dark field image of the nanowire (A) with the plasmon spectra (B) corresponding to the position given by the red cross.

The spectrum presents a dim bump around 550 nm corresponding to the excitation of the transverse plasmon and a double peak in the range 650 nm - 750 nm. This type of structure could be expected if the longitudinal plasmon of the nanowire is perturbed by the interaction with the ATTO 740 molecules. A strong coupling occurs between the molecule and the metal when the electronic resonance of the molecule and that of the plasmon are very close. It results in hybridization of the energy levels, leading to a splitting in the plasmon curve. The splitting depends linearly on the thickness of the molecular layer on top of the plasmonic structure. Such measurements have been performed in the case of gold nanorods [60]. The

observed plasmon splitting, in this particular case, could be a result of a large number of molecules deposited on top of the nanowire at this particular location where the plasmon and molecules is in resonance, resulting in partial hybridization. The other possibility for such a double peak is the contribution from the position of study of the nanowire. In fact almost all the spectra measured the ends of the nanowires present a double peak. It has been shown that the end of the nanowires are usually semi spherical in shape and have different symmetry compared to any other point on the nanowire [61]. Hence, the structure of the plasmon is different from that of the others. In fact it has been shown that the polarization dependence of the SERS signal varies significantly at the end of the nanowires from the any other position for the same reason [62].

We will present some more examples of the different plasmon spectra further in the chapter as we explain the spectroscopic results.

To summarize, the figures show very clearly that the structure at the position of measurement, that is, the presence of beads has a very big effect on the LSPR spectrum. Moreover the nanowires are relatively coarse on the surface because the removal of CTAB is not uniform. This also contributes to the different gaps or interactions between the nanowire and beads and consequently to the shape of the LSPR spectrum. Since the LSPR spectra are different at different locations of the nanowire-nanobead system, the dark field spectroscopy is essential to correlate the SERS signature to the plasmon resonance which is of great interest to use plasmonic structures as sensors.

## 4.4 Propagation measurements

The surface plasmon propagation (SPP) has been studied by launching plasmons at various positions on the nanowire and at different wavelengths. The propagation measurements on the gold nanowires are very difficult to measure owing to the heavy intrinsic losses of gold (see fig. 2). Therefore the SPP decay length is very small. It is possible to witness propagation from one end of the nanowire to another end only for short nanowires. The other possibility to have propagation in long nanowires is to increase the power. However with increased excitation powers the sample could be damaged. Hence, we discard this option to prevent the objective from damage while limiting huge scattering all over the sample and also to avoid the thermal effects of using high power.

Lukin et al have demonstrated that for a conducting nanowire of small enough radius  $R$ , surrounded by a dielectric medium, there is a single TM mode that can propagate inside the nanowire whose transverse area is of the order of  $R^2$ . It indicates that the mode has nearly the same cross-section as that of the nanowire and that it is strongly confined around the structure [63]. The authors have also

calculated the energy relaxation paths of a dipole emitter located close to the nanowire and we will discuss these results in the paragraph related to the spectroscopic data. Our system (gold nanowire of radius 30 nm surrounded by CTAB) satisfies the requirements of the model. As a consequence, we expect that the field will be confined around the nanowire. Moreover if a strong coupling between the excitation and the nanowire is expected, so are the propagation losses. Therefore the propagation length is expected to be limited in such thin nanowires. We have used the plasmon mode equation from their calculations to foresee the dependence of plasmon decay with wavelength.

The plasmon decay length has been calculated considering the nanowire as a cylinder of radius  $R$  of dielectric permittivity  $\epsilon_2$  which is centered along the  $z$  axis and the surrounding dielectric medium is given by  $\epsilon_1$ . Here  $k_{\parallel}$  is the longitudinal component of the wavevector, which is related to the vacuum wavevector  $k_0 = \omega/c$ . The  $K_0$  and  $I_0$  represent the modified Bessel functions.

$$\frac{\epsilon_2}{\epsilon_1} = \frac{K_0'(k_{\parallel}R)I_0(k_{\parallel}R)}{K_0(k_{\parallel}R)I_0'(k_{\parallel}R)} \quad (4.1)$$

The model assumes that the nanowire is infinite and the retardation effects during the plasmon propagation is not taken into account. Nevertheless, it gives a trend about how the propagation evolves with respect to the wavelength. It is seen clearly from figure 4.5 that with the decrease in wavelength the losses increase and hence plasmon propagation length decreases. Also the solution to the equation requires that  $k_{\parallel}R = C$  to be constant which leads us to the scaling law  $k_{\parallel} = 1/R$  of the plasmon fundamental mode. The propagation length is inversely proportional to the imaginary part of  $k_{\parallel}$ .

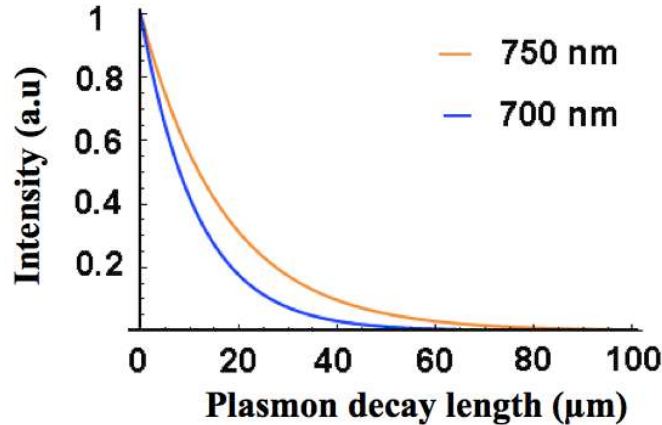


Figure 4.5: Plasmon decay curves for the nanowire under excitation at 700 nm and 750 nm calculated using the equation given above.

There are a few techniques for visualizing locally excited surface plasmons propagating along nanostructures. In some of the reported experiments, the excitation intensity and the structure (shape, kind of metal) of the nanowires allow for the direct observation of photons exiting the nanowire at the distal end. In such situations, the propagation length is quite easy to measure since it can be derived by the measurement of the ratio of the emission intensities at the launching and exit sites on different nanowires. The situation where the propagation length is shorter or of the same order than the length of the nanowire is much more difficult to handle. The propagation length can be determined by near-field optics as it has already been done on different structures [64]. Other optical methods have also been demonstrated, such as the one recently on the analysis of the bleaching length of a luminescent polymer coating the nanowire [65]. The dye is excited by the surface plasmon field and subsequently emit radiation into the far field, which is detected with a CCD camera through a microscope objective. In this way a spatial mapping of the SP field distribution is obtained. However, the fluorescence of dye molecules in direct contact with a metal surface will be completely quenched, and the excitation and emission rates will depend strongly on the distance to the metal surface.

Another possibility is to use the SERS signature of molecules located close to the nanowire, as it has been demonstrated in the case of silver nanowires. Finally, one can combine both previous methods by using a reporter whose resonance is close to the plasmon resonance of the metallic structure. We have used this last possibility in our work. Even if the results depend on the presence of a molecule at the studied location, it offers the possibility to extract much information about the plasmonic properties of the system despite the inhomogeneous coating of CTAB along the nanowire, since one can measure both metal-enhanced fluorescence (MEF) and SERS. We have tried to study deposited nanowires with near-field optics, but unfortunately the residue CTAB particles on the sample made it difficult to confidently extract signatures from the nanowires.

The propagation here has been measured using the dark field imaging. The implementation of the technique is easy and the results are straightforward to understand. The energy transfer between the propagating plasmons and the fluorescent molecules used for analysis is the key and the optical signals emerging from this interaction are used to measure the propagation. However, one limiting factor common to all the methods except SNOM is the spatial dimension of the PSF. Even with very efficient filters (optical density  $\approx 8 - 10$ ) to remove the blinding excitation signal, the image has a spot with a diameter of the order of  $1 \mu\text{m}$ , corresponding to the emission of molecules close to the surface of the nanowire. If the propagation is of this order of magnitude, the length of propagation cannot be accurately measured. On the contrary, if the propagation occurs beyond  $1 \mu\text{m}$ ,

the center to center distance between the excitation spot and the emission spot can be accurately determined (for a known PSF).

The propagation of the plasmons is easy to visualize as there is either SERS excitation or enhanced fluorescence all along the path of propagation. We have also witnessed remote excitation (blinking bright spots at locations distinct from excitation spot). These different situations and possible emissive processes will be discussed in the next section. The argument that the signal is the result of direct excitation of the molecule by the laser can be disproved with two simple facts. There is ATTO 740 everywhere on the substrate but we see the fluorescence only on the nanowires which indicate the plasmon involvement. Secondly, the direct interaction of the laser with the analytes will result in rapid photobleaching of the molecules which suggests that our case is the one of indirect excitation.

## 4.5 Plasmon propagation dependence on Wavelength

We have studied the plasmon propagation at four different wavelengths. The dark field images that are recorded simultaneously helps to make the measurements at the same spot for different wavelengths. The wavelengths chosen were 702 nm, 728 nm, 750 nm and 772 nm. They have been chosen to exploit the range of tunability of the excitation up to 770 nm beyond which the sensitivity of the camera decreases considerably. This upper limit is a satisfying compromise in order to excite ATTO 740 above its emission peak. Appropriate filters were used for each wavelength.

It is important at this point, to discuss the different kinds of images that are displayed here. The dark field image, as we have already seen gives the nanowire structure. It is taken with the white lamp. The second image, what will hereafter be denoted as propagation image, is recorded with the excitation laser at single wavelength. Appropriate filters (two filters, OD = 8 - 9) were used to filter the laser and as the name suggests, it helps to visualize the propagation of plasmons in the structure. Another important point to be noted is that the propagation length is a concept related to the exponential decrease of the intensity of the surface plasmon whereas what we deal with is the propagation distance which gives the length over which propagation is observed. The images are automatically adjusted with respect to the brightest spot to prevent the saturation of the camera.

We present here an example of a study of plasmon dependence on wavelength. The system is quite interesting because there are two nanowires that are partly bridged by at least one or may be several nanobeads. The two nanowires are clearly observed in dark field microscopy but also in bright field imaging. The figure 4.6 gives the dark field and white field image of the structure analyzed.

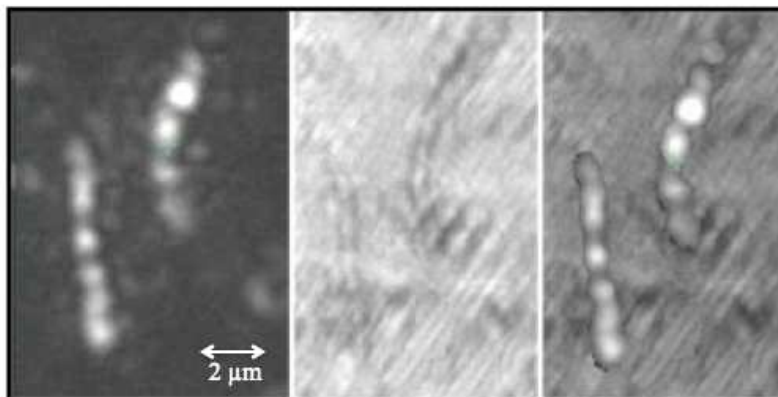


Figure 4.6: Dark field image of the system (left), the bright field (center) and the superimposed image of dark and bright field (right)

#### 4.5.1 702 nm

At 702 nm, we are quite far from the absorption and emission of ATTO 740, the analyte molecule used, which peaks at 740 nm and 760 nm. We do not observe any appreciable propagation at many points of excitation. The dark field images show a bright spot at the point of excitation or closer to it. This is because the plasmon spectra of the nanowires is broad and hence the localized plasmons are excited at this wavelength but not the propagating plasmons. However, as explained earlier the plasmons can be different at different positions of the nanowire. Hence when the plasmon peak is in near proximity to the excitation wavelength, we see propagation as in the example.

In the figure 4.7, we see the dark field image of propagation and the plasmon spectra corresponding to the excitation position. Here the plasmon spectrum consists of two peaks, one at 698 nm. This explains the propagation that we witness. The redline gives the excitation wavelength. The propagation distance is found to be 1.8  $\mu\text{m}$ .

#### 4.5.2 728 nm

The figure 4.8 shows an example of propagation at 728 nm. The plasmon at this location is broad and peaks around 720 nm close to the excitation wavelength. In addition, the plasmon also overlaps with the absorption curve of the dye molecule, ATTO 740 almost completely. As a result we are able to see the nanowire structure being reproduced by a combination of processes taking place at the same time. There is efficient SERS excitation along the nanowire. The resolution of our imaging system and the proximity of the exit points gives an image which looks

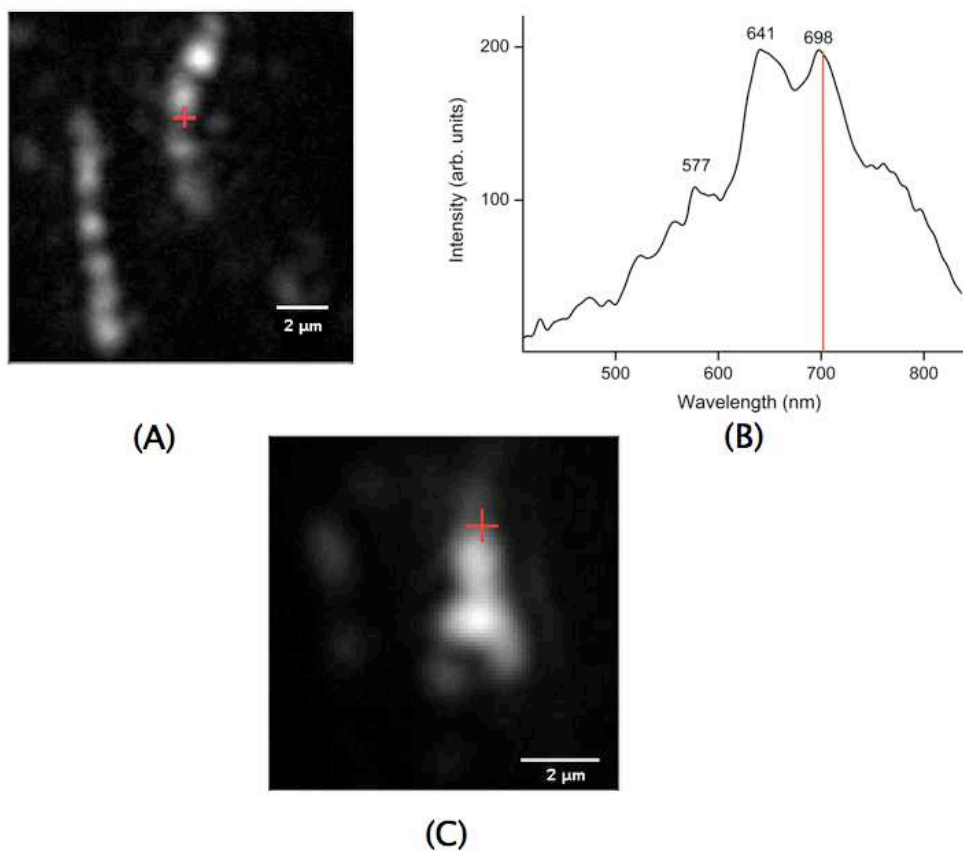


Figure 4.7: Dark field image of the system (A) and of propagation (C) at 702 nm. The red cross gives the excitation point. The plasmon spectrum (B) is given and the red line denotes the excitation wavelength.

like there is a continuous enhancement all along the nanowire. In the studied situation, the image additionally displays a kind of bright structure shaped like H, bridging the two nanowires. A close look at the pattern shows that a bright path starts from the excited nanowire on the right to the direction of the bright spot in between the two nanowires. This suggests that leakage occurs at the bent part of the nanowire on the right and that the energy is transferred to the metallic structure in the middle of the bridge where emission is enhanced. The same energy transfer process allows for the lightening of the left hand side nanowire. Different processes can explain the propagation of energy along the bridge. The first one is resonant energy transfer between the resonantly excited molecules sitting between the two nanowires. Such a complex process has been widely studied [66] and is beyond the scope of this work. It is important nevertheless to mention that it can lead to the quenching of the emission in line with the observation that no light is

observed in between the structure in the middle of the bridge and the left hand side nanowire. Moreover, if the ATTO 740 molecules form aggregates, the energy transfer would be rather mediated by excitons.

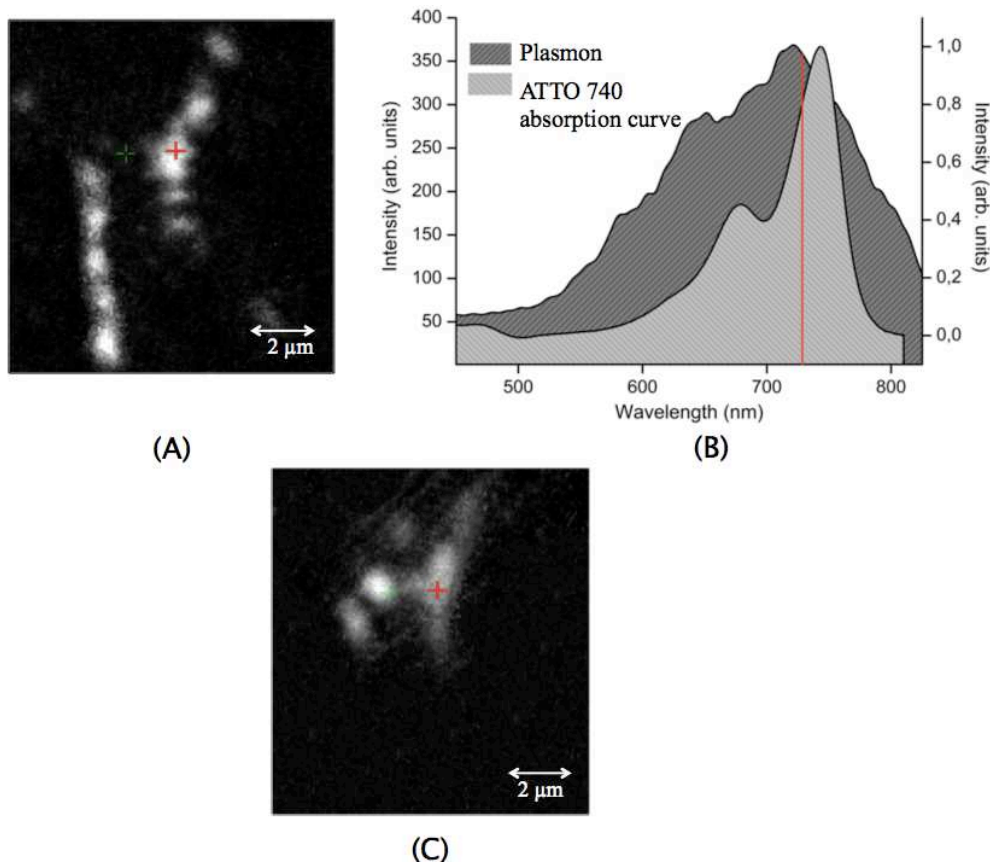


Figure 4.8: Dark field image of the system (A) and of propagation (C) at 728 nm. The red cross gives the excitation point. The plasmon spectrum (B) is overlapped with the absorption spectra of ATTO and the red line indicates the excitation wavelength.

A second possibility that could contribute to the observed pattern is the long distance indirect excitation of plasmonic structures that has been very recently demonstrated as a result of the coupling of near fields of several randomly dispersed scatterers [67]. We can conclude that the molecules do play a role in such a long-distance energy transfer since this H-like structure definitively disappears after several sequences of illumination, which can be reasonably attributed to photobleaching of the molecules. On the contrary, a bright channel is still observed on the right hand side nanowire and the bright fraction of it is unchanged, demonstrating that the observed emission is more robust. We will demonstrate in the later part of this chapter that it corresponds to SERS.

### 4.5.3 750 nm

The emission curve of ATTO 740 peaks at 760 nm and the excitation at 750 nm lies perfectly in between the absorption and emission curve of the probe. However the plasmon spectrum plays a larger role in deciding the propagation at this wavelength. In general, the plasmon spectra are broad and hence in most cases the excitation wavelength is within the spectra. Therefore good propagation has been observed in average and in some cases remote excitation as well. The figure. 4.9 shows the plasmon has a double peak and a small bump at 535 nm corresponding to a bead. The excitation wavelength is close to the peak at 755 nm which enables efficient excitation of propagating plasmons. The propagation length is found to be  $1.8 \mu\text{m}$ .

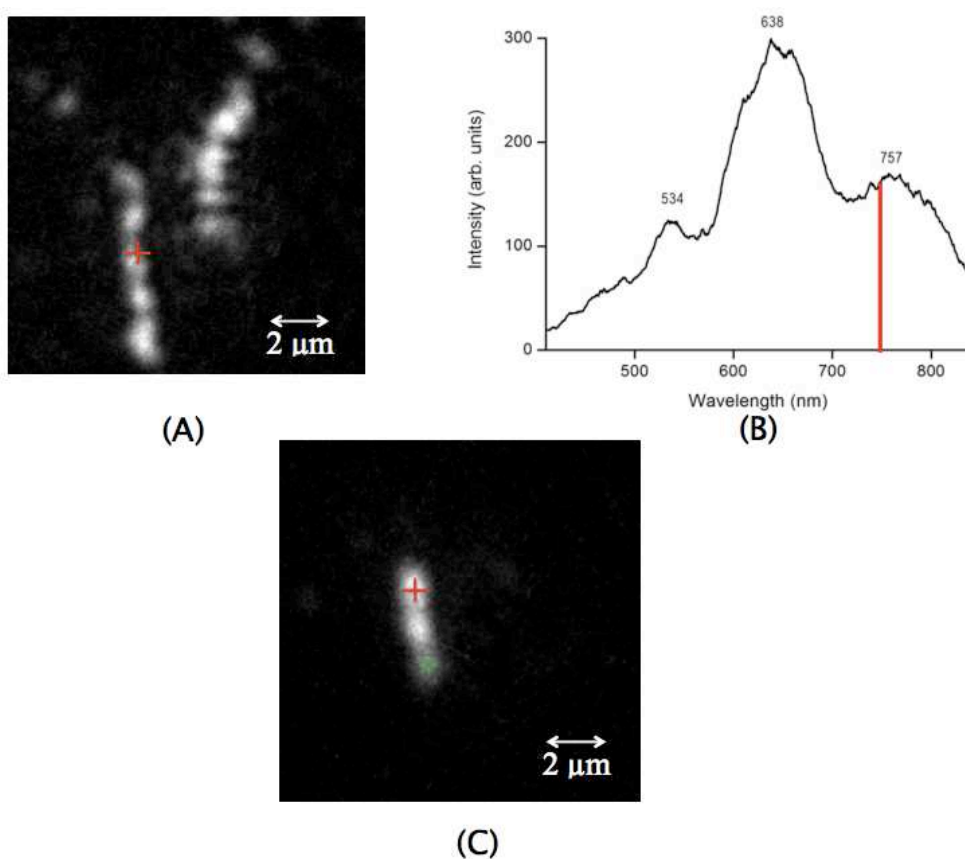


Figure 4.9: Dark field image of the system (A) and of propagation (C) at 750 nm. The red cross gives the excitation point. The corresponding plasmon spectrum (B) is given and the red line denotes the excitation wavelength.

The results at this wavelength are a clear evidence of the best possible situation for visualization of the propagation. The fluorescence as well as the SERS signals

should be enhanced efficiently in this case.

#### 4.5.4 770 nm

Theoretically, the losses during propagation at this wavelength should be lower than the others which would increase the propagation length. However, at 770 nm, the excitation wavelength is far from both the peak of the plasmon spectrum at this position and also of the absorption and emission curves of the probe used. Hence, the plasmon excitation is not strong enough for any propagation to occur. In case the plasmon spectrum of the nanowire peaks close to 770nm, propagation is observed albeit a weak one. This is the case presented here (fig. 4.10). The excitation wavelength is far from the plasmon peak at 799 nm. Hence we observe a very feeble propagation.

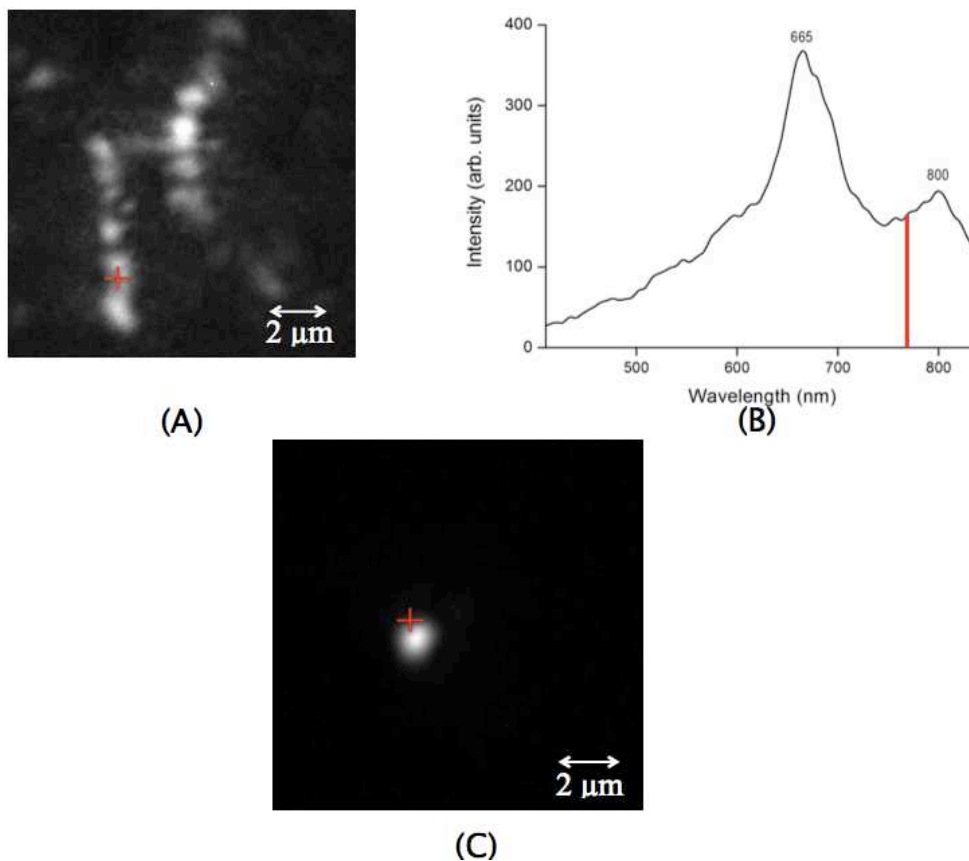


Figure 4.10: Dark field image of the system (A) and of propagation (C) at 770 nm. The red cross gives the excitation point. The corresponding plasmon spectrum (B) is given below and the red line denotes the excitation wavelength.

### 4.5.5 Summary of the different mechanisms

When the nanowire-nanobead system is excited, a number of processes occur individually or at the same time which are summarized below. The figure. 4.11 gives the schematic of the different mechanisms witnessed in our system. When the sample is excited at the surface plasmon resonance, propagating plasmons couple to the nanoparticles at the junction between the nanoparticles and nanowires and exit as photons. With the molecules that are close enough or directly in contact with the metal, we observe resonant emission. This SERRS emission is from the molecules that are in the near field of the propagating plasmons. The near field decreases exponentially in the direction perpendicular to the axis of the nanowire. Hence to visualize the SERRS the molecules need to be close enough. However recent reports have suggested that it is possible to visualize such an effect as far as  $\mu\text{m}$ .

When the excitation wavelength is also in resonance with the molecule in addition to the sample, we can see other effects too. The molecules that are far from the metal lead to fluorescence. We have seen metal enhanced fluorescence at many excitation points in our examples. The next process that is evident is the resonant energy transfer between close randomly dispersed molecules and fluorescence of a molecule enhanced near the metallic nanostructure. There can be SERS seen at the junction between two beads and additionally long-distance indirect excitation of beads and subsequent fluorescence enhancement [67].

The third image gives the schematic of what is observed in a propagation imaging. As already explained, the emission imaging results from the convolution of the point source emission (the molecule) with the PSF of the microscope. As a result each emissive molecule gives a spot of around  $0.9 \mu\text{m}$  along the nanowire and depending on the density of emitters at efficient locations, the image can be a continuous segment along the nanowire, or a series of bright spots possibly remote from the launching site.

### 4.5.6 Comparison

The figure. 4.12 gives the comparative study of the propagation at different wavelengths on the same spot on the nanowire. Here the excitation point is at the edge of the bridge between the two nanowires. The plasmon spectrum recorded at this place reveals a double peak, one at 601 nm and the other at 754 nm. It is seen that the propagation follows the trend as explained earlier.

At 702 nm, we see a good propagation over  $1.7 \mu\text{m}$  that manifests itself as two adjacent spots. This is facilitated by the fact that the plasmon spectrum is broad. At 728 nm, the dark field image reveals the enhancement along the solitary beads on top of the nanowire. At this point, it is important to remember that the

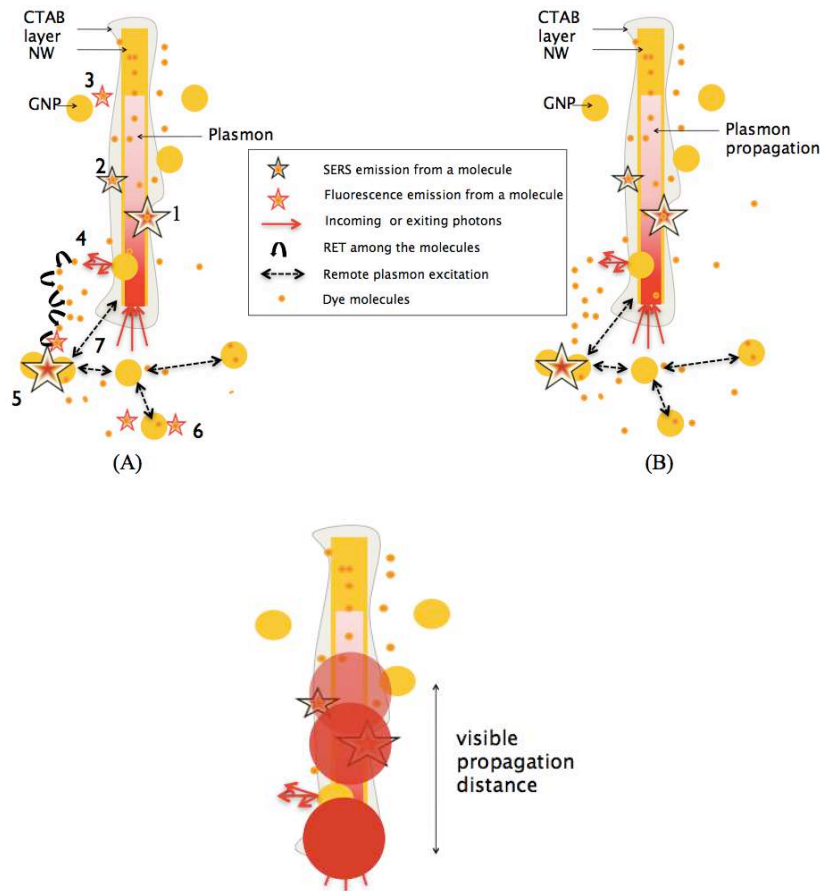


Figure 4.11: Schematic of the different processes of ATTO 740 emission. (A) The excitation wavelength excites both the surface plasmon resonance and the electronic transition of ATTO 740. The schematic shows the nanowire, with plasmon propagation in shaded red to account for intrinsic losses. The launching point is at the bottom end of the NW. The CTAB coating displayed in light grey shows an irregular thickness owing to the partial removal of CTAB. The following processes are displayed: 1 and 2: SERS emission from molecules in the near-field of the propagating plasmon. 3: fluorescence from a molecule farther from the gold surface; 4: photons outgoing from the nanowire at the junction with a GNP, and resonant energy transfer between close randomly dispersed molecules and fluorescence of a molecule enhanced near the metallic nanostructure; (5), 7,6,5: Long-distance indirect excitation of beads and subsequent fluorescence enhancement (6) or SERS at a junction between two beads (5). (B): Situation when the excitation does not excite the molecule resonance. C : A schematic of what is observed in “propagation” “imaging”.

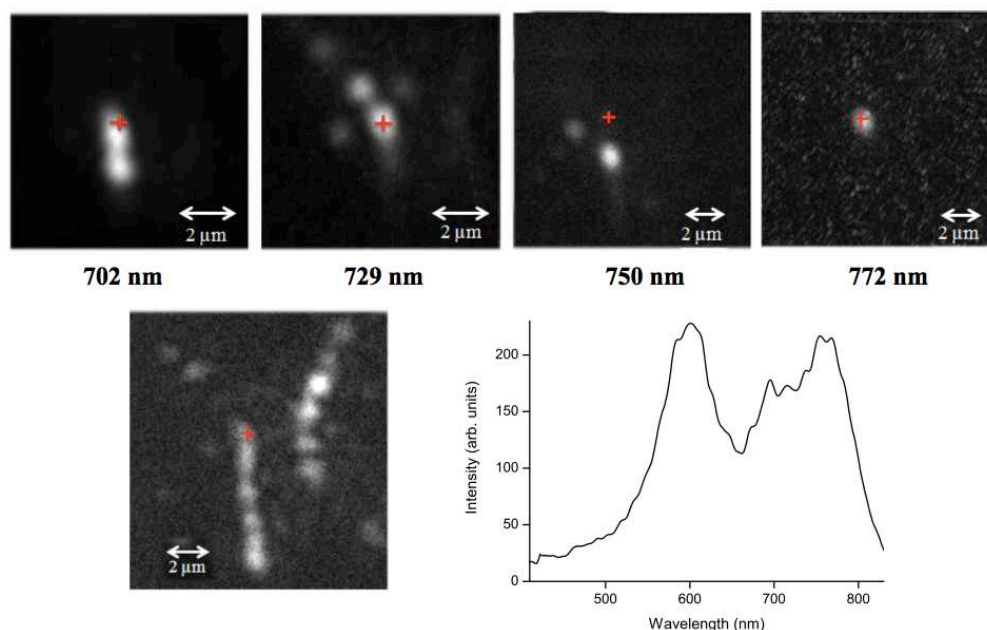


Figure 4.12: Comparison of the propagation at different wavelengths. The excitation is at the end of the nanowire denoted by the red cross and the corresponding plasmon spectrum is given.

possibility of direct illumination of the beads has been excluded. This is again a result of the energy transfer between the molecules. At 750 nm, we see remote propagation. The excitation wavelength is close to resonance with the plasmon peak at 754 nm. As a result, there is an efficient excitation of the plasmon and the distance over which the propagation is attained is  $2.5 \mu\text{m}$ . As expected, there is no visible propagation at 770 nm. A bright spot is seen at the excitation spot. It is out of resonance with the dye and in this case also with the plasmon spectrum. The best propagation in all the cases is observed at 728 nm. The excitation wavelength in this case is quite close to the plasmon resonance in many cases and it overlaps the absorption spectrum. This situation is the most favourable for plasmon propagation in the nanowire but at the same time it is also the most favourable for any other emissive process that can occur when the molecules are excited at resonance. As a result different kinds of emissions are observed at the same time on the same image. Regarding the plasmon propagation along the nanowire, the observation of propagation on the longest segments (it has been observed in similar situations on different NWs) confirms the idea that efficient launching and then propagation is attained if the excitation is close to the maximum of the plasmon resonance at the launching point. Secondly, it clearly demonstrates that the method used to visualize propagation is more efficient when the reporter is reso-

nantly excited. In such a situation, different processes are expected to contribute to the signal. One is SERRS, surface-enhanced resonant Raman scattering, which corresponds to an enhancement of the order of 10 to  $10^4$  compared to the SERS signal. The others rely on the fact that molecules randomly deposited on the sample are resonantly excited. As a result if several molecules are closely located they can form a channel of excitation without any metallic structure lying underneath. The excitation propagates either between neighbour molecules like in homo-FRET or by excitonic propagation. When the excitation reaches a metallic structure, new channels of transfer are open and metal-enhanced fluorescence (MEF) can be observed. As a result such a situation for which the excitation matches both the plasmon resonance and the electronic resonance of the reporter offers the opportunity of efficiently mapping the details of the complex metallic structure, otherwise hidden. The MEF as an imaging technique is a relatively new. The increased sensitivity in this method improves the detection limits. The technique exploits the enhanced electrical fields associated with the surface plasmons. The fluorescence of the molecules are quenched when they are in contact with the metal. However at distances between 5 to 200 nm, there is a coupling between the molecule and the enhanced local field near the metal and it results in increased absorption cross section and radiative decay rates [68].

Finally, an important result that can be derived from this experiment is the validation of the observation method. When the excitation is properly focused on a given location of the sample, even if the excitation is in resonance with the molecules, the imaging process is selective. The image is neither blurred nor blinded by the fluorescence of the molecules dispersed all over the sample. Moreover, if we change the excitation location, the image is modified, which clearly demonstrates that the origin of the lightening of the bridge is a leakage from the excited nanowire and not from a direct excitation of the molecules.

The example (figure 4.13) below, where the system is excited at the top of the left hand side nanowire at the same wavelength does not display any bridging channel to the other nanowire even if weak MEF is still observed at some close locations.

The figure 4.14 gives another example of the comparative study of the plasmon propagation with wavelength. Here the excitation point is at the end of the nanowire. The plasmon spectrum recorded at this place reveals a double peak, one at 566 nm corresponding to the bead and the other at 723 nm. The dark field images are consistent with our observation in the previous case. At 702 nm, there is no visible propagation. At 728 nm, the dark field image reveals the enhancement along the nanowire. This is the result of SERS enhancement due to plasmon propagation along the nanowire. The propagation distance is found to be  $4.2 \mu\text{m}$ . The plasmon peak is far from the excitation at 750 nm and hence there is no propagation seen. At 770 nm, as expected there is no propagation seen.

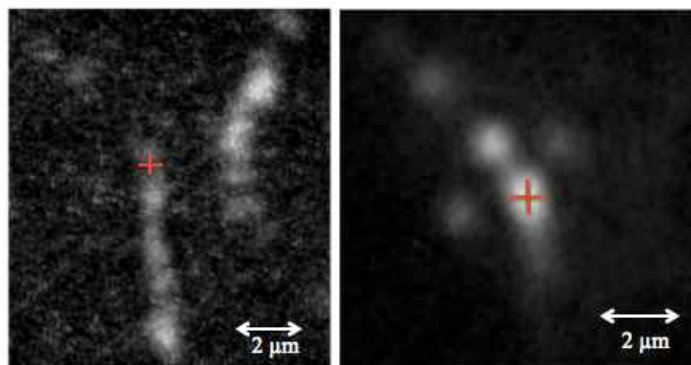


Figure 4.13: An example where the system is excited at the top of the left hand side nanowire (similar to previous case) at the same wavelength but does not display any bridging channel.

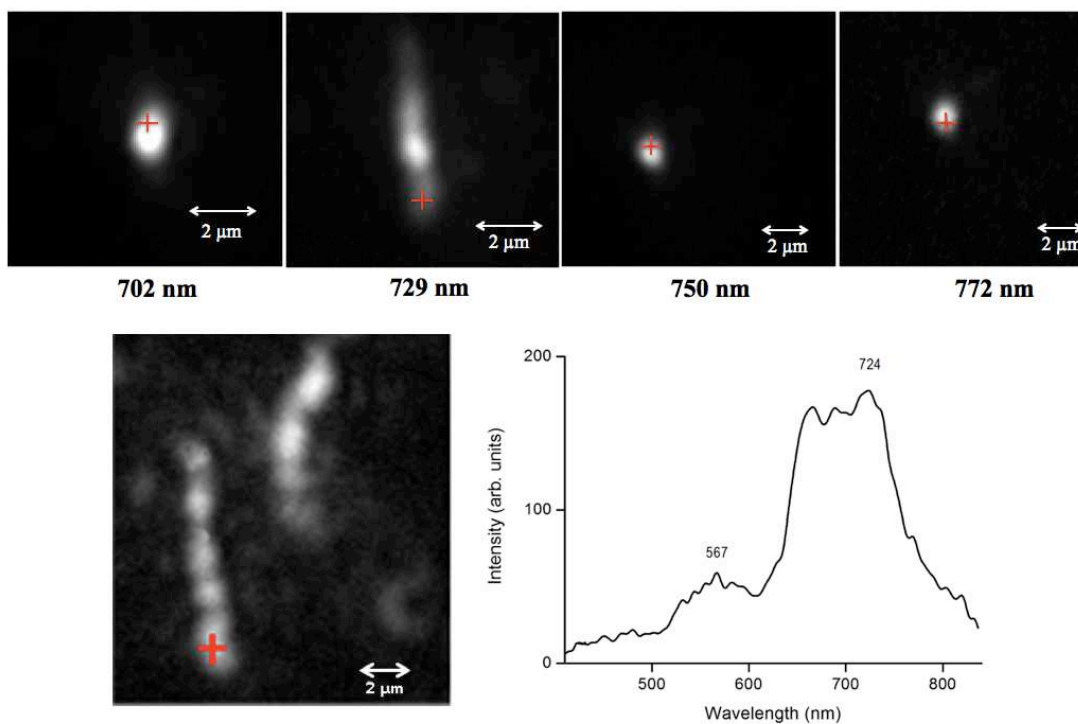


Figure 4.14: Another example for comparison of the propagation at different wavelengths. The excitation is at the end of the nanowire and is denoted by the red cross. The corresponding plasmon spectrum is given.

Thus the propagation depends on both the relation between the excitation wavelength with the plasmon of the structure and with the resonance of the molecule.

However the contribution from these two factors can be clearly identified in our case with the help of the plasmon spectrum recorded in the same position. Also, the two factors give two different outputs. The resonance with the molecule leads to metal enhanced fluorescence whereas the former leads to SERS signal as will be detailed below.

## 4.6 Propagation Lengths

When the laser is focussed in the NW end or at a nanobead on the nanowire, the SPs are launched and they propagate along the nanowire. When there is a discontinuity in the nanowire, the plasmons couple out as photons.

There are two important points to be considered.

- The photon and plasmon do not couple exactly in the same way at every point of launch, that is, the coupling strength varies at each point.
- The radiative losses depending on the crystallinity of the nanowire as explained earlier are significant compared to the dissipation along the nanowire.

Hence what we present here is only a scale of the propagation lengths in our experiments and not the accurate values which could be longer under the ideal conditions. Krenn et al have reported a plasmon propagation length of  $2.5 \mu\text{m}$  on gold nanowires of 30 nm diameter [69] by fitting the intensity profile with an exponential function and taking the propagation length as where the intensity falls by  $1/e$ . Link et al have reported a plasmon propagation distance of  $1.8 \mu\text{m}$  for chemically grown gold nanowires at 532 nm [65] by bleach - imaged plasmon propagation. The SPP propagation distance in their experiments were determined considering the MEF photobleaching as a first order decay reaction due to two components: direct laser excitation at one end of the gold nanowire modeled by a Gaussian intensity profile and indirect excitation through plasmon-exciton coupling between the MEF and the exponentially decaying SPP near-field along the gold NW. In short both the experiments calculated the distance where the intensity of the plasmon falls exponentially. We cannot use the distance measured by the law of exponential decay of intensity since the coating on the nanowire is not homogeneous and is not completely controlled. Moreover, most of the times we are in the single molecule regime. The intrinsic intensity fluctuations associated with the single molecules prevent intensity analysis.

In our experiments, we have witnessed longer propagation distances up to a maximum of  $3.8 \mu\text{m}$  including remote propagation. In some cases we have observed remote propagation, especially on silane nanowires which will be explained in the next sections. The spectra at the detection points reveal SERS signals proving true plasmon propagation.

## 4.7 SERS

The SERS signal has been probed using two different molecules ATTO 740 and Rh6G whose structure and properties have been discussed in the previous chapter. They have been used separately or both at the same time for different experiments. The results of the various experiments are presented below. Fig. 4.15 gives the typical SERS spectra of the two dyes and the Raman lines are tabulated besides the spectra. As mentioned earlier, Rh6G is a well known SERS probe and hence they have been studied extensively [47]. Instead the spectra of ATTO 740 has been recorded with our setup (grating 300 lines/mm) on a flat substrate. Usually, the dyes in the infra red region are less efficient than those at the visible region. This is the same with ATTO 740 and it was not possible to record the lines using a cuvette. Fig. 4.16 tabulates the typical Raman lines of ATTO 740 and Rh6G.

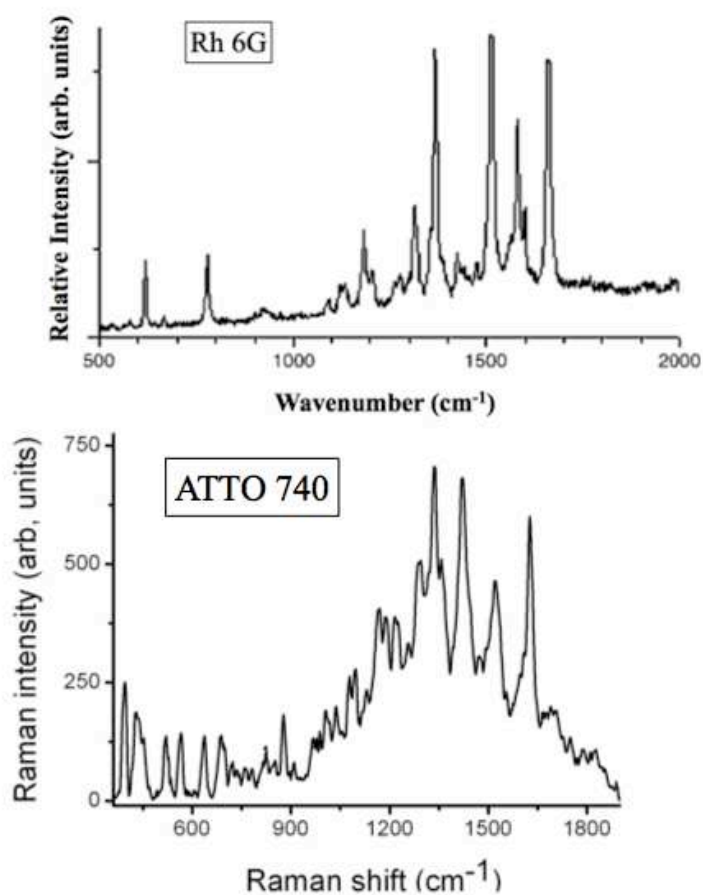


Figure 4.15: The typical SERS spectra of Rh6G (from [47]) and ATTO 740.

Rh6G*			ATTO 740®	
396	(w)		395	w
			428	vw
			437	vw
			520	vw
			565	vw
614	(m)	C-C ip bend	637	w
			688	w
774	(m)	C-H oop bend	877	w to m
			1077	vw
931	(w)		1095	vw
			1168	] - triplet, w
1124	(w)	C-H ip bend	1187	
			1216	
			1290	w to m
			1337	st
			1357	m
			1420+1442	vst
			1472	w, 5h
			1518	st, broad
			1626	vst
* from Vosgröne and Meixner				

Figure 4.16: The typical Raman lines of Rh6G and ATTO 740.

## 4.8 Dependence of SERS on wavelength

It is well known that there are multiple mechanisms that contribute to the SERS enhancement as seen in the previous chapter. In fact it is evident also from the previous section on the plasmon propagation that there are MEF and SERS acting at the same time. To probe into the details and understand the contribution of these factors, it is necessary to study the system at different wavelengths. Such a study will help greatly to improve the understanding of SERS. The wavelength dependence of SERS has not been investigated extensively because of the obvious difficulties presented by such a study. The number of data points are limited by the tunability of the excitation laser and the detection system. These are the major limitations that prevent the generalization of the effect of wavelength on SERS as the measurements suffer from low data points. As result many experiments have

been done on substrates that are well characterized, mostly lithographic samples to eliminate other factors of influence on the SERS.

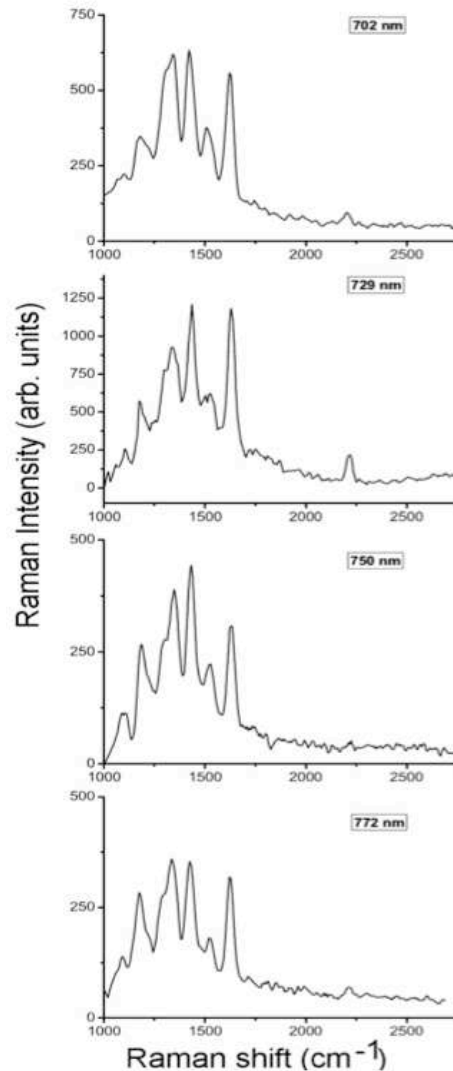


Figure 4.17: SERS spectra of the ATTO at different excitation wavelengths with the same excitation power and with an acquisition time of 10 s.

We have investigated the SERS dependence on the wavelength. Four different wavelengths have been investigated similar to the ones used for propagation measurements. The spectra are in good agreement with the reference spectrum displayed in figure 4.15. Care has been taken to record the spectra at different wavelengths at the same point of excitation (at one end of the left-hand side nanowire, see Fig. 4.17). we have successively recorded the spectra at different wavelengths,

under a careful control of the laser intensity, without moving the position of the sample and only inserting the appropriate filters in the detection path. In fact, in order to have the most reliable comparison as possible, the spectra recorded at the first three lowest wavelengths have been acquired with the same filters (2 long-pass filters at 760nm, OD=4.5 x 2 ). Then the spectra at 750 nm has been recorded again with filters at 785 nm needed for recording the signal with the last wavelength (772 nm). The filter transmission has been calibrated to account for the correction factor, as is systematically done for the whole spectrometer system (grating +camera). Several series of spectra have been acquired for each wavelength in order to take into account possible fluctuations. The excitation power on the sample was  $6.4 \text{ kW/cm}^2$  ( $52 \mu\text{W}$ /excitation spot) with an acquisition time of 10s.

Due to the low-resolution of the grating (chosen on purpose to acquire the whole spectrum at a time) the wings of the Raman lines partly overlap and the comparison of the relative intensities of the strong lines given a spectrum can only be achieved by a fitting procedure. This procedure assumes that each line can be satisfyingly fitted by a Lorentzian profile. It allows one to obtain the contribution of each line to the Raman intensity. Such a fit is displayed in figure 4.18, as an example.

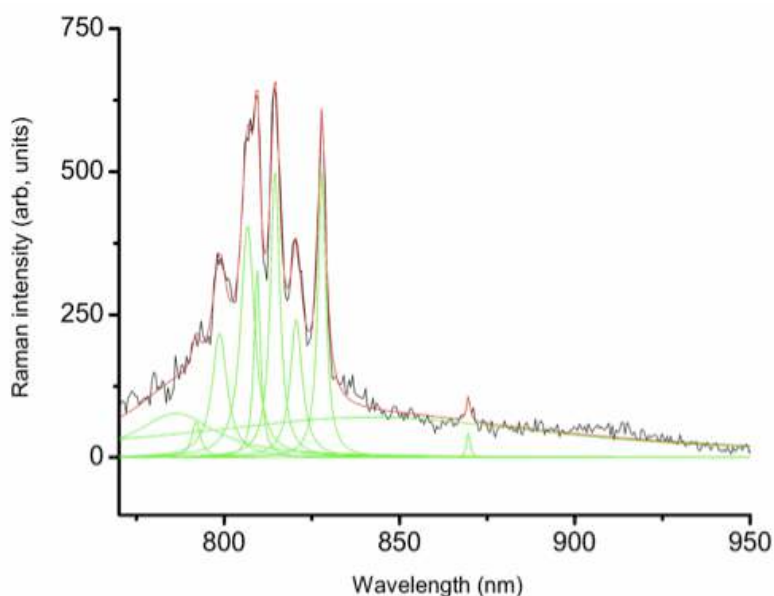


Figure 4.18: An example of fitting procedure with Lorentzian profiles.

We have used such a fitting procedure for many of the recorded spectra at different wavelengths to determine a possible selectivity of the enhancement of the different

modes with the wavelength. We did not observe selectivity in the enhancement, even close to the resonance of ATTO 740.

As an example, a series of spectra acquired on a given location of the nanowire every 10 s with an excitation power of  $60 \mu\text{W}/\text{cm}^2$  is displayed in figure 4.19. The general shape of the SERS signal is stable during the whole series, which is not contradictory to the observations of global intensity fluctuations.

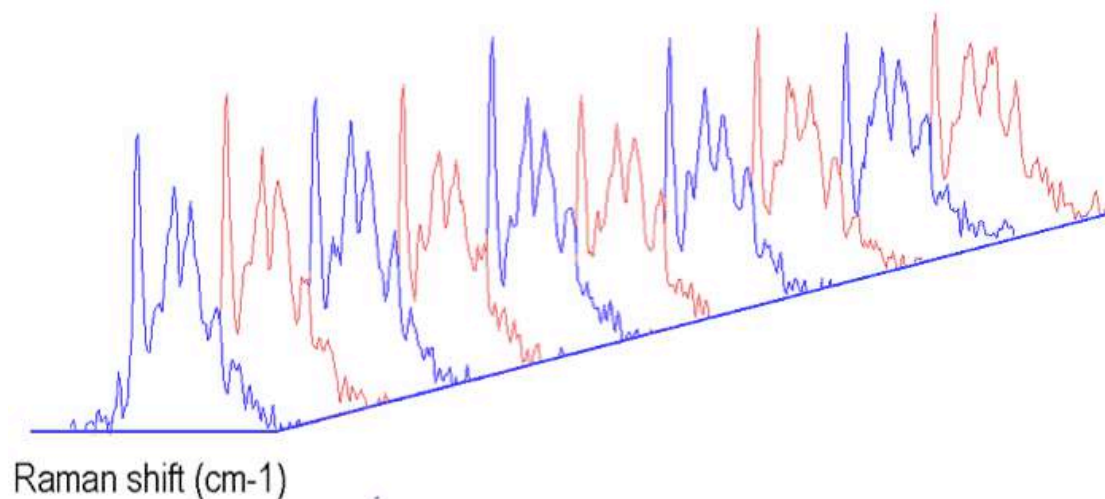


Figure 4.19: Evolution of the spectral shape in a series of 10 consecutive acquisitions of a SERS signal (see text).

We can thus conclude that the wavelength has no strong effect on the Raman modes that are active (unfortunately it is not possible to make an assignment of those modes because the molecule is a trademark one) and that the whole Raman intensity follows the same trend as in the analysis of the propagation images: Raman scattering is more efficient for wavelengths close to the surface plasmon resonance peak and especially if there is a resonance contribution from the electronic excitation of the molecule.

Of interest is the systematic observation of the four strong lines listed in the Table 1, even if the line at  $1518 \text{ cm}^{-1}$  is often weaker than in the reference spectrum. These strong lines all have counterpart in the Rh6G spectrum, slightly shifted. Such a shift also observed in the series of xanthene dyes studies by Meixner [47] is a result of the different groups attached to the aromatic cycles and depends on their position (meta, para or ortho). It is thus reasonable to consider that the two highest frequency, strong lines still correspond to an elongation  $\text{C}=\text{C}$  vibration of an aromatic cycle, as in rhodamine 6G. In fact many fluorescent molecules in the NIR domain possess such aromatic cycles. The clear observation of such vibrations in any spectrum that has been acquired on isolated nanowires is a sign that the

molecule is generally not much distorted in the locations where it sits since these modes correspond to a vibration or elongation in the plane of the cycle.

The reproducibility of the spectral shape and the very few relative spectral shifts observed on the huge number of spectra acquired at different locations and on different nanowires is an indication that the SERS (or SERRS) active molecules do not experience a strong so called chemical effect. We have additionally observed that in many cases the signal abruptly drops to zero from one acquisition to the next one and then reappear after a delay. This is one of the well-known properties of single molecule SERS (SM-SERS) [35]. So the SM-SERS regime is attained, which will be clearly demonstrated in the following sections. The two combined observations, SM-SERS and spectral shape stability strongly suggest that the Raman signal is only enhanced by the electromagnetic factor and that the molecule is trapped in a defect of the CTAB coating, without the possibility to reach the gold surface, still protected by a layer of CTAB. This property of the SERS spectra acquired on isolated nanowires will be further discussed in the following chapter on the nanowire arrays, which demonstrate a different behaviour. Finally, it was not possible to have, with ATTO 740 alone, a sufficient enhancement to reduce the excitation to powers down to a  $\mu\text{W}/\text{cm}^2$  and to attain very short acquisition times. Beyond the absence of chemical enhancement, it indicates that either the electromagnetic enhancement does not reach the highest factors of  $10^9$  to  $10^{11}$  as often claimed to be needed to observe SM-SERS [45] or that ATTO 740 is not a very efficient scatterer. This observation confirms the recent trend demonstrating that the SM regime can be reached with a more moderate electromagnetic enhancement ( $10^6$  to  $10^7$ ) as explained for example in a recent paper of Ru et al [24].

When analyzing the plasmon propagation, we have discussed the two competitive processes that take place, the enhanced fluorescence and SERS. The figure. 4.20 presents an evidence to the case of SERS by plasmon propagation. The system is excited at 728 nm and the dark field image of propagation is presented in the figure. The SERS spectra are recorded at three positions, one at the same point of excitation, another at a distance of 2.9  $\mu\text{m}$  and the final one at a distance of 3.8  $\mu\text{m}$ . It is evident from the figure that the intensity of the SERS signal drops progressively as we move away from the excitation. This is in accordance with the fact that the plasmon loses its strength as it propagates along the nanowire and hence at the farthest point from the excitation the SERS signal is the weakest. It is also seen that the all the lines are reproduced identically in all the three cases.

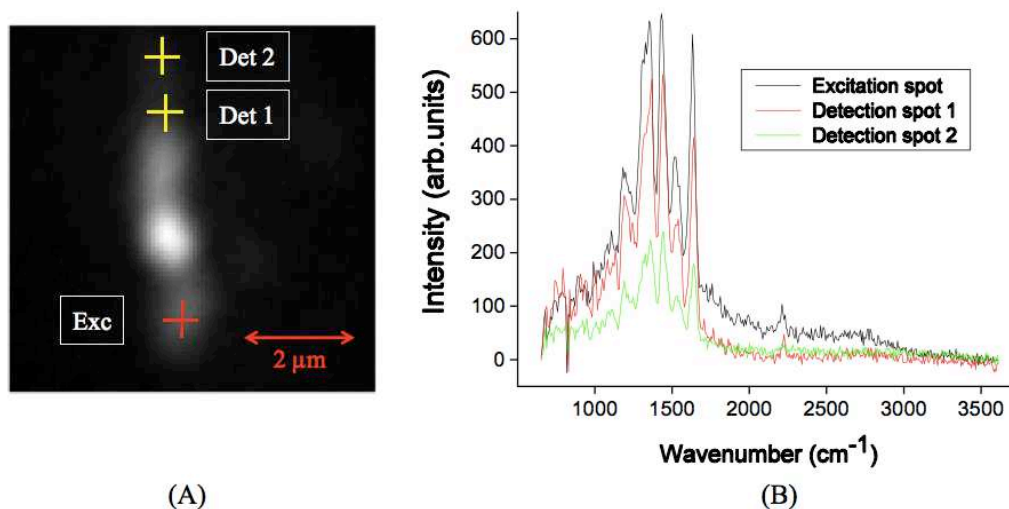


Figure 4.20: (A) The dark field image of propagation. The red cross marks the excitation spot and the detection spots are marked by the yellow crosses. (B) The corresponding SERS spectra to the three positions marked by crosses. The drop in intensity with the distance is evident.

## 4.9 Blinking

The figure. 4.21 shows the propagation measurements and the corresponding spectra on the CTAB coated nanowires. On the left is the bright field image of the nanowire and on the right are the corresponding propagation images. The length of the nanowire is 6 microns. The excitation is in the middle of the nanowire with a wavelength of 750 nm and a power of  $80 \mu\text{W}/\text{excitation spot}$ . The images have been made with the integration time of 1 second and the SERS spectra recorded for 20 seconds. It is seen clearly that the propagation length and the intensity fluctuates with time.

The bright field image displays a defect at the middle of nanowire, probably a bead, which is confirmed by the corresponding dark field image that clearly shows a bright spot at the same location. This location is selected to launch the plasmon into the nanowire. The excitation wavelength is 750 nm centered on the plasmon resonance (not shown). On closer examination of the evolution of the brightness of the launching spot (the excitation light is removed by severe filtering), it is seen that the intensity fluctuates from one recording to the other and at the same time not following a regular decrease as it should be for photobleaching.

This kind of blinking in the nanowires shows that the sensitivity of our substrate is quite high and we are in the single molecular regime. The molecule also probes the localised surface plasmons. The LSP fields of plasmonic structures are usually

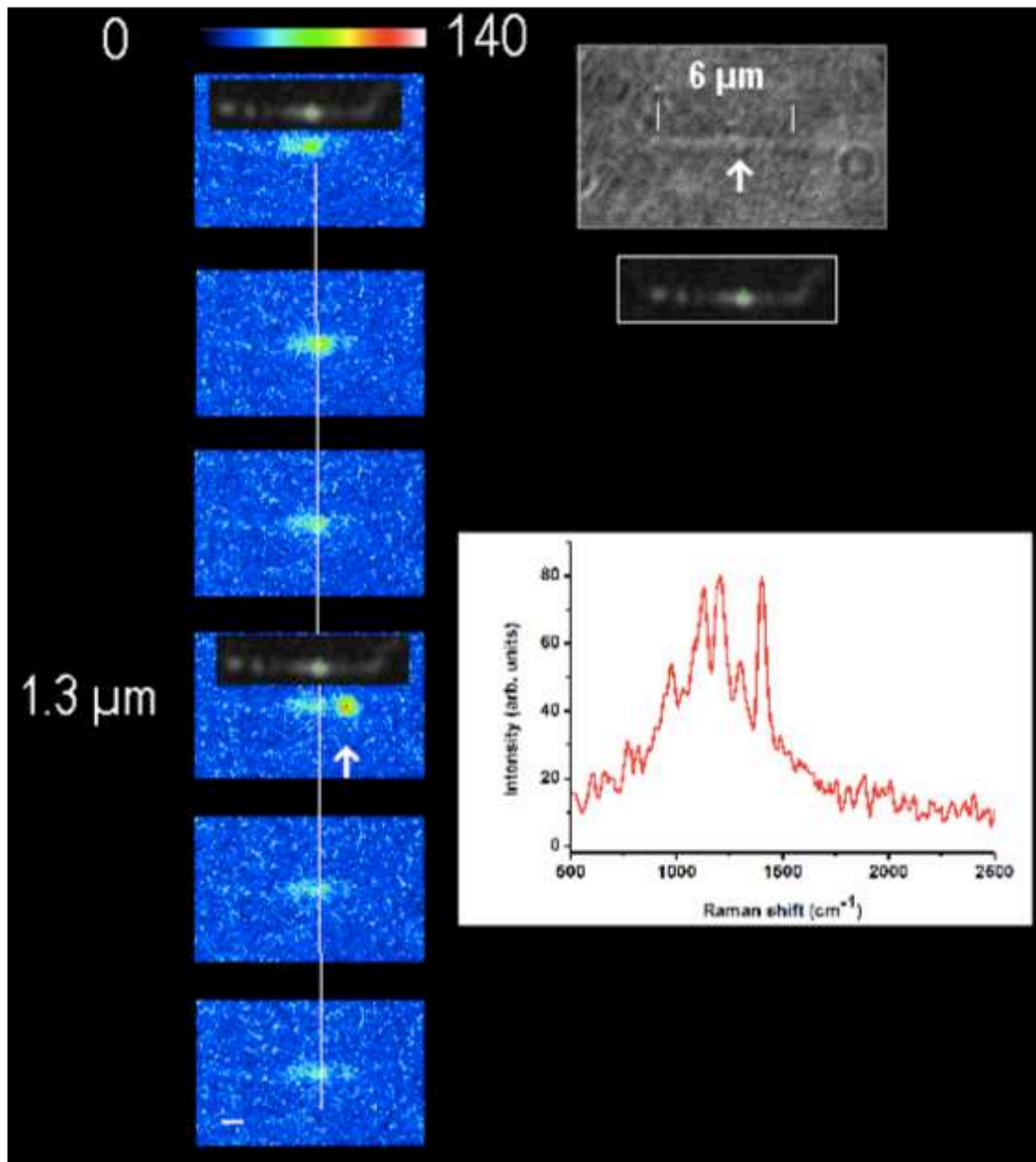


Figure 4.21: White field image of the nanowire (top right) and the corresponding propagation images (left). The SERS spectra (left) recorded at the point of blinking ( $1.3 \mu\text{m}$ ) from the excitation.

probed in the far field by registering their light spectra using dark field microspectroscopy [70]. This method is sensitive at the single particle level and also allows the spectral shape to be registered in detail. The blinking time scale is one second

here in our case. Adsorbate diffusion are also one of the major causes of blinking. This phenomenon has been observed in the silane coated nanowires and we will discuss a few more examples of such kind in the following section.

Three different locations of emission can be identified. The launching site, a less efficient emission site immediately to its left and a remote site, which is often not very active except on the fourth recording where a burst of light is clearly visible. This series of images clearly demonstrate that the single molecule regime is reached, as reported by the intensity fluctuations observed at each emissive site. Secondly, it demonstrates that the plasmon can propagate in both directions from this central launching spot. We have shown a sequence of six images for clarity, but the SERS signatures could be recorded for a longer time without bleaching. It gave the opportunity to analyse the spectral profile of the emission at each site. The spectrum displayed on the figure 4.21 has been acquired in 20 s at the bright spot of image 4 (from the top). It is the SERS spectrum of ATTO 740, with nearly no background and all the expected lines clearly visible. This remote SERS emission is an unambiguous proof of plasmon propagation. The SERS spectrum recorded at the blinking spot also gives the proof that the fluctuations arise from the surface enhanced Raman scattering and not from any other process like Rayleigh scattering. The quite low power used for launching proves that the coupling at a defect (an artificial defect in this case) is quite efficient and that at 1.3  $\mu\text{m}$  away the strength of the plasmon field is still high enough to efficiently excite a SERS signal. Very few measurements of propagation lengths have been performed on gold nanowires, leading to short propagation length, and the present results are the first obtained with SERS as the reporter. We can conclude that the overall apparent length of propagation in this example is of the order of 2  $\mu\text{m}$ , which is satisfactory compared to the few reported values discussed earlier. Owing to the observation of a remote excitation, we know that the propagation length could be larger, but we cannot access its measurement.

## 4.10 Silane coated nanowires

Here I present the results of the SERS measurements on the commercial isolated gold nanowires coated with silane. The silane nanowires are supposed to be better than the CTAB coated nanowires for deposition on the glass substrates due to the properties of silane. However, we observed that in the drop cast method, the density of the deposited nanowires did not vary hugely in both cases.

The samples were prepared by mixing the nanowires, 50 nm nanobeads and the dye (ATTO 740) in the ratio 2:2:1. The dark field images revealed well defined nanowires, better than the CTAB coated nanowires.

Unfortunately, the silane nanowires do not show any propagation or SERS en-

hancement at when excited at low power ( $80 \mu\text{W}$ ). So the excitation was increased to higher powers up to  $1.3 \text{ mW}$ . At higher excitation powers, both propagation, MEF and SERS were witnessed. However, the probability to have SERS signal was quite low compared to that of the CTAB nanowires. The reason could be that the CTAB has been partly removed with our processing and it is porous by nature and thus allows the dye to be closer to the nanowire which is not possible with the silane coating.

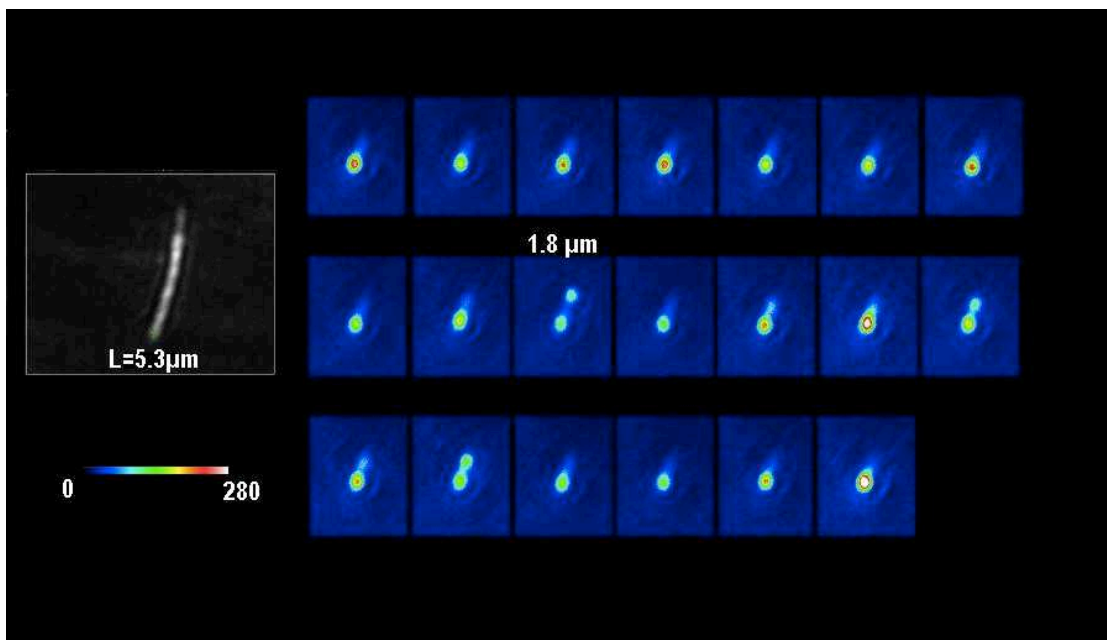


Figure 4.22: Dark field image of the silane coated nanowire and the propagation images taken over 20 consecutive seconds.

The figure 4.22 shows the propagation measurements on the silane coated nanowires. On the left is the dark field image of the nanowire and on the right are the corresponding propagation images. The length of the nanowire is about 5 microns. The excitation is in the middle of the nanowire with a wavelength of  $750 \text{ nm}$  and a power of  $1.3 \text{ mW}$ . It is seen clearly that the propagation length and the intensity fluctuates with time. The images have been made with the integration time of 1 second and the SERS spectra recorded for 20 seconds.

We recover the same characteristics as that of CTAB coated nanowires but the launching power needs to be higher.

## 4.11 Background

The figure 4.23 shows another example of the propagation measurements on the silane coated nanowires. The spectra corresponding to the measurements show two contributions; a background due to fluorescence which dominates and the Raman spectrum which is embedded on top of it. On the lower left of the image, the points of high intensity in the propagation image have been superimposed on the dark field image. We can clearly see that they coincide with the bright spots of the dark field image, corresponding to one end of the nanowire and to a kink or a bead located on the other side. As said earlier, the SERS effect with these nanowires were not as efficient as those with CTAB and hence the lines are not strong. Intense bursts of signal are witnessed from time to time as explained in the previous section.

## 4.12 Single molecule regime evidenced by a two analyte analysis of propagation

In order to demonstrate more clearly the plasmon propagation along the nanowire, we decided to directly coat the beads separately with the reporters. In this case the sample is slightly different from the ones discussed previously. It includes nanowires, beads and molecular reporters, but there are no molecules randomly dispersed on the system as in the previous situation. In order to realize the sample, the nanobeads were incubated with just the molecules separately, after which it was filtered using a sephadex column to obtain a solution of marked beads without any free molecules. Different trials were made in order to get efficiently tagged beads and evanescent concentration of molecules in the solution. The use of ATTO 740 as the tag molecule did not prove to be very efficient. This will be further discussed in the next chapter on nanowire arrays. So we turned to Rh6G which was already intended to be used as a co-analyte. The nanobeads were incubated overnight with a  $10^{-6}$  M Rh6G solution and then filtered. The freshly prepared nanobeads (low concentration) were mixed with a solution of CTAB coated nanowires just before deposition to prevent as much as possible the desorption of the molecules from the beads.

The choice of Rh6G as the other analyte was motivated by two reasons. Firstly Rh6G has been extensively studied as an efficient SER scatterer and its spectrum is known (see table 1). Secondly Rh6G cannot be resonantly excited in our range of wavelengths. As a result, it could be a way to discriminate plasmonic enhancement from resonant effects that could be sometimes difficult to disentangle in the case of ATTO 740.

We have indeed observed SERS from Rh6G molecules on such system, but only

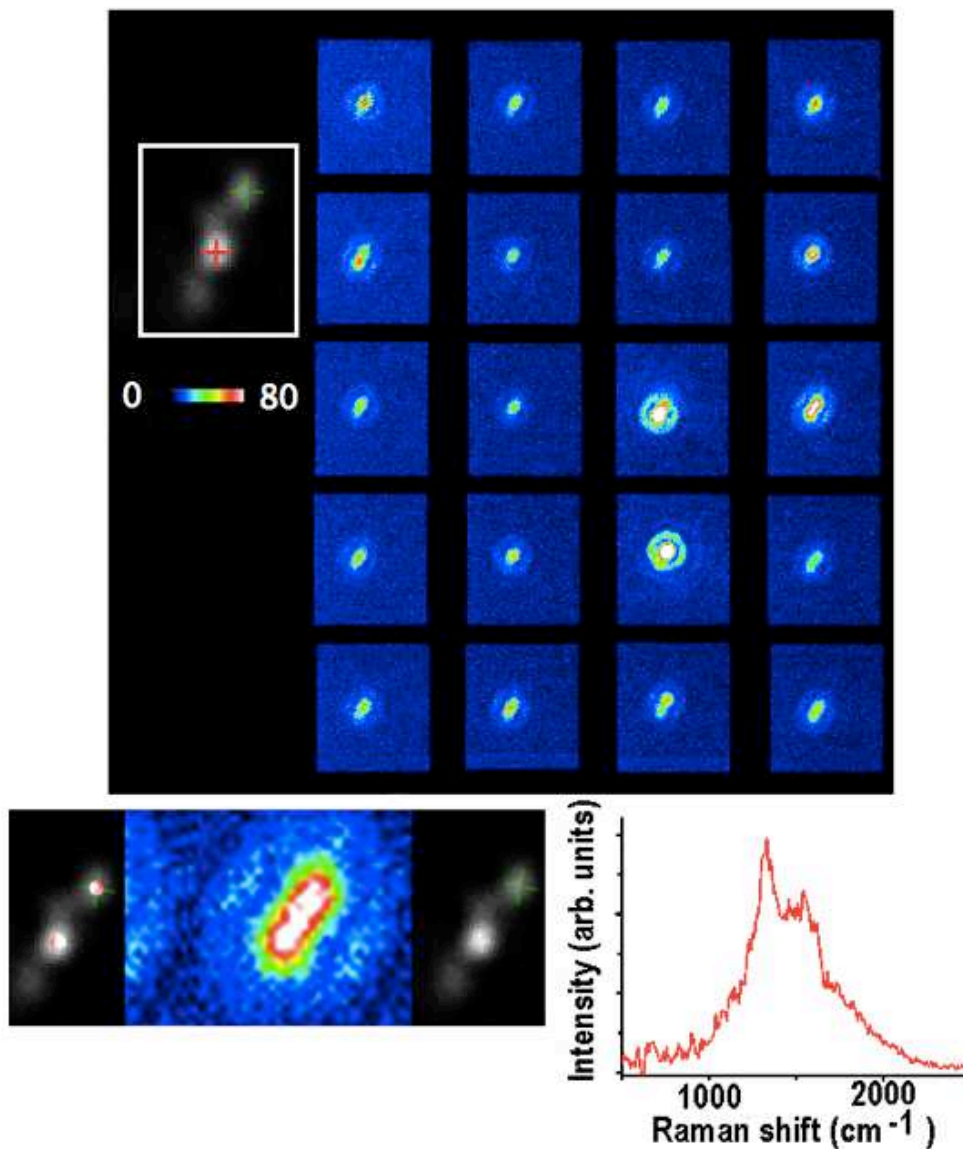


Figure 4.23: Dark field image of silane coated nanowire and the corresponding propagation images (top). The SERS spectra (lower right) has the SERS signal superimposed with the fluorescence background. On the left, the dark field image is superimposed with the contour of maximum propagation witnessed. The excitation wavelength is 702 nm and the excitation power is 1.3 mW.

at a very few locations on a given nanowire (1 or 0) and on a limited number of nanowires. This is in favour of the reports about observation of the SERS signal in the gap between the nanowire surface and a tagged nanobead. The other

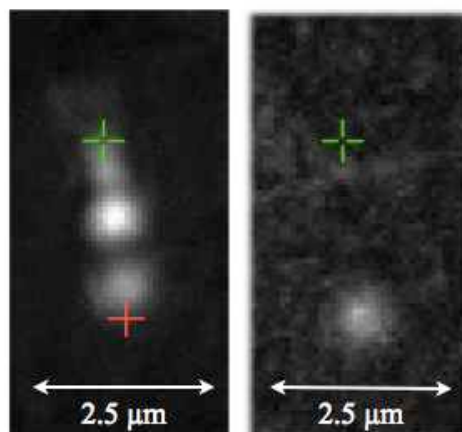


Figure 4.24: Observation of propagation in a short CTAB-coated nanowire in the presence of Rh6G tagged nanobeads. On the left, dark field imaging of the nanowire (length  $2.5 \mu\text{m}$ ) on the right, propagation image, with a bright spot at the end of the nanowire. Green cross gives the excitation spot and the red cross detection spot.

locations on the nanowire did not show SERS signatures. We have also observed propagation in few cases where a bead favored the launching and another bead was located further on the nanowire. In that case propagation is witnessed by the presence of two bright spots and the nanowire segment in between is dark. An example is depicted on the figure 4.24. The excitation corresponds to the green cross and emission is observed at the distal end of the short nanowire on the propagation image. The propagation distance in this case is the length of the short nanowire, of the order of  $2.5 \mu\text{m}$ .

The spectrum of the light emitted at the bright spots have been analyzed. It systematically corresponds to SERS signature of rhodamine 6G, when compared with the reference SERS spectrum of Rh6G (Fig. 4.15). Two examples of such spectra are displayed in figure 4.25.

The spectra show a limited number of thin lines compared to the reference spectrum (fig. 4.15). These lines correspond to the range of frequencies from  $900 \text{ cm}^{-1}$  to  $1575 \text{ cm}^{-1}$  and the last line is often very weak, if it is present. It can be explained by the fact that the excitation wavelength (typically around  $710 \text{ nm}$  is these experiments) is quite far in the red compared to the resonance of Rh6G. Consequently, the highest frequency modes are not efficiently excited and that the modes in low frequency range, observed at resonance, are not detected either. The recorded spectra are in line with what is expected for near IR excitation of Rh6G SERS [47]. An interesting point is related to the intensity of the lines. Rh6G SERS can be observed with a rather weak excitation energy compared to that of

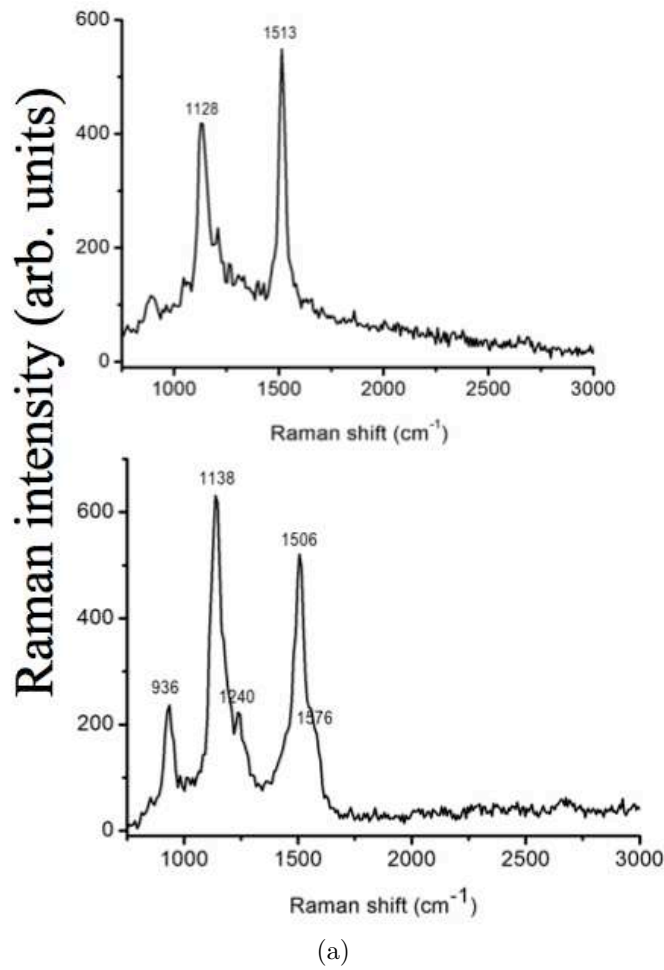


Figure 4.25: SERS signature at the bright spots in the figure 4.24. The lines correspond to Rh6G and agree with the reference spectrum (fig. 4.15).

ATTO 740. On the top spectrum of figure 4.25, the raw spectrum is obtained with an excitation energy of  $4 \mu\text{W}$ /excitation spot and the acquisition time is 10 s. The spectrum displays a high signal to noise ratio, with nearly no background. It suggests that the electromagnetic field in the gap between the bead and the nanowire is quite high and that the location of the molecule directly on the surface of the bead to efficiently enhance its response.

## 4.13 Single molecule regime

In order to get more insight in the distribution of the field in such gaps, we performed an experiment with the two analytes, Rh6G and ATTO 740, in the system.

The figure 4.26 presents an irrefutable evidence to the single molecule regime discussed earlier. The sample is made as in the above experiment but a tiny drop of ATTO 740 ( $10^6\text{M}$ ) is thereafter deposited onto the sample, studied after drying. The three spectra displayed on figure 4.26 have been recorded on a location where a bright emission was observed. They have been extracted from a series of spectra acquired successively at this location without any change in the excitation wavelength or intensity. They are representative of all the different types of spectra observed during a long acquisition sequence (100 spectra, each made with an acquisition time of 2 s at an excitation wavelength of 702 nm and a power of  $40 \mu\text{W}/\text{excitation spot}$ ). During the acquisition process, the spectral profile is, in general, stable for several successive acquisitions and undergoes a sudden change in the spectral profile, which is stable for further acquisitions.

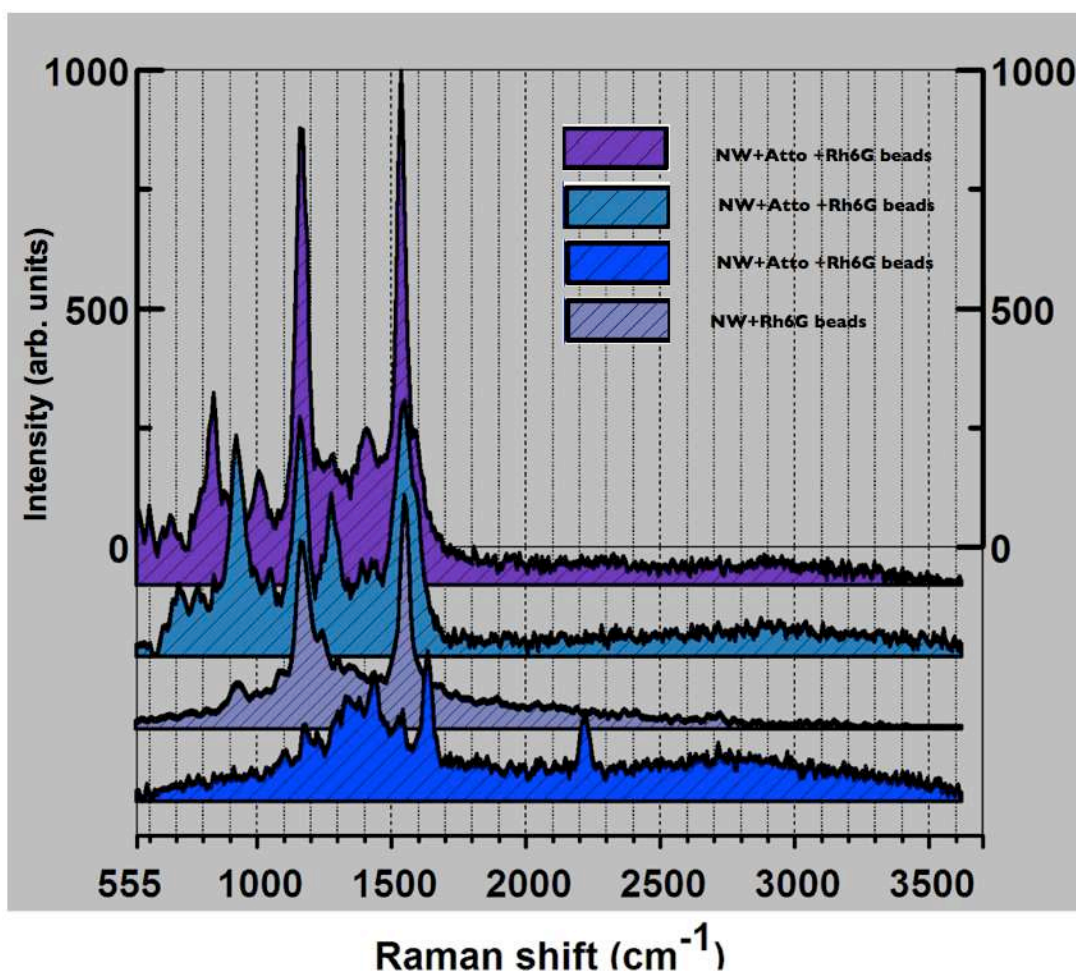


Figure 4.26: Evidence of single molecule regime. The different systems investigated show that the presence of only one molecule is witnessed at any given point of time.

A similar experiment has been reported by Ru et al [24] who simultaneously used two different analyte molecules to unambiguously prove the single (or few) molecule nature of the signals.

It is not likely that the different shapes observed for the profiles only result from the spectral fluctuations of a single molecule. The fourth spectrum (the second one from bottom 2) is a spectrum acquired on the previous sample with only Rh6G as a reporter. It has been added for a comparison purpose. It has been inserted in the series of the three investigated spectra for clarity. The spectrum 1 is a typical spectrum of ATTO 740, specifically characterized by the presence of the high frequency mode at 1628 cm<sup>-1</sup> and by the combination line at around 2200 cm<sup>-1</sup> (combination with a non displayed low-frequency mode and the mode at 1628 cm<sup>-1</sup>). These lines are not observed on the two other spectra. The latter have been fitted and the lines correspond to those of Rh6G (Fig. 4.15), except for the lowest frequency line of spectrum 4. We thus either observe SERS from Rh6G or SERS from ATTO 740. At no point, do we have the signature lines of both the dyes present together. It obviously demonstrates that only a single molecule can sit in the hot-spot at a time. We observe that the signal can jump from ATTO 740 to Rh6G and vice and versa several times within 200 s. This experiment unambiguously demonstrates that we have reached the single molecule regime and that the hot-spot is very tiny as expected if it corresponds to the gap between the bead and the nanowire.

This situation can be explained by imagining a strong SERS active site or a hot spot between the bead and the nanowire. These sites are highly compact and have high enhancement. When a molecule is present in this position, ie the '*eye of the storm*' a high intensity signal is observed. The huge enhancement capacity of these active site is evident by the high intensity signal of the Rh6G molecule which is quite far from resonance of the nanowire. With the passage of time, the molecule moves away from the hot spot due to a lot of factors like thermal diffusion or vibration. It is also important to remember that the spot is highly concentrated and quite small. The ATTO 740 molecule replaces the rhodamine and we see the signature of ATTO 740 molecule.

This replacement behaviour is consistent with the changing signals in the SERS spectra recorded over a period of time. The dynamic behaviour of the molecule is a result of the two reporter molecules competing for the single hot spot. Spectral diffusion, spectral wandering and abrupt spectral jumps are often encountered in single-molecule spectroscopy and are among the best investigated feature in single-molecule spectroscopy. As these spectroscopic phenomena disappear in the ensemble average they can serve as a spectroscopic proof for the single-molecule limit.

## 4.14 Synopsis

The novelty in our technique is the fact that we are able to correlate the structural and optical properties of the gold nanowires. Though such an experiment has been reported recently by Van Duyne et al [71], it has been for nanoparticle arrays. Moreover, we relate the plasmon structure to the SERS spectra and the propagation. Thereby paving way for a better understanding of the contributing factors.

For example, the figure 4.27 summarises our work on isolated nanowires in a compact way.

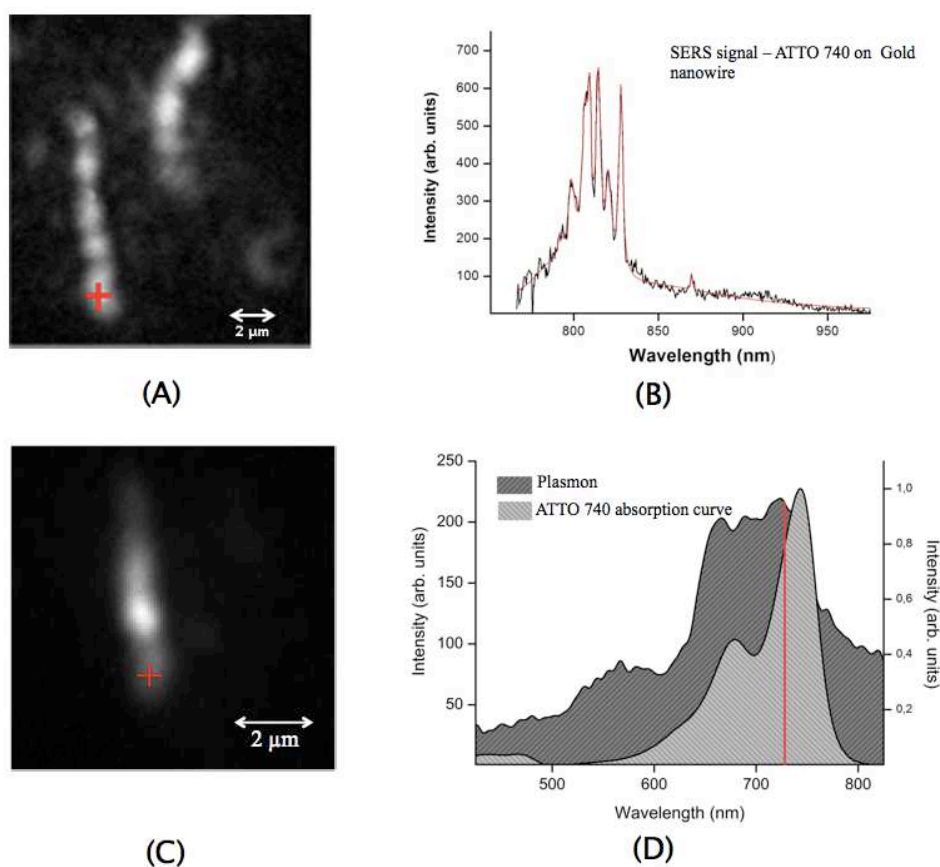


Figure 4.27: The summary of the experiment on isolated nanowires. (A) Dark field image of the system. Red cross is the excitation point. (B) SERS spectra of the ATTO molecule on the system fitted using the lorentzian function. (C) Dark field image of the propagation and (D) Plasmon spectra at the position of excitation.

The structure is ascertained using the dark field imaging. The propagation is studied by exciting the plasmon at the point denoted by the red cross in the

figure. The excitation wavelength is 728 nm. The LSPR spectra at the point of excitation is recorded and finally the SERS spectra is registered at the same point. This technique of correlating the structure and function is an effective way to understand the chemical and physical properties of any system. Especially in metal nanoparticles, the optical properties are hugely defined by their structure, as evidenced in our studies. For example, the presence of beads changes the structure of the plasmon spectra. Hence such a study becomes an invaluable tool to understand the various phenomena taking place in a hot spot. In the example presented the plasmon propagation along the nanowire is favoured by two factors. The plasmon peak in the proximity of the excitation wavelength and the complete overlapping of the absorption spectra of ATTO and the plasmon spectra. Two competitive processes take place at the same time, one involving the resonance of the molecule and the other one out of resonance. This results in good propagation that is witnessed by the signal all along the path of propagation. The SERS, as we have already seen, follows the same trend as the propagation. Hence we have good SERS signal which is in concurrence with the typical lines of ATTO (fig 4.16). Different experiments have been done on the nanowires. Different dyes have been used separately or at the same time to investigate the effect of the plasmon of the system and the spectra of the molecule. Various tests were done by changing the combination of the dyes and the beads. It was seen that the CTAB nanowires though initially were difficult to deposit on the substrate due to the excess CTAB in the solution, later proved to be very efficient both for propagation and SERS when compared to silane coated nanowires.



---

*To do successful research, you don't need to know everything, you just need to know of one thing that isn't known.*

Arthur Schawlow

# 5

## SERS - Nanowire arrays

### 5.1 Introduction

In this chapter, I present the results of our SERS measurements on the nanowire arrays. In order to understand better the properties of these samples, we have used the same SERS reporters as on the isolated nanowires. There are many differences between the nanowire arrays and the isolated nanowires and the most important is the possibility of coupling between the successive nanowires. This coupling should induce a marked difference between the plasmon resonances in two orthogonal polarizations, one along the nanowire, further named H, and the other across the nanowires, further named V. As a consequence, a dependence of the SERS signature with the excitation polarization is expected, in line with macroscopic measurements of dichroism.

This kind of sample is of great interest as a SERS substrate because it is synthesized in just two steps as discussed in the chapter 2. One step to shape the glass substrate and a second step during which gold is sputtered at a controlled angle in order to produce the nanowire array. The deposition dosage offers the opportunity to modify the aspect ratio and subsequently the plasmon resonance of the nanowires. As a consequence of the synthesis procedure, the crystallinity of the nanowires is different from that of the previously studied isolated nanowires, which are chemically-grown. Particles of different sizes and shapes decorate the nanowire arrays which offer an additional possibility of SERS enhancement, especially in the gaps between the particles or at the junction between two nanowires.

Before discussing the experimental results, I briefly present the models that I have used to perform some simulations. The idea was to understand the behaviour of such systems to explain our experimental results.

## 5.2 Dipolar coupling model

We have used the simple principle of interacting point dipoles to calculate the plasmon shifts with various factors. A brief outline of the dipolar coupling model is given below. The electric dipole moment of the single particle in an electric field  $E$  is given as

$$\mu = \alpha \epsilon m E \quad (5.1)$$

where  $\alpha$  is the Clausius-Mossotti dipole polarizability for an isolated metal nanoparticle in the quasistatic approximation, which is proportional to the particle volume  $V$  as:

$$\alpha = \epsilon_0 V (1 + \kappa) \left( \frac{\epsilon - \epsilon_m}{\epsilon + \kappa \epsilon_m} \right) \quad (5.2)$$

where  $\epsilon = \epsilon_r + i\epsilon_i$  is the wavelength dependent dielectric function of bulk gold,  $\epsilon_m$  is the medium dielectric constant,  $\epsilon_0$  is the vacuum permittivity and  $\gamma$  is a factor which depends on the nanoparticle shape.  $V$  is the particle volume,  $\kappa$  is a factor which depends on the particle shape, being equal to 2 for a sphere. In the presence of a neighboring particle, the electric field felt by each particle is the sum of the incident light field  $E$  and the near-field of the electric dipole on the neighboring particle, which decays as the cube of the distance  $d$  from the particle:

$$E' = E + \frac{K \mu'}{4\pi \epsilon_m \epsilon_0 d^3} \quad (5.3)$$

where  $K$  is an orientation factor, which depends on the alignment of the two single-particle dipoles. The net polarizability  $\alpha'$  of the two-particle system is given as

$$\alpha' = \frac{\alpha}{\left( 1 - \frac{K \alpha}{4\pi \epsilon_m \epsilon_0 d^3} \right)} \quad (5.4)$$

## 5.3 Electrostatic approximation

The electrostatic approximation is used on very small particles to calculate the extinction efficiency. The extinction efficiency of the ellipsoid  $Q_{ext}$  is the sum of the absorption and scattering efficiencies defined as  $Q_{abs} = C_{abs}/G$  where  $C_{abs} = k \text{Im}(\alpha)$  is the absorption cross-section of the ellipsoid and  $G$  is the particle cross-sectional area projected onto a plane perpendicular to the incident beam (For a

sphere of radius  $a$ ,  $G = \pi a^2$ ). The scattering efficiency is given by  $Q_{scat} = C_{scat}/G$  where  $C_{scat} = (K^4/6\pi) |\alpha|^2$ .

The condition for the validity of the electrostatic approximation is given by  $x \ll 1$  and  $|m| \times d \ll 1$  where  $d$  is the distance between the dipoles. Hence the particle should be smaller than the wavelength of light.

In this case we have used the electrostatic approximation to calculate the extinction cross section of an ellipsoid. The polarizability of such an ellipsoid is given by

$$\alpha_n(\omega) = \frac{4}{3}\pi abc \frac{\epsilon(\omega) - \epsilon_m}{\epsilon_m + L_n[\epsilon(\omega) - \epsilon_m]} \quad (5.5)$$

where  $a$ ,  $b$ ,  $c$  are the half length of the three axes of ellipsoid and  $n = a, b, c$  and  $\epsilon(\omega)$  and  $\epsilon_m$  denote the dielectric function of the ellipsoid and the medium respectively.

The polarizability associated with the  $n$  axis depends on geometrical parameters through the factor  $L_n$ . The figure 5.1 shows the schematic of the structure we have considered for our simulations.

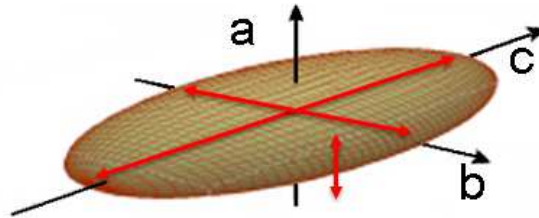


Figure 5.1: Notations for the ellipsoid dimensions; the three axes lengths,  $a$ ,  $b$  and  $c$  along with the axis to which they refer (Adapted from wikipedia.fr).

The extinction cross section has been calculated for such a system by Buatier et al for a nanowire of length 3000 nm [72]. The polarizability of a coated ellipsoid has been calculated in the frame of electrostatic approximation by Bohren and Huffman [26]. The expression is quite lengthy and I have not reported it. It depends on the refractive indices of the metal, of the coating medium and of the medium surrounding the coated particle. It also depends on the thickness of the coating. Using this expression, we could calculate the polarizability of the system of two-coated ellipsoids in the case where the particles have smaller dimensions compared to the wavelength.

## 5.4 Discrete dipole approximation

The discrete-dipole approximation (DDA) is a flexible and powerful technique to compute scattering and absorption of electromagnetic waves by particles of arbitrary geometry and composition. Owing to the development of efficient algorithms

and the availability of inexpensive computing power, DDA has become the popular method of choice for many scattering problems.

The DDA was introduced by Devoe in 1964 [73, 74]. He applied the method to study the optical properties of molecular aggregates which were small compared with the wavelength. The limitation of his method was that it did not include the retardation effects. Purcell and Pennypacker later included the retardation effects [75].

The DDA is an approximation where the scatterer is replaced by a set of point dipoles. The dipoles interact with each other through their electric fields [76, 77]. The DDA is also referred to as the coupled dipole approximation [77, 78]. The theoretical basis for the DDA, including radiative reaction corrections, is summarized by Draine [76]. The DDA was further developed by Draine and coworkers, who popularized the method by developing a publicly available computer code DDSCAT [79, 80, 76]. Later it was shown that the DDA also can be derived from the integral equation for the electric field, which is discretized by dividing the scatterer into small cubical subvolumes.

### Validity Criteria

There are two criteria for validity of the DDA.

1.  $|m|kd \ll 1$  which means the lattice spacing  $d$  should be small compared with the wavelength of a plane wave in the target material and  $m$  is the relative refractive index of the material and the medium.
2.  $d$  must be small enough to describe the target shape satisfactorily which means the number of dipoles into which the target is divided should be large enough to get an accurate value.

These criteria are much less restrictive than those of the electrostatic approximation since the dimension of the particle is now replaced by the distance between the dipoles. The scattering and coupling between quite large particles can be calculated. Nevertheless, these advantages are at the expense of the calculation time.

We have used the DDA method to simulate the extinction efficiency ( $Q_{\text{ext}}$ ) spectra of the ellipsoids. As explained earlier, as per the DDA procedure the target geometry is discretized into several virtual dipoles. The interaction of the light with each dipole is solved taking into account the inter-dipole interactions. Besides, by defining each nanoparticle by several thousand dipoles, finite size effects including retardation and higher-order oscillation modes are accounted for, unlike a purely dipolar model where each particle is represented by a single dipole. The

number of dipoles in DDA is ensured to be large enough such that the discrete-dipole spacing is much smaller than the wavelength of light and the nanostructure size to achieve reliable results.

### **DDSCAT**

The simulations have been carried out using DDSCAT 6.1 [79]. DDSCAT is a software package to calculate scattering and absorption of electromagnetic waves by targets with arbitrary geometries using the (DDA). The working of the DDSCAT is explained in detail in the appendix. In all the simulations, the dielectric function of the target material was assumed to be that of bulk gold and the dielectric function of the environment was chosen to be either water or the dielectric function of the coated dye.

The choice of water in most cases rather than air is guided by the fact that we work at air and not under vacuum. Under these conditions, it has been often reported that a layer of water is deposited on the sample. Regarding the dielectric function of the dye (Rhodamine 6G as explained later) the data of the dielectric function of rhodamine are those obtained in the work of Vanduyne et al [81].

## **5.5 Comparison between electrostatic approximation and DDSCAT**

The figure 5.2 shows the comparative study between the electrostatic and discrete dipole approximations. The simulations have been done on an ellipsoid of dimensions 200 nm x 80 nm x 20 nm. The surrounding medium is assumed to be water in both cases and the extinction coefficient is calculated for the plasmon along the b direction (further named V). It is seen that for the same system, the extinction peaks differ between the two methods.

In the electrostatic approximation, the plasmon peaks at 580 nm. The peak is quite sharp when compared to the one calculated using DDSCAT. In the DDSCAT, the plasmon is peaked at 630 nm.

In general, the electrostatic approximation is easier to implement since it is quite straight forward to change the parameters in contrast to DDSCAT. At the same time, it is difficult using the electrostatic approximation to get accurate details about the system that is being studied. The major difference between the two techniques is the inadequacy of the electrostatics theory to take into account the multipolar effects and retardation effects. Thus the extinction efficiency calculated is not as accurate as using that of DDA as soon as the particle is not small enough compared to wavelength.

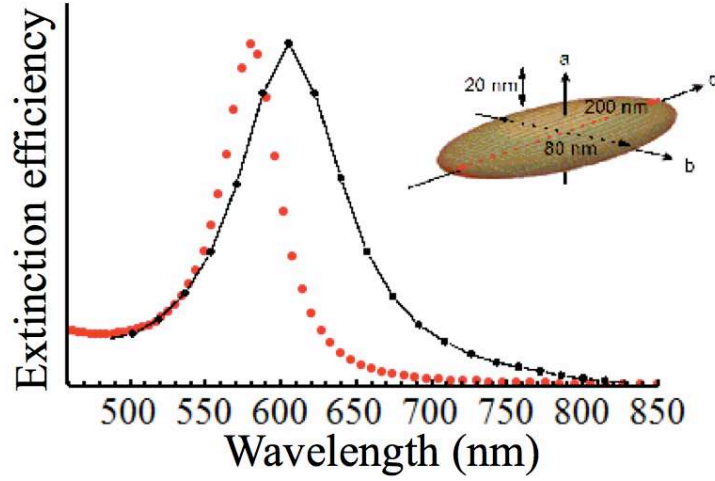


Figure 5.2: Comparison between electrostatic and discrete dipole scattering. The black curve represents the DDA made using DDSCAT and the dots represent the electrostatic approximation.

## 5.6 Dependence on Inter particle distance

As said earlier in the previous chapters the plasmon depends on the inter particle distance. When more than one particle is involved, the plasmon of the particle shifts due to the coupling between the particles. The magnitude of the induced plasmon shift depends on the strength of the inter particle coupling, which, in turn, depends on the proximity of the individual nano- particles.

Here we have simulated the evolution of the plasmon intensity between two ellipsoids with different inter particle distances, in the frame of the electrostatic approximation. The dimensions of the ellipsoids, coated with a monolayer of rhodamine, are identical and are 200nm x 80 nm x 20 nm. The figure 5.3 gives the evolution of the plasmon when the excitation is across the ellipsoids (V direction). Jain et al have studied the plasmon decay with the inter particle distance [82]. They have derived a plasmon ruler equation which gives an universal scaling law for plasmons. The near-exponential distance decay and the interesting universal scaling behavior of inter particle plasmon coupling can be qualitatively explained on the basis of a dipolar-coupling model as being due to the interplay of two factors: the strength of the coupling between the two particles decreases as the cube of the distance between the particles and the restoring potential of the plasmon of the particles, which increases as the volume of the particle [82].

$$\frac{\delta\lambda}{\lambda_0} \approx 0.18 \exp\left(\frac{-(s/D)}{0.23}\right) \quad (5.6)$$

With this equation they find the inter particle separation for a given plasmon shift

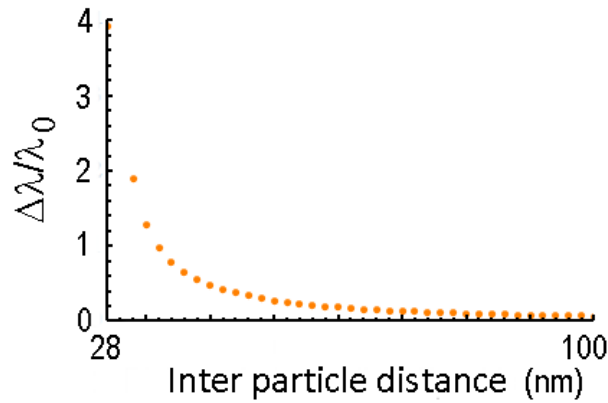


Figure 5.3: Plasmon decay with the interparticle distance when the excitation is across the ellipsoids (V direction).

and vice versa. In the equation,  $s = d + D$  where  $D$  is the particle dimension along the axis coupling both particles. The figure 5.3 shows that the coupling effect falls very rapidly with the inter particle distance, even if the exponential decrease fit is not so good. The reason could be the too large size of the ellipsoids for the electrostatic approximation.

## 5.7 Simulation of an ideal sample sample

The figure 5.4 shows the extinction curves of one, two or three ellipsoids with wavelength. The idea is to understand the effect of plasmon coupling in the real samples we have used. As explained earlier, the samples are made by sputtering on rippled substrates. Hence we have calculated the extinction of ellipsoids that are tilted or rather deposited on a rippled surface as shown in the figure. The dimensions of the ellipsoid are considered to be 120 nm x 20 nm x 80 nm. The length has been limited to 120 nm, because of the large number of dipoles needed to accurately describe the case of 3 ellipsoids. As it will be seen later, the length of the ellipsoid plays a role on the peak values of both resonances along H and V but the coupling trend will be maintained. The centre to centre distance between two ellipsoids is taken as 160 nm. The surrounding medium is taken to be water and the ellipsoid is bent by an angle of  $11^\circ$  accounting for the angle of sputtering, the deposited dose and the distance between two valleys of the rippled structure. The extinction curves have been calculated for both incident polarization directions (V

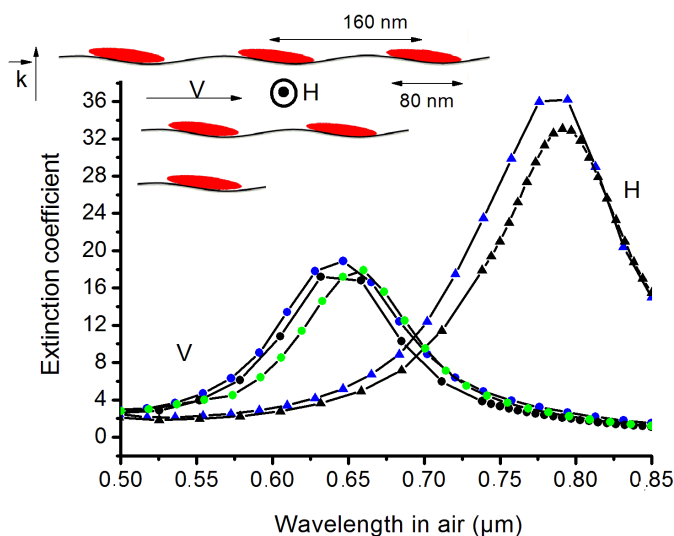


Figure 5.4: Extinction efficiency of two and three ellipsoids. Black : two ellipsoids; blue : three ellipsoids; triangles : H configuration; dots : V configuration; Green dots : V configuration for a single ellipsoid.

and H) for two and three successive nanowires. It is clearly seen from the figure that for the single ellipsoid, the plasmon peaks at 660 nm. When we consider two plasmons, the plasmon is slightly blue shifted for V configuration. In the H configuration, the plasmon peaks at about 800 nm. On moving to three ellipsoids, there is nearly no additional shift. This simulation demonstrates that the coupling between the nanowires is evanescently weak, which is in agreement with the dependence of the shift of the plasmon resonance with the distance between two particles described above. It indicates that the effect of coupling between several nanowires takes importance only if they are sufficiently close.

## 5.8 ATTO 740

The idea is to probe the dependence of the optical properties of the sample on polarization by investigating its SERS properties. We have probed the SERS response of a reporter as a function of the polarization of the excitation field in order to investigate the coupling between the nanowires, which could be at the origin of the dichroism properties of the nanowire array.

The excitation spot in our experimental conditions as described in the previous chapter is an Airy disk of diameter  $0.9 \mu\text{m}$ . Efficient excitation is obtained at half-width maximum. Consequently, owing to the patterning of the sample, we probe 4 to 5 successive nanowires on a limited length of some hundreds of nm that

are efficiently illuminated by the excitation spot. The SERS response corresponds to the average of the SERS signatures of all the molecules deposited on these structures.

A drop of ATTO 740 dispersed in water ( $2 \times 10^{-7}$  M measured by absorption in cuvette) was deposited on top of the substrate and let to dry overnight. We started with ATTO 740 as a reporter because it can be resonantly excited in the excitation wavelength range, as already explained in the previous chapter.

The first investigations started with systematic studies to map the SERS properties of the sample. The SERS spectrum of ATTO 740 was recorded on a grid of 49 and 64 continuous points on two different places of the sample (that is square maps of  $7 \mu\text{m}^2$  and  $8 \mu\text{m}^2$  respectively), with the excitation polarization in two orthogonal directions at each location. One polarization is along the mean direction of the nanowires and the other one perpendicular to it. These directions will be further named H and V respectively. Moreover, most of time, we have recorded series of spectra at the same location to get information on possible intensity and spectral shifts. Additional spectra were acquired at random locations in order to screen as efficiently as possible the sample, despite the time consuming procedure and the huge amount of data to be analyzed. The first observation is the absence of visible propagation of plasmon or remote emission irrespective of the wavelength or the polarization of the excitation.

Some examples of the typical SERS spectra are displayed in the following figures. The spectrum in the figure 5.5 features quite a broad band. It can be observed in

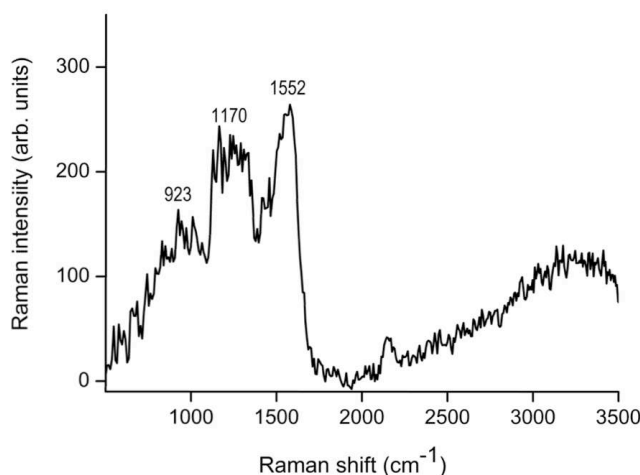


Figure 5.5: Spectrum featuring three broad bands, observed either on H or V polarization at many active locations.

V as well as H configurations. Nevertheless, in time series, this kind of signature is not more stable than the spectra with well defined lines. It often cancels from one

acquisition to the next one, suggesting that it is the response of a single molecule rather than that of several molecules at the same site. The width of the band is an example of a fast on-off spectral diffusion of the molecule, at least fast compared to the acquisition time, which could not be reduced under 5 to 10 s to get a satisfying signal to noise ratio.

The data analysis reveals several general behaviors. First, no SERS signature can be detected on many of the studied locations. The signal is either a weak residue of the laser excitation or a weak and broad background. Second, when a SERS response is observed at a given location, showing different Raman lines, the evolution of the signature in time features a strong molecular dynamics. The blinking process is huge and the lines are often observed only once or twice during a sequence of 10 or 20 successive acquisitions. The general trend is that the SERS profile does not change a lot, when it is detected at the same location but rather that the intensity of nearly all the lines drops at the same time and SERS is no longer observed. This systematic study demonstrates that ATTO 740 molecules do not bind strongly on the surface and there is an efficient thermal diffusion. Moreover, the observation of sudden drops of the SERS signature rather than a progressive decrease of its intensity strongly suggests that the single molecule SERS (SM-SERS) is attained. This indicates that there is at most a single hot-spot on average in the excitation spot, where the enhancement is large enough to record clear Raman lines of ATTO 740. Two main causes for dynamics have been reported in literature. The first one is the change of conformation of the molecule in the SERS site, the second one is a spatial diffusion process, the molecule drifting into and out of the hot-spot in a random way. The former process essentially modifies the shape of the profile, which is not so often the case in our study. The later process, which corresponds to blinking, is in agreement with what is observed. It has been reported that the origin of the blinking is possibly due to a thermal diffusion of an individual molecule on the surface [83]. This explanation is convincing in case of physisorbed molecules, for which the thermal energy is of the same order of magnitude as the binding energy. In the case of chemisorption, the situation must be carefully examined for different molecules.

On some locations well-defined spectra were also observed (figure 5.6), generally with a very weak intensity. These were not stable in time either.

As mentioned above, on very scarce locations, a high signal to noise ratio SERS could be observed, with well-defined lines. However, the signal still displayed several blinking periods during the whole recording time (10 to 20 acquisitions). The main difference between the above cases is that the strong thin lines could be observed on some spectra. It mostly indicates that the studied location is a well defined hot-spot, where a very limited number of molecules can simultaneously sit. Another example displays an unusual spectrum that happened to be observed on

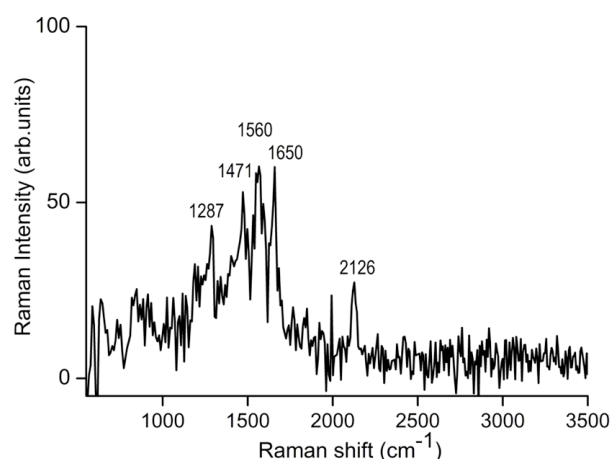


Figure 5.6: Example of well defined SERS spectrum. The spectrum was recorded at an excitation wavelength of 697 nm, intensity of  $1200 \text{ W/cm}^2$  for 10 s.

some locations, where only a single mode is sufficiently active to give a signal (figure 5.7).

The figure 5.8 presents three spectra acquired in the same series, but separated in time. The signal observed in between these active periods is similar to that of figure 5.9 and is not displayed. On the top spectrum one can observe lines in the frequency domain around  $3000 \text{ cm}^{-1}$ . These lines are not often observed, they can correspond to C-H stretching modes and combination of high frequency modes. The presence of such high-frequency weak vibrations gives a bump often observed. The mode that gives a signature on the top spectrum at  $1566 \text{ cm}^{-1}$  could be a C=C stretching mode of an aromatic cycle. All the other C=C modes cannot be detected, which indicates that the molecule has a distorted configuration at this location.

All the spectra that have been reported above are recorded at an out of resonance excitation (mainly around 698 nm). This choice aimed to be as close as possible to the absorption peak of the sample, blue shifted compared to our excitation range, and to start studying as far as possible SERS rather than SERRS. The figure 5.9 shows the spectral dynamics seen with ATTO 740 on the substrate.

As mentioned earlier, very few such spectra as in figure 5.8 have been observed despite the screening of the sample. Such a signature can be observed either in H or in V polarization. There is no preferential excitation polarization. As a result, the molecule sits in a hot-spot, that is probably a gap between two coupled particles and not necessarily in the gap between two successive nanowires.

This is nicely illustrated by the simulations when the dimensions of the particles are changed. The previous study demonstrates that it is indeed possible to obtain a SERS signature stronger in H configuration than in the V configuration in nearly

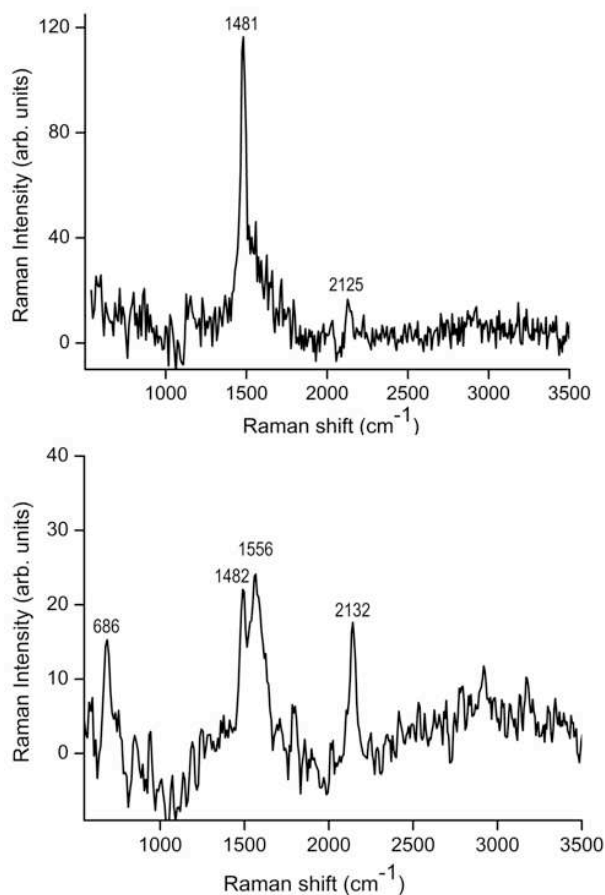


Figure 5.7: Two spectra successively acquired on a location. The top spectrum was recorded with V configuration and the bottom with H configuration.

half the situations on ATTO 740 alone. As it has been reported in different studies, the enhancement effect of isolated particles is quite weak, the SERS is more likely to arise from molecules trapped in the junction between two particles. The plasmon resonance along the axis joining the centers of the particles and along the perpendicular axis is very sensitive to the size of the gap between the particles, as I have already demonstrated, but also on the dimensions of the particle as it will be explained below.

Figures 5.10 and 5.11 summarize the dependence of the nanoparticle plasmon resonance on the nanoparticle dimensions. They show the plot of extinction efficiency versus the wavelength for ellipsoids with increasing lengths of the long axis. Figure 5.10 shows the extinction efficiency of two ellipsoids of dimensions 80 nm x 60 nm x 20 nm, when the excitation is along and across the nanowires, with rhodamine 6G as the surrounding medium.

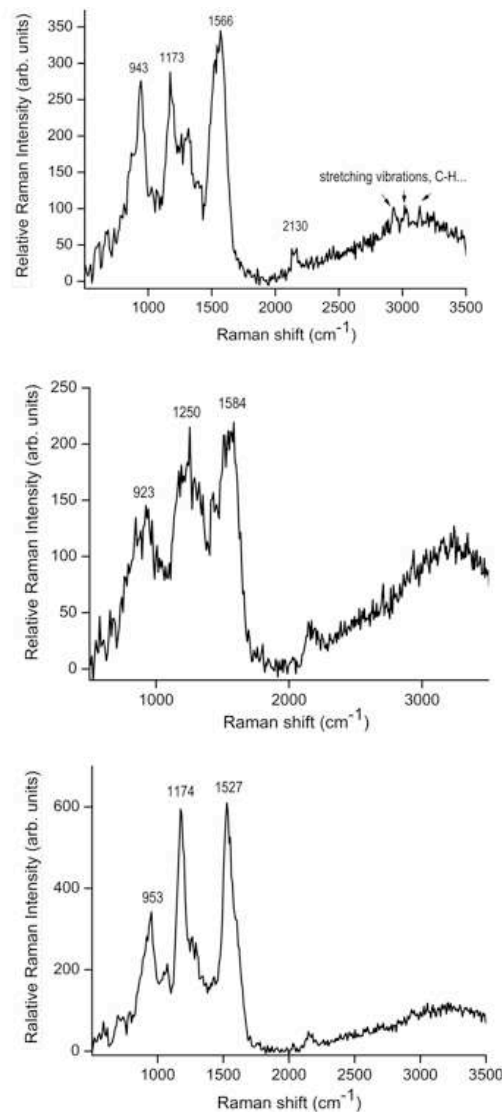


Figure 5.8: Example of series of spectra recorded at the same location and separated in time. The signal corresponds to active periods. Raw data; acquisition time 10 s, intensity 1500 W/cm<sup>2</sup>.

Figure 5.11 is under the same condition except the dimension along the long axis is increased from 60 nm to 200 nm. In both the cases the two ellipsoids have been separated by a distance of 10 nm. With increase in the length from 60 to 200 nm, there is a blue shift in the plasmon resonance across the ellipsoids (along V direction) from 760 nm to 700 nm. On the other hand the plasmon resonances along the nanowires (H direction) undergoes a huge red shift and the plasmon peak shifts from 600 nm to beyond the visible range. Similar red-shift has been

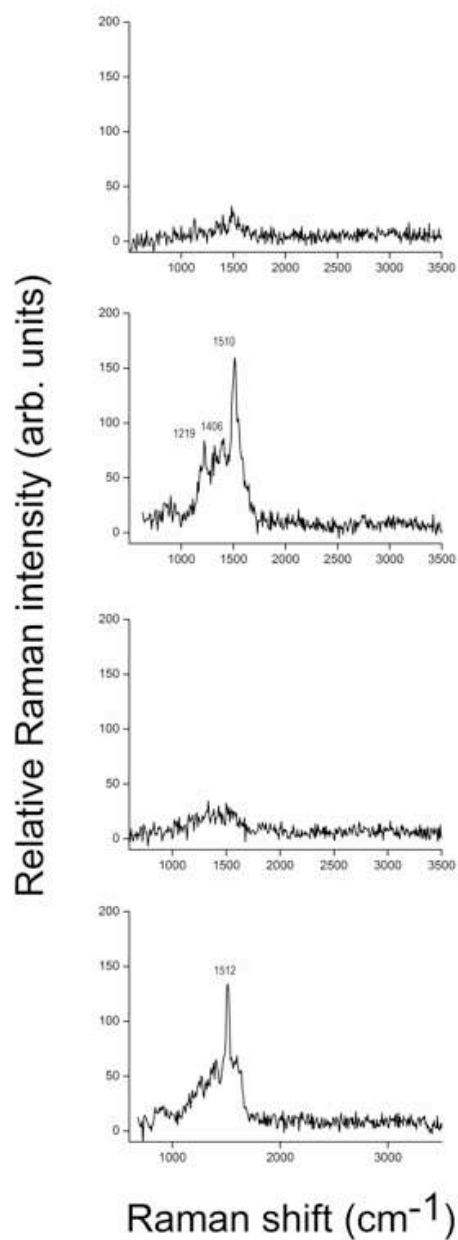


Figure 5.9: Example of blinking in ATTO 740 SERS spectra. These spectra are recorded at 701 nm at an excitation intensity  $10^3 \text{ W/cm}^2$  for 6 s.

observed in the measured optical spectra of gold nanoparticles and is attributed to the effect of electromagnetic retardation in larger nanoparticles.

The change in the length of the ellipsoids along  $c$  induces a blue shift (towards higher frequency) of 60 nm of the V plasmon resonance. This is mainly explained

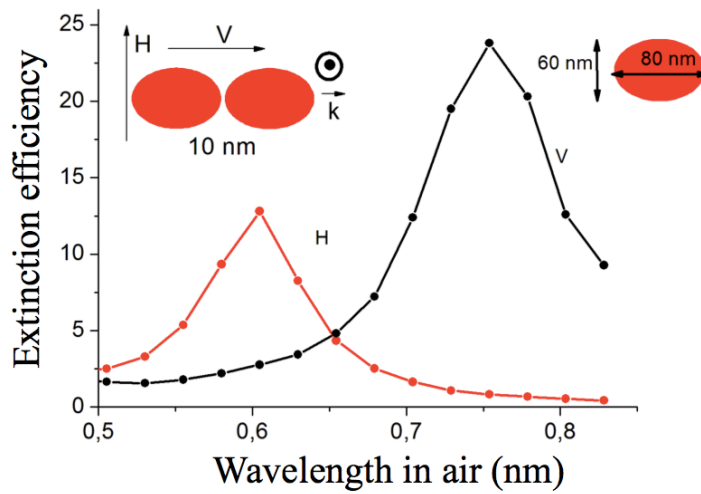


Figure 5.10: Extinction efficiency with wavelength of two ellipsoids with the long axis of 60 nm. The other two dimensions are 20 nm and 80 nm.

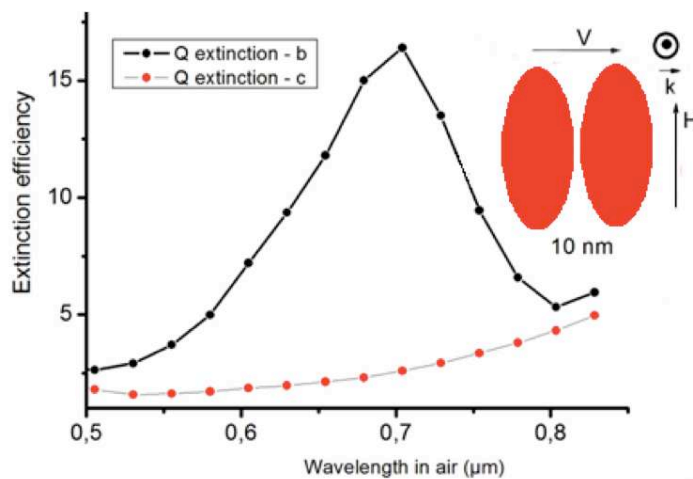


Figure 5.11: Extinction efficiency with wavelength of two ellipsoids with the long axis of 200 nm. The other two dimensions are 20 nm and 80 nm.

by the change of the shape of the gap between the two ellipsoids because the curvature of surfaces that face each other is reduced for the most elongated ellipsoids. For the H polarization, the calculation predicts a huge red-shift in agreement with a large change in the  $c$  dimension. In that direction, the coupling between the ellipsoids is not very sensitive. When the dimension of the ellipsoid along  $c$  is 60 nm, the ellipsoid is close to a sphere and the plasmon in H direction was indeed expected to be not too far from 520 nm. This simulation aims at demonstrating

that i) the roles of H and V are exchanged when there is a gap between two metallic structures along a nanowire, and ii) the plasmon resonance and thus the SERS enhancement is very sensitive to the dimensions of the particles and to the gap in between. As a result, we can conclude that the observation of SERS signatures being stronger when the polarization is along the nanowire or the reverse is not surprising and that it depends on the local properties of the substrate. The ability to obtain enhancement in both cases in the study demonstrates that gaps also exist along the nanowires and not only between successive nanowires.

Because of the quite weak SERS signals, we have decided to investigate the response of the molecule-substrate effect at resonance (740 nm). The main result was even if Raman spectra with well defined lines were observed on some locations, the blinking dynamics was much accelerated than in the previous case, making any polarization study impossible. The acceleration of the dynamics is in line with the thermal process of desorption but it also underlines a possible light-induced contribution as recently discussed by Nie et al [84].

The main conclusions of the experiments with ATTO 740 molecules are the following:

- ATTO 740 does not have a strong affinity with the gold surface and is readily desorbed as soon as it is excited.
- The SERS enhancement of ATTO 740 on the nanowire array is low.
- The variety of SERS spectra that have been recorded indicate that the sample includes many gaps between particles of different sizes and that as such no clear polarization dependence is observed.

## 5.9 Rhodamine 6G

Next we have added Rh6G to the sample along with ATTO 740. The original idea behind such a step was to study the SERS effect on the nanowire arrays with two different molecules, one at resonance and the other non resonant. We believed such an experiment with two different analytes combined with the polarization measurements will give an insight into the resonance contribution and to a number of other mechanisms. However on addition of rhodamine 6G different effects are observed, the most important of which is the global shift of plasmon which will be discussed in the coming sections.

As already mentioned in the chapter on nanowires, the lowest electronic transitions of Rhodamine 6G are far from the plasmon resonances. In most of locations of the sample the SERS enhancement of Rhodamine 6G is expected to be quite low even if it is observed.

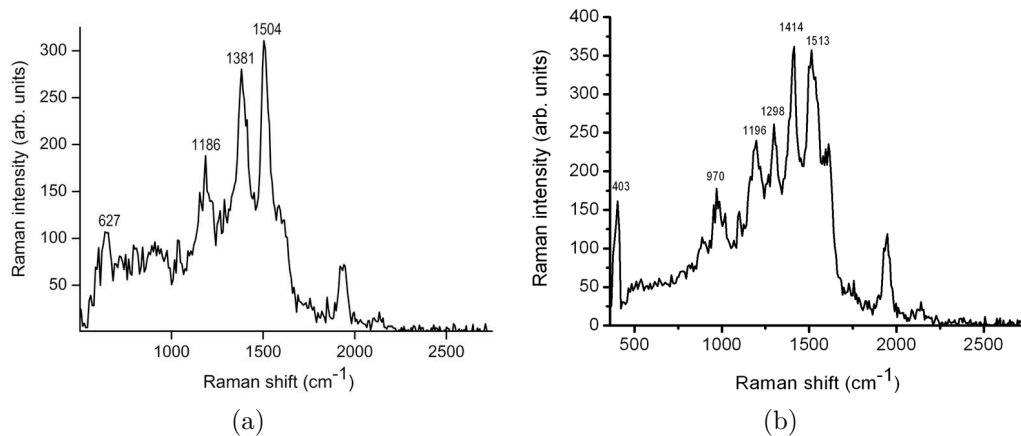


Figure 5.12: Two types of rhodamine spectra observed on the sample; (a) with a weak excitation ( $1200 \text{ W/cm}^2$ ) and (b) with a strong excitation  $5 \times 10^4 \text{ W/cm}^2$ .

The scattering signal have been recorded at many locations on the sample, where only a drop of rhodamine ( $\approx 10^{-6} \text{ M}$ ) has been deposited then dried. At rather weak excitation ( $\approx 100 \mu\text{W/spot}$ ;  $\approx 1200 \mu\text{W/cm}^2$ ) generally used for the studies, Rh6G scattering is not observed. On some locations it is observed as a background with broad bumps on top. In very scarce locations a SERS signature can be obtained where the medium to high frequency lines of RH6G can be identified as displayed in figure 5.12. Moreover at high excitation intensity ( $\approx 1200 \mu\text{W/cm}^2$ ) some more low frequency lines can also be observed, such as the low frequency mode at  $396 \text{ cm}^{-1}$  (observed at  $403 \text{ cm}^{-1}$ ). This mode gives rise to the combination line near  $1900 \text{ cm}^{-1}$  ( $403+1513$ ). Such SERS spectra of quite moderate intensities could be due to the contribution of a Rh6G molecule positioned in the junction between two gold particles that decorate the surface, as observed in the AFM image, or located in another kind of gap. In both cases the high frequency modes at  $1650 \text{ cm}^{-1}$  and  $1575 \text{ cm}^{-1}$  are not observed, in agreement with the NIR excitation of rhodamine 6G (see discussion in previous chapter). The observation of low frequency modes nevertheless suggest that the molecule is very close to the surface such that vibronic excitation occurs [47]. This effect will be discussed further in the chapter.

The plasmon shift induced by rhodamine 6G is due to its refractive index. The plasmon resonance frequency is highly sensitive to the dielectric properties of the medium surrounding the nanoparticle. This has been already discussed in the chapter on plasmons. The plasmon resonance frequency is sensitive to any refractive index change in the local medium around the nanoparticles, including the solvent or the presence of adsorbates or surface-capping molecules [85]. The sim-

ulations support the idea of shift of plasmons with different environment. The ellipsoids have been considered in three different environments air, water and rhodamine 6G with increasing refractive indices.

Since the increase in the medium refractive index also reduces the effective wavelength of light in the medium, the size of the nanoparticle relative to the effective medium wavelength increases. This results in the increase in the electromagnetic retardation, damping and multipolar effects, and significant broadening of the plasmon resonance.

The figure 5.13 shows the calculated plasmon resonance of a slender ellipsoid surrounded by the air. The plasmon along the short axis peaks at 550 nm and that along the long axis is beyond the visible range. The dimensions of the ellipsoid are 80 nm along the short axis, 200 nm along the long axis and a thickness of 20 nm.

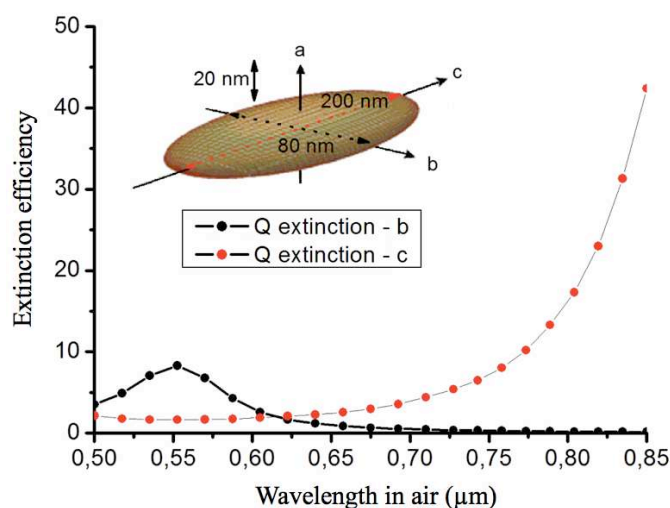


Figure 5.13: Extinction efficiency of the ellipsoid with wavelength. The ellipsoid is surrounded by air. The black curves give the extinction efficiency along the short axis and the red one along the long axis of the ellipsoid ( $a_{eff} = 0.034 \mu\text{m}$  and  $d = 2\text{nm}$ ).

The figure 5.14 shows the calculated plasmon resonance of the same ellipsoid surrounded by water. The refractive index of the medium increases to 1.33 for the case of water. As a result the plasmons are shifted. The plasmon along the short axis is red shifted and peaks at 610 nm and that along the long axis is beyond the visible range.

The figure 5.15 shows the calculated plasmon resonance of the same ellipsoid surrounded by rhodamine. The refractive index of the medium is taken to be 1.39 for

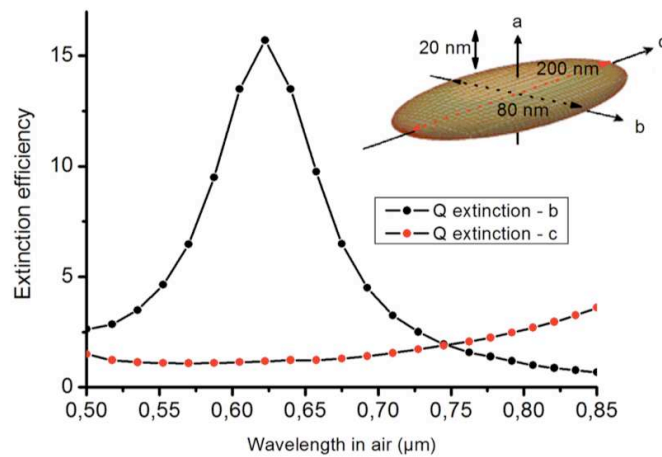


Figure 5.14: Extinction efficiency of the ellipsoid surrounded by water with wavelength. The black curves give the extinction efficiency along the short axis and the red one along the long axis of the ellipsoid ( $a_{eff} = 0.034 \mu\text{m}$  and  $d = 2\text{nm}$ ).

the case of rhodamine. The plasmon along the short axis peaks at 640 nm. The shift of the plasmon with respect to the case when the surrounding is taken to be air is quite large, around 100 nm. The plasmon shift with respect to water is small compared to the case with water. However, it is still significant.

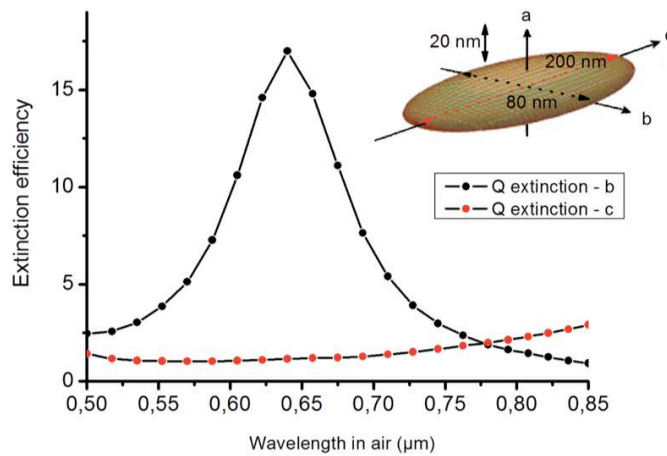


Figure 5.15: Extinction efficiency of the ellipsoid surrounded by rhodamine 6G with wavelength. The black curves give the extinction efficiency along the short axis and the red one along the long axis of the ellipsoid ( $a_{eff} = 0.034 \mu\text{m}$  and  $d = 2\text{nm}$ ).

This possibility to shift the plasmons by using rhodamine 6G has been effectively

used in our experiments. Nevertheless, we cannot expect a shift as large as predicted in the calculation that assumes that the medium is rhodamine and not only a monolayer of rhodamine 6G. The effect of a single monolayer is difficult to model with DDA, but we can get an idea with the electrostatic approximation using the polarizability of a monolayer-coated and uncoated ellipsoid. The calculation demonstrates that there will be a non negligible shift of around 40 nm in the case of rhodamine 6G.

## 5.10 Effect of two reporters

The original idea behind the addition of rhodamine 6G, as explained earlier, was to shift the plasmon of the nanowire array such that it falls deeply in resonance with ATTO 740. This was expected to increase the enhancement and consequently the signal intensity of ATTO 740. However, the first striking observation when analyzing the spectra with both Rh6G and ATTO 740 is the stability of the spectra. Though the enhancement increases, it is not huge whereas the spectra do not have any shift that was a common when we had just ATTO 740. It remained stable for longer periods of time during the series of acquisitions made over one minute. Such stability was immensely useful to carry out the intended studies on the SERS dependence on excitation wavelength and polarization.

The figure 5.16 shows a series of spectra obtained on such a system with both the reporters on the sample. It is seen clearly that the spectral profile does not change with time and does not have any spectral shift. Besides slowing the dynamics of ATTO 740, a larger number of SERS efficient sites were observed. The probability of finding a hot spot with a good SERS signal was much more than with just ATTO 740.

Before we try to explain the effect of rhodamine on the system, I digress a bit to discuss some important points which are related to this observation. There are two contributions to the overall SERS enhancement which has already been discussed in the introduction chapter to SERS. The electromagnetic contribution, which is taken as the global effect and the other one is a local effect, which is due to the chemical effect or charge transfer. The charge transfer will be discussed in detail in the coming sections. When a molecule is deposited on the surface there are two ways in which they are positioned on the surface. The first kind of adsorption is unspecific in nature. It does not require any specific features or sites on the substrate. This is a random distribution. This is a possibility in our case with just ATTO 740 molecules where we have poor binding of the molecules to the surface of the nanowires, although we do not have any proof of this except the spectral shifts and blinking combined with low signal. The second kind is the chemisorption that occurs in the presence of ions. The effect of the ions on the SERS enhancement has

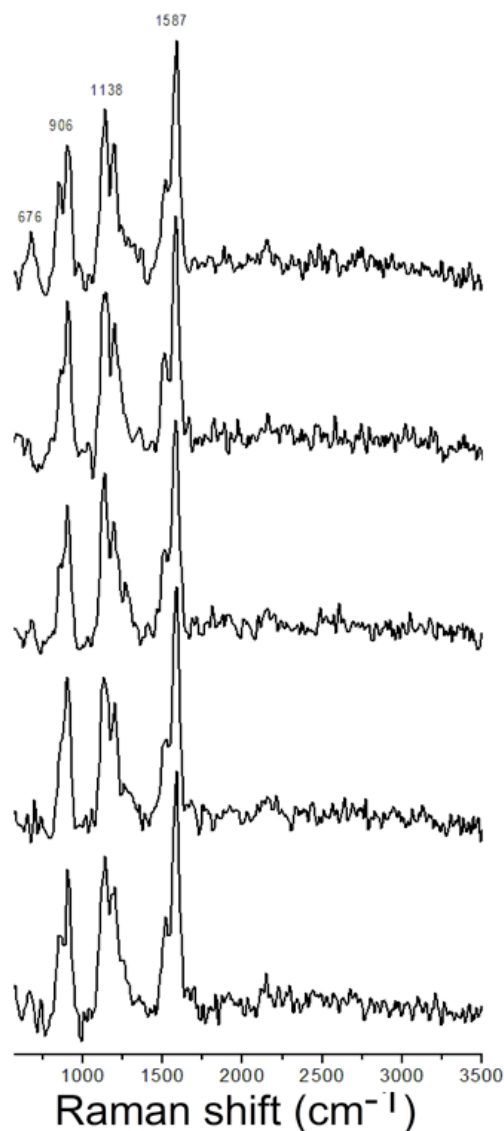


Figure 5.16: Example of a stable spectra recorded in the presence of two reporters.

been studied for a long time. Such studies have been traditionally made on silver aggregates or substrates and always using anions. Hildebrandt and Stockburger have studied the effect of ions on SERS spectra of Rh6G adsorbed on colloidal silver [86]. This is one among the many important works that followed in this study [87, 88]. They found that on addition of a small amount of chloride ions to the sol, there was a significant increase in the Raman intensity. They did not find any morphological changes in the sol and concluded that the effect is a result of the activation of specific sites and that the anions help in better binding of the

molecules since they influence the conformation of the adsorbed molecules.

With anions on silver it has been shown that SERS is enhanced for  $\text{Cl}^-$  for example, but not for  $\text{I}^-$ . Also, it has been suggested that the ions partly remove the heterogeneity of the silver surface by creation of a complex and consequently the changes in the local work function are reduced. As a result, there are less fluctuations in the charge transfer transition from site to site and the spectral dynamics of the SERS is reduced, even if the molecule diffuse on the surface. Rh6G could partly play a similar role on the gold surface since it has already been demonstrated that Rh6G can help gold clustering [89]. Additional studies are necessary to elucidate why ATTO 740 itself cannot play the same role as it is also a cation in solution. Nevertheless we have to remember that the chemical properties of both dyes are different since ATTO 740 is soluble in water, whereas rhodamine is more soluble in ethanol. A unique gold aggregate system has been shown experimentally to be useful for SERS detection of R6G and several biological molecules. In this experiment they have shown that Rh6G is generally difficult to detect on gold substrates but it readily adsorbs to the gold nanoparticle aggregates [90]. This could explain the effect of rhodamine on our samples, since otherwise they have low affinity for gold surfaces.

Having said these, we look at what happens in our system in the presence of two reporters. The first look at the spectra confirms that Rh6G satisfies the purpose that it was intended for. There is a global plasmon shift. The evidence for such an effect is the presence of low frequency lines that are observed in this case which were not seen previously. The intensity of the low frequency lines are substantial and comparable to that of the high frequency lines which means the plasmon of the sample is deeply in resonance with the ATTO 740 molecule. This gives the irrefutable evidence for the plasmon shift.

This has been verified with the theoretical calculations of the effect of different surrounding medium with varying refractive index on the plasmon of the sample. The more stable signature of ATTO 740 in the presence of Rh6G is difficult to explain precisely. Both the molecules are cationic in nature and we have seen earlier that the signal of Rh6G on the substrate is quite weak. So the possibility rhodamine 6G molecule forming a strong complex with gold is too few. It is the same for the two molecules to form a complex with new properties. The solutions to this question is related to the surface chemistry between the molecules and the substrate which in itself is a huge study and at the same time it is beyond the capabilities of our experimental set up.

One reason that could be attributed for such a behaviour is competitive binding of the two molecules with the substrate. SERS studies have been done on silver colloids with the addition of two anions, one in resonance and another out of resonance. It is seen that with the addition of the non resonant anion, the SERS

signal increases considerably without the presence of the SER signal of the non resonant anion itself. The resulting signal depends on the species that occupies the surface sites and are enhanced. We can draw an analogy to this experiment to our case with two cationic molecules. The rhodamine 6G probably helps in the increased binding of the ATTO 740 by the competitive process. However, there is no propagation observed in any case.

## 5.11 Polarization dependence of SERS

Polarization studies on SERS has been done extensively by different groups [91]. A number of systems like dimers, trimers, array of nanorods or nanowires have been investigated for this. The studies are made consistently to make structures that have strong polarization dependent SERS activity. The importance of such polarization experiments is that they have the potential to elucidate the fundamental aspects of molecule - surface interactions like physical orientation and chemical interaction. Such studies will yield a deeper insight into the SERS phenomenon and provides an invaluable tool for surface science based analysis of single molecules. We have observed in different locations SERS signatures which are highly polarized. Such kinds of studies are quite challenging because the SERS signature must be stable enough to perform several acquisitions at the same polarization angle, before photobleaching. Furthermore, it is very important to get sure that an increase of the signal does not result from a fluctuation of intensity. As we have already mentioned, in the presence of rhodamine 6G, the SERS signature is more stable allowing for long acquisitions at different locations.

In general, with the polarization studies on our samples, two different kinds of hot-spots have been observed. One where there is a strong polarization effect along the nanowire (H direction) and the other hot-spots where the signature is polarized along the V direction and no enhancement or very weak enhancement along H. The latter is what is expected if the molecule is present in a hot-spot between the nanowires.

### 5.11.1 Polarized hot-spot along the nanowires

Here, we report an example of SERS signature observed in the H configuration, with an excitation intensity of  $1200 \text{ W/cm}^2$ . The excitation wavelength is 698 nm. The analysis of the evolution of the signal with the direction of polarization is measured with respect to the angle between the H direction ( $0^\circ$ ) and the successive positions of the excitation obtained by rotating a broadband half waveplate in the path of the excitation beam, as depicted in figure 3.3. The figure 5.17 clearly demonstrates that the signal is highly peaked in the H direction, and that the

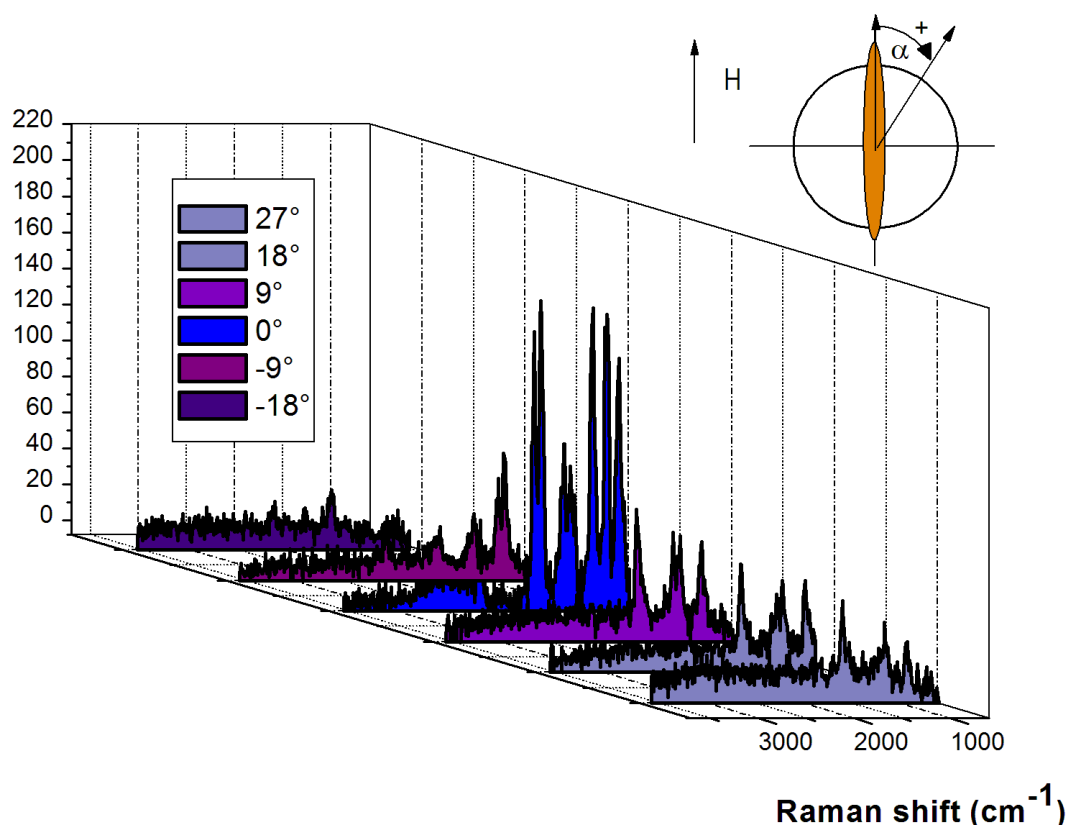


Figure 5.17: Polarization dependence of SERS on the nanowire arrays. The spectra were recorded at 698 nm with an excitation intensity of 1200 W/cm<sup>2</sup>.

intensity decreases even more rapidly than a  $\cos(\alpha)^2$  law. It strongly suggests that the molecule is located in a tiny hot-spot, where the field is highly confined and only intense in the H direction. Nevertheless, the SERS enhancement is not so high. The signal could come from a hot-spot created in the gap between two particles located on top of the nanowires, as it has been nicely demonstrated in the case of gold dimers or trimers [92] or in the gap between two nanowire segments.

The spectra strikingly depart from those observed on the isolated nanowires (previous chapter) and from the reference spectrum (Fig. 4.15). I have plotted in Fig. 5.18 the spectrum recorded with the orientation of the excitation field along H.

As in the previous case of ATTO 740 SERS spectra reported on the nanowire arrays, when ATTO 740 was deposited alone, the spectrum is more disturbed compared to the case of isolated nanowires, where the spectra were very similar to the reference spectrum. Especially in a vast majority of cases, the highest

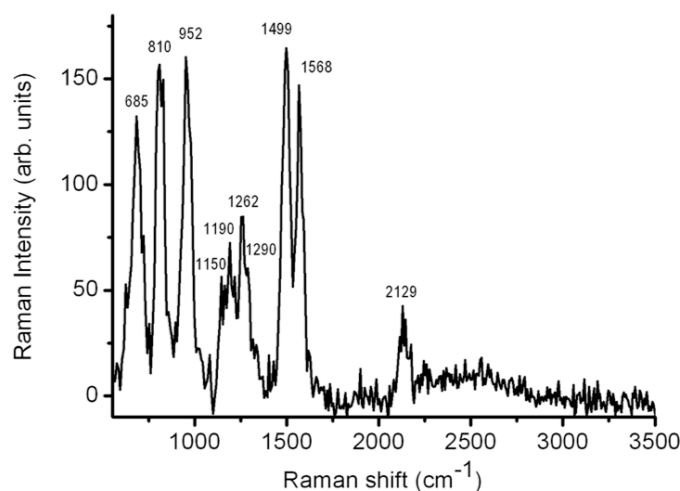


Figure 5.18: ATTO SERS Spectrum recorded with H orientation in the presence of rhodamine.

frequency mode at  $1626\text{ cm}^{-1}$  is not observed. It suggests that in the hot-spots, where a signature of ATTO 740 is detected, the molecule generally undergoes a conformational distortion. The bump around  $2500\text{ cm}^{-1}$  arises from combination modes of the “low-frequency” modes and the aromatic stretching ones (for example  $952+1568$ ).

The most striking feature of the spectrum is the strong intensity of the lines corresponding to active modes in the  $600\text{ cm}^{-1}$  to  $1000\text{ cm}^{-1}$  range. The intensity of the lines is of the same order of magnitude as those of the high frequency modes. The latter can reasonably assigned to aromatic stretching modes, assuming the presence of aromatic cycles in the structure of ATTO 740. They are expected to have a dominant strength for an excitation not so far from the resonance. This was indeed observed in the case of isolated nanowires. In the  $600\text{ cm}^{-1}$  to  $1000\text{ cm}^{-1}$  range, different out of plane and in plane C-H bending modes have been reported for the aromatic compounds, as well as deformation modes. These modes, whose strength is weaker than that of the high frequency aromatic C-C stretching modes gain importance when the excitation wavelength approaches resonance value. It is the case for example for rhodamine 6G [47]. These modes gain strength from a vibronic coupling. In the present case, ATTO 740 is not resonantly excited. The shape of the spectrum could be rather interpreted as a chemical effect of charge transfer between the molecule and the substrate. As explained earlier, the chemical effect results in a resonant process and it could explain the enhancement of the low frequency modes on such location. It indicates that the molecule is located very close to the surface. It partly explains the ability of recording the signal

for a quite large number of acquisition cycles since photobleaching is reduced in agreement with the formation of a molecule-surface complex. The enhancement is not so strong at this location, but these kind of sites contribute to lower the ratio between V and H intensities in a macroscopic experiment.

The increased significance of the low frequency modes and the absence of high frequency modes suggests that there is a *first layer effect* that plays an important role. The first layer SERS effect is usually ascribed to dynamical charge transfer (DCT) between metal and absorbate. It is known as the first layer effect since the mechanism requires direct coupling between the molecule and the metal. It can be explained as a possible enhancement mechanism attributed to specific interactions like electronic coupling between molecule and metal or formation of an adsorbate surface complex, resulting in an increased Raman cross section of the adsorbed molecule in the complex compared with the cross section of a free molecule in a normal Raman experiment. The charge transfer effect will be discussed in detail in the following section.

### 5.11.2 Charge transfer effect

The chemical effect is known to have a much weaker contribution than the pure electromagnetic effect (discussed in the chapter on introduction to SERS). Nevertheless, this effect is important to explain the change of the shape of the SERS spectra when the molecule is really adsorbed on the surface. Moreover, the chemical effect gains importance in the locations where the electromagnetic field is strong since one among the different contributions is the so-called photon driven charge transfer (PDCT). Among other contributions to the chemical effect, one is related to the chemical bonding interaction. The later depends on the adsorption configurations of the molecule on the surface. In particular, it depends if the molecule has a single bond with the substrate or if the adsorption configuration implies a double end adsorption. This effect modulates the enhancement of the different modes of vibrations depending on their symmetry. The SERS spectrum shape will be different for different configurations. The figure 5.19 shows the schematic of the charge transfer mechanism.

Even if such processes are very complicated and directly depends on the reporter as well as on the SERS substrate, I would like to introduce a little bit further the photon driven charge transfer effect. This effect implies that either the metal or the molecule borrows energy from the other, depending on the relative energies of the HOMO and Fermi levels on the one hand and on the Fermi and LUMO levels on the other hand. If one of them is close to the photon energy, then a resonant process can take place, from the molecule to the metal or the reverse. As in the case of resonant Raman scattering the theory predicts that the signal will result from three different contributions that depict the vibronic coupling [94]. The first

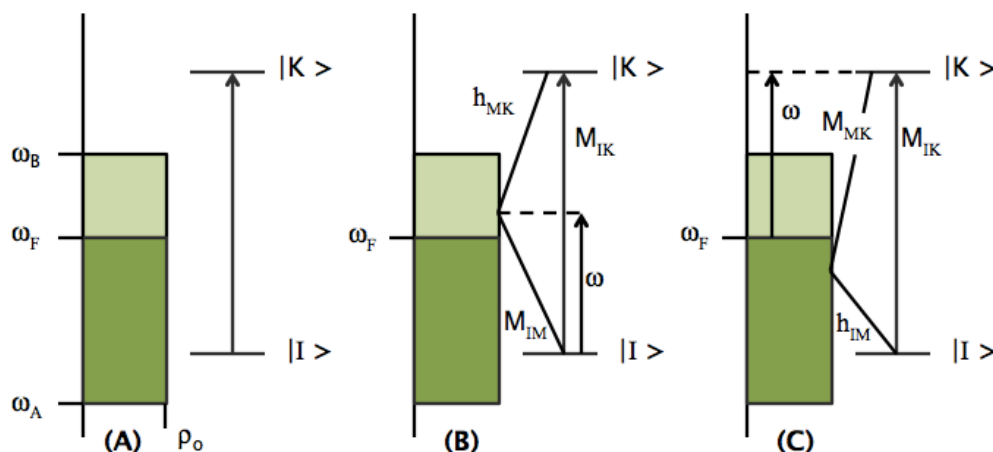


Figure 5.19: Energy level scheme for metal-molecule system. The left graph illustrates the energy levels of the allowed transition of the molecule ( $I$  and  $K$ ) and the conducting band of the metal filled from  $\omega_A$  to the Fermi level  $\omega_F$  and empty from  $\omega_F$  to  $\omega_B$ . The figure B describes the molecule to metal type charge transfer. The metal borrows energy from the molecule excited by the laser (frequency  $\omega$ ); The figure C illustrates the process in the case where the molecule borrows energy from the metal. Adapted from Lombardi et al [93].

one, known as the A term is the Franck Condon contribution. It is generally the dominant contribution when strong allowed transitions are excited. Only symmetric modes can be enhanced by this mechanism. The second contribution, known as B, corresponds to the Hertzberg-Teller contribution. It allows the enhancement of modes by vibronic coupling between a weakly-allowed transition and a nearby strongly allowed transition. Both symmetric and non totally symmetric modes can be enhanced. This term corresponds to the case where the transfer operates from the molecule to the surface (case B in Fig. 5.19). The last term also involving a Hertzberg-Teller contribution is generally weak compared to the two others. It corresponds to the case where the transfer operates from the metal to the molecule (case C in Fig 5.19). Consequently, the chemical effect cannot be neglected, as it often modifies the shape of the spectrum, even in pre-resonance situations.

### 5.11.3 Polarized hot-spot across the nanowires

Another case of SERS signature highly dependent on the excitation polarization has been observed, peaking when the excitation polarization is along V. The probability of finding such a location is not negligible. It occurs every 4 to 6  $\mu\text{m}$  when scanning a line with a 1  $\mu\text{m}$  step. Some examples of such signals are depicted at

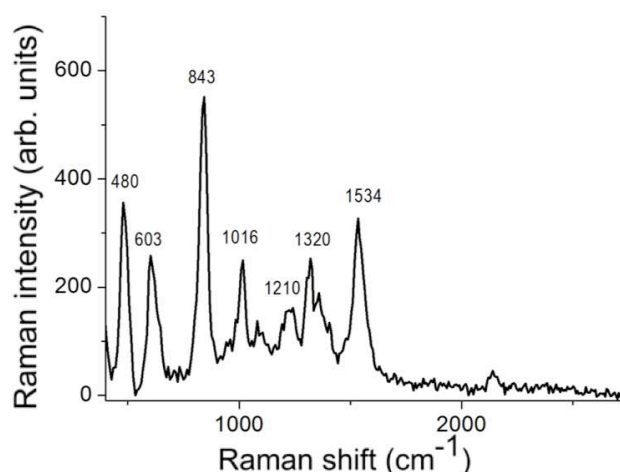


Figure 5.20: ATTO SERS Spectrum recorded with V orientation in the presence of rhodamine at 740 nm with an excitation power of 100  $\mu$ W for 6s.

different locations in the following. The first example is depicted in figure 5.20. The lines are strong and most of them are thin, which indicates the signature of a very few number of molecules. The signal is recorded with a polarization perpendicular to the average direction of the nanowires. Except for the missing high frequency mode at 1626  $\text{cm}^{-1}$  the spectrum shape in the range 1150  $\text{cm}^{-1}$  - 1535  $\text{cm}^{-1}$  is not very different from that obtained on single nanowires. The high frequency mode at 1534  $\text{cm}^{-1}$  has gained intensity and is slightly shifted to higher frequencies. On the contrary, the spectral shape is completely different in the range between 400  $\text{cm}^{-1}$  and 1150  $\text{cm}^{-1}$  where the intensity of the lines is much larger than expected and the frequencies systematically downshifted. The corresponding signal with an excitation oriented along H, only appeared as a very weak background resulting from the residue of unfiltered laser wing, with no SERS signature. Since the molecule is resonantly excited, a possible interpretation is that the low frequency modes are enhanced by a vibronic coupling, as observed in different molecules with aromatic cycles. Modes at 850  $\text{cm}^{-1}$  and 606  $\text{cm}^{-1}$  are observed in benzene for example, corresponding to an out-of-plane C-H mode and an in-plane ring deformation, respectively. Nevertheless, the relative intensities of the modes (especially the very strong line at 843  $\text{cm}^{-1}$ ) and their shifts cannot only be explained by SERRS mechanisms. In fact, ATTO 740 has been excited at resonance in the study on isolated nanowires and such enhancement has not been observed. As in the case of the preferential enhancement along the H direction, reported above, a reasonable explanation is the conjugation of SERRS and chemical enhancement. The molecule is located in a tiny hot-spot whose shape leads to a strong enhancement in the V direction. Moreover, the configuration of the

molecule itself in the hot-spot determines the relative enhancement of the different modes.

Another example is displayed in figure 5.21. The spectrum is very similar to that described just above. It indicates that the molecule sits in the same type of hot spot and that its configuration and binding to the surface is quite similar to the previous one.

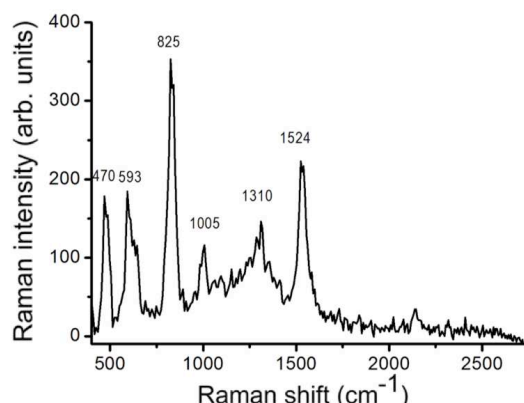


Figure 5.21: ATTO SERS Spectrum recorded with V orientation in the presence of rhodamine at 740 nm.

The two following spectra (figure 5.22) are rather different. Both the spectra are also obtained at 740 nm, in resonance with the molecule. The modes around 1500 - 1600  $\text{cm}^{-1}$  are quite broad and embedded in the increasing background. The spectrum is largely dominated by the signal of the modes of lower frequencies. The intensity of these lines is quite high, much higher than in the previous cases. These hot-spots prove that the sample present efficient active sites. However, the two spectra differ from each other.

The spectra in the figure 5.22 (right) does not present any line below 875  $\text{cm}^{-1}$ , in the low frequency domain, whereas in the case of the other figure 5.22 (left), the spectrum displays several lines in this domain. The dominant line at 1279  $\text{cm}^{-1}$  could be a result of the combination of the 443  $\text{cm}^{-1}$  and 833  $\text{cm}^{-1}$  modes. In both the cases the weak activity of the high frequency modes suggests that the polarizability components of these modes are quite far from being perpendicular to the surface. If these modes correspond to the in-plane stretching modes of aromatic cycles, it indicates that these cycles are rather parallel to the surface. Consequently, the most active modes should be out-of-plane modes. This can explain the shape of the second spectrum with many low frequency modes, generally not observed when the high frequency modes are active. The limited number of active modes in the first spectrum could be the result of a site where the molecule is quite distorted. In an interesting experiment Haran and his collaborators have

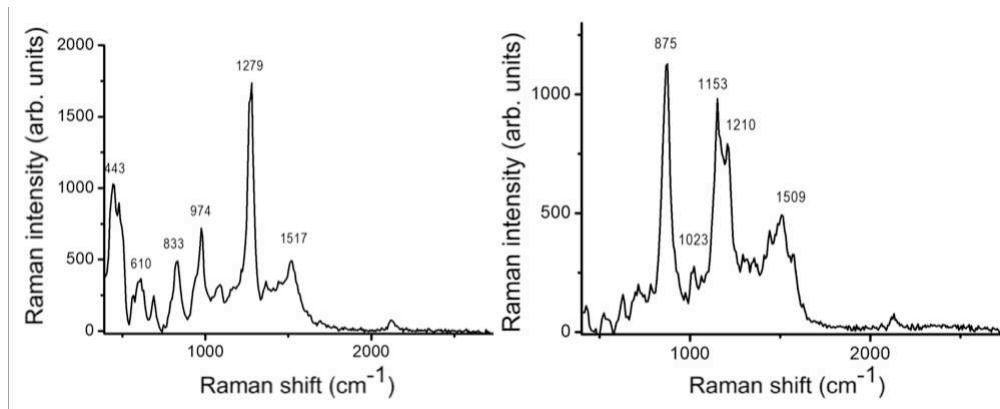


Figure 5.22: ATTO SERS Spectrum recorded with V orientation in the presence of rhodamine at 740 nm. They represent the different spectra that can be observed on the system, where there can be significant low frequency lines and also high frequency lines.

demonstrated that the size of the particles forming the gap play a role on the relative enhancement of the different modes [87]. As demonstrated in the simulation part, for a given gap, the plasmon resonance blue shifts when the dimension of the ellipsoids along the nanowire increases and vice and versa. The size of the particles forming the gap can be different in both cases.

In both the cases, the signal in the H direction is very weak as displayed in the figure 5.23, for the H configuration corresponding to the spectrum of figure 5.22, acquired in the V configuration.

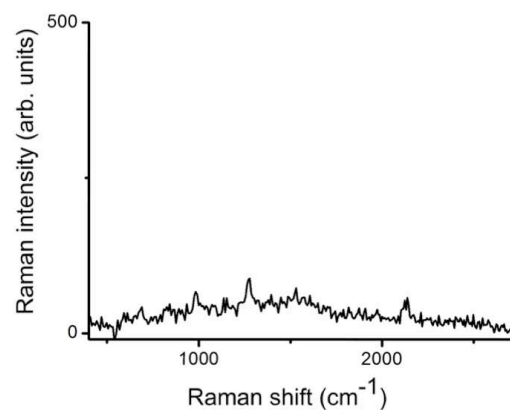


Figure 5.23: ATTO SERS Spectrum recorded with H orientation in the presence of rhodamine at 740 nm.

## 5.12 Wavelength dependence of SERS

The wavelength dependence of SERS is hardly investigated as such a study would require a tunable excitation source and appropriate filters. This has been explained in detail in the previous chapter on isolated nanowires. We have studied the evolution of SERS with wavelength on the nanowire arrays. It was not possible to make the dark field image since there was presence of gold particles on the sample as a result of sputtering. The figure 5.24 shows the plasmon of the sample recorded where the wavelength measurements reported here has been carried out. The plasmon has been recorded in the same way as with the isolated nanowires. It is seen that the plasmon peak is at 750 nm at the position of investigation.

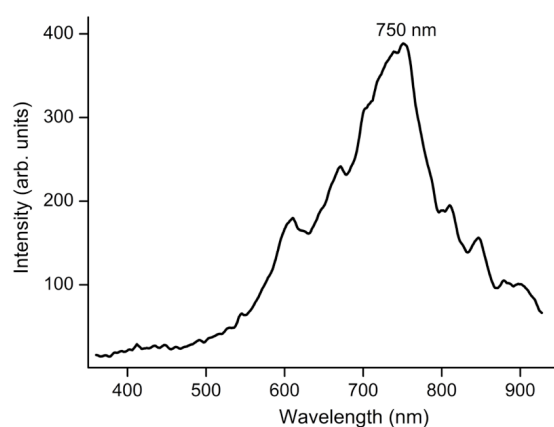


Figure 5.24: Plasmon spectrum of the sample at the analyzed spot.

The figure 5.25 shows the evolution of SERS with wavelength. Eight different wavelengths have been analyzed from 700 nm to 780 nm. The wavelengths were chosen in order to explore the regions beyond the resonance of the molecule on either side. Appropriate filters were used and care has been taken to cut off the excitation laser efficiently and to keep the excitation conditions equal at every wavelength. To make a careful comparison, only the lines that are observed in every wavelength has been taken. In the graph below only the lines between  $1450\text{ cm}^{-1}$  and  $1600\text{ cm}^{-1}$  have been considered and their intensities have been summed to get the true comparison graph. The excitation power has been kept constant at  $450\text{ }\mu\text{W}$  and the spectra have been recorded for 10 s each. Let us look at the evolution of the signal in the V direction (polarization across the nanowires). On increasing the wavelength from 700 nm, the signal gradually increases and peaks around 745 nm after which it drops. This is in accordance with the results of the isolated nanowires. As said earlier, it has been proven and is well known that the SERS is highly efficient when the excitation wavelength is between the plasmon

resonance and the resonance of the molecule. In this case the condition is satisfied and hence we have the highest efficient signal at 745 nm.

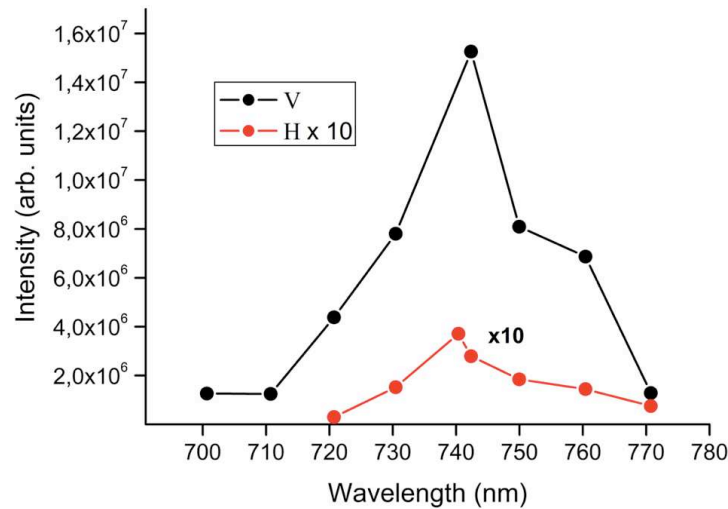


Figure 5.25: Evolution of SERS with the wavelength.

In the case of signal along H direction (along the nanowires), the trend is the same as that of the other polarization. However, the signal is very weak compared to the V direction. It is to be noted that the signal has been multiplied ten times here to plot both the curves in the same frame.

The figures 5.26 (a) and (b) display clearly the change of intensity of the SERS spectra with V and H polarization respectively. Though the signal in V direction it is decisively higher than the other, the signal in the H configuration is not zero. It could be because, the mean directions of the nanowires are not very rigid. This can be easily visualized if we understand the field present between two nanowires. We have calculated the field between two ellipsoids when they are excited with two mutually orthogonal polarization directions.

The electric field around the ellipsoids have been calculated using the DDSCAT [95] and plotted using the software Origin. The near-field at each dipole location results from the superposition of the field of incident wave and of the contribution due to all the other point dipoles at the given location. The calculation of the fields needs to solve  $N$  linear equations,  $N$  being the number of polarizable dipoles describing the structure. As a result the challenge is to develop a fast algorithm, such as the one proposed by Flatau and B. T. Draine.

The figure 5.27 shows the electric field around a single ellipsoid (80 nm x 200 nm x 20 nm) when it is excited with light having polarization along its short axis. The field has been calculated at the wavelength where the extinction efficiency is maximum. In short where there is the plasmon peak. The discretized appearance

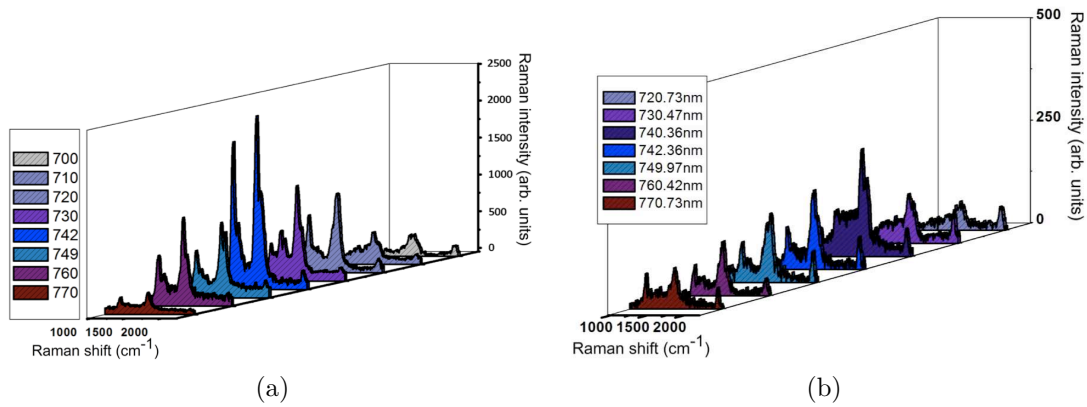


Figure 5.26: Evolution of SERS with wavelength when the excitation is (a) across (V configuration) and (b) along the nanowires.

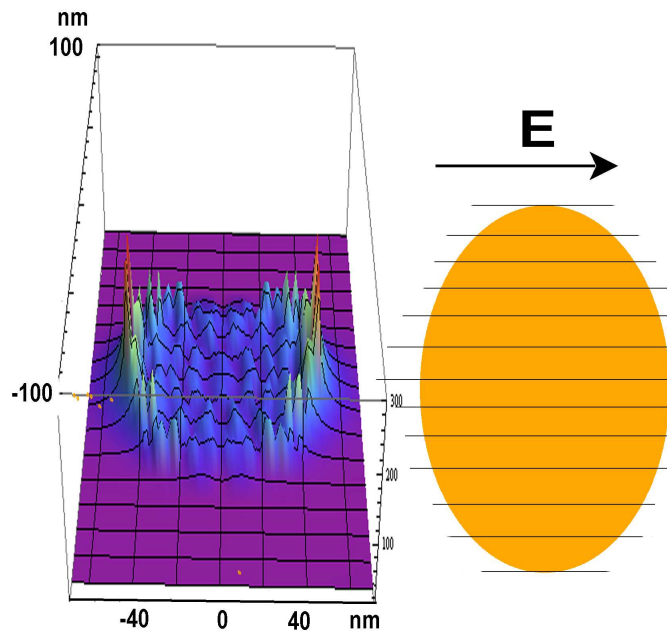


Figure 5.27: Simulation of the electric field around an ellipsoid with excitation along the short axis.

of the field is a result from the way the calculation has been performed. In order to limit the calculation time, the field has been calculated along a rectangular grid of points, with a spacing of 12.5 nm along the long axis of the ellipsoid and a spacing of 2 nm in along the direction of the field. Despite, the discretization, the field

map corresponds to a dipolar field as expected.

The figure 5.28 shows the near-field in a system of two ellipsoids (each 80 nm x 200 nm x 20 nm) when the excitation is across the nanowires. The distance between the two ellipsoids has been taken as 10 nm. It is seen clearly that from the figure that the field is highest at the gap between the ellipsoids which is expected. The

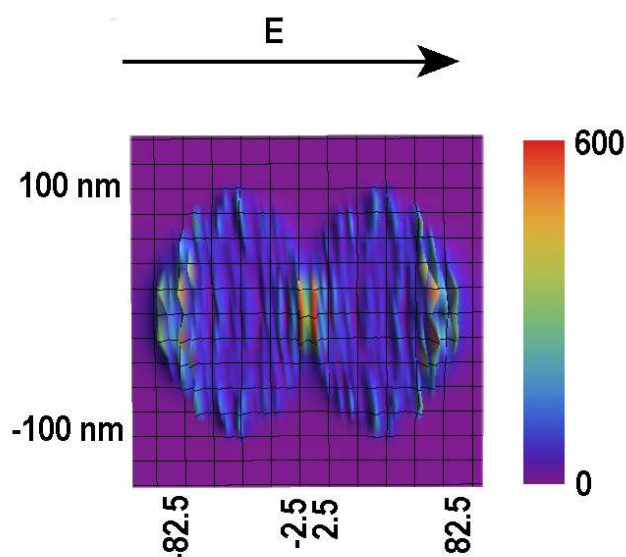


Figure 5.28: Simulation of the electric field around 2 ellipsoids with excitation in V configuration.

field is more confined than in the case of the single ellipsoid and the amplitude of the field is more than two times larger than in the previous case. This field amplitude will increase further as the gap is reduced. We can thus expect that if two nanowires are closely connected at a location, there will be a hot-spot at this location, where optical property could dominate the signal.

Finally, the figure 5.29 shows the electric field in a system of three ellipsoids (each 80 nm x 200 nm x 20 nm) when the excitation is along the nanowires. The two gaps between the ellipsoids is equal to 10 nm each. On this Fig.5.29 is also demonstrated, the array of dipoles used to calculate the field.

The field inside the gaps between the ellipsoids is even larger than in the case of two ellipsoids. At bottom is displayed the map of the field when the incident field is along the long axis. In this situation, there is no coupling between the successive ellipsoids and the field is much weaker compared to that in the V direction.

These calculations serve as a guide to explain the results described above. The field here has shown a strong polarization dependence. The SERS signatures depicted

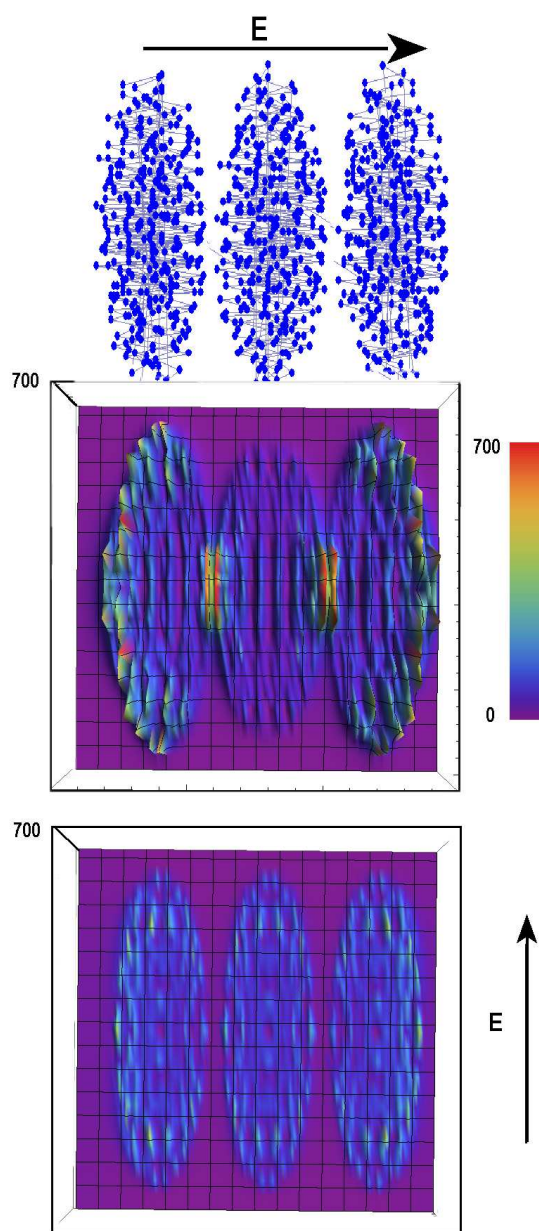


Figure 5.29: Simulation of the electric field around 3 ellipsoids with excitation in V configuration (top) and H configuration (bottom).

above could be those of molecules sitting in the gap between close connected nanowires. Such locations are demonstrated by the AFM image of the sample. Such highly polarized SERS signals contribute to the macroscopic response of the sample.

## 5.13 Synopsis

The heterogeneous gold substrate is of huge interest because biological tissues have minimum absorption in the NIR and SERS of these materials can best be performed in this spectral region, however, a substrate with NIR absorption is required. Few substrates utilized have been capable of this, however aggregated gold nanoparticles have strong NIR absorption. The development of SERS substrate such as this is potentially important for detecting biomolecules non-invasively which are necessary for many biomedical applications. Not only is there a strong NIR absorption in our samples but it is tunable by varying the aspect ratio.

We have shaped the response of the sample using two different analytes in line with the emerging field of molecular plasmonics. As a result the sample proves to be very interesting because it offers two different opportunities at least. They are related to the fact that the elaboration process creates simultaneously two patterns : an underlying rather well organized array of nanowires on top of which are a lot of particles of different sizes. We have different sites which offer the opportunity to understand different mechanisms. A number of such sites have been analyzed. The polarization dependence which is not clear with one molecule is much more evident in the second case. When sites are activated here with the help of two analytes co-deposited, our study demonstrates that on average the number of sites where a strong signature is observed along V is higher than the number of sites along H. Despite the large number of sites where SERS is very faint and does not display a clear polarization dependence, this result is on average in agreement with the macroscopic dichroism that has been observed.

The ATTO 740 which is unstable and inefficient changes for better in the presence of another analyte, Rh6G in our case. The presence of different modes of SERS presents an irrefutable evidence for us to understand the various contributions like charge transfer in such a system. These nanowire arrays cannot be really compared to the isolated nanowires. The arrays are important to understand some effects that cannot be visualized in the other case. Also, there is not a clear polarization dependence in the isolated nanowires. It could be due to the fact that the polarization dependence in that case depends on how the nanobead is coupled to the nanowire.

To summarize, between these two systems, the isolated nanowire and the nanowire arrays, and the co-analyte technique we have been able to investigate and understand a number of underlying mechanisms and contributions to the SERS.

---

*An expert is a man who has made all the mistakes, which can be made, in a very narrow field.*

Niels Henrik David Bohr

# 6

## SNOM

### 6.1 Introduction

As early as the 16th century, the ball was set rolling with the invention the microscope. The simple instrument created quite a revolution in biology by being able to visualize small organisms like the bacteria and blood cells. This simple instrument developed manifold in the following years enabling its use in various fields. However, the efficiency or the resolution of the microscope was limited by diffraction. This proved to be a big barrier to keep up with the ever growing (or rather ever shrinking) nanotechnology. Scanning near field optical microscopy was the savior in this situation coming up with an excellent combination of the power of optical probe and the potentials of scanning probe microscopy.

SNOM circumvents the diffraction barrier and allows in principle any kind of optical analysis to be carried out with sub-diffraction space resolution including absorption, photoluminescence and Raman scattering [96]. Imaging the sample within the near field of the probe gives a tremendous resolution when compared to other far field techniques like confocal microscopy.

### 6.2 Rayleigh criterion and diffraction limit

The resolution of an optical microscope is defined as the shortest distance between two points in an image of a sample that can still be distinguished as separate entities. Rayleigh criterion is generally applied to define this distance. The criterion

states that two points are resolved in an image when the first minimum of the Airy (diffraction) pattern of one point is aligned with the central maximum of the diffraction pattern of the other point.

In the 1870s, German physicist Ernst Abbe demonstrated that, due to the diffraction, lens-based microscopes are limited in their lateral resolution to

$$D = 0.61 \frac{\lambda}{n \sin \theta} \quad (6.1)$$

where  $D$  is the shortest distance between two points on a specimen that can still be distinguished as separate entities,  $\lambda$  is the wavelength of the light producing the image,  $n$  the refractive index of the medium separating the specimen and the objective lens, and  $\theta$  the aperture half-angle of the optical system.

Let us look at the optical image formation to understand better the diffraction limit and how to overcome it. Consider an object in a plane  $(x, y, 0)$  and a plane wave  $E$  incident on a transverse plane  $(x, y, 0)$  propagating in the positive  $z$  direction (fig. 6.1).

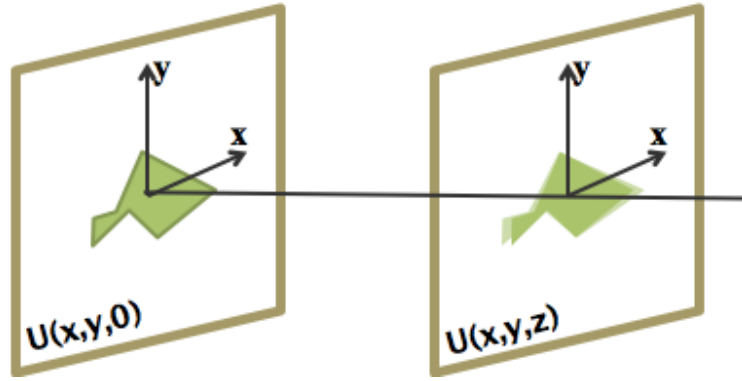


Figure 6.1: Optical image formation: field distribution at  $z$  due to the field at  $z=0$ .

The 2-dimensional Fourier transform of the electric field in the plane of the object  $(x, y, 0)$  is:

$$\vec{E}(f_x, f_y) = \int_{-\infty}^{+\infty} \int_{-\infty}^{+\infty} \vec{E}(x, y, 0) e^{-2\pi i(f_x x + f_y y)} dx dy \quad (6.2)$$

In this equation  $f_x$  and  $f_y$  are spatial frequencies of the plane structures, which can generally take any value between 0 and  $\infty$ . Thus,  $\vec{E}(x, y, 0)$  can be written as the inverse Fourier transform of its frequency spectrum:

$$\vec{E}(x, y, 0) = \int_{-\infty}^{+\infty} \int_{-\infty}^{+\infty} \vec{E}(f_x, f_y) e^{2\pi i(f_x x + f_y y)} df_x df_y \quad (6.3)$$

The field at the object can therefore be regarded as a superposition of plane waves propagating in the direction determined by the wave-vector  $\vec{k} = (k_x, k_y, k_z) = (\alpha, \beta, \gamma) \frac{2\pi}{\lambda}$ , with the direction cosines:

$$\alpha = \lambda f_x, \quad \beta = \lambda f_y, \quad \gamma = \sqrt{1 - \alpha^2 - \beta^2} \quad (6.4)$$

Similarly to equation 6.3, the electric field for  $z > 0$  is given by

$$\vec{E}(x, y, z) = \int_{-\infty}^{+\infty} \int_{-\infty}^{+\infty} \vec{E}(f_x, f_y, z) e^{2\pi i(f_x x + f_y y)} df_x df_y \quad (6.5)$$

In homogeneous, isotropic and linear media the E field has to satisfy the Helmholtz equation  $\nabla^2 \vec{E} + k^2 \vec{E} = 0$ . Direct application of this requirement to equation 6.5 leads to the following solution:

$$\vec{E}(f_x, f_y, z) = \vec{E}(f_x, f_y) e^{2\pi i z \sqrt{\frac{1}{\lambda^2} - f_x^2 - f_y^2}} \quad (6.6)$$

In this equation,  $\vec{k} = 2\pi/\lambda$  is the magnitude of the wave-vector  $\vec{k}$  of the propagating wave. The combination of equations 6.6 and 6.5 gives the value of the electric field for  $z > 0$ :

$$\vec{E}(x, y, z) = \int_{-\infty}^{+\infty} \int_{-\infty}^{+\infty} \vec{E}(f_x, f_y) e^{2\pi i(f_x x + f_y y + z \sqrt{\frac{1}{\lambda^2} - f_x^2 - f_y^2})} df_x df_y \quad (6.7)$$

Two cases can be distinguished:

1.

$$f_x^2 + f_y^2 > \frac{1}{\lambda^2} \quad (6.8)$$

: the argument of the exponential function in equation 1.6 is imaginary, corresponding to a wave that propagates in the  $z$  direction towards the observation plane.

2. The equation 6.6 can be rewritten as

$$\vec{E}(f_x, f_y, z) = \vec{E}(f_x, f_y) e^{-2\pi z \sqrt{f_x^2 + f_y^2 - \frac{1}{\lambda^2}}} \quad (6.9)$$

The argument of the exponential function in the equation 6.9 is real. As a consequence, the amplitude of the wave decreases exponentially in the  $z$  direction. For low spatial frequencies, the waves propagate in the  $z$  direction towards the observation plane. These components are the far-field components of the angular frequency spectrum. The high spatial frequency

components are only present near the sample and decay exponentially in the  $z$  direction.

In conventional optical microscopy, lenses with a limited numerical aperture ( $NA = n \sin\theta$ ) are placed in the far-field. Consequently, only waves propagating with their  $k$ - vector within the NA will reach the detector.

Equation 6.9 reveals that waves containing the high spatial frequency information of the object do not propagate but decay exponentially away from the object. Thus essentially to get an high resolution we need to have access to the high frequency components which will be seen in the next section.

### 6.3 Breaking the diffraction barrier

With the Abbe's diffraction limit it is seen clearly, the resolution is limited to the order of wavelength of light. For example, in the visible range of wavelengths (400 - 700 nm) using the confocal techniques with this diffraction limit the maximum resolution that is attainable will be around 250 nm. To attain a true nanometer resolution, the diffraction barrier should be overcome.

As we have seen in the previous section, the diffraction limit becomes less of a deterrent if the concept of free wave propagation is abandoned and evanescent waves are used. Evanescent waves are characterized by amplitudes that decay rapidly into at least one direction in space. Strong evanescent waves are excited preferentially at the boundary of two different media. Due to their rapid decay, they are of importance only close to the interface. Therefore, these fields are called near fields. The diffraction limit is circumvented completely by performing the experiments with the optical source or the detector held much closer to the sample than the wavelength of the light. In this near field regime, the resolution that is attained is defined not by the wavelength of light but by the size of the source or the detector. This could be achieved by combining optical spectroscopy with the scanning probe microscopy. The SNOM exploits the optical interaction between a probe and the sample to investigate surfaces with a resolution far higher than that of traditional optical microscopy techniques.

### 6.4 Why SNOM?

With the rapid growth of the nanotechnology, there is a great need for the knowledge of exact size, shape and other physical properties of the nanostruc-

tures. The conventional microscopes are limited by diffraction and so their spatial resolution is not up to the mark. The shift to electron microscopes for better spatial resolution brings up other problems like their inefficiency in analyzing the optical properties.

SNOM on the other hand, has exceptional characteristics that makes it stand apart from other techniques and also very useful. It is non destructive in nature and relatively cheaper compared to the other techniques. The SNOM allows you to study the optical properties of the system. Spectroscopic studies with a lateral resolution reaching tens of nanometers is possible with SNOM. With the SNOM, there is a simultaneous acquisition of both topographical and optical characteristics of a system which helps to relate the optical property to the morphology on a local scale.

The most important feature of SNOM is its versatility. It could be used in a number of configurations depending on the analysis to be done. In short SNOM is a practical and efficient tool that can be used in various fields like chemistry, physics, biology and materials science.

## 6.5 A brief history and evolution of SNOM

"A Suggested Method for extending Microscopic Resolution into the Ultra-Microscopic Region" - This paper published by E.H. Synge in 1928 [97], is the very first idea conceived about SNOM. He envisioned an experiment that would have a sub-wavelength resolution. He proposed to use a small aperture to image the surface at the nanometer level. He suggested to use a pinhole in a metal plate or a quartz cone that is coated with metal except at the tip for the small opening. He also proposed to record the images point by point by detecting the light transmitted by the sample with a sensitive photodetector. He discussed his theory with Einstein who pointed out the difficulties with the experiment and helped him develop his ideas. In 1932, Synge published another paper [98] where he suggested the use of piezo electric actuators to scan the aperture at a few nanometers from the sample with great precision.

In 1956, J. O Keefe [99], a mathematician proposed the concept of near field microscopy without knowing about Synge's earlier papers. He detailed the practical difficulties that could be faced in realizing this design but did not give any solution.

Forty four years after Synge's paper, in 1972, the first near field experiment was published by E.A. Ash and G. Nichols. They demonstrated an aperture type near-field experiment in the micro-wave region ( $\lambda = 3$  cm), showing a

resolution of  $\lambda/60$ . This was the first experiment that proved the validity of Synge's proposal and showed promise for the future.

In 1984, Pohl and his coworkers at IBM Zurich took the next important step. They published the first near field experiment in the optical domain [96, 100]. They made the first SNOM instruments that worked with the visible light. They used a metal coated quartz tip which was pressed against a surface to create an aperture. Around the same time, the possibility of such SNOM was also reported by A.Lewis et al [101].

In 1991, Betzig et al [102] introduced the single mode optical fibers as near field optical probes. This is used till date. From then on, the SNOM has evolved at a rapid rate. The efficiency of the SNOM has improved greatly with the use of different probes and different applications have been realized. The present day SNOM is used with different configurations to suit the experimental needs.

## 6.6 Basic working principles of SNOM

A typical SNOM setup, as it is realized in many laboratories and commercial instruments, consists of these primary components: light source, feedback mechanism, the scanning tip, the detector and the piezoelectric sample stage. Laser light of a suitable wavelength is coupled into an optical fiber that has a probe (apertured or not depending on the experiment) at its far end. Control of the polarization and spectral filtering of the light can be necessary before coupling into the fiber. A strongly gapwidth-dependent signal is used to measure and control the gapwidth between tip and sample. This is done with the help of shear force feedback which will be explained in the next section.

In the case of emission-mode SNOM, light that is emitted by the aperture locally interacts with the sample. It can be scattered, absorbed, phase shifted, or locally excite fluorescence, depending on the sample and the contrast mechanism of interest. The light emerging from the interaction zone is collected with the highest possible efficiency. For this purpose, high NA (oil immersion) microscope objectives or mirror systems are often used. The collected light is directed via a (dichroic) mirror either to a visual inspection port of the microscope or to a suitable detector. Filters can be inserted to remove unwanted spectral components. Standard optical detectors, such as avalanche photodiode, photomultiplier tube (PMT) or CCD, are used.

## 6.7 Shear force

In order for the near field to interact with the sample surface, the probe tip has to be maintained very close to the sample at a constant distance of less than 10 nm (typically). The most commonly used technique to control this distance is the shear force feedback. It was realized by Betzig [103] and Toledo-Crow [104] almost at the same time. The shear force is a short-range force and its intensity is significant only up to a few nanometers from the sample. In the shear force set up, the fiber is fixed to a dither piezo and the short part of the tapered end of the probe extends outside the dithering element. Resonant lateral oscillations are induced in the tip by applying an AC voltage to the dither piezo and the probe tip is brought close to the sample. It is seen that, when approaching the sample, that is at a distance of few nanometers, the amplitude of the oscillation decreases. This decrease is generally attributed to the damping of the oscillation by the shear forces at the surface. Being often there to be glued onto a piezoelectric transducer (a quartz tuning fork), the damping in the oscillation is experienced also by the tuning fork, which generates a piezo electric voltage proportional to the amplitude of oscillation. This is used as a feed back to control the movement of the tip in the z-direction to have a constant tip sample distance. Typically, the best results are obtained with 10 % damping with respect to the amplitude of free oscillations (tip far away).

## 6.8 Experimental Set up

For our measurements the SNOM has been used in the collection mode. This means that the probe, rather than being used as a near field emitter serves as a near field collector and illumination is provided in the far field. The set up is based on a three axis nanopositioner (Physik Instrumente PI 517.3) which allows for a maximum travel of 100  $\mu\text{m}$  and 20  $\mu\text{m}$  in the lateral and vertical directions, respectively. The tablet, low-voltage driven by a Physik Instrumente controller (PI Series 500), operates in closed-loop, preventing hysteresis and non-linearity typical in piezoelectric translators. This ensures efficient repeatability of the scans. The sample is placed on the tablet, which owing to its large size, gives complete accessibility to the sample and hence its precise positioning.

The near field probe is of the aperture type, consisting of a tapered optical fiber (Lovalite) with a nominal aperture of 50 nm. The probe tip is approached to the sample by means of a PI mechanical translator and then

kept in the near field range (tip-to-surface distance below 10 nm). The constant distance between tip-to-surface and sample topography are obtained through the shear-force method, as described earlier. The probe is preliminarily glued to a quartz tuning-fork and the assembly is held by a custom made probe holder equipped with a dithering piezoelectric slab. The dithering piezo is put in oscillation by a function generator and the signal produced by the tuning-fork is duly amplified by a preamplifier and sent to an analog lock-in referenced to the oscillation. The output of the lock-in represents the actual oscillation amplitude and hence depends on the tip-to-sample distance. It is sent to the microscope controller (RHK SPM 1000) in order to drive the feedback circuitry. The figure 6.2 gives the schematics of the set up.

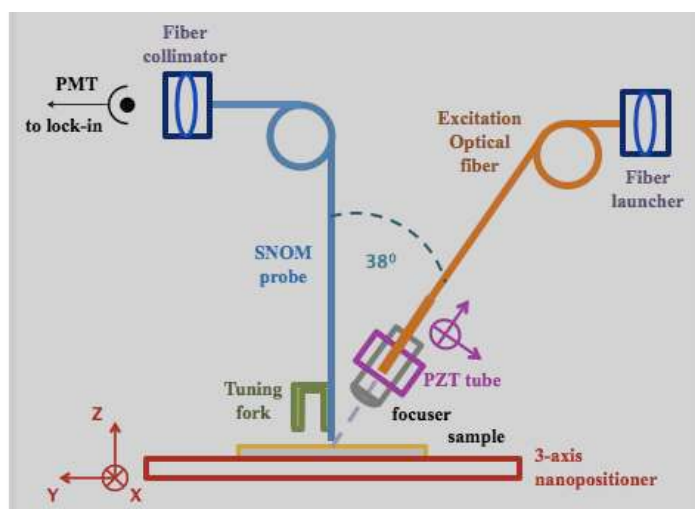


Figure 6.2: Sketch of the SNOM set up.

The most crucial part of the instrument is the one devoted to the excitation. The excitation set up employs a custom made assembly (Oz-Optics) composed of a focuser and a single-mode optical fiber. This illumination source produces a quasi-diffraction-limited spot with a diameter on the order of 2-3  $\mu\text{m}$  in the operating conditions of the experiment. The focuser axis forms an angle of 38 degrees with respect to the probe axis. The compactness and light weight of the assembly enables integration with a hollow-tube piezoelectric translator (PZT), of the kind frequently used in force microscopes. In addition, a set of manual or electrically actuated mechanical micrometer translators allows precise positioning relative to the tip with a space resolution reaching the sub-micrometer range.

The probe optical fiber is coupled to a photomultiplier (Hamamatsu R2658),

which provides a sufficiently large amplification considering the very small power collected in the near field. Noise is suppressed by using synchronous detection referenced to amplitude modulation of the laser light and a dual digital lock-in (Stanford Research SRS830DSP) is employed.

A useful feature of the system is the ability to perform the scans in two distinct modes. The availability of low-voltage and high-voltage outputs in the microscope controller enables the PZT to be driven by the same controller as the sample scanner. In this way, lateral (XY) motion of the sample and of the excitation spot can be made synchronous each other, the probe tip being fixed in the laboratory frame.

### Constant excitation mode

This first configuration is designed to get constant illumination conditions during the scan. It is realized by disconnecting the PZT and by duly adjusting the spot position below the probe tip. It is used to analyze the map of the near-field intensity upon constant illumination conditions. Local field enhancement effects following resonant plasmon excitation have been directly imaged and mapped to the local morphology.

### Fixed excitation mode

In the fixed excitation mode the excitation spot position is fixed with respect to the sample. It is obtained by connecting the PZT to the microscope controller. By properly using the micrometer translators, this operation mode allows to select a predefined excitation position on the sample surface, which is maintained during the scan. It is aimed at observing phenomena related to spatial decay of excitation, for instance, in the propagation and damping of surface plasmon polaritons. Propagation of the excitation mediated by collective plasmon resonances, as well as by possible surface plasmon polaritons sustained by the quasi-continuum gold layer are studied in our case using this system [105].

The samples have been analyzed with two different lasers, green ( $\lambda = 532$  nm) and red ( $\lambda = 690$  nm). The motivation is to explore the optical behavior in two different spectral positions, that, according to the macroscopic characterization, enables exciting the LSPR in different parts of its spectrum. In the first part of the experimental procedure, the two wavelengths have been explored in the same scan due to the possibility to switch on and off

separately the laser beam synchronously with the forward (green) and backward (red) scan of the raster pattern followed by the probe. This has been accomplished with the help of a pair of simple electromechanical shutters placed in the optical path of the two laser beams, controlled by a dedicated signal produced by the electronics of the instrument.

The scans have been repeated by using the same linear polarizations for both lasers, either parallel or perpendicular to the nanowire axis. To achieve this, the polarization of the laser beam has been controlled prior to coupling to the optical fiber which delivers the radiation to the sample, by means of a quarter wave plate followed by linear polarizers.

---

*The outcome of any serious research can only be to make two questions grow where only one grew before.*

Thorstein Veblen

# 7

## SNOM measurements - Nanowire arrays

### 7.1 Introduction

In this chapter, I present a selection of the results of the near field measurements carried out on the gold nanowire arrays. Different samples have been analyzed using the collection mode SNOM, which has been explained in detail in the previous chapter.

The main goal of these measurements is to map the near field intensity distribution at the sample surface while it is illuminated at different wavelengths and polarizations. The configuration mimics experiments where the sample is used as a substrate, illuminated from the top by a far field. To achieve this, the “constant excitation mode” has been used, ensuring that the illumination conditions do not change during the scan. The primary motivation of the experiment is in fact to detect spatial inhomogeneities in the near field intensity map as a function of the properties of the light used to illuminate the sample.

Owing to its unique capability of measuring the near field intensity in the vicinity of a surface, SNOM in collection mode is in principle an excellent tool to identify the sites of local field enhancement (hot-spots) and to locate them

relative to the sample morphology. Indeed, collection mode SNOM has been frequently used for this purpose in the last decade [106], especially for quasi-continuous metal films featuring a close-packed array of randomly distributed nanoparticles [107, 108, 109, 110, 111, 112, 113]. There are however a few important aspects, well discussed in the literature, which must be carefully taken into account when using the SNOM for visualizing hot-spots.

- The electric field enhancement due to plasmon resonances depends dramatically on the distance from the surface. When plasmon resonances are exploited as an enhancement vehicle for SERS purposes, the adsorbed molecules, being typically at a distance of a few nanometers, or even less, from the metal surface, can fully feel the effects of the enhancement. This can lead to measure huge enhancement factors. On the contrary, typical enhancement factors found in SNOM analysis are of an order of magnitude, or even smaller. This is easily explained by considering that, in typical operating conditions, the SNOM probe scans the surface at a distance of several nanometers.
- When corrugated samples are investigated, as in our case, the large physical size of the probe apex prevents to precisely follow the topography modulation. As a consequence, the probe to surface distance gets even larger values when nanosized grooves, or valleys, have to be analyzed. This can further decrease the recorded near field intensity, smearing out the enhancement.
- There is a general consensus that the spatial resolution of an apertured-SNOM is ruled by the size of the tip aperture, i.e., 50 nm (nominal) in our case. The collected signal is obviously averaged over such a size scale. Strong nanosized hot-spots can result in broader and weaker features.
- The quantitative evaluation of the enhancement factor requires to set a reference value against which the enhancement is calculated. In SERS experiment this can be accomplished by repeating the measurements on a reference substrate, where the same molecules are adsorbed with similar concentration. In some cases, the reference value can be chosen unambiguously also in SNOM measurements, for instance when dark field illumination is used, such as in Photon Scanning Tunneling Microscopy (PSTM) configuration, and when the sample shows well defined regions where metal nanoparticles are absent [110]. However, in our experiment there is no way to identify the reference value. In fact, the sample surface is completely coated by the metal (with a spatially modulated thickness) and the specific illumination configuration makes

scattering to heavily contribute to the recorded signal.

For such reasons, determination of the enhancement factor at the local scale is a cumbersome task which prompted the researchers to find statistical tools able to detect the field enhancement even in the presence of small local variations of the near field intensity. Such statistical tools will be used in our analysis along with an attempt to quantify the relative enhancement factor and to correlate the occurrence of the hot-spots with the local morphology of the samples.

## 7.2 Constant excitation mode

The measurements in this section have been taken with the constant excitation mode explained earlier, where the excitation spot, focused onto a diameter on the order of 2- 3  $\mu\text{m}$  (fwhm), is constantly directed to the region probed by the tip which collects the near field. For this purpose, the spot is centered with respect to the probe carefully. The various micrometer screws of the tablets allow the precise alignment of the spot to maximize the collected near field signal. The operation is done in the approach condition to avoid misalignment due to spurious phenomena such as diffraction and direct coupling of the light with the probe.

In our setup, the geometry of the illumination is rather specific. Most of the literature appeared so far on the near field analysis of metal nanostructures exploits either excitation of surface plasmons (e.g., through evanescent waves, in the PSTM configuration [107, 108, 110]) or configurations where light is sent to the back of the (transparent) substrate [112, 114]. Illumination/collection mode, where the apertured probe serves at the same time as near field emitter and collector, is reported as well [111, 113] in the literature dealing with local optical analysis of nanostructured metal samples.

In our experiment, the far field is directed onto the top of the surface, along an oblique direction at  $\approx 38$  degrees angle with respect to the normal. Ideally, this arrangement allows getting rid of issues related for instance to coupling of the evanescent waves with the nanostructure, relevant in PSTM, and absorption/extinction of the radiation by the material, occurring when illumination is made from the bottom. Both issues are potentially able to mask or affect the near field map at the sample surface, hence preventing their occurrence can lead to maps acquired in “truly” constant illumination conditions. On the other hand, the configuration is accompanied by several crucial aspects, the most important being the possible shadow effects due

to the interaction of the far field light with the probe. In fact, the large physical size of the tip (featuring an overall diameter on the order of 300-500 nm) prevents the illumination light to directly reach the sample surface. This may result in shadowing effects, typically reflected in the appearance of strong topographical artifacts (collected optical signals fully correlated with topographical slopes). Such effects, which are expected to be almost independent of polarization and wavelength, turn obviously to depend on the mutual alignment of the spot and the tip, which has been carried out in order to minimize them. It must be also noted that, in the actual operating conditions of SNOM in collection mode, the interaction between the illumination radiation and the surface can involve mechanisms different from those of the ray optics used in conventional microscopy. For instance, interaction of the sample with the near field locally scattered by the probe [115], in particular at its borders, could occur due to the very short probe to sample distance (below 10 nm, in typical operating conditions). Moreover, the metal coating of the probe could lead to local enhancement effects, not too different from those used to achieve very high spatial resolution in tip-enhanced microscopy [116].

As usual for this kind of experiments (see, for instance, [106, 110, 111]), scans of the same region have been carried out by using two different excitation wavelengths, in the green (semiconductor laser at 532 nm) and red (diode laser at 690 nm) portions of the spectrum, respectively. In order to save time and ensure reliable comparisons, green and red laser radiations are switched on and off alternatively synchronously with the forward and backward directions of the raster scan. The rationale for using different wavelengths is to highlight any effect related to (wavelength-dependent) excitation of plasmon resonances. The best way would be to vary continuously the wavelength for reconstructing the optical response of the sample on the whole spectrum, as customarily accomplished in extinction spectroscopy for, e.g., colloidal solutions of metal nanoparticles, but this is very cumbersome in the world of near field microscopy, because of the need for high power and good beam collimation to couple with single-mode optical fibers.

Two different directions of polarization have been investigated in subsequent scans. The presence of mutually aligned patterns of nanowires makes the optical properties highly dependent on the polarization [117]. This is well confirmed by the polarimetry measurements carried out with conventional optics [10, 118, 119], hence space-averaged over a region much larger than the typical inter-wire period (that is around 100-150 nm). Therefore, we expect a marked dependence of the near field intensity map on the polarization, which is switched between the two directions orthogonal and parallel to the

nanowire axis. Such directions are set according to the reference directions established in the fabrication procedure, related to the gross (space-averaged) orientation of the nanowires. Due to their irregular features, the direction of the polarization may vary up to 20-30 degrees with respect to the actual (local) orientation of the nanowire axis. Moreover, comparison of maps acquired upon different polarization directions, recorded in distinct, subsequent scans, requires care to compensate for the spatial drifts of the sample, which can slightly slip over the microscope platform in the re-positioning step (at the end of the scan). Compensation can be easily accomplished by looking at topographical features.

Figure 7.1 demonstrates the effects of this kind of drift: topography features highlighted in the figure appear clearly shifted by a certain quantity ( $\sim 500$  nm, in this case) in the subsequent scan. The same occurs to the features of the optical map. The figure also demonstrates another typical aspect of our measurement, that is the weak signal-to-noise ratio. Weakness of the signal is inherently related to the use of near fields. Neglecting the above mentioned possible shadowing effects, the region below the probe is illuminated with a power typically on the order of a few  $\mu\text{W}$ , which is only partly scattered in the near field. The limited throughput of the optical fiber probes (typically  $10^{-4} - 10^{-6}$ , mainly depending on the actual aperture size) and additional loss mechanisms (e.g., coupling with the detector), make the radiation intensity impinging onto the detector rather small. Typically, the signal read by the detector, a general purpose photomultiplier tube (Hamamatsu R955), corresponds to an average power in the range 10-100 pW, depending on the experimental parameters of the scan. A lock-in amplifier is used to improve the signal-to-noise ratio, referenced to a ( $\sim 1$  kHz) modulation of the laser amplitude. The noise floor of the electronics is below 10% of the signal of interest (neglecting other possible sources of noise, such as spurious light reaching the detector, which have been carefully suppressed by due shielding).

In order to allow for quantitative comparisons, the power sent onto the sample surface has been kept constant (within 10%), independently of polarization and wavelength. To achieve this, an optical chain comprising of waveplates and neutral density filters has been developed and used. Since an optical fiber is exploited to direct the illumination light onto the sample, the (originally) linear polarization of the laser beams can get deteriorated. We have assessed that the extinction ratio (the ratio between the power measured using a polarizer rotated along one or the other orthogonal directions) is at least 10:1 (or better).

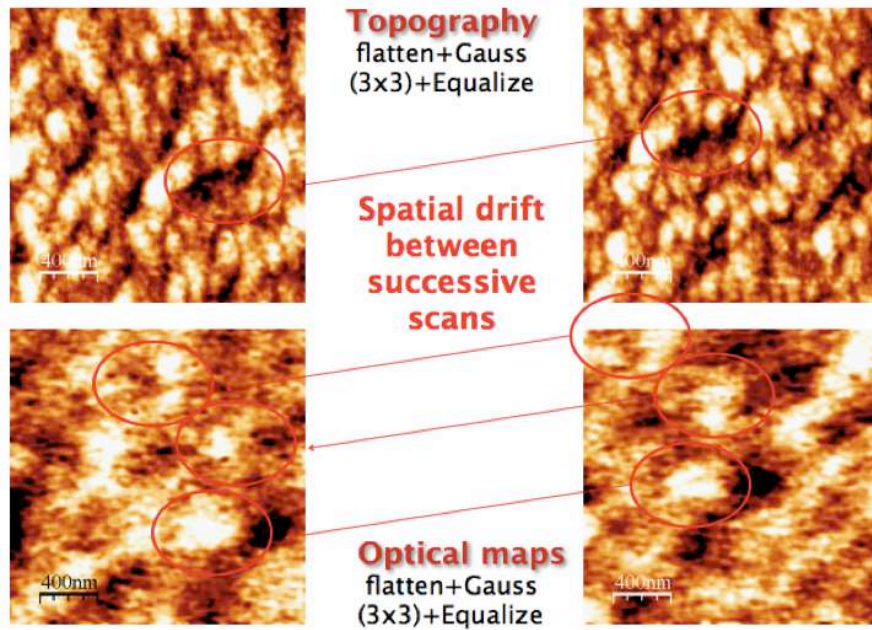


Figure 7.1: The topography and optical maps recorded in successive scans. The system shows good repeatability (taking into account the spatial drift).

### 7.2.1 Produced maps

Each measurement consists of two subsequent scans and produces a total of eight maps (neglecting additional maps such as, the error signal of the topography or the phase of the demodulated optical signal, not essential for our studies): four topography maps, two optical maps at one polarization direction and two distinct wavelengths (green and red), two optical maps at the orthogonal polarization. There is redundancy in the topographical information, so for each polarization choice we will consider only one topography map (the forward and the backward scans being very similar each other).

Topography, produced through the shear-force method, is representative of the sample morphology which is correctly reconstructed in all scans: all topography maps are in fact similar to the AFM images on the same samples. Features sized in the few tens of nm range are typically discerned. The dynamics of the topography maps, i.e., the maximum detected height, is generally smaller than the expected thickness of the film, evaluated on the basis of the nominal film thickness calculated for the duration of the deposition process. This can be ascribed to the impossibility for the used (large) probe to fully penetrate inside the inter-wire regions.

The optical maps represent the spatial distribution of the intensity at (or

close) the surface of the sample. Therefore, they are expected to contain specific information on any localized increase in the field and any other phenomena related to plasmon excitations. In general terms, in a metal nanostructured sample the optical maps are ruled by scattering of radiation. Scattering in the far field, which is typically analyzed in conventional experiments, will contribute to the observed maps as well. However, owing to the small size of the apertured probe and to the close distance to the surface, far field effects are expected to give a minor contribution. This is confirmed by the circumstance that the contrast in the optical maps strongly deteriorates when the tip is raised from the sample surface. Scans intentionally carried out without having approached the probe to the surface show no sub-wavelength features, being dominated by a weak, broad and poorly contrasted background.

Scattering in the near field is thus expected to be the dominant mechanism ruling the spatial distribution of the optical maps. There is a wide literature on the acquisition of near field maps from metal nanoparticles or nanostructures featuring plasmon resonances (see, for instance, [120]); since from the first observations (see, for instance, [121]), the results stimulated a huge interest for potential applications in the area of the so-called plasmonics [23]. When nanostructured surfaces are investigated, single or multiple scattering events can occur, depending on the mutual distance between individual scatterers and on the morphology of the sample. Multiple scattering effects, where the collective response of different localized plasmon resonance is involved, are of paramount importance for the applications, owing to their ability to “manipulate” the radiation in a sub-wavelength size scale [122].

The possibility to correlate topography and optical maps, a unique feature of SNOM, is also a key point in assessing localized plasmon resonances and in interpreting the origin of the local optical properties. Since in our experiment, topographical and optical features are measured with distinct integration times, ruled by the time response of the feedback and of the lock-in amplifier connected to the detector, respectively, they do not appear simultaneously, i.e., corresponding to the same point of the raster scan. Typically, the lock-in amplifier used for the optical channel has been set to a 100 ms integration time, longer than the time needed for the raster scan to travel from one point to the next one. The choice of the integration time and of the line speed was in fact a compromise between the need for a sufficiently long integration time, hence a better signal-to-noise ratio, and the impossibility to reliably operate the SNOM for too long times, due do unavoidable drifts of the mechanical and optical components occurring in the long term (few hours). The problem has been fixed in the post processing, where the

lag between topography and optical maps has been evaluated with a  $\pm 0.5$  pixel uncertainty thanks to the comparison of forward and backward scans acquired in the same experimental conditions. Finally, we cannot rule out the possibility of non-perfectly cylindrical symmetry in the probes, which might lead to a systematic shift between optical and topography maps. The occurrence of such a problem was controlled by checking the overlap between topography and optical maps in samples with almost point-like defects, and properly corrected in the presented measurements.

### 7.3 Sample 1

This sample is made by the off-axis metal deposition onto ion-beam pre-patterned glass substrates [118, 123, 119]. Therefore, the metal impinges onto a rippled dielectric substrate and shadow effects lead to a metal pattern resembling the rippled structure. The thickness of the metal deposition is around 20 nm (nominal). Figure 7.2 shows the AFM image and the macroscopic transmission curves of the sample, recorded at polarization parallel and orthogonal to the nanowire axis. It shows a rather broad absorption peak at the orthogonal polarization which can be attributed to the LPR. The wavelengths used in the SNOM analysis fall both within the broad resonance, but the dichroic ratio (i.e., the normalized ratio between transmission for light polarized along two mutually orthogonal directions) is rather different, being  $\gamma_{green} \approx 0.2$  and  $\gamma_{red} > 0.4$ . This definitely indicates that the red excitation falls well within the plasmon resonance of the sample.

Figure 7.3, shows an example of the set of maps produced in the experiment. Presented data are almost raw, since a minimal post processing has been applied. In particular, as customarily accomplished in scanning probe microscopy, data have been treated with a flatten filter (an algorithm, provided by a freely available software [124], which is intended to remove unavoidable planes in the map and to mitigate effects of long term drifts) and Gaussian-smoothed in order to prevent oversampling artifacts and match the point-to-point distance with the actual spatial resolution of the instrument (expected to be  $\sim 50$  nm owing to the aperture size). We did not find a dramatic dependence of the results on the data treatment in any case. We remark that, as a consequence of the flattening, the optical maps are referenced to the average value (indicated as zero in the color scales, measured in units of photocurrent). In other words, the maps are representative of local variations of the near field intensity.

The two topography maps (corresponding to subsequent scans) are affected

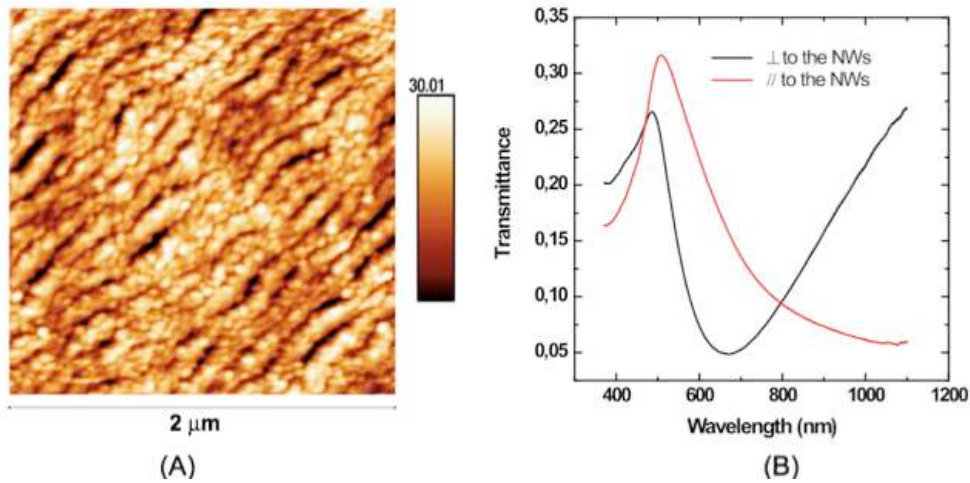


Figure 7.2: AFM image of sample 1 (A) and the corresponding macroscopic transmission curves (B). The red and black curves indicate the polarization parallel and orthogonal to the nanowires respectively.

by the problem of drift, or sliding of the sample onto the translator stage, mentioned earlier. Despite that, it is clear that the sample morphology is reconstructed with good accuracy revealing a rather irregular network of nanowires mutually spaced by around 100 nm. Topography is similar to what is obtained with AFM except for the already mentioned limitations related to the large physical size of the SNOM probe.

On the contrary, the optical maps appear to be all different from each other and none of them closely resembles the morphology, even though traces of the nanowire pattern can be discerned in the optical maps acquired upon green laser illumination. While being apparently surprising, the poor correlation between optical and topographical maps is typical for near field analysis of plasmonic nanostructures [106]. As a matter of fact, reconstructing the topography through optical signals acquired at the local scale implies that optical properties are dominated by local absorption and/or reflection of light. This is not the case when nanoparticles are studied, where scattering in the near field is the prominent process. Moreover, when plasmon resonances can occur, the picture of the process gets even more complicated, since collective effects can take place.

The first approach reported in the literature to analyze the near field distribution at the surface of a nanostructured sample, in particular with a random distribution, is based on statistical methods. Within this frame, the probability distribution function (PDF) of the optical maps is plotted. The PDF represents the frequency distribution histogram of the intensity level

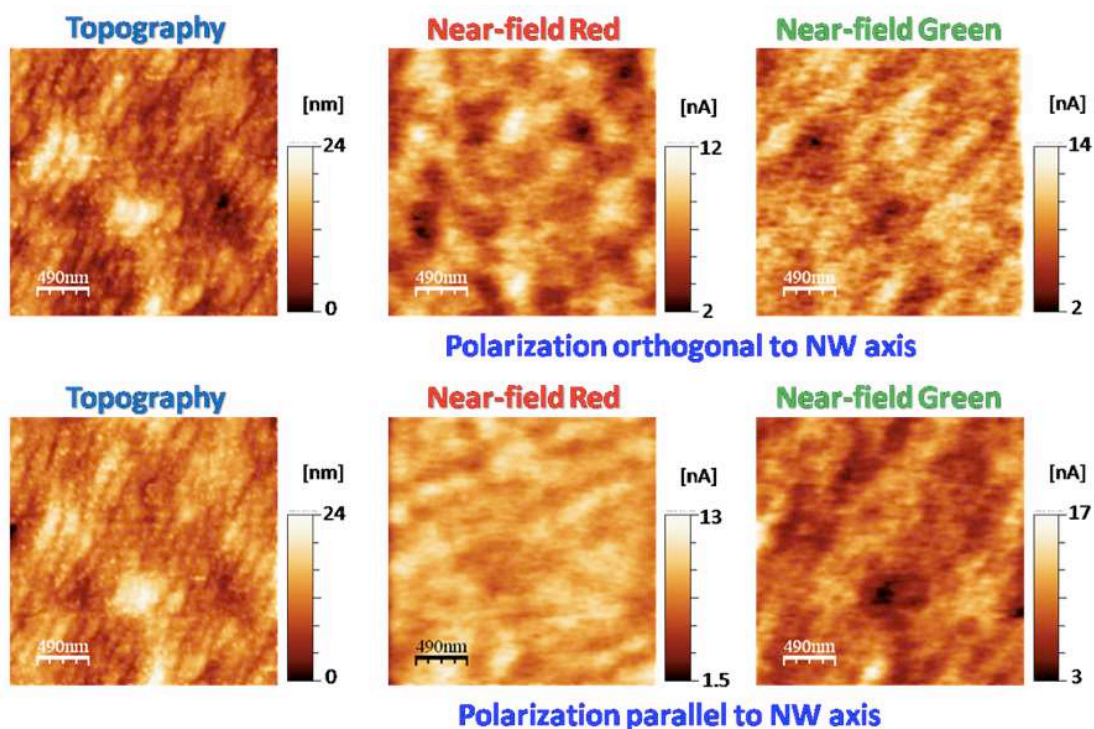


Figure 7.3: Topography and optical maps acquired on sample 1 as described in the text. The meaning of each map is indicated in the figure. Color scales are in units of height for the topography and in units of photocurrent for the optical maps (referenced to the average value of the map): 1 nA of photocurrent produced by the photomultiplier nominally corresponds to 4 or 6 pW, in the green or red, respectively. Images have been treated with a line-flatten followed by a mild Gaussian smoothing ( $5 \times 5$ ). The inter-pixel spacing is  $\approx 12$  nm.

recorded in the map. It has been postulated that single scattering events without contribution of plasmon excitation results in a nearly Gaussian-shaped PDF [107], reflecting the random-like character of the scattering. On the contrary, multiple scattering due to collective excitation of plasmon resonances gives rise to a tail in the PDF, which extends towards stronger intensity. Typically, this tail follows an exponential decrease, which is a signature of collective effects involving scale invariance of the system [106].

Figure 7.4 shows the PDF for the four optical maps of Fig. 7.2. For the sake of clarity, every PDF has been normalized to its maximum and the horizontal scale has been set in order for the center of mass of the distribution to be normalized to one. While the PDFs for green (both polarizations) and red (parallel polarization) follow an almost Gaussian behavior, the PDF for the red illumination, orthogonal polarization, exhibits a markedly asym-

metric shape, with a tail extending towards higher intensity which can be well fitted by an exponential decrease (the curve black superposed on the histogram). This is a definite indication of plasmon resonances, which is in perfect agreement with the expectations and take place exclusively when red laser excitation is provided, polarized across the nanowire axis.

The samples investigated in this work possess a peculiar morphology: roughly speaking, on the disorder at the local scale due to self-organization processes of the metal, a global order is superposed (the presence of the nanowires), which, however, is strongly anisotropic. The interplay between order and disorder is probably responsible for the occurrence of an almost bimodal distribution, peaked at above average intensity.

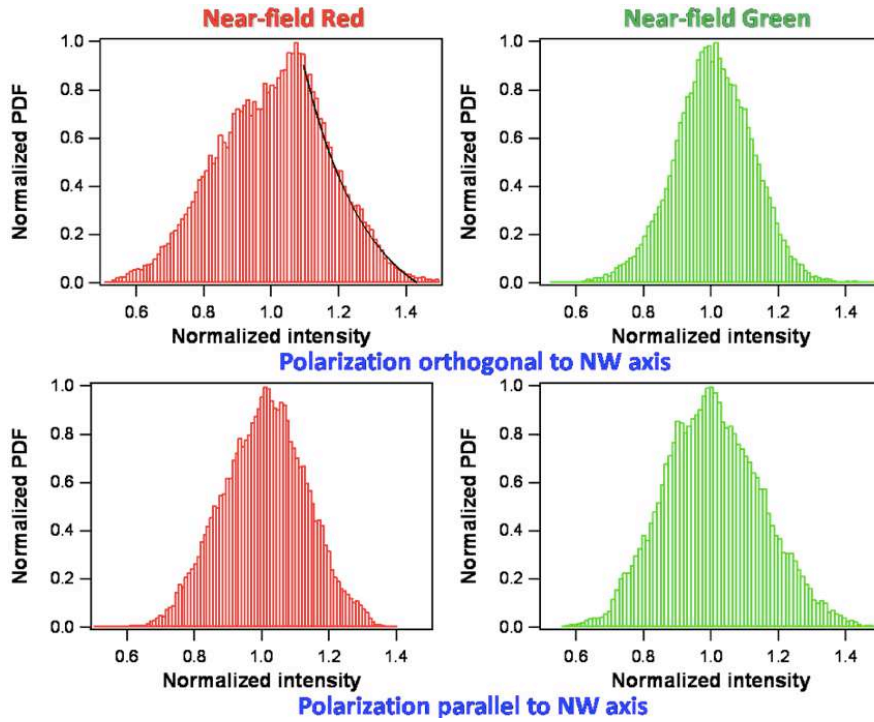


Figure 7.4: Normalized PDF, as described in the text, obtained from the maps of Fig. 7.2.

Another statistical tool frequently used to analyze near field optical maps is based on the auto-correlation function (ACF) [113]. The intensity correlator  $C(\vec{R})$ , displayed in the ACF maps as a function of the position  $\vec{R}$ , is defined as

$$C(\vec{R}) = \langle \Delta I(\vec{r}) \cdot \Delta I(\vec{r} + \vec{R}) \rangle, \quad (7.1)$$

where  $\Delta I(\vec{r}) = (I(\vec{r}) - \langle I(\vec{r}) \rangle) / \langle I(\vec{r}) \rangle$  is the normalized intensity

variation of the signal at the position  $\vec{r}$ , i.e., the optical signal displayed in the original maps. Thus, ACF maps give information of the spatial extent (and shape) of the correlation between spatially different portions of the original maps.

Figure 7.5 reports the ACF maps produced with the data shown in Fig. 7.2 (only the red laser excitation is displayed, ACF upon green laser excitation does not add any significant knowledge). Auto-correlation of the topography leads to a prominent feature, with a transverse size similar to the inter-wire spacing ( $\sim 100$  nm), appearing tilted in the map, with a direction almost parallel to the nanowire axis. ACF of the optical map acquired upon green laser excitation is similar, while being less contrasted and more noisy. This is a consequence of the fact that, in such excitation conditions, the near field optical map is dominated by scattering from the nanostructured surface. Therefore, even though this cannot be immediately seen in the original map, the optical signal modulation is affected by the morphology modulation. We note that, the statistical treatment beats the long range fluctuations due to far field contributions, which are very likely the responsible for the blurred oblique broad features observed in the optical maps. We also point out that the small transverse size is a definite proof of the near field operation, since it demonstrates the ability to resolve structures spaced by less than half a wavelength.

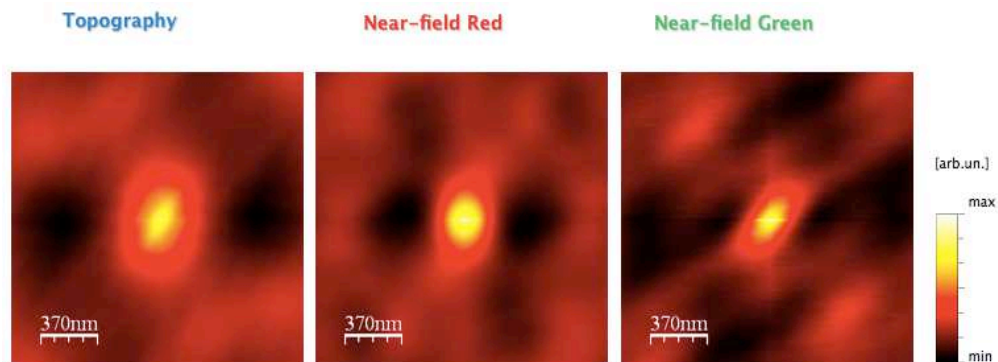


Figure 7.5: Auto-correlation (ACF) maps produced as described in the text from data shown in Fig. 7.2.

On the contrary, the ACF produced from data acquired upon red laser, orthogonal polarization has a different shape. The stronger spot at the center of the map is in fact almost round shaped, hence no longer correlated with the anisotropic morphology. Moreover, it appears markedly larger than in the other maps; the transverse size is above 200 nm. We attribute such a

specific feature to the excitation of plasmon resonances, involving multiple nanowires.

### 7.3.1 Local field enhancement

One of the most striking effects consequent to the excitation of LPR is the possibility of local field enhancement [106], which has important outcomes, for instance in the realization of substrates for SERS [17]. As already mentioned, while being in principle a powerful method to detect the so called “hot-spots” [125], SNOM fails in providing with a quantitative evaluation of the enhancement factor because of several technical and fundamental problems. The most relevant one is probably the occurrence of a strong background which contributes to the near field collected at the sample surface. Such an unavoidable background is mostly due to scattering from the metal nanoparticles at the sample surface, from the metal film in case of quasi-continuous layers, from the rippled substrate. Moreover, even though care has been devoted to suppress such effects, we cannot completely rule out far field contributions or other spurious sources of signal (e.g., direct coupling of light to the optical fiber probe).

A reliable independent measurement of the background is out of our possibilities. This task would require to produce specific samples, featuring accessible regions from where the scattered signal can be considered as the background, for instance metal free zones [106, 110]. The samples investigated here are densely coated by the metal, and there is no way to access the underlying substrate. On the other hand, replacing the sample with a blank (reference) one implies strong differences in the alignment conditions, in particular the actual probe-to-sample distance which depends on the approach process. As it will be briefly presented in the following sections, we have investigated reference samples consisting of continuous metal films onto rippled substrates (sample 3) and bare rippled (glass) substrates (sample 4). The near field intensity recorded from those samples as well as their variations are much smaller than for the nanowire samples (a factor of 5-10 for the continuous film and more than one order of magnitude for the rippled glass substrate). However, due to the above technical reasons, we will not use such findings for attempting a quantitative evaluation of the “absolute” enhancement factor.

Following the procedure outlined in the literature (see, for instance, [106, 108, 111]), we will concentrate on the relative enhancement factor  $\Gamma$ , which evaluates the local variations of the near field intensity within the imaged regions of the sample. We start noting that the flatten filter used to process

the acquired images removes contribution of the background by referencing the signal, practically, to the average value of the map. However, the scale obtained in such a way cannot be directly used to evaluate  $\Gamma$ . In fact, the average value of the background corresponds to the zero of the scale. According to the literature, we set to one, the minimum value of the flattened map. In this way, the color scale is calibrated in units of enhancement with respect to the minimum value of the scattered intensity within the same map. The procedure is obviously prone to a large uncertainty in the definition of the minimum value, which is another good reason to consider the so-obtained  $\Gamma$  as an estimation, rather than a quantitative evaluation. However, being the same procedure applied to maps acquired in different conditions (wavelength and polarization), it leads to reliable comparisons of the sample behavior as a function of the illumination properties.

Figure 7.6 shows near field optical maps acquired on the sample 1 upon different illumination conditions and treated according to the procedures mentioned above. For the sake of clarity, the dynamics of the representation is set in such a way that only regions of the map with intensities above twice the minimum level are shown. This allows getting rid of background scattering from the nanoparticles and the substrate as well as of other spurious phenomena (in both the near and the far fields). Illumination conditions other than red laser, orthogonal polarization produce almost flat maps, except for the occurrence of isolated spikes (see, e.g., green laser, parallel polarization) possibly due to the occurrence of strong resonances with LPR sitting in isolated nanodefects or nanoholes [122], due to dipoles induced by electric and magnetic field, which will lead to localized plasmonic resonances similar to those seen in noble metals [126]. Experiments reported in the literature [127] have shown that nanoholes, either single or distributed in arrays on gold thin films, support excitations which are qualitatively very similar to the LPR. This effect may occur with different wavelengths and different states of polarization depending on the morphology (size and orientation [128]) of nanoholes. Finally, we cannot exclude the possibility of non-resonant phenomena, for example, related to the so-called tip effect [129], which can occur in the case of highly irregular morphologies, able to concentrate the field lines in a very small area.

The main result of our analysis is rather straightforward to comment: only when using red laser excitation polarized across the nanowires, that is in the conditions leading to excite LPR from the nanowire pattern, (hot) spots are observed, in agreement with the PDF analysis presented earlier. Moreover, as suggested by the ACF maps, the hot-spots appear to be sized in the few hundreds of nanometers (200-300 nm, typically) range. Due to the finite res-

olution of the instrument, we cannot exclude enhancements at the very local scale, which might be smeared out due to spatial averaging [110]. However, we point out that the observed lateral size of the hot-spots is larger than the actual spatial resolution of our SNOM, estimated according to the nominal aperture size (50 nm) and to the presence of smaller features which can be easily detected in the optical images (see Fig. 7.2).

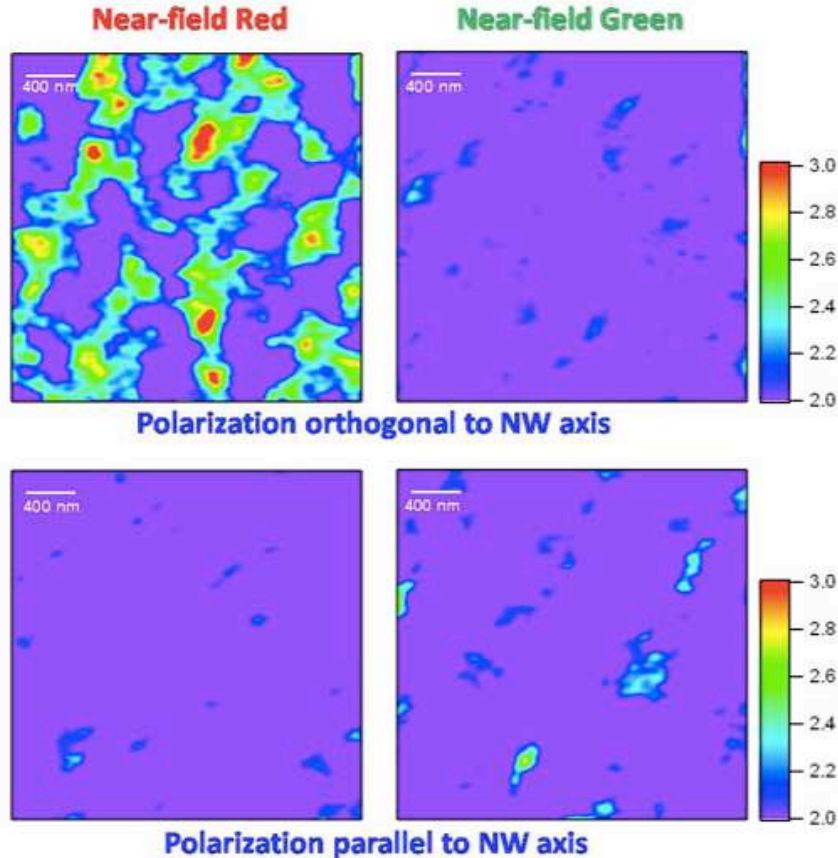


Figure 7.6: Near field optical maps acquired in different illumination conditions and scaled in units of the relative enhancement factor  $\Gamma$ , as defined in the text. Note that the dynamics of the representation is chosen in such a way to mask features with intensities smaller than twice the minimum intensity.

In order to have a slightly improved estimation, a comparison can be made between the amplitude of the near field intensity variations for the red and the green illumination. The rationale of the method, originally proposed in [130], is that the background affecting the intensity measurement is expected to be independent of wavelength and polarization. As a consequence,

normalization of the maps can be accomplished with respect to the minimum recorded signal, independently of the wavelength used. Following this procedure, and also taking into account the spectral response of our detector (more sensible in the green than in the red by nearly 50% nominally), we get a relative enhancement factor exceeding one order of magnitude for the brightest hot-spots. This result is in line with the figures reported in the literature for SNOM analysis of samples featuring plasmon enhancement such as random nanostructured metal films grown close to the percolation threshold.

Thanks to the ability of SNOM to collect simultaneously (in the same scan) topographical and optical information, we made an attempt to identify the morphology of the sites giving rise to hot-spots. There are a few experimental issues to be taken into account prior to analyzing the results, which we recall here in the following.

- The spatial resolution in both topographical and optical channels is limited due to the finite physical size of the probe tip and of the aperture. Moreover, as already stated, the presence of rather sharp valleys or grooves, for instance in the inter-wire (gap) regions, prevents a detailed reconstruction of the morphology. Therefore, our analysis is not suitable to identify enhancement sites associated with small morphological features such as spikes, nanosized holes or protrusions.
- The occurrence of different time responses for topographical and optical data, mentioned already, requires a post-processing alignment procedure which brings some uncertainty. This can be evaluated as  $\pm 5$  nm, at least.
- Filters applied to the maps in the data treatment tend to smear out small details. In order to reduce such effect, we have not applied the Gaussian-smoothing algorithm to the considered maps. On one hand, this improves the apparent resolution, i.e., the distance between adjacent pixels in the images, on the other hand oversampling artifacts might occur.
- Due to the inherent inhomogeneity of the sample morphology, we have found a large variety of correlations or anti-correlations between topography and optical features. Here we will illustrate only a few representative examples.

Figure 7.7 shows an example of the comparison between topography and optical features in four distinct blow ups, sized  $1 \times 1 \mu\text{m}^2$ . Superposed on the topography (treated with a FFT filter to remove long and short scale

noise and enhance the contrast of the nanowires) are the contour plots of the optical signal (the same color scale of Fig. 7.6 is used). It is clear that hot-spots appear to sit mostly in depressed regions, and their occurrence is more likely in the vicinity of nanowire defects such as, interruptions, bifurcations, bends.

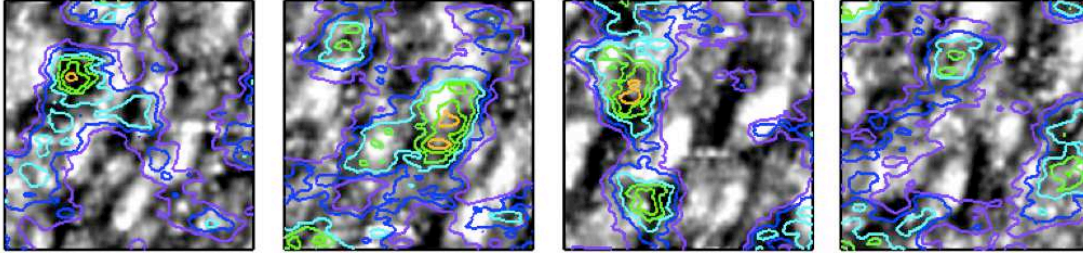


Figure 7.7: Blow ups of the topography in selected regions showing hot-spots (red laser illumination, orthogonal polarization) with superposed the contour plots of the near field optical signal. Color scale of the contours is the same as for Fig. 7.6 and the topography has been treated with an FFT filter to remove long and short scale noise. The lateral size of the maps is  $1 \times 1 \mu\text{m}^2$ .

In general, a rough estimation of the correlation between optical and topography maps suggests that, in the conditions ensuring LPR occurrence, more than 70% of the optical signal is found in the inter-wire (gap) regions. This is in agreement with the literature stating that enhancement is mostly found in the gaps between nanoparticles [114], being essentially due to co-operative, or collective, excitation of plasmon resonances in separate nanoparticles. In our case, the entities contributing to the field distribution are the nanowires, hence the maximum field intensity is typically found in the inter-wire regions. Hence, co-operative plasmonic resonances [131][132][133][134] between different nanostructures can be thought to have the major role in determining the near field distribution at the sample surface.

## 7.4 Sample 2

Sample 2 is prepared in the same way as Sample 1. However they differ from each other for the metal thickness (20 nm vs 12 nm), which is expected to be reflected into a minor degree of inter connection for the thinner film. Sample 2, being the thinner and less interconnected metal film exhibits a narrower resonance than sample 1. The dichroic ratio at the two different excitation wavelengths is  $\gamma_{green} \approx 0.2$  and  $\gamma_{red} < 0.1$  (figure 7.8). In other words, both

the green and the red laser excitations fall in the tails of the resonance for sample 2 and none of the available wavelengths fully corresponds to the LPR.

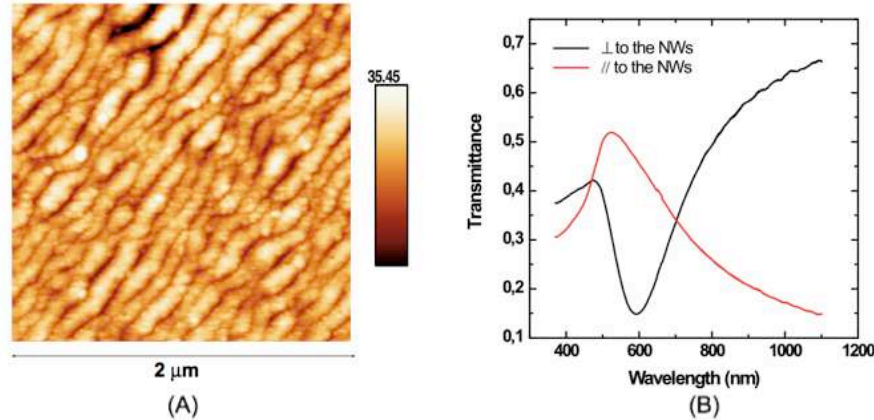


Figure 7.8: AFM image of sample 2 (A) and the corresponding macroscopic transmission curves (B). The red and black curves indicate the polarization parallel and orthogonal to the nanowires respectively.

Sample 2 has been analyzed with the same approach and methods as sample 1. We anticipate that the results are less interesting, in the sense that the effects observed in sample 1 ascribed to LPR excitation are here much less pronounced or absent.

Figure 7.9 reports representative topographical and optical maps (note the dark rectangle in the red optical map, orthogonal polarization, due to accidental problems in the laser switch: the corresponding region must obviously be disregarded in the analysis) obtained on sample 2.

Topography looks rather different with respect to sample 1. The morphology is more rough and strong graininess (grain average size on the order of 150-200 nm) is detected. This is due to the smaller amount of gold deposited onto this sample, leading to less efficient coalescence processes of the self-organized metal islands. Though the dynamics of the topography representation turns similar to sample 1, it does not imply similar film thickness in the two cases, due to the poor reconstruction of holes and valleys related to the large lateral size of the probe used, as mentioned already.

Roughness and graininess are so evident that it is even difficult to clearly discern the nanowire pattern in the topography maps. In other words, the local disorder prevails on the long scale order. Nevertheless, it is still possible to distinguish an array of diagonal lines representing the “nanowire direction”. In fact, by heavily filtering the image with FFT algorithms aimed

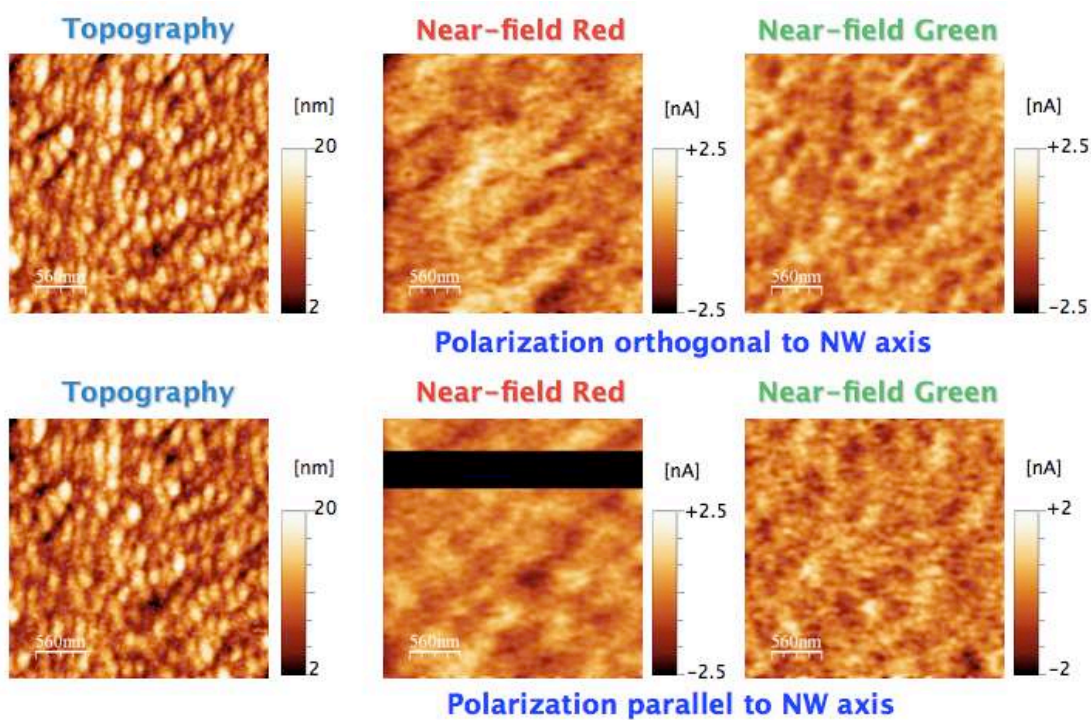


Figure 7.9: Topography and optical maps acquired on sample 2 as described in the text. Data treatment is similar to Fig. 7.2.

at smoothing along the diagonal direction, it is still possible to reveal the nanowire pattern, roughly aligned as for the previous sample.

The morphology of sample 2 is dominated by the nanoparticle nature of the metal islands. The nanoparticle shape appears mostly elliptical, and they are mutually aligned (the alignment direction corresponding to the nanowire axis). This morphological difference along with the mentioned plasmon resonance spectrum suggest a behavior more similar to that of random nanostructured films.

Optical maps exhibit some general features in agreement with sample 1. It is for instance confirmed that green laser excitation produces maps apparently richer of small features. Moreover, for the red laser excitation some polarization-dependent behavior is observed. In particular, brighter spots are detected with the orthogonal polarization. However, differently from sample 1, they do not appear round-shaped, but rather elongated.

Results of the statistical data treatment will not be reported here for the sake of conciseness. As expected, PDFs are almost Gaussian-shaped in all cases, and no relevant difference is observed in the ACFs. Due to the weak

superposition of the used wavelength with the plasmon resonance spectrum, local field enhancement is not expected to be ruled by the illumination conditions. Figure 7.10 shows the analogous of Fig. 7.6 for sample 2. Note, that the color scale is here arranged to show features with a near field intensity larger than 1.5 the minimum (it was 2 times the minimum in Fig. 7.6).

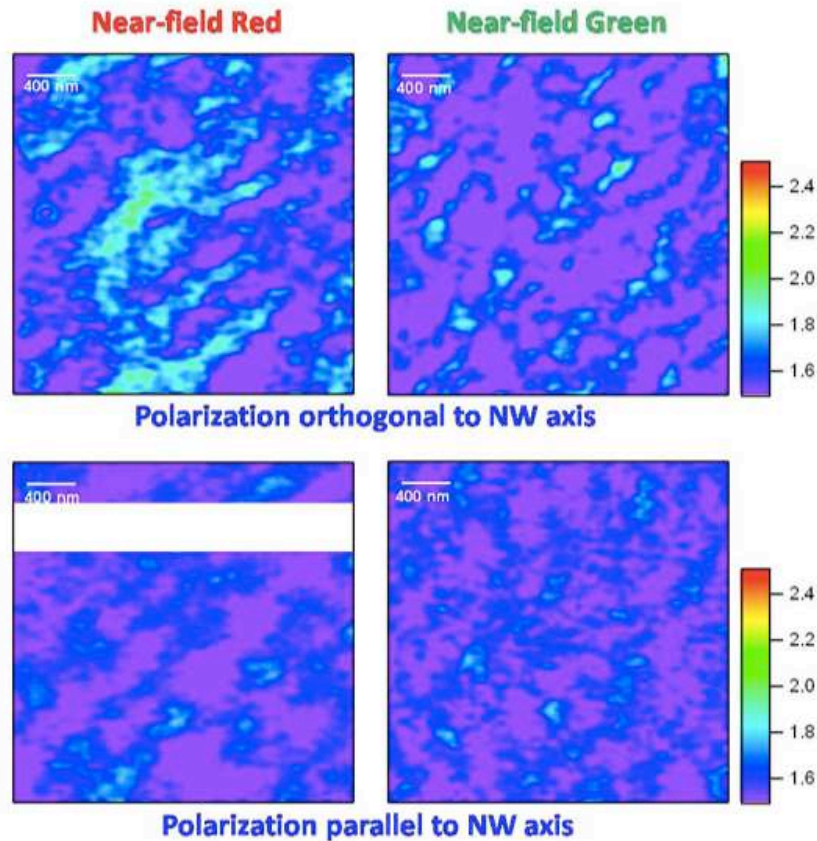


Figure 7.10: Near field optical maps acquired in different illumination conditions and scaled in units of the relative enhancement factor  $\Gamma$ , as defined in the text. Note that the dynamics of the representation is chosen in such a way to mask features with intensities smaller than 1.5 the minimum intensity.

The spatial distribution of the relative enhancement factor does not show any peculiar behavior. There are indeed regions exhibiting stronger field intensity, in particular when red laser, orthogonal illumination is used, but such regions appear to be rather broad and the corresponding spots rather weak. Rather than involving co-operative (interwire) effects, we might expect here plasmon resonances not too different from those of isolated nanowires which can be found in the literature [135, 136, 137], although the marked

graininess of the morphology might lead also resonances from individual nanoparticles to play a role.

## 7.5 Reference samples

Reference samples (blanks) have also been investigated with the main aim to point out the capabilities of our instrumentation. Two different blanks have been considered, both produced with the same apparatus used for samples 1 and 2. In particular, sample 3 is a quasi-continuous gold film deposited onto a pre-patterned substrate. Due to a longer deposition time, the gaps of the rippled substrate are completely filled and no disconnection is detected, meaning that nanowires are absent even in the presence of a topography modulation (with a spacing similar to the previous samples). This leads the sample to possess no LPR-related properties, as ascertained through conventional (macroscopic) measurements. Sample 4 is instead a bare rippled substrate. Due to the absence of the noble metal coating, also in this case no LPR-related properties is detected.

The topography of Fig. 7.11 shows a rather flat surface, with clear signatures of the ripples in the substrate, but no evidence of disconnected nanowires. On the top right a big morphological defect is detected. The optical maps, which have been acquired with an increased sensitivity with respect to the nanowire samples presented earlier (see the color scales), are dominated by a strong scattering from the defect, which is particularly evident upon green laser illumination. It is interesting to note that, in particular with the green laser, the pattern due to the ripples is easily detectable. This is a clear indication that, when optical features are dominated by scattering (from an almost flat and continuous metal layer), spatial resolution of our SNOM is adequate to resolve structures separated by  $\sim 100$  nm, that confirms the near field operation. Red laser illumination leads to a substantial decrease of the average optical signal, as expected considering the reflectivity of a gold layer (and the decreased sensitivity of the detector in the red). On one hand, the small average signal makes scattering in the far field to contribute (the broad oblique features in the map), on the other hand it confirms that the local enhancement observed in sample 1 is due to genuine plasmon effects occurring with that sample. There is clearly no enhancement in the reference sample.

The same applies also to sample 4, whose images are not reported here. In this case, very weak (variations below 0.1 nA), noisy and rather flat optical maps are obtained, as expected due to the absence of the gold coating.

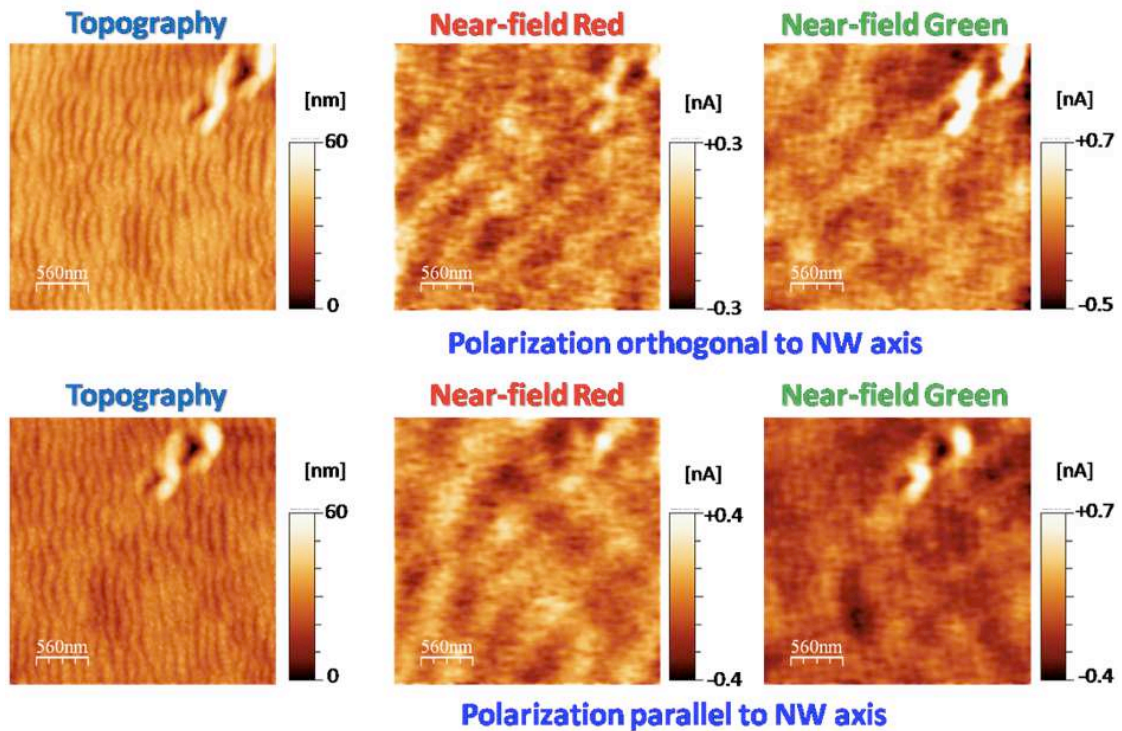


Figure 7.11: Topography and optical maps acquired on sample 3 as described in the text. Data treatment is similar to Fig. 7.2.

## 7.6 Fixed excitation mode

As described earlier, a key point of our SNOM apparatus is the ability to control the position of the illumination spot relative to the probe. In the measurements reported so far, the spot has been directed constantly (during the whole scan) onto the region probed in the near field. Since the apparatus is designed to have the probe fixed and the sample moving with respect to the laboratory frame, constant illumination is achieved by simply keeping constant the position of the spot.

With the focuser mounted on a piezoelectric translator which can be controlled independently of the sample scanner, illumination can be directed to any predefined position onto the sample. By moving the piezoelectric translator synchronously with the sample scanner, the illumination position can be kept fixed with respect to the surface all during the scan. Despite the simple explanation, from the experimental point of view the method required a careful development, aimed for instance at calibrating the travel of the spot as a function of the control signal. Details of the instrumental development

will not be given here.

The developed instrument is able to ensure synchronous motion of the spot and the sample (with a pointing uncertainty on the order of 100 nm or less) in a range  $\sim 12 \times 12 \mu\text{m}^2$ , limited by the maximum travel of the hollow piezoelectric tube holding the focuser. Obviously, by acting on the various mechanical translators, it is possible to fix the spot position either within or outside the scanned region. In other words, the illumination can be “observed” in the scan, or not, depending on the initial alignment, which can be set with a spatial resolution on the order of a few  $\mu\text{m}$ .

The so-conceived system is a perfect tool to investigate guiding, or propagation, of light at the sub-micrometer scale. For instance, the setup has been used to analyze propagation of surface plasmons (SPP) in metal waveguides [138]. In those samples, made in the form of thin gold stripes connected to a gold film with a micro-fabricated grating, illumination was sent onto the grating in the conditions leading to SPP excitation, and the near field intensity was probed far away from the spot, demonstrating propagation (and the associated effects) along the waveguide.

Motivations for using such a configuration with the nanowire samples studied in this work are less stringent. As a matter of fact, our samples do not sustain SPP modes because of the non-continuous morphology of the gold layer and the highly defective structure [17]. Efficient guiding and manipulation of electromagnetic radiation, as accomplished in plasmonic devices [23, 122], requires designing and realizing specific architectures conceived to enhance the co-operation between LPRs excited in different nanoparticles. For instance, regular arrays of closely packed (mutual distance in the near field range) metal nanospheres can be used to efficiently guide the radiation for relatively long distances.

The inherently irregular morphology of our samples prevents macroscopic propagation and guiding effects. However, the analysis of effects at the local scale might be of interest in order to better understand the behavior of the nanowire samples, in particular in terms of cooperative effects. To the best of our knowledge and contrary to the field intensity mapping reported above, such an investigation has not been carried out in the past and the literature cannot be of great help in unraveling the results, which should be considered as preliminary, in the absence of final confirmation and comprehensive interpretation.

## 7.7 Sample 5

The measurements here presented have been carried out on sample 5. While featuring an array of gold nanowires with a typical periodicity  $\sim 100\text{-}150\text{ nm}$ , similar to samples 1 and 2, sample 1 has been grown with a variant of the ion beam method using a single fabrication step. A defocused ion beam is in fact sent to cross the gold vapor during the deposition, leading to the formation of the quasi-periodic structure without the need for pre-rippled substrates. As a consequence of the different fabrication procedure, morphology appears different with respect to sample 1 and 2. Figure 7.12 shows the AFM image (along with a line profile analysis) and the optical properties of the sample measured with conventional (macroscopic) methods.

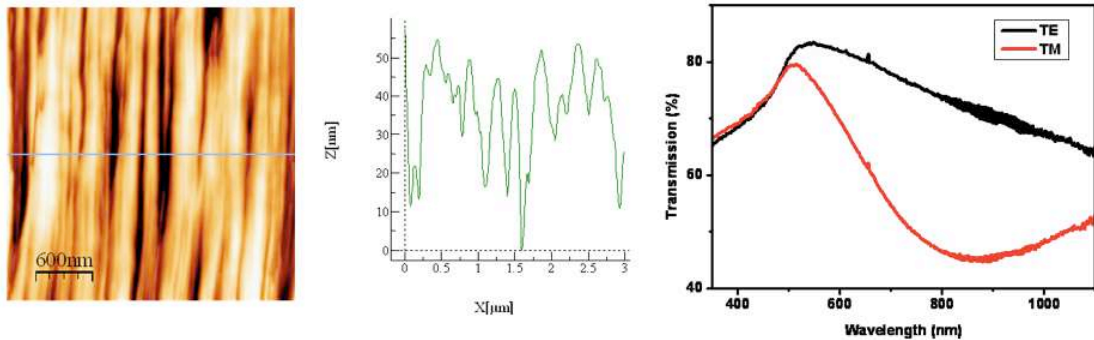


Figure 7.12: AFM image, line profile of the same along the marked horizontal direction, and macroscopic transmission spectra at two orthogonal polarizations of sample 1.

Remarkably, a much more smooth morphology is achieved, which exhibits a sharp gap between the nanowires. The shape of the nanowires is not regular, in terms of direction (frequently bent) and transverse size. However, the isolated nanoparticles detected in samples 1 and 2 are practically absent in this case. The optical properties are instead similar to those of the previously considered samples, suggesting that the optical behavior at the macro-scale is dominated by the occurrence of the (quasi-regular) nanowire pattern rather than by the presence of (irregularly distributed) nanoparticles or metal islands. In fact, the transmission spectrum for the polarization orthogonal to the nanowire axis displays also in this case a resonance which can be ascribed to the occurrence of LPR. We note that the resonance is rather broad and that it is located mostly in the near infrared range. For this reason, we have used a single wavelength to probe the sample in the near field tuned around 850 nm (a diode laser has been used), i.e., close to the peak of the resonance. The dichroic ratio at such a wavelength is  $\gamma \approx 0.3$ .

Since a single wavelength is used, comparing the behavior within or outside the resonance is not feasible. Besides the position of the illumination spot, which can be freely adjusted, the experimental parameters explored in the investigation are the polarization direction (parallel to the nanowire axis, orthogonal to them, or at 45 degrees) and the wavevector  $\vec{k}$  direction of the illumination radiation. The choice of varying  $\vec{k}$ , set parallel, orthogonal or at 45 degrees with respect to the nanowire axis, is inspired by the role the wavevector plays in exciting SPP. Even though, as already mentioned, SPPs are not expected here, changing the  $\vec{k}$  can lead to detect propagation effects involving combined SPPs and co-operative LPRs. The set of measurements presented here is made of subsequent scans, each one with defined experimental parameters (polarization and wavevector directions). For the sake of comparison, the illumination power has been kept constant (within  $\pm 10\%$ ) in all scans. However, no control has been applied to the position of the sample at sub-nm scale. We note that, in order to modify the wavevector direction, we had to physically rotate the sample, that prevents to recover exactly the same region in the scans. Efforts are being presently devoted to develop an experimental arrangement able to circumvent the problem.

The measurements have been carried out by placing the illumination either within or outside the scanned region. The rationale of the latter choice is evident. The near field intensity associated with propagation at some distance from the spot is expectedly very small. In order to allow its detection, an infrared extended photomultiplier tube has been used (Hamamatsu R2658, InGaAs (Cs) photocathode, nominal quantum efficiency  $> 1\%$  at 850 nm) and its supply voltage has been set to the maximum allowed (1.25 kV) to improve sensitivity. However, when the probe crosses the illuminated region a large signal is detected, which can lead to blinding effects of the detector. They are avoided when the spot is directed onto a zone outside the scanned region.

An example of near field optical maps acquired in such conditions is reported in Fig. 7.13. The figure shows the predefined position of the illumination spot (at the right of the map, with its center at around  $3 \mu\text{m}$  for the scan border). The  $\vec{k}$  direction is in this case always set orthogonal to the nanowire axis (no observable signal has been detected for  $\vec{k}$  parallel to the nanowires) and the three panels refer to different choices of the polarization, as indicated in the figure.

The figure suggests some dependence of the observed near field intensity on the polarization. In particular, for polarization orthogonal to the nanowires, the central part of the scan brings some intensity (features are detected

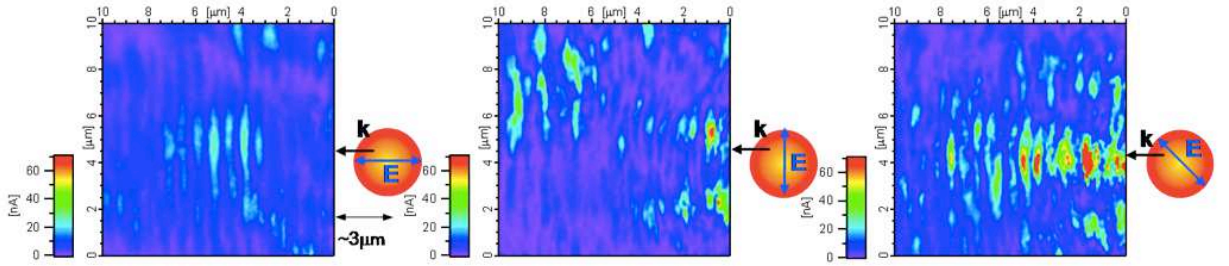


Figure 7.13: Optical near field scans of sample 5 upon illumination with different polarization directions, as reported in the figure. The illumination spot is directed outside the scanned region, approximately in the position marked by the shadowed circle (its size is similar to the actual size of the spot). The axis of the nanowire array is oriented vertically with respect to the figure, as suggested by the features observed in the maps and confirmed by the corresponding topography maps, not shown here. The color scale is the same for all maps.

aligned as the nanowires, in agreement with the topography map, not shown here). We cannot exclude spurious contributions to that, for instance due to diffraction fringes of the illumination spot. More intense, randomly distributed spots, generally found corresponding to topographical valleys (the inter-wire regions, or gaps) appear with polarization parallel to the nanowires, which get a wake-like character, visually suggesting propagation, when the polarization is set at 45 degrees. We remark that the finding is still awaiting for experimental confirmations, which should also assess the absence of spurious effects such as, the occurrence of diffraction fringes, the illumination of portion of the sample with extraordinary morphologies and should lead to, possibly, an improved control on the experimental parameters. By provisionally assuming negligible all spurious phenomena and related artifacts, the results appear rather puzzling. As a matter of fact, the occurrence of co-operative LPRs involving adjacent nanowires, which might be a vehicle to transfer the electromagnetic field at some distance from the illumination spot, requires a polarization direction crossing the nanowire axis, in agreement also with our results presented earlier on the local field enhancement. On the other hand,  $\vec{k}$  parallel to the nanowires would be required in case of excitation of SPPs to propagate along the nanowire. This is however not expected in our experimental conditions. Besides the already mentioned highly defective character of our gold layer, which should suppress plasmon propagation, the nanowire width is well below the cut-off size to support plasmon modes [17] and excitation of the SPP should be possible only through local (point-like) defects at the illumination site, which are expected to cancel the

memory of the original wavevector direction. If confirmed, the interpretation of this finding, which has been achieved thanks to the unique features of our versatile collection-mode SNOM, will require further efforts, out of the scope of the present thesis, substantially aimed at understanding the features of the scattering (in both far and near field) from the surface of our samples.

Finally, we report here in the following some examples of the measurements carried out by keeping the illumination spot within the scanned range. For these measurements the sensitivity has been suitably reduced in order to avoid saturation. Therefore, long-range (micron-sized) propagation cannot be observed, but the local features of the coupling between the illumination spot and the sample structure is seen. In principle, the measurements are similar to those acquired in the constant excitation mode, but for the circumstance that here the spot is scanned, hence its shape can be recovered by acquiring the scattered near field. This provides us with the opportunity to analyze the apparent shape of the illumination spot in different experimental conditions.

Prior to briefly presenting the results, we point out that the shape of the illumination spot depends on several factors. Being the spot produced by a focuser rigidly coupled (glued) to a single mode optical fiber suitable for the used wavelength, there are no degrees of freedom in the relative position of the fiber to focuser alignment. However, the shape can depend on the input alignment of the laser beam with the optical fiber. Care has been put in order to keep constantly (during subsequent scans) the alignment able to produce an almost Gaussian-shaped spot. We found a slightly astigmatic behavior of the system, causing an elliptical shape: the focuser assembly was rotated in order to have the short axis of the ellipse aligned along the wavevector. When projected onto the sample surface, this helps in obtaining an almost circular-symmetric distribution of the light intensity within the spot. Moreover, being the focuser mounted on the same mechanical plate holding the probe, the distance between the focuser and the plane of the surface depends on the approach conditions, which can hardly be controlled. Even if the Rayleigh length of the spot is expected to be in the tens of micrometers range, the waist size can slightly change in subsequent scans requiring an approach in between, as, for instance, when physical rotation of the sample is required.

Figure 7.14 reports a series of near field optical maps acquired in different illumination conditions, as specified in the figure. The first panel of the series refers to a flat continuous gold film, to be used as a reference. We note that in this case scattering in the far field (reflection) should play the major role in determining the intensity distribution. An almost Gaussian-

shaped map is produced, with some distortion and a fwhm transverse size around  $2.5 \mu\text{m}$ , that confirms tight focusing of the illumination spot. Images acquired on the nanowire sample look markedly different. First of all, this is due to the strong scattering experienced by the light when it impinges onto the irregular surface of the film. The shape is generally asymmetrical, with a shorter dimension transverse to the  $\vec{k}$  direction. This can be due to the geometrical arrangement of our setup, where the illumination spot is directed obliquely onto the surface: the (irregular, scattered) spot is then elongated according to the wavevector direction. The apparent transverse size is also a function of the illumination conditions. Its evaluation is however quite cumbersome, being also affected by the average intensity of the map (the color scale of all displayed maps is the same). In addition, it may depend on the actual waist size which, as already discussed, cannot be controlled exactly when repeated approaches are made.

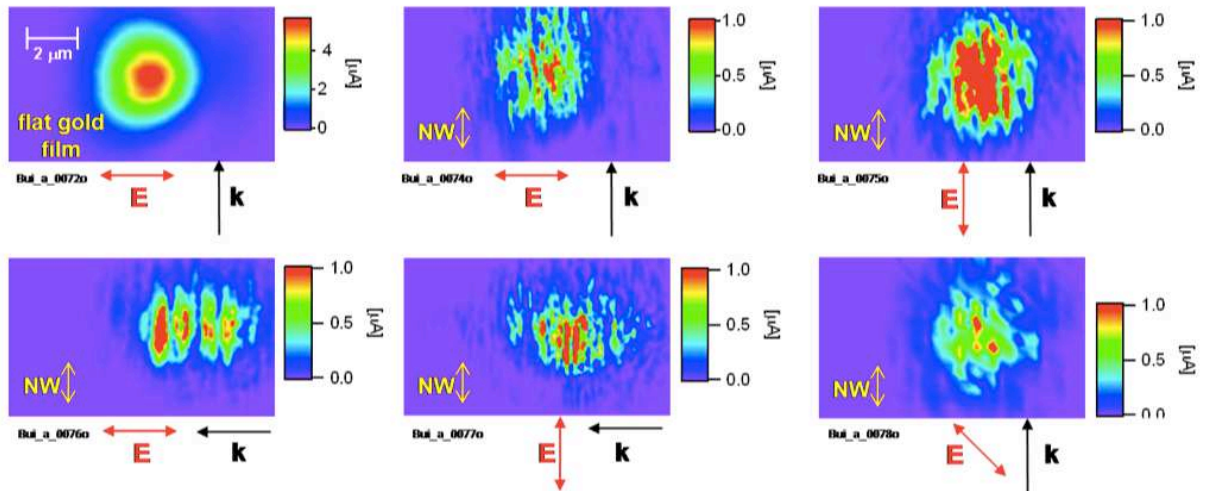


Figure 7.14: Optical near field maps of sample 5 upon illumination with different polarization and wavevector directions, as indicated in the figure. The illumination spot is inside the scanned region, as can be easily seen. The first panel is the optical near field map acquired on a reference sample, consisting of a flat, continuous gold film. The axis of the nanowire array, deduced from the corresponding topography maps (not shown here), is indicated with a double white arrow. Red and black arrows indicate the orientation of polarization and  $\vec{k}$ , respectively. The color scale is the same for all maps.

We concentrate here in the following on another feature of the maps, dealing with the spatial distribution within the illuminated spot. This is clearly affected by the nanowire pattern, as demonstrated by the modulation of the optical signal along the horizontal direction of the images, corresponding to

a direction crossing the nanowires in all the presented maps. Since scattering from the nanostructured sample is expected to be modulated (at some extent) by the topography, the observed behavior is in line with the expectations. However, the features of the modulation turn to depend on the illumination conditions. This is well clear, for instance, in Fig. 7.15, reporting two subsequent scans of the same region of the sample with the same wavevector direction (orthogonal to the nanowire axis) and two distinct polarization directions (either orthogonal or parallel to the nanowires). For the sake of completeness, the corresponding topography maps are also shown.

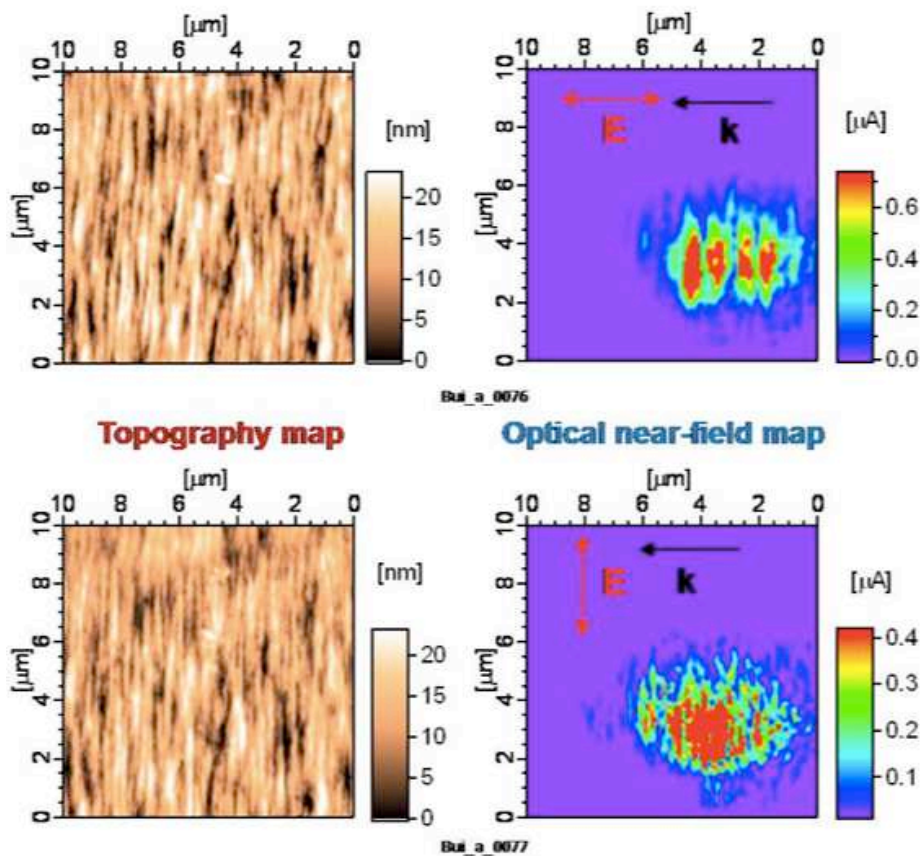


Figure 7.15: Topography and optical near field maps of sample 5 upon illumination with different polarization directions, as indicated in the figure.

While elongated features are observed in both cases, whose direction corresponds to the nanowires, the apparent spatial resolution, that is the presence of well contrasted details, is enhanced in the case of parallel polarization. This is in agreement with the expectations: orthogonal polarization excites the local plasmon in a co-operative fashion involving adjacent

nanowires. Therefore, the map acquired with parallel polarization, dominated by scattering, should lead to detect the subwavelength topographical features, whereas with the orthogonal polarization the optical intensity is ruled by the occurrence of plasmon resonances. The behavior is somehow similar to what we observed in sample 1, where the plasmon excitation with the consequent local field enhancement led to an auto-correlation function markedly different with respect to that built on the topography. In this case, due to the different morphology of the sample, more homogeneous along the nanowire direction owing to the different fabrication procedure, the near field intensity distribution associated with the plasmon resonances gets an asymmetrical (elongated) shape, with a transverse size on the order of at least two or three times the interwire spacing. Remarkably, the spatial distribution of the optical spots is generally centered in the gap regions, confirming that this is the site where preferential field enhancement occurs.

Thanks to the orientation of the sample in these measurements, rather than using the ACF method we can exploit another tool able to give information on the spatial distribution of the spots. We can in fact sum all the lines of the map (both for topography and optical signals) and perform a Fast Fourier Transform (FFT) analysis by using a suitable algorithm. The peaks appearing in the FFT spectrum, which will be treated as a function of the spatial frequency (the inverse of the spacing) along the horizontal direction (relative to the images), will highlight the occurrence of periodicity. Due to the limited number of points in the original map (512 points or lines) the accuracy of the method will not lead to identify precisely the relevant length scales, but will rather give an approximate picture of the spatial distribution along the horizontal direction (relative to the images).

Figure 7.16 reports an example of this procedure, carried out on data shown in Fig. 7.15.

The FFT of the topography (black line) shows several peaks, which can be generally associated with the interwire spacing and their harmonics. In particular, families of peaks are found corresponding to spacing of 110 and 140 nm, well in agreement with the morphology (the occurrence of a double periodicity can partly be explained by the irregular nanowire pattern, featuring bifurcations and entanglements). The periodicity found in the so-produced FFT for the optical maps looks rather different each other (and both different with respect to the topography). Besides the low frequency peaks, possibly associated with the finite (and small) extension of the considered region, illuminated by the spot, and the general broadening of the features, possibly associated with the poor signal-to-noise ratio, we can observe that the peaks corresponding to the periodicity of the nanowire pattern disappear, and are

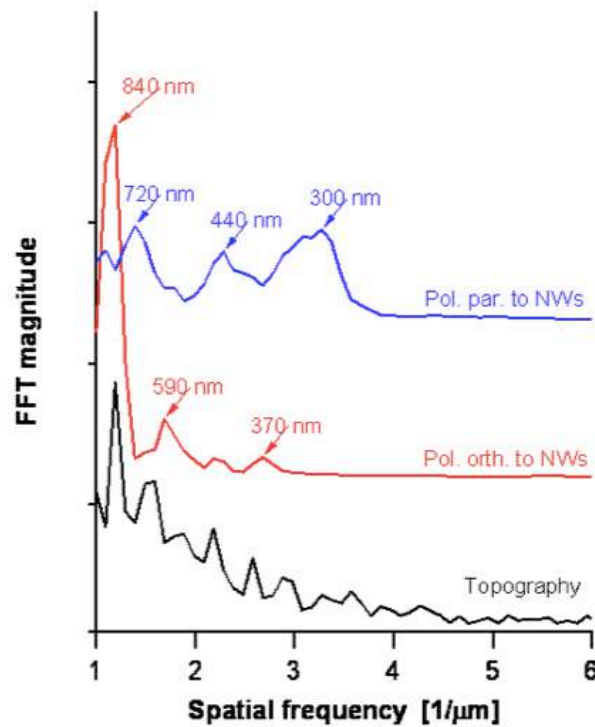


Figure 7.16: FFT spectra of the topography and optical maps shown in Fig. 7.15, line-by-line summed, produced as described in the text.

replaced by new, relatively strong, peaks corresponding to spacing above 300 nm. This phenomenon, which is much more marked when orthogonal polarization is used, pinpoints the occurrence of co-operative effects involving adjacent nanowires. Further efforts will be devoted to improve the accuracy of the method (e.g., by collecting images with a larger number of pixels and by carefully accounting for the actual spatial resolution of the probe) and to find a physical interpretation to the finding.

## 7.8 Synopsis

Near field microscopy is certainly a very powerful tool to overcome the diffraction limit in spatial resolution while keeping, at the same time, the versatility of conventional microscopy. However, using a SNOM requires a great deal of care to achieve meaningful and understandable results. First of all, this is inherently due to the nature of the instrument. Even though the technique has been introduced since a relatively long time, the setups are

typically custom-made and efforts are often required to tailor the operation to the requirements of a specific research. Such efforts, although not documented in this thesis, have been spent in order for the instrument to reliably build the map of the near field intensity.

As mentioned in the chapter, the goal is accompanied by unavoidable limitations, mostly associated with the physical size of the probe and of the aperture. A larger spatial resolution might be achieved by using an apertureless instrument, which, however, requires a much more complicated interpretation scheme, where the local interaction between the probe and the sample surface should be described in details. Similarly, using the apertured-SNOM in the emission mode might lead to stronger signal to noise ratio and enhance the contrast mechanism. However, our choice was to setup the most straightforward configuration for mapping the near field intensity when the sample is used in conditions similar to those typical for SERS experiment, where the sample is illuminated by a far field. This goal can be reached using the collection mode, at least in principle, neglecting the various technical problems discussed earlier.

SNOM analysis has been restricted to the gold nanowire arrays. As a matter of fact, SNOM studies of model systems, such as isolated nanowires or systems including nanowires and nanobeads, appear much less stimulating even if in those cases comparison with the expectation would be much simpler. In this thesis we intended to analyze real systems, with the main aim to characterize at the local scale those effects which are masked in conventional experiments owing to spatial integration over a scale larger than the typical nanostructure size. Therefore, result of the SNOM investigation can be considered as complementary to those achieved in this thesis by using the SERS technique. Advantages of the SNOM approach can be seen in the possibility to correlate the optical maps with the local morphology and in the absence of molecular probes, causing the entangled effects discussed in the previous chapters.

The visualization of the hot-spots attained by the SNOM data is in substantial agreement with the expectations. Sample 1, illuminated with a wavelength well in the resonance of LPR and polarized across the nanowire axis (V configuration), shows enhancement of the local near field intensity in isolated spots. The enhancement factor, on the order of ten if referenced to the background scattering upon green laser illumination, is not as large as reported in the literature dealing with SERS experiments, but it is in line with data obtained by SNOM in random nanostructured gold samples. Interpretation of the discrepancy, provided in the literature, can be quite straightforwardly related to technical issues, in particular with the limita-

tions of the apertured-SNOM in collecting the near field very close to the surface and from tightly localized regions. However, the hot-spots detected in our maps show a transverse size (200-300 nm fwhm) relatively large compared to both the spatial resolution of the instruments ( $\sim 50$  nm) and the typical length scale of the investigated samples ( $\sim 100$ -150 nm, i.e., the inter-wire spacing). This can be interpreted as a signature of the co-operative plasmon excitation in adjacent nanowires. The result, and its characterization in terms of statistical tools, agrees with literature data on random distributions of nanoparticles in quasi-continuous metal films. In our case, the interplay between the global, anisotropic spatial regularity imposed by the nanowire pattern and the disorder associated with the single nanoparticles forming the nanowire and giving rise to irregular morphological features, can rule the collective behavior of the plasmon excitation. A theoretical picture of the whole optical behavior, which would deserve efforts beyond the scope of the present thesis, might use the theoretical model presented in Chapter 5 as the starting point, to be implemented with an approximate description of the uneven spatial distribution of the ellipsoids on the sample surface.

The occurrence of hot-spots in sample 1 turns to depend on the polarization of the illumination light. In other words, polarization is confirmed to be a handle suitable to control the behavior of the sample, i.e., the local enhancement at its surface. Remarkably, hot-spots are practically absent in sample 2, featuring a morphology not dissimilar to sample 1, but a resonance wavelength not coincident with any of those used in the investigation. We cannot rule out, however, that the heterogeneous nature of the nanowire arrays emerging at the local scale gives rise to other enhancement phenomena, associated, for instance, to nanoholes. As a matter of fact, near field intensity is generally found to increase in regions corresponding to depressions, or valleys, of the topography, where the reduced thickness of the metal layer can produce nanohole or pits. Unfortunately, the spatial resolution of the topography, which in SNOM is typically in the few tens of nanometers range, prevents direct observation of such nanosized defects. The same applies to the interwire regions (gap), where the enhancement effects are expected to be stronger owing to the large literature on optically-interacting nanoparticles. Comparison between optical maps and topography at the hot-spot sites, while generally suggesting that the field intensity increases in between the nanowires, cannot rely on an adequate spatial resolution to definitely assess the correlation between enhancement and morphological gaps. As expected, enhancement phenomena are completely absent in the reference samples (blanks), whose analysis, only partially reported here for the sake of conciseness, was relevant to assess the instrumental capabilities of our

SNOM.

Besides mapping the optical near field intensity in diverse samples and different illumination conditions, SNOM was also used to have a preliminary description of possible phenomena involving transfer of the near field intensity across the nanowire array. This was made possible by the ability of our instrument to operate in different illumination conditions, which we named constant and fixed excitation modes. The latter, enabling illumination of a predefined spot onto the sample surface, is specifically suited to point out any phenomena causing propagation of the plasmon excitation.

Plasmon propagation is one of the most appealing features of plasmonics, since it allows guiding and manipulating light in a size scale smaller than its wavelength, that owns an extremely important applicative potential in nanophotonics. Roughly speaking, manipulation of electromagnetic energy through plasmons can take place either at a smooth, regular metal/dielectric interface (surface plasmon polaritons, SPP), or in engineered arrangements of closely packed nanostructures featuring local plasmon resonances (LPR). Our nanowire arrays do not belong to any of such classes of devices. In particular, the absence of a smooth and continuous gold layer and the strongly defective morphology are expected to prevent SPP propagating modes. However, the fabrication process used for samples 1 and 2 can be modified in order to obtain more regular samples, as sample 5 examined in this thesis, whose morphology does not exhibit heterogeneity at the scale of the individual gold nanoparticle, or nanoisland.

Analysis of sample 5 in the fixed excitation mode led to interesting, while not yet confirmed nor interpreted, results. For instance, the shape of the illumination spot and the apparent spatial resolution of the optical maps, evaluated through the presence of sub-wavelength details, turn to depend on the excitation of the plasmon resonance, which in this case is located in the near infrared range. In agreement with the results acquired on sample 1, the transverse size of the prominent optical features increases when the polarization of the illumination beam is orthogonal to the nanowire axis (V configuration). Moreover, local maxima of the field intensity are typically found corresponding to the interwire gaps. However, the smoother morphology of sample 5 causes a different shape of the intense spots, which appears elongated, thus resembling the nanowire morphology. Such a behavior suggests that the electromagnetic energy directed onto the surface spreads out the directly illuminated region.

Measurements aimed at studying propagation effects in the micrometer range, carried out by displacing the illumination spot out of the imaged region in

---

order to avoid blinding of the detector and enabling high sensitive detection, suggest an unexpected behavior. Propagation of the excitation, expected to involve adjacent nanowires in a co-operative mechanism, should be more effective in the conditions leading to excitation of the LPR, that is by illuminating with a polarization direction orthogonal to the nanowires. On the contrary, our results indicate that the near field intensity far away from the illuminated spot gets larger when the wavevector of the illumination is orthogonal to the nanowires, but the polarization is rotated by 45 degrees. Such a finding, if confirmed through the acquisition of a larger set of measurements in different regions of the sample or in different samples, might have applications to further enhance the usability of the samples as SERS substrates enabling a controllable (through the polarization direction) size increase of the surface potentially interested by field enhancement effects.



---

## Conclusions and future perspectives

Plasmonics is a steadily developing field with fascinating promises for fundamental science as well as for various potential applications. The ability to confine, guide and redirect electromagnetic energy at nanometer length scales makes plasmons an interesting research object for studying light-matter interaction. We have studied plasmonic structures made of gold. The gold nanostructures are advantageous because of their biocompatibility and in the present days a number of applications are realized using gold nanoparticles. We have used scanning near field optical microscopy and surface enhanced Raman microscopy to study the gold nanowires.

Both isolated nanowires and nanowire arrays have been investigated with SERS. The idea was to understand the various mechanisms that contribute to SERS. Chemically grown commercial nanowires were used for the study. We have studied the propagation properties of these nanowires and have seen a propagation distance of  $3.8 \mu\text{m}$ . The excitation of the isolated nanowires has been achieved by mixing them with nanobeads which act as mediators to couple light. The measurements were made using ATTO 740 dye as a reporter molecule. The evolution of the propagation properties with wavelength has been analyzed and it is seen that more than one factor contributes to the overall effect. The proximity of the excitation wavelength to either the plasmon resonance of the sample or the molecular resonance decides the propagation at the position. We have investigated the SERS dependence on wavelength which is seldom studied due to requirement of a tunable laser. We see that this dependence follows the same trend as propagation. Later we have co-deposited Rh6G along with ATTO 740 and have shown that we attained single molecule regime with the help of two molecules. The technique of using two molecules is relatively new and another original idea of our experiment is to correlate the optical properties of the samples. We have analyzed the propagation and SERS properties of the sample at a particular point and correlated it to the plasmon resonance shape. This gives a better insight into the contributing mechanisms and such an experiment has not been reported in the literature to the best of our knowledge.

In the case of nanowire arrays, the experimental results presented with the simulations made in order to understand the behaviour of such systems. ATTO 740 dye was used which proved to be highly instable and the SERS signature was continuously shifting. With the addition of the second dye molecule, the stability of the signal increased along with its efficiency. This is seen as a result of the shift of plasmon of the metal due to the change of refractive index with the addition of the dye. The other possibility is the chemical interaction of Rh6G with the nanostructured metal surface. Wavelength dependence studies have been made on the samples along with the polarization studies. The results have been substantiated with the simulations.

These results are very encouraging and they open up new avenues in terms of molecular plasmonics. We have seen experimentally that with the addition of rhodamine, the efficiency of SERS increases considerably. New experiments with different dye molecules which have different ionic properties and different molecular resonances will give a better understanding of the interactions that take place. Such a system when understood completely can be highly advantageous from a practical point of view. The plasmons of the system can be shifted with the appropriate dye molecules. The ability to tune the plasmon with such experiments will open up a whole new path to understand and utilize plasmonics since they will be both time effective and cost effective. The use of such samples can also be exploited in a favourable way since it is possible to visualize different scenarios in the same sample. The other possibilities are to make use of model systems comprising of lithographically made arrays of nanowires with varying interwire distances. Such samples will allow us to understand the plasmon coupling behaviour between the nanowires experimentally. The field enhancement in such a system could be studied with the help of appropriate dye molecules.

Collection-mode SNOM has been used on the nanowire arrays in order to have a spatial resolved picture of the optical behavior at the local scale. Collection-mode SNOM has been already reported in the past as an effective method to analyze plasmonic samples. There are however two original aspects in our investigation: the use of a specifically developed setup, featuring far field illumination from the top, in a predefined spot; the inherent interplay between local scale morphological disorder and global scale order of our samples, which make them to differ from both regular, lithographed systems and irregular nanoparticle samples.

With the SNOM we have mapped the intensity distribution of the near field at the sample surface aimed at the local field enhancements on the nanowire arrays and tried to relate their occurrence to the morphology of the sample.

Two different excitation wavelengths have been investigated in the same scan, one during forward and the other in the backward scan direction with the help of simple shutters. It is seen that the observations are in agreement with the macroscopic optical properties of the sample. Local field enhancements are in fact observed only in conditions suitable to excite local plasmon resonances. Two different excitation polarizations have been investigated. One along the nanowires and the other across them. The results are in agreement with what is observed in the SERS measurements. We have also made use of two different illumination modes. One in the constant excitation, where we map the hotspots on the sample. The local field enhancement is discussed in detail with the results comparing the polarization and wavelength of the illumination. The second one is the fixed excitation mode. In this case, the excitation spot is kept fixed with respect to the sample and propagation measurements can be made with such a set up. As far as we know, such a system has not been reported in the literature earlier. These measurements while not yet completely analyzed will turn useful to understand the specific mechanisms occurring in irregular metal nanowire arrays, where co-operative processes can take place involving adjacent nanowires. .

The future work in this line will be to demonstrate the role of plasmon resonance in ruling the scattering process in the near field with additional measurements. The occurrence of unexpected phenomena when the polarization of the excitation radiation is at 45 degrees with respect to the nanowire axis is to be analyzed carefully since such an analysis will be helpful to understand the complicated interplay between the disorder at the local scale, due to the nanoparticle-like morphology of the sample, and the global anisotropic ordering imposed by the nanowire structure. The application of two distinct, advanced and rather sophisticated techniques, which, for the SNOM at least, own a non conventional and non standard character, led to draw a picture of the plasmonic phenomena investigated where the effect of different, often concurrent, mechanisms has to be taken into account. This is for instance the case of SERS measurements on the nanowires with two co-deposited dye molecules (ATTO 740 and Rh6G) and the consequent shift of the plasmon resonance which can enhance the intensity of the SERS signal stemming from one of the dyes. In a similar fashion, the analysis of local optical properties enabled by SNOM suggest a complex scenario in which both the global anisotropy of the sample morphology (an array of parallel nanowire) and the inhomogeneity at the local scale contribute jointly to determine important effects, such as the intensity distribution, the occurrence of hot spots, the transfer of plasmon excitation across the sample.

Most of the findings coming out from this thesis are not documented in the

literature, even though methods and tools are not always original. This is probably a consequence of the fact that the literature is often aimed at demonstrating theories on model systems, accurately tailored to achieve specific results. On the contrary, in our case the analysis has been carried mostly on real systems, featuring properties not always tuned to exhibit a specific response to the variation of a specific parameter. As already stated, while being puzzling from the point of view of interpretation, which in some cases will deserve further confirmation and interpretative efforts, such a situation stimulates the search for practical applications of the samples, tools and methods used within this thesis beyond those presently available.

---

# Appendix

## .1 DDSCAT

DDSCAT is the most popular code available for the implementation of the DDA method. The code has been developed by astrophysicist B. T. Draine (Princeton University) and P. J. Flatau (UCSD) and is freely available along with a comprehensive user guide. Here I have described some important steps and considerations that were involved in my experience with DDSCAT. The DDSCAT 6.1 code that I used in my studies is available in Fortran and therefore standard compilers were used to build the DDSCAT executable for

- (a) Windows-based PC
- (b) UNIX/LINUX system. The procedure for running the DDSCAT executable differed slightly depending on the system used.

### .1.1 Input

In addition to the executable, two additional files serve as the input for the program. The first one is the `diel.tab` (a sample available with the DDSCAT package), which contains the information of the dielectric function of the target material. In this file, real and imaginary parts of the material refractive index,  $n$  and  $k$  are listed sequentially for the different wavelengths in the spectral range in which the calculations are to be run. Note that values of the wavelength,  $n$  and  $k$  have to be normalized by the medium refractive index. Thus, the wavelength of light used in the calculation is that in the medium. In the case of structures with multiple components, a separate dielectric file corresponding to each component has to be used. The second file is the parameter file `ddscat.par` (a sample available with the DDSCAT package), which specifies all other input parameters for the DDA simulation. Important parameters include

- (a) The shape definition: The shape is defined by the variable CSHAPE. A number of standard definitions are available within DDSCAT including ellipsoids (ELLIPS), cylinders (CYLNDR) and triangular prisms (PRISM3), which I have used commonly. The relative dimensions of the target are specified by the shape parameters PAR1 PAR2 PAR3, which are the number of dipoles along each dimension of the shape. For example, a spheroid of aspect ratio 4 can be represented as 40 10 10 or 80 20 20.
- (b) Number of dipoles: The difference between the above two cases is that the latter case simulates the structure with 8x greater number of dipoles. The greater the number of dipoles, the better is the accuracy of the calculations, but the higher is the computational cost. I have used on a case-to-case basis between 0.5 to 2 dipoles per nm dimension of the nanostructure with good results. The general rule is that the interdipole lattice spacing should be much smaller than the wavelength of the light and the size of the nanostructure to get reliable results. For instance, it would not be reasonable for a spheroid of 10 nm width and 40 nm length to be defined by (PAR1, PAR2, PAR3) = (4, 1, 1).
- (c) Size: The number of dipoles along each dimension does not specify the real size of the structure. The actual size of the target structure is defined by its effective radius, which is equal to  $(3V/4\pi)^{1/3}$  where V is the total volume occupied by the target.
- (d) Wavelength: The range of wavelengths has to be specified (same units, i.e. microns, as the effective radius) along with the number of intervals at which the calculations are to be run.
- (e) The polarization of the light can be chosen to be along the x, y, or z directions by defining e01 vector. E.g., e01 = (0.,0.) (1.,0.) (0.,0.) implies polarization along the y-axis. However, it must be noted that the target orientation with respect to light can also be changed by specifying the angles beta, theta, and phi.
- (f) The number of components can be specified by NCOMP along with the identification of each of their dielectric files.

## .1.2 Non-standard Shapes or Structures

For defining target shapes or structures, which are not standard to DDSCAT, a third file shape.dat has to be used as the input for the shape definition. CSHAPE is set to FRMFIL in this case and the name of the file is passed

instead of the shape parameters. The shape.dat file specifies the number of dipoles and the (x,y,z) lattice positions of all the dipoles. While any suitable method can be used to generate a dipolar array that defines a custom shape, I have frequently used the graphing software Origin to combine standard shapes to give the custom shape. DDSCAT provides a separate routine that generates a target.out file for a specified standard shape. The target.out file has a format very similar to shape.dat. It specifies the total number of dipoles in the specified shape and (x,y,z) positions of each one of them. All the standard shape definition (target.out) files that need to be combined are imported into an Origin worksheet. The different shapes can be moved, rotated, or truncated along any of the dimensions by use of standard Origin add, multiply or subtract operations on the X, Y, Z columns. Very basic knowledge of vectors helps to determine the operation to be used. Once the custom shape is built, it can be plotted in 3-D to verify accuracy, following which the worksheet can be exported into a shape.dat file. A couple of examples of custom-built shapes are given below.

- (a) A colloidal nanorod shape can be generated by combining in Origin a cylinder with a hemisphere (diameter = cylinder width) capping each end of the cylinder. The hemispheres can be obtained by splitting a sphere into half.
- (b) For defining dimers, trimers, or larger assemblies of particles of given shape, the shape definition file of the single particle can be duplicated the desired number of times in Origin. In order to change the inter-particle spacing, the different particles can be moved with respect to one another by Origin column operations.

### .1.3 Program Execution

Once all the input parameters and files have been set, the executable is run. The executable terminates immediately if there is an error in any of the parameter definitions or in the file formats of ddscat.par or diel.tab. In addition, if the number of dipoles exceeds that allowed by the memory allocation of the DDSCAT program, it will terminate. In order to run DDSCAT on the supercomputer (to take advantage of fast parallel computations), all the files including the UNIX/LINUX-compiled executable, the parameter file, the dielectric files, and shape.dat files, if any, have to be transferred by an ssh utility to the user folder, which in my case was located on Egate (egate.chemistry.gatech.edu). The executable cannot be run directly on the supercomputer. Instead, an additional job file (with .cmd extension) is re-

quired to be submitted, which contains the details of the program/job to be run.

### **.1.4 Output**

In the case of a successful run, an output file is created for each of the wavelengths, e.g. w000r00ori.avg, w001r00ori.avg, w000r00ori.avg, and so on. Note that multiple effective radii can also be specified in `ddscat.par` in which case a file will be generated for each combination of wavelength and effective radius. The important quantities calculated are  $Q_{ext}$ ,  $Q_{abs}$ , and  $Q_{sca}$  which can be found in the output file (for each wavelength) along with several other quantities, that may or may not be needed depending on the user or the end-utility.

---

# Bibliography

- [1] Faraday. M. *Philos. Trans. R. Soc. London*, 147:145, 1857.
- [2] A. M. Schwartzberg and J. Z. Zhang. Novel optical properties and emerging applications of metal nanostructures. *J. Chem. Phys. C*, 112:28, 2008.
- [3] J.-Y. Kim and J.-S Lee. Synthesis and thermally reversible assembly of DNA' gold nanoparticle cluster conjugates. *Nano Lett.*, 9:4564, 2009.
- [4] M. C. Daniel and D. Astruc. Gold nanoparticles: assembly, supramolecular chemistry, quantum-size-related properties, and applications toward biology, catalysis, and nanotechnology. *Chem. Rev.*, 104:293, 2004.
- [5] K. J. Prashant, Kyeong S. L., H. Ivan, M. El Sayed, and A. El Sayed. Calculated absorption and scattering properties of gold nanowires of different size, shape and composition: Applications in biological imaging and biomedicine. *J. Phys. Chem. B*, 110:7238, 2006.
- [6] J. Yang, J. You, C. C. Chen, W.-C. Hsu, H.-R. Tan, X. W. Zhang, Z. Hong, and Y. Yang. Plasmonic polymer tandem solar cell. *ACS Nano*, 5:6210, 2011.
- [7] S. Eustis and M. A. El Sayed. Why gold nanoparticles are more precious than pretty gold: Noble metal surface plasmon resonance and its enhancement of the radiative and nonradiative properties of nanocrystals of different shapes. *Chem. Soc. Rev*, 35:209, 2006.
- [8] E. Ozbay. Plasmonic: Merging photonics and electronics at nanoscale dimensions. *Science*, 311:189, 2006.
- [9] W. L. Barnes, A. Dereux, and T. W. Ebbesen. Surface plasmon sub-wavelength optics. *Nature*, 424:824, 2003.

- [10] A. Toma, D. Chiappe, D. Massabo, C. Boragno, and F. Buatier de Mongeot. Self organised metal nanowire arrays with tunable optical anisotropy. *Appl. Phys. Lett.*, 93:163104, 2008.
- [11] A. Toma, F. Buatier de Mongeot, R. Buzio, G. Firpo, S. R. Bhattacharyya, C. Boragno, and U. Valbusa. Ion beam erosion of amorphous materials: evolution of surface morphology. *Nucl. Instrum. Methods Phys. Res., Sect. B*, 230:551, 2005.
- [12] S. Rusponi, G. Costantini, F. Buatier de Mongeot, C. Boragno, and U. Valbusa. Patterning a surface on the nanometric scale by ion sputtering. *Appl. Phys. Lett.*, 75:3318–3320, 1999.
- [13] K. M. Mayer and J. H. Hafner. Localized surface plasmon resonance sensors. *Chem. Rev.*, 111:3828, 2011.
- [14] J. Homola, S. Y. Sinclai, and G. Gauglitz. Surface plasmon resonance sensors: review. *Sens. Actuators, B*, 54:3, 1999.
- [15] J. Prashant, X. Huang, I. El-Sayed, and M. El-Sayed. Review of some interesting surface plasmon resonance-enhanced properties of noble metal nanoparticles and their applications to biosystems. *Plasmonics*, 2:107, 2007.
- [16] J. Zhang, L. Zhang, and W. Xu. Surface plasmon polaritons: physics and applications. *J. Phys. D: Appl. Phys.*, 45:113001, 2012.
- [17] H. Raether. *Surface Plasmons on Smooth and Rough Surfaces and on Gratings*. Springer Tracts in Modern Physics, 1988.
- [18] E. Kretschmann and H. Reather. Radiative decay of nonradiative surface plasmon excited by light. *Z. Naturforsch., A: Phys. Sci.*, 23:2135, 1968.
- [19] E. Kretschmann. Die bestimmung optischer konstanten von metallen durch anregung von oberflächenplasmaschwingungen. *Z. Phys.*, 241:313, 1971.
- [20] V. Z. Anatoly, I. I. Smolyaninov, and A. A. Maradudin. Nano-optics of surface plasmon polaritons. *Phys. Rep.*, 408:131, 2005.
- [21] A. Otto. Excitation of nonradiative surface plasma waves in silver by the method of frustrated total reflection. *Z. Phys. A: At. Nucl.*, 216:398, 1968.

- [22] M. W. Knight, N. K. Grady, R. Bardhan, F. Hao, P. Nordlander, and N. J. Halas. Nanoparticle-mediated coupling of light into a nanowire. *Nano Lett.*, 7:2346, 2007.
- [23] S. A. Maier. *Plasmonics: fundamentals and applications*. Springer, 2007.
- [24] E. C. Le Ru, M. Meyer, and P. G. Etchegoin. Proof of single-molecule sensitivity in surface enhanced raman scattering (sers) by means of a two-analyte technique. *J. Phys. Chem. B*, 110:1944, 2006.
- [25] G. Mie. Beitrage zur optik truber medien. *Ann. d. Physik*, 25:377, 1908.
- [26] C. F. Bohren and D. R. Huffman. *Absorption and scattering of light by small particles*. Wiley VCH, 1983.
- [27] J. J. Mock, M. Barbic, D. R. Smith, D. A. Schultz, and S. Schultz. Shape effects in plasmon resonance of individual colloidal Silver nanoparticles. *J. Chem. Phys.*, 116:6755–6759, 2002.
- [28] J. J. Mock, D. R. Smith, and S. Schultz. Local refractive index dependence of plasmon resonance spectra from individual nanoparticles. *Nano Lett.*, 3:485, 2003.
- [29] Fleischman M., Hendra P. J., and McQuillian A. J. Title. *Chem. Phys. Lett*, 26:123, 1974.
- [30] D. L. Jeanmaire and R. P. V. Duyne. abc. *J. Electroanal. Chem.*, 84:1, 1977.
- [31] M. G. Albrecht and J. A. Creighton. Anomalous intense Raman spectra of pyridine at a silver electrode. *J. Am. Chem. Soc.*, 99:5215, 1977.
- [32] M. Maskovits. Surface enhanced Raman spectroscopy. *J. Raman Spectrosc.*, 36:485, 2005.
- [33] K. Kneipp, Y. Wang, R. Dasari, and M. Feld. Approach to single molecule detection using surface-enhanced resonance raman scattering (serrs): A study using rhodamine 6g on colloidal silver. *Appl. Spectrosc.*, 49:780, 1995.
- [34] K. Kneipp, Y. Wang, H. Kneipp, L. T. Perelman, I. Itzkan, R. Dasari, and M. Feld. Single molecule detection using Surface Enhanced Raman spectroscopy. *Phys. Rev. Lett*, 78:1667, 1997.

- [35] S.M. Nie and S. Emory. Probing single molecules and single nanoparticles by surface enhanced Raman scattering. *Science*, 275:1102, 1997.
- [36] A. Otto. What is observed in single molecule SERS, and why? *J. Raman Spectrosc.*, 33:593, 2002.
- [37] X. Zhang, C. R. Yonzon, M. A. Young, D. A. Stuart, and R. P. Van Duyne. Surface-enhanced Raman spectroscopy biosensors: excitation spectroscopy for optimisation of substrates fabricated by nanosphere lithography. *IEE Proc.-Nanobiotechnol.*, 152:195, 2005.
- [38] L. Billot, M. Lamy de la Chapelle, A.-S. Grimault, A. Vial, D. Barchiesi, J.-L. Bijeon, P.-M. Adam, and P. Royer. Surface enhanced Raman scattering on gold nanowire arrays: Evidence of strong multipolar surface plasmon resonance enhancement. *Chem. Phys. Lett.*, 422:303, 2006.
- [39] J. Grand, M. L. de la Chapelle, J.-L. Bijeon, P. M. Adam, A. Vial, and P. Royer. Role of localized surface plasmons in surface-enhanced Raman scattering of shape-controlled metallic particles in regular arrays. *Phys. Rev. B*, 72:033407, 2005.
- [40] H. Wei, F. Hao, Y. Huang, W. Wang, P. Nordlander, and H. Xu. Polarisation dependence of surface enhanced Raman scattering in Gold nanoparticle nanowire systems. *Nano Lett.*, 8:2497, 2008.
- [41] C. Sonnichsen, S. Geier, N.E. Hecker, G. Von Plessen, and J. Feldmann. Spectroscopy of single metallic nanoparticles using total internal reflection. *Appl. Phys. Lett.*, 77:2949, 2000.
- [42] C. V. Raman and K. S. Krishnan. A new class of spectra due to secondary radiation. Part I. *Indian J. Phys.*, 2:387–398, 1928.
- [43] E.C. Le Ru, M. Meyer, E. Blackie, and P.G. Etchegoin. Advanced aspects of electromagnetic SERS enhancement factors at a hot spot. *J. Raman Spectrosc.*, 39:1127, 2008.
- [44] E. Le Ru and P. Etchegoin. *Principles of surface enhanced Raman spectroscopy and related plasmonic effects*. Elsevier, 2009.
- [45] K. Kneipp, H. Kneipp, I. Itzkan, R. R. Dasari, and M. S. Feld. Surface enhanced Raman scattering and biophysics. *J. Phys. Condens. Matter*, 14:R597, 2002.

- [46] A. A. Stacy and R. P. Van Duyne. Surface enhanced Raman and resonance Raman spectroscopy in a non-aqueous electrochemical environment: Tris(2,2-bipyridine)ruthenium(ii) adsorbed on silver from acetonitrile. *Chem. Phys. Lett.*, 102(4):365 – 370, 1983.
- [47] T. Vosgrone and A. J. Meixner. Surface- and resonance-enhanced micro-raman spectroscopy of xanthene dyes: From the ensemble to single molecules. *ChemPhysChem*, 6:154, 2005.
- [48] M. Futamata and Y. Maruyama. Electromagnetic and chemical interaction between Ag nanoparticles and adsorbed rhodamine molecules in surface enhanced raman scattering. *Anal. Bioanal. Chem.*, 388:89, 2007.
- [49] P. Drake, H.-W. Chang, and Y.-J. Lin. The design of peptide linker group to enhance the SERS signal intensity of an atto680 dye-nanoparticle system. *J. Raman Spectrosc.*, 41:1248, 2010.
- [50] M. L. Tran, S. P. Centeno, J. A. Hutchison, H. Engelkamp, D. Liang, G. Van Tendeloo, B. F. Sels, J. Hofkens, and H. Uji-I. Nanoparticle-mediated coupling of light into a nanocontrol of surface plasmon localization via self-assembly of silver nanoparticles along silver nanowires. *J. Am. Chem. Soc.*, 130:17240, 2008.
- [51] R. Yan, P. Pausauskie, J. Huang, and P. Yang. Direct photonic plasmonic coupling and routing in single nanowires. *Proceedings of the National Academy of Sciences*, 106:21045, 2009.
- [52] X. Huang, I. H. El-Sayed, W. Qian, and M. A. El-Sayed. Cancer cells assemble and align gold nanorods conjugated to antibodies to produce highly enhanced, sharp, and polarized surface Raman spectra: A potential cancer diagnostic marker. *Nano Lett.*, 7:1591, 2007.
- [53] E. Podstawka, Y. Ozaki, and L. M Proniewicz. Part i: Surface-enhanced Raman spectroscopy investigation of amino acids and their homodipeptides adsorbed on colloidal silver. *Appl. Spectrosc.*, 58:570, 2004.
- [54] E. S. Grabbe and R. P. Buck. Surface-enhanced Raman spectroscopic investigation of human immunoglobulin G adsorbed on a silver electrode. *J. Am. Chem. Soc.*, 111:8362, 1989.
- [55] D. Naumann. Ft-infrared and ft-raman spectroscopy in biomedical research. *Appl. Spectrosc. Rev.*, 36:239, 2001.

- [56] A. W. Sanders, D. A. Routenberg, B. J. Wiley, Y. Xia, E. R. Dufresne, and M. A. Reed. Observation and plasmon propagation, redirection, and fan-out in Silver nanowires. *Nano Lett.*, 6:1822, 2006.
- [57] J. A. Hutchison, S. P. Centeno, H. Odaka, H. Fukumura, J. Hofkens, and H. Uji-i. Subdiffraction limited surface enhanced Raman scattering. *Nano Lett.*, 9:995, 2009.
- [58] Z. Wang and L. J. Rothberg. Origins of blinking in single-molecule Raman spectroscopy. *J. Phys. Chem. B.*, 109:3387, 2005.
- [59] K. H. Su, Q. H. Wei, X. Zhang, J. J. Mock, D. R. Smith, and S. Schultz. Interparticle coupling effects on plasmon resonances of nanogold particles. *Nano Lett.*, 3:1087, 2003.
- [60] Y. Maruyama and M. Futamata. Elastic scattering and emission correlated with single-molecule SERS. *J. Raman Spectrosc.*, 36:581, 2005.
- [61] Y. Huang, Y. Fang, and M. Sun. Remote excitation of surface-enhanced Raman scattering on single Au nanowire with quasi-spherical termini. *J. Phys. Chem. C*, 115:3558, 2011.
- [62] S. J. Lee, J. M. Baik, and M. Moskovits. Polarization-dependent surface-enhanced Raman scattering from a silver-nanoparticle-decorated single silver nanowire. *Nano Lett.*, 8:3244, 2008.
- [63] D. E. Chang, A. S. Sorensen, P. R. Hemmer, and M. D. Lukin. Strong coupling of single emitters to surface plasmons. *Phys. Rev. B*, 76:035420, 2007.
- [64] I. P. Kaminow, W. L. Mammel, and H. P. Weber. Metal-clad optical waveguides: Analytical and experimental study. *Appl. Opt.*, 13:396, 1974.
- [65] D. Solis, W. S. Chang, B. P. Khanal, K. Bao, P. Nordlander, E. R. Zubarev, and S. Link. Bleach-imaged plasmon propagation (BIIPP) in single gold nanowires. *Nano Lett.*, 10(9):3482, 2010.
- [66] P.G. Wu and L. Brand. Resonance energy transfer: Methods and applications. *Anal. Biochem.*, 218:1, 1994.
- [67] W. Khunsin, B. Brian, J. Dorfmueller, M. Esslinger, R. Vogelgesang, C. Etrich, C. Rockstuhl, A. Dmitriev, and K. Kern. Long-distance indirect excitation of nanoplasmonic resonances. *Nano Lett.*, 11:2765, 2011.

- [68] M. E. Stewart, C. R. Anderton, L. B. Thompson, J. Maria, S. K. Gray, J. A. Rogers, and R. G. Nuzzo. Nanostructured plasmonic sensors. *Chem. Rev.*, 108:494, 2008.
- [69] J. R. Krenn, B. Lamprecht, H. Ditlbacher, G. Schider, M. Salerno, A. Leitner, and F. R. Aussenegg. Non diffraction-limited light transport by gold nanowires. *Europhys. Lett.*, 60:663, 2002.
- [70] M. Hu, C. Novo, A. Funston, H. Wang, H. Staleva, S. Zou, P. Mulvaney, Y. Xia, and G. V. Hartland. Dark-field microscopy studies of single metal nanoparticles: understanding the factors that influence the linewidth of the localized surface plasmon resonance. *J. Mater. Chem.*, 18:1949, 2008.
- [71] A. I. Henry, J. M. Bingham, E. Ringe, L. D. Marks, G. C. Schatz, and R. P. Van Duyne. Correlated structure and optical property studies of plasmonic nanoparticles. *J. Phys. Chem. C*, 115(19):9291–9305, 2011.
- [72] A. Toma, D. Chiappe, C. Boragno, and F. Buatier de Mongeot. Self-organized ion-beam synthesis of nanowires with broadband plasmonic functionality. *Phys. Rev. B*, 81:165436, 2010.
- [73] H. DeVoe. Optical properties of molecular aggregates. i. classical model of electronic absorption and refraction. *J. Chem. Phys.*, 41:393, 1964.
- [74] H. DeVoe. Optical properties of molecular aggregates. ii. classical theory of the refraction, absorption, and optical activity of solutions and crystals. *J. Chem. Phys.*, 43:3199, 1965.
- [75] E. M. Purcell and C. R. Pennypacker. Scattering and absorption of light by nonspherical dielectric grains. *Astrophys. J.*, 186:705, 1973.
- [76] B. T. Draine. The discrete-dipole approximation and its application to interstellar graphite grains. *Astrophys. J.*, 333:848, 1988.
- [77] S. B. Singham and G. C. Salzman. Evaluation of the scattering matrix of an arbitrary particle using the coupled dipole approximation. *J. Chem. Phys.*, 84(5):2658–2667, 1986.
- [78] S. B. Singham and C. F. Bohren. Light scattering by an arbitrary particle: a physical reformulation of the coupled dipole method. *Opt. Lett.*, 12(1):10–12, Jan 1987.
- [79] B. T. Draine and P. J. Flatau. User guide for the discrete dipole approximation. <http://arxiv.org/abs/astro-ph/0409262v2>, 1:83, 2004.

- [80] B. T. Draine and P. J. Flatau. Discrete-dipole approximation for scattering calculations. *J. Opt. Soc. Am. A*, 11:1491, 1994.
- [81] J. Zhao, L. Jensen, J. Sung, S. Zou, G. C. Schatz, and R. P. Van Duyne. Interaction of plasmon and molecular resonances for rhodamine 6g adsorbed on silver nanoparticles. *J. Am. Chem. Soc.*, 129:7647, 2007.
- [82] P. K. Jain, W. Huang, and M. A. El-Sayed. On the universal scaling behavior of the distance decay of plasmon coupling in metal nanoparticle pairs: A plasmon ruler equation. *Nano Lett.*, 7:2080, 2007.
- [83] Y. Maruyama, M. Ishikawa, and M. Futamata. Thermal activation of blinking in SERS signal. *J. Phys. Chem. B*, 108:673, 2004.
- [84] X-M. Qian and S. M. Nie. Single-molecule and single-nanoparticle SERS: from fundamental mechanisms to biomedical applications. *Chem. Soc. Rev.*, 37:912, 2008.
- [85] S. Underwood and P. Mulvaney. Effect of the solution refractive index on the color of gold colloids. *Langmuir*, 10(10):3427–3430, 1994.
- [86] P. Hildebrandt and M. Stockburger. Surface-enhanced resonance Raman spectroscopy of Rhodamine 6G adsorbed on colloidal silver. *J. Chem. Phys.*, 88:5935, 1984.
- [87] G. Haran. Single-molecule Raman spectroscopy: A probe of surface dynamics and plasmonic fields. *Acc. Chem. Res.*, 43:1135, 2010.
- [88] A. Debarre, R. Jaffiol, C. Julien, P. Tchenio, and M. Mostafavi. Raman scattering from single Ag aggregates in presence of EDTA. *Chem. Phys. Lett*, 386:244, 2004.
- [89] N. Chandrasekharan, P. V. Kamat, J. Hu, and G. Jones. Dye-capped Gold nanoclusters: Photoinduced morphological changes in Gold/Rhodamine 6G nanoassemblies. *J. Phys. Chem. B*, 104:11103, 2000.
- [90] A. M. Schwartzberg, C. D. Grant, A. Wolcott, C. Talley, E. Chad, E. Huser, R. Thomas, R. Bogomolni, and J. Z. Zhang. Unique Gold nanoparticle aggregates as a highly active surface-enhanced Raman scattering substrate. *J. Phys. Chem. B*, 108(50):19191–19197, 2004.
- [91] B. Fazio, C. d’Andrea, F. Bonaccorso, A. Irrera, G. Calogero, C. Vasi, P. G. Gucciardi, M. Allegrini, A. Toma, D. Chiappe, C. Martella, and

- F. Buatier de Mongeot. Re-radiation enhancement in polarized surface-enhanced resonant Raman scattering of randomly oriented molecules on self-organized gold nanowires. *ACS Nano*, 5(7):5945–5956, 2011.
- [92] K. Imura, H. Okamoto, M. K. Hossain, and M. Kitajima. Visualization of localized intense optical fields in single gold, nanoparticle assemblies and ultrasensitive raman active sites. *Nano Lett.*, 6:2173, 2006.
- [93] J. R. Lombardi, R. L. Birke, T. Lu, and J. Xu. Charge-transfer theory of surface enhanced Raman spectroscopy: Herzberg-Teller contributions. *J. Chem. Phys.*, 84:4174, 1986.
- [94] A. C. Albrecht. On the theory of Raman intensities. *J. Chem. Phys.*, 34:1476, 1961.
- [95] P. J. Flatau and B. T. Draine. Fast near field calculations in the discrete dipole approximation for regular rectilinear grids. *Opt. Express*, 20:1247, 2012.
- [96] U. Durig, D. W. Pohl, and F. Rohner. Near-field optical-scanning microscopy. *J. Appl. Phys.*, 59:3318, 1986.
- [97] E. H. Synge. A suggested model for extending microscopic resolution into the ultra-microscopic region. *Phil. Mag.*, 6:356–362, 1928.
- [98] E. H. Synge. An application of piezo-electricity to microscopy. *Phil. Mag.*, 13:297, 1932.
- [99] J. A. O’Keefe. Resolving power of visible light. *J. Opt. Soc. Am.*, 46:359, 1956.
- [100] D. W. Pohl, W. Denk, and M. Lanz. Optical stethoscopy: Image recording with resolution  $\lambda/20$ . *Appl. Phys. Lett.*, 44:651, 1984.
- [101] A. Lewis, M. Isaacson, A. Harootunian, and A. Muray. Development of a 500 Angstrom resolution light microscope. *Ultramicroscopy*, 13:227, 1984.
- [102] E. Betzig, P. L. Finn, and J. S. Weiner. Combined shear force and near-field scanning optical microscopy. *Appl. Phys. Lett.*, 60:2484, 1992.
- [103] E. Betzig, M. Isaacson, and A. Lewis. Collection mode near-field scanning optical microscopy. *Appl. Phys. Lett.*, 51:2088, 1987.

- [104] R. Toledo-Crow, P. C. Yang, Y. Chen, and M. Vaez-Iravani. Near-field differential scanning optical microscope with atomic force regulation. *Appl. Phys. Lett.*, 60:2957, 1992.
- [105] F. Tantussi, V. Clerico, C. Martella, P. Vasanthakumar, F. Fuso, M. Allegrini, A. Toma, D. Chiappe, C. Boragno, and F. Buatier de Mongeot. Surface plasmon “hot spots” detected by near-field polarization spectroscopy. page PDPB3. Optical Society of America, 2010.
- [106] S. I. Bozhevolnyi. *Localization Phenomena in Elastic Surface Plasmon Polariton Scattering*, volume 82 of *Optical Properties of Nanostructured Random Media*. Topics Appl. Phys., 2002.
- [107] S. I. Bozhevolnyi and V. Coello. *Phys. Rev. B*, 64:115414–1–7, 2001.
- [108] S. Ducourtieux, V. A. Podolskiy, S. Grésillon, S. Buil, B. Berini, P. Gadenne, A. C. Boccara, J. C. Rivoal, W. D. Bragg, K. Banerjee, V. P. Safonov, V. P. Drachev, Z. C. Ying, A. K. Sarychev, and V. M. Shalaev. Near-field optical studies of semicontinuous metal films. *Phys. Rev. B*, 64:165403–1–13, 2001.
- [109] P. Gadenne and J. C. Rivoal. *Surface Plasmon Enhanced Nonlinearities*, volume 82 of *Optical Properties of Nanostructured Random Media*. Topics Appl. Phys., 2002.
- [110] K. Seal, M. A. Nelson, Z. C. Ying, D. A. Genov, A. K. Sarychev, and V.M. Shalaev. Growth, morphology, and optical and electrical properties of semicontinuous metallic films. *Phys. Rev. B*, 67:035318–1–13, 2003.
- [111] J. Laverdant, S. Buil, X. Quelin, and J. Lumin. Local field enhancements on gold and silver nanostructures for aperture near field spectroscopy. *J. Lumin.*, 127:176, 2007.
- [112] V. Krachmalnicoff, E. Castanie, Y. De Wilde, and R. Carminati. *Phys. Rev. Lett.*, 105:183901–1–4, 2010.
- [113] J. Laverdant, S. Buil, J.-P. Hermier, and X. Quelin. Near-field intensity correlations on nanoscaled random silver/dielectric films. *J. Nanophoton.*, 4:049505–1–6, 2010.
- [114] H.-Y. Chui, C.-H. Huang, C.-H. Chang, Y.-C. Lan, and H.-C. Chui. *Opt. Expr.*, 18:165, 2010.

- [115] G. Kaupp. *Open Surf. Sci. J.*, 3:20, 2011.
- [116] A. Bouhelier, J. Renger, M. R. Beversluis, and L. Novotny. *J. Micr.*, 210:220, 2003.
- [117] G. Shider, J. R. Krenn, W. Gotshy, B. Lamprecht, H. Ditlbacher, and A. Leitner. Optical properties of Ag and Au nanowire gratings. *J. Appl. Phys.*, 90:3825, 2001.
- [118] A. Toma, D. Chiappe, D. Massabo, C. Boragno, and F. Buatier de Mongeot. *Appl. Phys. Lett.*, 93:163104–7, 2008.
- [119] A. Toma, D. Chiappe, C. Boragno, and F. Buatier de Mongeot. *Phys. Rev. B*, 81:165436–1–7, 2010.
- [120] A. V. Zayats, I. I. Smolyaninov, and A. A. Maradudin. Nano-optics of surface plasmon polaritons. *Phys. Rep.*, 408:131, 2005.
- [121] J. R. Krenn and et al. *Phys. Rev. Lett.*, 82:2590, 1999.
- [122] A. Degiron, H. J. Lezec, N. Yamamoto, and T. W. Ebbesen. Optical transmission properties of a single subwavelength aperture in a real metal. *Opt. Commun.*, 239:61, 2004.
- [123] A. Belardini, M. C. Larciprete, M. Centini, E. Fazio, C. Sibilia, M. Bertolotti, A. Toma, D. Chiappe, and F. Buatier de Mongeot. *Opt. Expr.*, 17:3603, 2009.
- [124] I. Horcas, R. Fernández, J. M. Gómez-Rodríguez, J. Colchero, J. Gómez-Herrero, and A. M. Baro. WSXM: A software for scanning probe microscopy and a tool for nanotechnology. *Rev. Sci. Instrum.*, 78:013705, 2007.
- [125] S. Grésillon, L. Aigouy, A. C. Boccara, and J. C. Rivoal. Experimental observation of localized optical excitations in random metal-dielectric films. *Phys. Rev. Lett.*, 82:4520, 1999.
- [126] R. Hillenbrand, F. Keilmann, P. Hanarp, D. S. Sutherland, and J. Aizpurua. Coherent imaging of nanoscale plasmon patterns with a carbon nanotube optical probe. *Appl. Phys. Lett.*, 83:368, 2003.
- [127] J. Prikulis, P. Hanarp, L. Olofsson, D. Sutherland, and K. Mikael. Optical spectroscopy of nanometric holes in thin gold films. *Nano Letters*, 4(6):1003–1007, 2004.

- [128] A. Degiron and T.W. Ebbesen. The role of localized surface plasmon modes in the enhanced transmission of periodic subwavelength apertures. *J. Opt. A: Pure Appl. Opt.*, 7:s90, 2005.
- [129] K. S. Lee and M. El Sayed. Dependence of the enhanced optical scattering efficiency relative to that of absorption for gold metal nanorods on aspect ratio, size, end-cap shape, and medium refractive index. *J. Phys. Chem. B*, 109:20331, 2005.
- [130] S. Buil, J. Aubineau, J. Laverdant, and X. Quelin. Local field intensity enhancements on gold semicontinuous films investigated with an aperture nearfield optical microscope in collection mode. *J. Appl. Phys.*, 100:063530–1–5, 2006.
- [131] J. R. Krenn, J. C. Weeber, A. Dereux, E. Bourillot, J. P. Goudonnet, B. Schider, A. Leitner, F. R. Aussenegg, and C. Girard. Direct observation of localized surface plasmon coupling. *Phys. Rev. B*, 60:5029, 1999.
- [132] K.-H. Su, Q.-H. Wei, X. Zhang, J. J. Mock, D. R. Smith, and S. Schultz. Interparticle coupling effects on plasmon resonances of nanogold particles. *Nano Lett.*, 3:1087, 2003.
- [133] P. K. Jain, W. Huang, and M. A. El-Sayed. On the universal scaling behavior of the distance decay of plasmon coupling in metal nanoparticle pairs: A plasmon ruler equation. *Nano Lett.*, page 2080, 2007.
- [134] J. P. Kottmann and O. J. F. Martin. Plasmon resonant coupling in metallic nanowires. *Opt. Expr.*, 8:655, 2001.
- [135] G. Schider, J. R. Krenn, A. Hohenau, H. Ditlbacher, A. Leitner, F. R. Aussenegg, W. L. Schaich, I. Puscasu, B. Monacelli, and G. Boreman. Plasmon dispersion relation of Au and Ag nanowires. *Phys. Rev. B*, 68:155427, 2003.
- [136] J. J. Mock, S. J. Oldenburg, D. R. Smith, D. A. Schultz, and S. Schultz. Composite plasmon resonant nanowires. *Nano Lett.*, 2:465, 2002.
- [137] M. V. Sosnova, N. L. Dmitruk, A. V. Korovin, S. V. Mamykin, V. I. Myn-ko, and O. S. Lytvyn. Local plasmon excitations in one-dimensional array of metal nanowires for sensor applications. *Appl. Phys. B*, 340:3799, 2009.

- 
- [138] J. Berthelot, F. Tantussi, P. Rai, G. Colas des Francs, J. C. Weeber, A. Dereux, F. Fuso, M. Allegrini, and A. Bouhelier. *J. Opt. Soc. Am. B: Opt. Phys.*, 29:249, 2012.